Kinetics and Mechanisms of Halogen Reactions Involved in Atmospheric Ozone Depletion

Gavin Boakes
University College London

A thesis submitted in partial fulfilment for the degree of Doctor of Philosophy

ProQuest LLC
789 East Eisenhower Parkway
P.O. Box 1346
Ann Arbor, MI 48106-1346

Abstract

Kinetics and Mechanisms of Halogen Reactions Involved in Atmospheric Ozone Depletion

The purpose of this thesis is to address some of the uncertainties associated with the key gas phase reactions implicated in atmospheric ozone depletion. Laboratory studies, employing flash photolysis coupled with time resolved UV/visible absorption spectroscopy have been used to investigate the kinetics of several free radical reactions. The spectroscopy incorporated charge coupled device (CCD) technology which facilitated rapid time scale broad band data acquisition giving rise to unequivocal monitoring of multiple absorbing species. Classical or numerical models were used to simulate the experimental data by optimising kinetic parameters. The improvements in both the accuracy and the precision associated with the CCD studies have led to a profound improvement in our understanding of the roles of the free radical reactions studied in the Earth's atmosphere.

The focus of the studies in this thesis was the reactions of halogenated species. These species are known to destroy atmospheric ozone through the reaction schemes such as:

(1) $XO + XO \rightarrow 2X + O_2$

(2) $X + O_3 \rightarrow XO + O_2$

Here, species X represents a halogen atom: Cl, Br or I, and this halogen atom is continously regenerated following flux through reactions (1) and (2) promoting further ozone destruction. The relatively high atmospheric abundance of ozone (typically parts per million in the lower stratosphere) compared to halogen atoms and free radicals (parts per trillion) ensures that reaction (1) is the rate determining step in the ozone depletion cycle. Consequently, a knowledge of the rate of reactions of type (1) under appropriate atmospheric conditions is fundamental in assessing the extent of halogen induced atmospheric ozone depletion.

This thesis reports results from extensive investigations into three reactions of type (1)

(i) BrO + BrO A study at 298 K and 760 Torr

(ii) ClO + ClO A study over the ranges 206-320 K and 25-760 Torr, incorporating measurement of the differential ClO absorption cross section over this temperature range.

(iii) BrO + ClO A study over the ranges 210-320 K and 100-760 Torr.

Acknowledgements

There are several people to whom I would like to offer thanks for their support during the compilation of this thesis. I am happily in their debt.

First and foremost I would like to thank David Rowley for his encouragement and advice in the realm of the laboratory and his friendship and generosity beyond. Similarly I must thank my laboratory partners: Sarah Dixon, Kate Gawler, Daniel Stone and Amandeep Bolina. Although frustration forms an occasional but inevitable part of laboratory life, their presence was always a mitigating, never contributing factor. Special gratitude is also extended toward Hindy Mok, for her valuable help during the summer of 2002. I would also like express my appreciation for the support work carried out by the technical staff in the chemistry department at UCL. In particular I would like to single out Roy Northeast, who readily allowed me to jump the long queue for his services on numerous occasions when the laboratory was relocated.

I must also thank David Wilmouth and Jim Burkholder, who seemed genuinely delighted to supply me with vital kinetic or spectroscopic data. I am grateful to NERC for funding my research and lifestyle for the last three years.

I would also like to thank my family for their support, not only during the last four years, but all those preceding. On a similar note, I would like to thank my girlfriend, Gemma Moore, surely the most good-natured person in this city, for her encouragement and consideration, particularly during these last few unconventional months of our lives.

Finally, I would like to issue a collective thankyou to all those friends who supplied me with drinks during these frugal times. Their generosity did not pass unnoticed.

Gavin Boakes
London 2003

Preface

The following protocol has been applied to the use of equations and diagrams within this thesis:

- All figures and tables are numbered independently and sequentially within each chapter. Each example is headed with a title of the form *figure 2.4*, where *2* refers to the chapter number and *4* denotes the sequentially numbered figure within that chapter.

- All chemical are numbered sequentially within each chapter. Each example is annotated in the form *(3.6)*, where *3* refers to the chapter number and *6* denotes the sequentially numbered equation within that chapter. Where chemical equations are referred to in the text, the chapter number is dropped, hence *(6)*, to prevent cumbersome reading.

- All mathematical equations are ascribed sequential Roman numerals within each chapter. Each example is annotated in the form *(4.iv)*, where *4* refers to the chapter number and *iv* denotes the sequentially numbered equation within that chapter. Where chemical equations are referred to in the text, the chapter number is dropped, hence *(iv)*, to prevent cumbersome reading. Exceptions to the latter rule exist where a reference is made to a mathematical equation expressed within a different chapter, in which case the appropriate chapter number is reinstated for clarity.

- All external references are numbered sequentially within each chapter and annotated with superscripted numerals.

Chapter 1: Physics and Chemistry of the Atmosphere

Chapter 2: Photochemistry and Gas Kinetics

3. Flash Photolysis With UV/Visible Absorption Spectroscopy Incorporating CCD Detection

Chapter 1: Physics and Chemistry of the Atmosphere

1.1 Introduction

The composition of the Earth's atmosphere has interested philosophers and scientists since ancient times. The Greeks considered air as one of four elements comprising Earthly matter and it was not until as late as the seventeenth century that air was recognised as a mixture of gases. Nitrogen and oxygen were subsequently recognised as the major components of the atmosphere although for some time it was assumed that air must comprise some compound of these elements otherwise gravitational force would separate oxygen from its lighter counterpart. It is now known that gravitational separation is disrupted by mixing processes below altitudes of 100 km. This region is known as the homosphere. At higher altitudes gravitational separation can occur, indeed light gases can leave the atmosphere altogether. This region is termed the heterosphere and is characterised by an abundance of free electrons and ions such that ion-molecule interactions dominate its chemistry.

1.2 Atmospheric Pressure

Whilst gravitational force does not, therefore affect local atmospheric composition below 100 km it is responsible for the variation of atmospheric pressure with altitude, *via* the hydrostatic equation, (iii):

For an incremental increase in altitude, dz the drop in pressure can be expressed as dp, where g represents acceleration due to gravity and $\rho(z)$ the local air density:

(1.i) $dp = -\rho(z).g.dz$ since $dp = -dm.g/A$ and $dm = -\rho(z).A.dz$

dm represents the incremental change in the mass of air over an area, A with increasing dz. For an ideal gas $\rho(z) = Mp/RT$, where M is the mass of 1 mole of air, hence:

(1.ii) $dp = -Mp/RT\,.\,g.dz$

Rearranging and integrating between 0 and z leads to the hydrostatic equation:

(1.iii) $$p = p_0 \exp(-z/H)$$

where pressure, p is given at an altitude z, relative to p_0, the pressure at zero altitude. H refers to the scale height, which in turn is defined as $H = RT/Mg$. H can be evaluated as 7500 m by approximating T as 255 K (the average radiative temperature of the atmosphere) and M as 28.8 $gmol^{-1}$ (the average molar mass of an atmosphere composed of only N_2 and O_2 with a 4:1 abundance ratio). Hence atmospheric pressure falls exponentially with increasing altitude and H is the vertical distance over which atmospheric pressure falls by a factor of $1/e$.

Since atmospheric pressure and consequently density falls off exponentially with increasing height, it follows that the bulk of atmospheric matter is located at low altitudes. In fact the lowest 50 km of the atmosphere contains more than 99% of the total atmospheric mass. Since this region experiences less highly energetic solar radiation than at higher altitudes the prevailing view until recent times was that the homosphere was inert. This is now known to be untrue, indeed the structure and chemistry of the lower atmosphere is extremely complex.

1.3 Atmospheric Temperature

In contrast to the continuous fall in atmospheric pressure with increasing altitude, the vertical temperature profile of the atmosphere shows complexity and is illustrated schematically in figure 1.1.

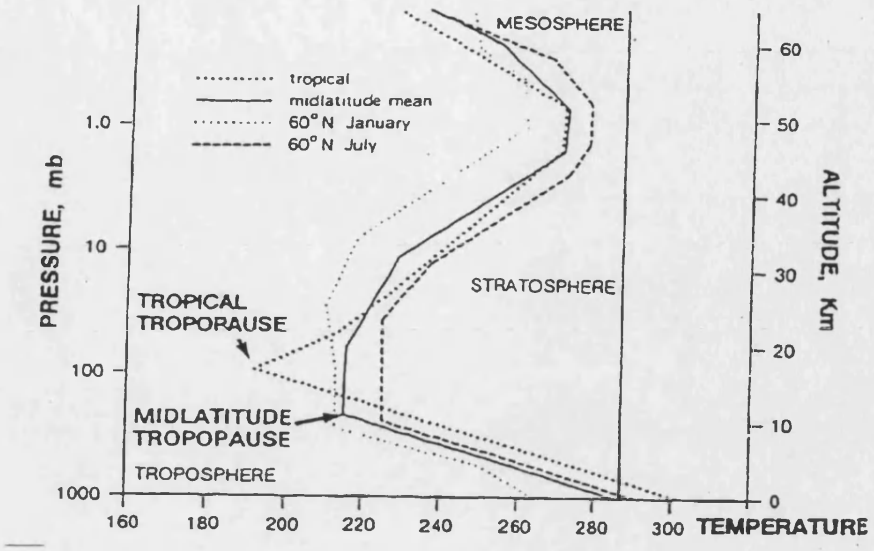

Figure 1.1: The temperature profile of the atmosphere.[1]

Beginning at ground level (z = 0), temperature falls with increasing altitude until a height of about 12-15 km. This lowermost region of the atmosphere is termed the troposphere. Any further increase in altitude is accompanied by an increase in temperature until a height of approximately 50 km is reached, defining the stratosphere. This temperature inversion can be attributed to the absorption of solar radiation dissociating ozone and subsequent recombination of the photolytic products. At higher altitudes the temperature falls once more until the edge of the homosphere at approximately 100 km. This region is known as the mesosphere. At altitudes in excess of this level apparent temperature inversion occurs once more. This increase in temperature arises from the very low number density at these high altitudes: molecular and atomic collisions become rare events so the absorption of high energy solar radiation leads to very high translational velocities.

1.4 Atmospheric Stability

The combination of the temperature profile and the pressure profile of the atmosphere determine the ease of vertical transport, the atmospheric stability. Consider an imaginary air parcel, initially in thermal equilibrium with its surroundings. Given that atmospheric pressure decreases with altitude, upward displacement of this parcel will

result in expansion, doing work. The First Law of Thermodynamics dictates that in the absence of heat transfer (adiabatic), the expanding air parcel will lose internal energy and cool. This process gives rise to a negative temperature gradient as a function of altitude. This rate of change of temperature with altitude for an air parcel devoid of any water is referred to as the dry adiabatic lapse rate (($\Gamma_d = (dT/dz)$) and has a value of -9.8 Kkm^{-1} at the Earth's surface. In reality the observed temperature gradient is somewhat more gentle at -6.5 Kkm^{-1}. This is because in practice the air parcels are not dry and upward transport is accompanied by condensation at lower temperatures. The consequent release of latent heat on condensation prohibits a truly adiabatic process and mitigates the temperature gradient.

The difference between the environmental lapse rate and that of a displaced air parcel determines the stability of the local atmosphere. Consider the case illustrated in figure 1.2, where an upwardly displaced parcel is warmer than the surrounding environment ($\Gamma_{parcel} > \Gamma_{env}$).

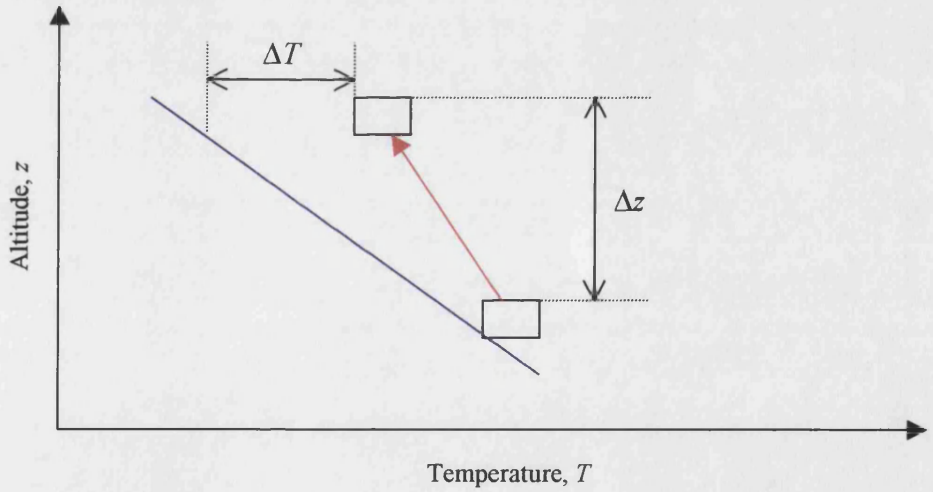

Figure 1.2: The parcel is unstable with respect to vertical transport. Γ_{env} and Γ_{parcel} are indicated in blue and red respectively.

Upon vertical displacement of the air parcel, the temperature change is dT_{parcel}. Over the same vertical displacement the environmental change is dT_{env}.

$$dT_{parcel} = \Gamma_{parcel}.dz \quad \text{and} \quad dT_{env} = \Gamma_{env}.dz$$

Thus, the difference, ΔT in temperature between the air parcel and its surrounding environment is:

$$\Delta T = (\Gamma_{parcel} - \Gamma_{env})dz$$

In the case illustrated in figure 1.2, $\Gamma_{parcel} > \Gamma_{env}$, thus the displaced parcel is warmer than its environment. It follows that at the same pressure the parcel will be less dense than its environment and will continue to rise. Hence vertical transport and mixing is promoted and the atmosphere is termed unstable. Conversely if $\Gamma_{parcel} < \Gamma_{env}$ such as the situation illustrated in figure 1.3, then the displaced parcel will be cooler and denser than its surroundings, thus a restoring force will act upon the parcel, returning it to its original altitude. Under these conditions the local atmosphere is resistant to vertical mixing and termed stable.

An extreme example is encountered in the stratosphere, where a positive environmental lapse rate is observed by definition. Γ_{parcel} meanwhile, is always negative since an expanding air parcel always does work, giving rise to a situation where $\Gamma_{parcel} << \Gamma_{env}$ hence ΔT is negative. This situation is shown in figure 1.4. As a result the stratosphere is extremely stable and vertical exchange times are long (months to years).

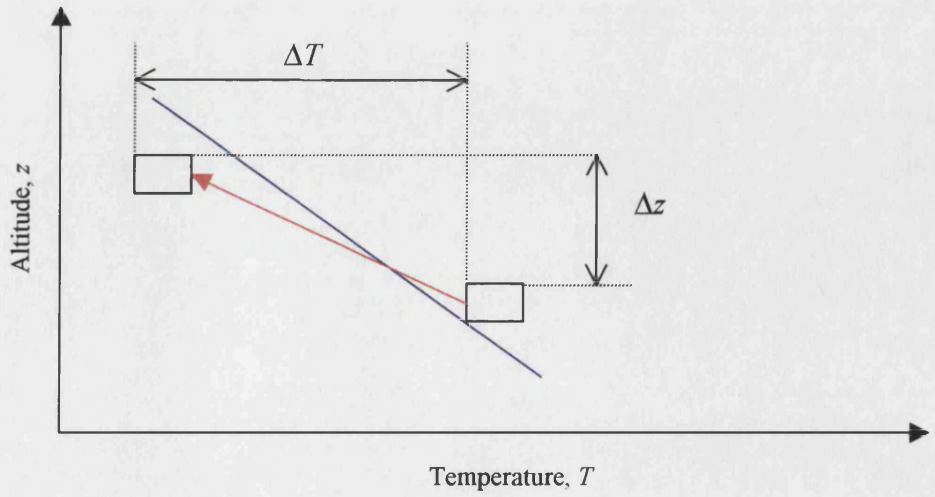

Figure 1.3: The parcel is stable with respect to vertical transport. Γ_{env} and Γ_{parcel} are indicated in blue and red respectively.

By contrast, in the troposphere where typically $\Gamma_{parcel} \approx \Gamma_{env}$ there is very little resistance to vertical movement and exchange times are short (days to weeks). The stability of the stratosphere inhibits exchange with the well mixed tropospheric air at their mutual boundary. This border between the troposphere and the stratosphere is termed the tropopause and effectively forms a barrier to vertical transport.

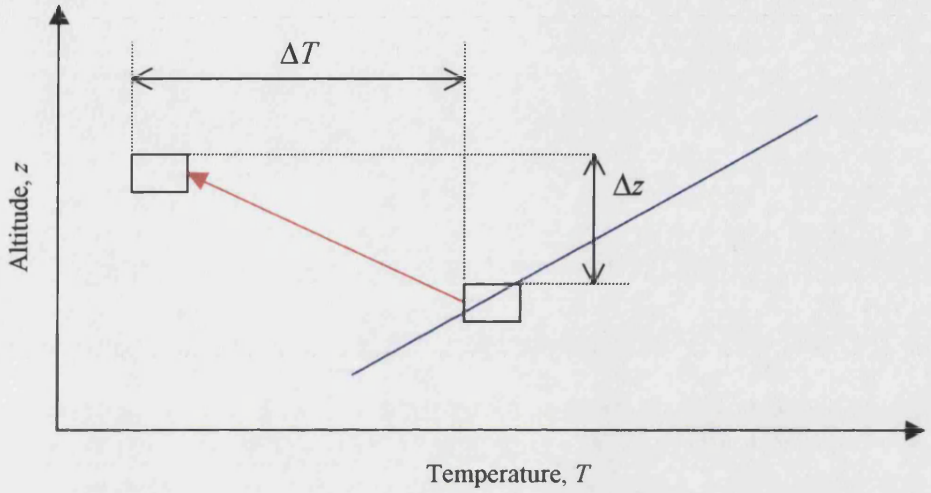

Figure 1.4: The parcel is extremely stable with respect to vertical transport, since Γ_{env} is positive. Γ_{env} and Γ_{parcel} are indicated in blue and red respectively.

The Earth's surface exerts a number of effects on the local atmosphere, giving rise to a lowermost region which is distinct from the free troposphere. The depth of this 'planetary boundary layer' (PBL) fluctuates (typically 0.5 to 2 km) according to surface fluxes of heat and water vapour in conjunction with larger scale structural effects associated with the rest of the atmosphere. Turbulent motion is induced by solar heating and frictional effects at the surface. These physical processes promote rapid mixing of air within the boundary layer, which in turn influences its chemical composition by bringing it in repeated contact with the Earth's surface.

1.5 Radiative Balance

The radiative balance of the atmosphere is controlled by its capacity to absorb solar radiation. This capacity, in conjunction with the competing processes of re-radiation

and conversion of photochemical into kinetic energy, leads to an effect on the Earth's surface temperature. Approximating the Earth to a black body with a non absorbing atmosphere whose clouds and surface backscatter 30% of the incoming solar radiation, balancing the energy flux provides an estimate of the surface temperature. The incoming energy per unit area is given by the solar constant, $S = 1370\ \mathrm{Wm^{-2}}$ and the effective area presented to the sun is approximated to a disc with the radius of the Earth. In contrast the outgoing energy is released from the entire surface of the planet. The Stefan Boltzmann law relates T to the emitted energy per unit area, thus:

$$\text{Energy absorbed at the surface} = \text{Energy emitted at the surface}$$

$$0.7 \times S \times \pi r_E^2 = \sigma T_E^4 \times 4\pi r_E^2$$

$$\therefore T_E = 255\ \mathrm{K}$$

Where σ is Stefan's constant ($5.67 \times 10^{-8}\ \mathrm{Wm^{-2}K^{-4}}$), r_E and T_E denote the Earth's radius and surface temperature respectively.

However, the mean surface temperature is evidently less hostile at a mean value of 288 K. This discrepancy arises from the photon energy (wavelength) difference in the characteristic emission spectra of the Earth and the Sun, due to the vast difference in surface (effective black body) temperature. The Sun has a mean surface temperature of 5780 K giving rise to a peak emission in the visible part of the electromagnetic spectrum. In contrast the 255 K terrestrial temperature has a spectral distribution maximised in the infra-red. As a result the Earth emits radiation at frequencies which can be absorbed and re-emitted by atmospheric molecules with appropriate IR modes, such as CH_4, O_3, H_2O and CO_2. This absorption and re-emission prevents a fraction of the Earth's radiation escaping from the planet and is known as the natural greenhouse effect. Concern has arisen in recent decades that the increase in anthropogenic emissions of these greenhouse gases may perturb the natural radiative balance of the atmosphere, potentially inducing climate change.

1.6 Atmospheric Photochemistry

Solar irradiation of the atmosphere is the driving force behind not only the physical conditions but also the spatial distribution of trace species. The relationship between ozone photochemistry and the atmospheric temperature profile illustrates the intimate link between physical and chemical processes. Moreover this link shows how the photochemical (and hence physical) environment changes as a result of the attenuation and scattering of solar radiation with increasing depth. Indeed solar radiation is not only responsible for the observed temperature profile *via* its interaction with ozone, but is also the original source of that ozone layer.

The spectrum of solar radiation at any given altitude is in principle controlled by the nature and abundance of any absorbing species overhead. Figure 1.5 compares the solar irradiation experienced at the top of the Earth's atmosphere, defined notionally as 100 km in altitude, with that at sea level.

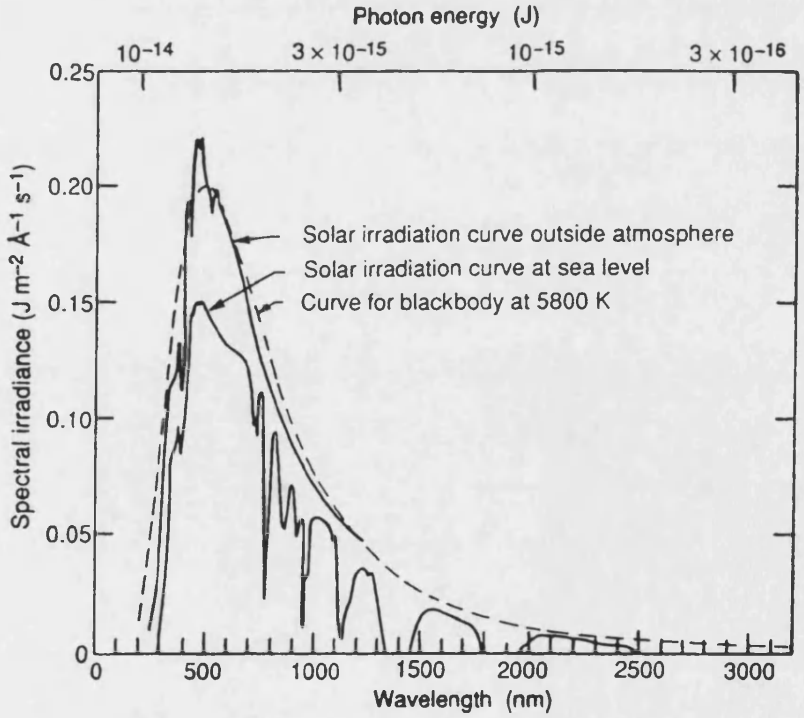

Figure 1.5: Comparison of the solar radiation experienced at the top of the Earth's atmosphere with that experienced at ground level.[1]

In practice, attenuation at UV and visible wavelengths is dominated by ozone and molecular oxygen. The strong absorptions by O_2 at wavelengths less than 240 nm and O_3 at wavelengths below 330 nm shield the Earth's surface from the most energetic of the Sun's rays. This has profound consequences for the Earth's biosphere since exposure to UV radiation can exert a direct effect on terrestrial biosystems, having been shown to induce erythema (skin cancer, see figure 1.6) and cataracts. Indirect influence on human welfare is exerted by the detrimental effect of UV on crop yields.

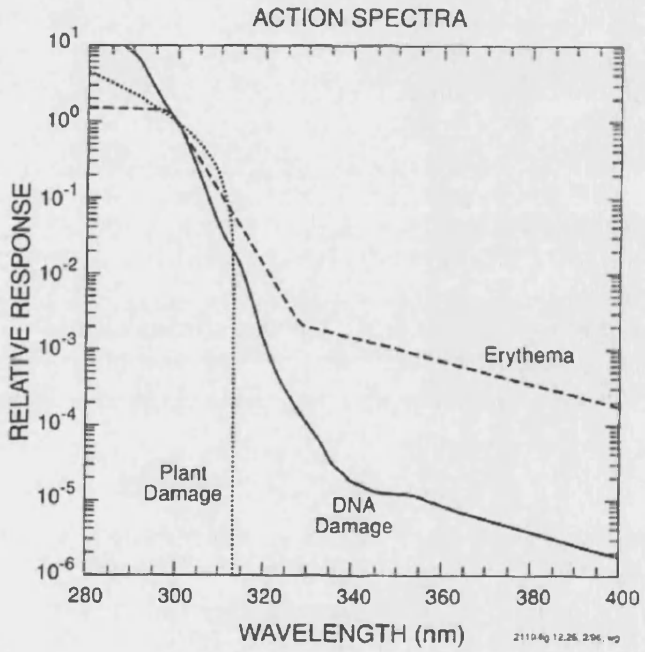

Figure 1.6: Action spectra for erythema induction, plant damage and DNA damage (normalised to unity at 300 nm).[2]

Solar radiation can lead to the photodissociation of molecular species in the atmosphere if the photon is sufficiently energetic and resonant with the molecular states which lead to an unbound state. The origin of stratospheric ozone lies in a photodissociative process, as alluded to above. Ozone production is initiated by the interaction of solar photons, whose wavelengths are less than 242 nm, with oxygen molecules. Absorption of such a photon gives rise to photolysis and subsequent reaction of the liberated oxygen atoms with molecular oxygen produces ozone. The

attenuation of of this short wave radiation with increasing atmospheric depth is responsible for the lower boundary of the ozone layer as will be discussed in section 1.8.

1.7 Chemical Composition

The bulk of the Earth's atmosphere is accounted for by just a few species. Contributions from N_2 (78% by volume), O_2 (21%), Ar (0.9%) and CO_2 (0.04%), together with a variable quantity of water vapour constitute more than 99.9% of atmospheric volume. The remaining fraction comprises many other molecules which are inevitably present in trace amounts. Despite their low abundances these species, summarised in table 1.1 exert a profound effect on the chemistry and physics of the atmosphere.

Of the key trace species in the atmosphere, water vapour assumes the most prominent role, exerting effects on many physical and chemical processes (e.g. the radiative effect of cloud formation). Water vapour is constantly recycled between the terrestrial reservoirs and the atmosphere, where it is primarily confined to the troposphere and typical content is a few percent. Transport of water vapour from the troposphere to the stratosphere occurs predominantly at low latitudes driven by solar heating (so called 'diabatic transport'). Moist tropospheric air is effectively freeze dried by the time it crosses the cold equatorial tropopause where temperatures are typically 190 K. Notwithstanding this efficient removal process, water is present in the stratosphere at a mixing ratio of a few ppmv. The principal source of this water vapour is thought to be the oxidation of methane.

Compound	Sources	Emission rate Tg/yr (1 Tg = 10^6 tonnes)
CH_4	Enteric fermentation, wetlands, natural gas leakage, combustion, biomass burning	400-500
CO	Atmospheric oxidation of VOC (volatile organic compounds), combustion, biomass burning	800
Isoprene (2-methyl 1,3 butadiene)	Natural vegetation	500
Other VOCs	Solvents, combustion, fermentation, natural vegetation, biomass burning	>>100
NO	Soil micro-organisms, lightning, combustion, aircraft	40
N_2O	Soil and marine micro-organisms, industrial processes, combustion	4.4 -10.5
NH_3	Breakdown of animal waste, soil micro-organisms	82
SO_2	Oxidation of DMS, volcanoes, fossil fuel combustion, refining & smelting	110
DMS	Marine micro-organisms	40
CH_3Cl	Marine and terrestrial micro-organisms, biomass burning	1.5
CH_3Br	Marine micro-organisms, agricultural application, biomass burning	0.1
CFCs/HCFCs	Solvents and refrigerants	1.1(*1990*)

Table 1.1: Sources and abundances of the trace constituents of the atmosphere.

In addition to its gas phase constituents, the atmosphere contains a significant amount of solid and liquid matter. Atmospheric aerosol is comprised of particles of varying radii, ranging from 10^{-3} to 10 micrometers. Aerosol may be matter swept or released (*e.g.* volcanic emission) from the surface. Alternatively, gas phase chemical processes

in the atmosphere can yield condensed products, such as the production of aerosol *via* the oxidation of SO_2 in the stratosphere. Atmospheric aerosol can play profound roles in the Earth's radiation budget directly by absorption and scattering, and indirectly by acting as cloud condensation nuclei. Aerosols can also influence the chemistry of the atmosphere by providing sites for heterogeneous reactions.

1.8 Atmospheric Ozone Chemistry

Ozone, the triatomic oxygen compound was first discovered by Christian Friedrich Schonbein in 1840, who noted its distinctive odour (the Greek verb *to smell* is *ozein*). Subsequent UV/visible spectroscopic investigation by Houzeay and later by Hartley indicated that ozone was present in the atmosphere, with greater concentrations at higher altitudes than at ground level. Crucially, Dobson and Fabry proved the existence of a distinct layer of ozone in the upper atmosphere during the early part of the last century.[3]

1.8.1 Stratospheric Ozone

In 1930 Chapman was the first to propose an explanation for the observed vertical distribution of atmospheric ozone.[4] He postulated the formation of a photostationary state incorporating the chemistry of oxygen alone:

(1.3)	$O_2 + h\nu$	$\rightarrow$	$O + O$	($\lambda < 242$ nm)
(1.4)	$O + O_2 + M$	$\rightarrow$	$O_3 + M$	
(1.5)	$O_3 + h\nu$	$\rightarrow$	$O_2 + O$	($\lambda < 1180$ nm)
(1.6)	$O + O_3$	$\rightarrow$	$O_2 + O_2$	
(1.7)	$O + O + M$	$\rightarrow$	$O_2 + M$	

It has since been shown that, given the abundance of O_2 and O_3 in the atmosphere, reaction (7) is too slow to compete with (4) and (6) and play a role in stratospheric ozone chemistry. Reactions (3) and (5) predominantly yield ground state $O(^3P)$ atoms, although higher energy (shorter wavelength) photons lead to some production of

excited $O(^1D)$ atoms. However, even at stratospheric number densities collisional deactivation to the ground state is their almost exclusive fate. The vertical $[O_3]$ profile observed in the atmosphere is a result of the variation in the balance of ozone production and destruction with altitude. In turn this balance is determined by the increase in number density and hence $[O_2]$, coupled with the decrease in solar radiation associated with descending altitude. Consequently there is an optimum altitude range for ozone production which is found in the stratosphere (z = 10-40 km). Given the vertical stability of the stratosphere this ozone is dynamically confined to a discrete layer.

Whilst the Chapman mechanism provides a qualitative explanation for the existence of atmospheric ozone, comparison of predictions from this mechanism with observations reveals that the scheme radically over predicts ozone mixing ratios over those observed in the stratosphere. This implies that either ozone production is overestimated or destruction underestimated. Moreover, since reactions (4) and (5) merely interconvert ozone with atomic oxygen they do not affect the overall abundance of these species which are collectively referred to as the "odd oxygen" (O_x) family. Reaction (3) is thus the source of odd oxygen and therefore ozone in the stratosphere. Reaction (6) is the sink of these species. Since the solar radiation profile and the stratospheric oxygen abundance ($[O_2]$ = 0.21[M]), which govern the rate of reaction (3) are well characterised, overestimation of ozone production through (3) is unlikely. By contrast the rate coefficient for reaction (6) has a high activation energy (E_a = 17 kJ mol^{-1})[5] and the rate of reaction (6) is too slow, especially at the temperatures associated with the stratosphere, to account for the lower than predicted ozone amounts. Ozone, being an intrinsically reactive molecule, does in fact react with many trace species in the atmosphere, forming O_2. The co-product of this reaction may then react further with atomic oxygen in the atmosphere (the source of atmospheric ozone) to form another oxygen molecule and also regenerate the original trace molecule. The generalised form of such a cycle is given below, note that flux through the cycle conserves X and XO and that the overall effect of this cycle is identical to reaction (6):

$$X + O_3 \rightarrow XO + O_2$$

	$XO + O$	$\rightarrow$	$X + O_2$
net:	$O + O_3$	$\rightarrow$	$2O_2$

A number of candidates for X/XO are present in the stratosphere, such as NO/NO_2, OH/HO_2, H/OH, Cl/ClO and Br/BrO. These species are present in the stratosphere in much lower abundances than ozone but because of its catalytic nature, the loss cycle may exert profound influences on odd oxygen mixing ratios. The efficiency of these catalytic cycles in ozone destruction is dependent on any competing processes which can perturb the cycle. Consider the NO/NO_2 catalytic cycle:

(1.8)	$NO + O_3$	$\rightarrow$	$NO_2 + O_2$	
(1.9)	$NO_2 + O$	$\rightarrow$	$NO + O_2$	
net:	$O + O_3$	$\rightarrow$	$2O_2$	

This cycle is believed to account for around 50% of the odd oxygen (defined as $O + O_3$) destruction in the stratosphere, despite the occurrence of a number of competing reactions. The most important of these is the rapid photolysis of NO_2. NO_2 photolysis in the sunlit stratosphere leads to odd oxygen production, constituting a null cycle since there is no net chemistry:

(1.8)	$NO + O_3$	$\rightarrow$	$NO_2 + O_2$	
(1.10)	$NO_2 + h\nu$	$\rightarrow$	$NO + O$	($\lambda < 398$ nm)
(1.4)	$O + O_2 + M$	$\rightarrow$	$O_3 + M$	
net:		no change		

Alternatively the catalytic ozone loss cycles can be broken completely by competing processes which convert the active, catalytic forms to inactive species which do not react with odd oxygen. Common examples of these species are $ClONO_2$ and HCl which can be formed as follows:

(1.11)	$ClO + NO_2 + M$	$\rightarrow$	$ClONO_2 + M$
(1.12)	$Cl + CH_4$	$\rightarrow$	$HCl + CH_3$

The fate of these species plays a key role in stratospheric ozone chemistry since they are sufficiently stable (hence long lived) to be transported to other regions of the atmosphere. On account of their ability to store active ozone destroying species, these less reactive forms are termed 'reservoir species'. Formation of these reservoirs may lead to removal. Moreover, recent studies have identified heterogeneous processes which can profoundly affect stratospheric ozone concentrations *via* their role in the partitioning between active and reservoir forms. For example, it is now recognised that the following reactions can occur on condensed atmospheric matter (sulphate aerosol, polar stratospheric clouds), liberating molecular chlorine which readily photolyses in the sunlit stratosphere to yield active chlorine atoms[6]:

(1.13) $ClONO_2 + HCl \rightarrow Cl_2 + HNO_3$

(1.14) $HOCl + HCl \rightarrow Cl_2 + H_2O$

1.8.2 Tropospheric Ozone

In addition to its profound influence in the stratosphere, ozone is also important in the troposphere where its abundance is much lower. This importance of lower atmospheric ozone stems from its pivotal role in defining the oxidising capacity of the troposphere. However, low altitude ozone is also a pollutant itself in elevated concentrations - a component of photochemical smog.

The attenuation of short wavelength radiation due to overhead photochemistry virtually precludes ozone production in the troposphere through reactions (3) and (4). Nevertheless a small amount of ozone is present in the troposphere, solar photolysis of which is rapidly followed by recombination of the oxygen atom with molecular oxygen reforming O_3. At shorter wavelengths of solar radiation (<310 nm) excited oxygen atoms O (^1D) may be produced by solar photolysis. The principal fate of these atoms in the troposphere is their collisional quenching to ground state O(^3P). However the high mixing ratios of water in this region of the atmosphere facilitate some competition of reaction (15) with the quenching process:

(1.15) $O(^1D) + H_2O \rightarrow 2OH$

This reaction is profoundly important in tropospheric chemistry since reaction with the hydroxyl radical represents the primary mechanism of removal of many trace pollutant gases in the atmosphere. OH also reacts with tropospheric CO:

(1.16) $CO + OH \rightarrow H + CO_2$

This is followed by the rapid combination of the H atom with O_2:

(1.17) $H + O_2 + M \rightarrow HO_2 + M$

The HO_2 radical may then react with ozone, regenerating OH:

(1.18) $HO_2 + O_3 \rightarrow OH + 2O_2$

Thus an interconversion of OH and HO_2 radicals is set up, and it is convenient to define the 'odd hydrogen' family: HO_x = OH + HO_2 in an analogous fashion to odd oxygen discussed above. It should be noted that formation of OH, and interconversion of OH and HO_2 remove ozone from otherwise unpolluted air. HO_x is eventually removed from the air following reactions such as the HO_2 self-reaction, forming H_2O_2 - a highly soluble product that is readily removed in wet deposition. Similar oxidation processes remove CH_4 from unpolluted air. This oxidation is initiated by OH induced H abstraction, followed by rapid combination of the methyl radical fragment with abundant atmospheric oxygen, forming methylperoxy, CH_3O_2:

(1.19) $OH + CH_4 \rightarrow H_2O + CH_3$

(1.20) $CH_3 + O_2 + M \rightarrow CH_3O_2 + M$

CH_3O_2 does not react appreciably with ozone in an analogue of reaction (18) but can self react and react with HO_2:

(1.21a) $CH_3O_2 + CH_3O_2 \rightarrow 2\,CH_3O + O_2$

(1.21a) $CH_3O_2 + CH_3O_2 \rightarrow CH_3OH + HCHO + O_2$

(1.22) $CH_3O_2 + HO_2 \rightarrow CH_3OOH + O_2$

The CH_3O radicals formed in reaction (21a) react rapidly with oxygen regenerating HO_2. Formaldehyde, HCHO, formed in this reaction and directly in (21b) is rapidly photolysed by sunlight, forming further HO_2.

(1.23) $CH_3O + O_2 \rightarrow HCHO + HO_2$

(1.24) $HCHO + h\nu \rightarrow H + CHO$

(1.25) $CHO + O_2 \rightarrow CO + HO_2$

The net effect of oxidation of CO and CH_4 in otherwise unpolluted air is thus the interconversion of OH with HO_2 and the destruction of ozone.

However, the composition of the local atmosphere can effect significant changes in these oxidation processes. In the polluted troposphere the presence of nitrogen oxides competes for reaction with HO_2 and CH_3O_2 radicals:

(1.26) $HO_2 + NO \rightarrow OH + NO_2$

(1.27) $CH_3O_2 + NO \rightarrow CH_3O + NO_2$

Reaction (26) regenerates OH directly, whilst reaction (27) produces HO_2 *via* the subsequent chemistry of CH_3O. Thus the interconversion of OH and HO_2 is preserved, at the same time generating NO_2. Since NO_2 is readily photolysed by solar radiation, this process leads to ozone production

(1.10) $NO_2 + h\nu \rightarrow NO + O$ ($\lambda < 398$ nm)

(1.4) $O + O_2 + M \rightarrow O_3 + M$

Higher hydrocarbons are successively degraded in similar oxidation chemistry, which in the presence of nitrogen oxides, produces ozone. The balance between ozone production and destruction is largely controlled by the competition between reactions of the peroxy radicals. Mitigating factors include the reaction between O_3 and NO, (8) which helps to maintain a photostationary state between NO, NO_2 and O_3. Numerical modelling has indicated that a tropospheric $[NO]/[O_3]$ ratio in excess of 2×10^{-4} is sufficient to ensure net ozone production[7]. In areas where NO_x emissions do exceed this critical value, the formation of low level ozone and photochemical smog has been observed.

1.8.3 Stratospheric Ozone Trends

The processes described above serve as a brief introduction to the principal sources and sinks of atmospheric ozone. However, it is clear that many factors influence ozone chemistry in the atmosphere. The aim of this dissertation is to characterise and quantify some of the key chemical processes which are of fundamental importance to ozone loss. The experimental studies described in subsequent chapters focus on the kinetics of halogen oxide (XO; X = Cl, Br) reactions. Crucially those XO reactions, which are implicated in stratospheric ozone depletion, are investigated with a view to assess their potential in propagating the catalytic cycles.

1.8.4 Sources of Atmospheric Halogens

The dominant natural source of atmospheric chlorine is methyl chloride, with a mixing ratio of about 0.6 ppbv at the tropopause. Whilst oceanic release is a significant source, 80% of its abundance originates from biomass burning and a further 10% from industrial release. However, the total stratospheric chlorine ratio is approximately 3.6 ppbv, the increase of 3 ppbv having taken effect over the last four decades. Figure 1.7 shows the temporal trend in stratospheric chlorine and its attribution to specific sources.

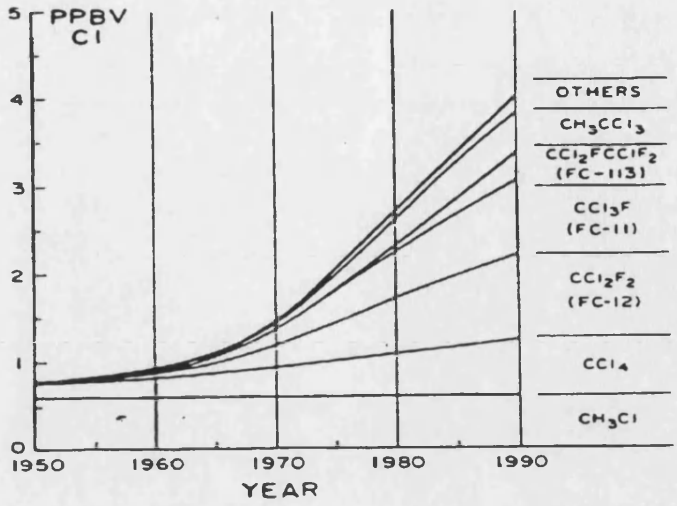

Figure 1.7: Temporal trend in selected CFC abundances since 1950.[8]

The major source gases of stratospheric chlorine include CF_2Cl_2 and $CFCl_3$. These chlorofluorocarbons (CFCs) were developed in the 1930s by General Motors in the search for non-toxic refrigerants to supersede ammonia and sulphur dioxide. Increased CFC production from the 1960s, fuelled by their use as propellants and blowing agents in foam production has given rise to the elevated abundances observed today. CFCs are not only non-toxic but are photostable in the lower atmosphere and chemically inert, characterising their industrial value. Largely unreactive with atmospheric oxidants such as OH, tropospheric CFC inertness was confirmed by James Lovelock in 1973, who reported the observation of halogenated hydrocarbons in the atmosphere.[9] Indeed atmospheric lifetimes of CF_2Cl_2 and $CFCl_3$ are about 100 and 50 years respectively. Molina and Rowland acknowledged that with such long lifetimes CFCs could undergo transport to the stratosphere and liberate chlorine atoms, initiating ozone depletion in the harsh photochemical environment[10]. Figure 1.8 shows the vertical distribution of $CFCl_3$, effectively constant in the troposphere but rapidly diminishing above the tropopause where short wavelength photolysis and reaction with excited oxygen atoms occur readily.

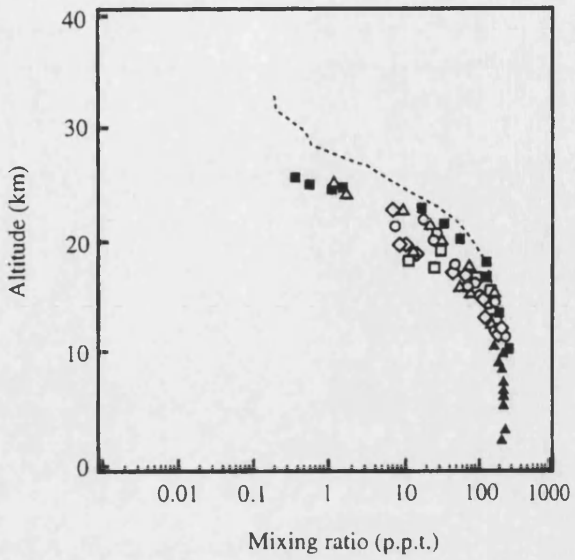

Figure 1.8: Vertical distribution of $CFCl_3$ in the northern hemisphere. Different symbols identify specific experiments performed on different days between 1987 and 1990.[8]

Bromine also plays a role in stratospheric ozone chemistry. The major source gases are methyl bromide and halons (bromine analogues of the CFC family). The former is produced naturally (chiefly by marine algae), although anthropogenic use as a soil fumigant and as an anti-knocking agent in petrol account for about half of its atmospheric release. Halon usage is largely restricted to specialist fire extinguishers. Once again the chemical and photostability of these compounds result in atmospheric lifetimes long enough to permit a degree of transport to the stratosphere. However, bromine source gases are shorter lived than their chlorine analogues.

1.8.5 Control Measures

Motivated by the potential threat identified in 1974, some developed countries began to curb non-essential CFC production in the late 1970s, temporarily replacing these compounds with HCFCs. HCFCs were designed with an intra-molecular C-H bond, rendering them liable to H atom abstraction by reaction with OH, facilitating tropospheric degradation of HCFCs, generally rendering their lifetimes too short for transport to the stratosphere. Prompted by the unexpected discovery of the Antarctic

ozone hole,[11] attempts to widen these restrictions lead to the Montreal Protocol (1987). The dramatic evidence linking the Antarctic hole with CFC derived chlorine[12] prompted amendments to the Montreal Protocol, enforcing more rapid, wider phase out of CFCs, HCFCs and halons.

1.8.6 Polar Stratospheric Ozone

The first report of polar stratospheric ozone depletion was by the British Antarctic Survey having monitored column ozone densities at Halley Bay, Antarctica for several decades. In 1982 Farman *et al.*[11] observed a decrease in springtime column ozone relative to measurements taken in 1977. Similar measurements made the following two years not only confirmed their suspicions but suggested increasing severity of ozone destruction with each elapsing year. Recent measurements have shown that total column ozone is typically depleted by 80% in the Antarctic Springtime and at some altitudes total depletion occurs (figure 1.9). This so called "Antarctic Ozone Hole" develops during the weeks following polar sunrise, until recovery takes hold in the early summer.

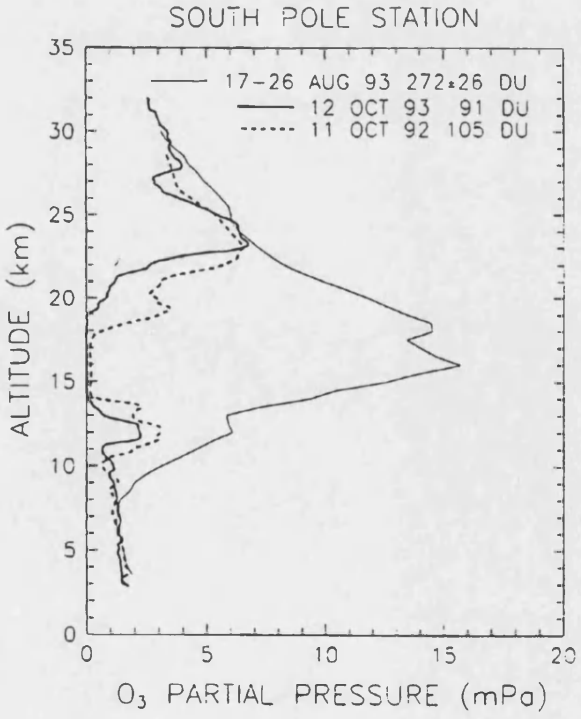

Figure 1.9: Ozone abundances at the south pole in the winter of 1993 (August) and the following springtime (October).[8]

Aircraft measurements made during the spring of 1987 simultaneously monitored O_3 and ClO mixing ratios in the Antarctic stratosphere.[12] The stark anticorrelation between these two species confirmed the implication of chlorine and ClO radicals in polar ozone depletion.

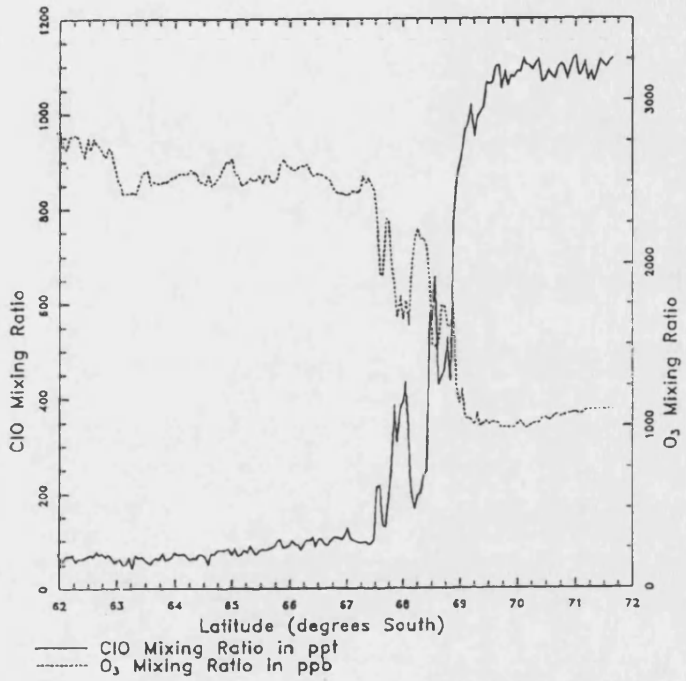

Figure 1.10: Simultaneous measurements of spatially resolved O_3 and ClO abundances near the south pole during springtime.[12]

A combination of chemical and meteorological effects are held responsible for these annual polar events. During the Antarctic winter strong Westerly winds inhibit North-South air mixing, giving rise to a relatively isolated vortex. Inside this dark vortex temperatures can fall as low as 180 K. Below a threshold of 194 K co-condensation of water and nitric acid can take place, giving rise to the polar stratospheric clouds (PSCs) composed of $HNO_3.3H_2O$ particles.[13] Temperatures below 188 K facilitate the rapid condensation of water upon these PSCs and particle growth occurs to the extent that denitrification of the stratosphere occurs *via* gravitational separation.[14]

Analogously to sulphate aerosols, PSCs provide sites for heterogeneous conversion of chlorine reservoirs to more active forms:

(1.13) $ClONO_2 + HCl \rightarrow Cl_2 + HNO_3$

(1.28) $ClONO_2 + H_2O \rightarrow HOCl + HNO_3$

This so called chlorine activation takes place throughout the polar winter. When sunlight returns in springtime the photolytic release of Cl atoms is followed by a buildup in ClO:

(1.29) $Cl_2 + h\nu \rightarrow 2Cl$

(1.30) $Cl + O_3 \rightarrow ClO + O_2$

With elevated ClO concentrations, the ClO self-reaction can take place followed by dimer photolysis. ClOO is known to be weakly bound, thus its rapid dissociation completes a catalytic cycle for ozone loss.

(1.30) $2 \times (Cl + O_3 \rightarrow ClO + O_2)$

(1.31) $ClO + ClO + M \leftrightarrow Cl_2O_2 + M$

(1.32) $Cl_2O_2 + h\nu \rightarrow ClOO + Cl$

(1.33) $ClOO + M \rightarrow Cl + O_2 + M$

net: $2O_3 \rightarrow 3O_2$

Under normal stratospheric conditions the extent of this cycle would be limited by reformation of reservoir chlorine forms *via* reaction (11):

(1.11) $ClO + NO_2 + M \rightarrow ClONO_2 + M$

However, uptake of NO_x species by the denitrification process limits the availability of NO_x until the vortex breaks up sufficiently to mix in NO_2 from lower latitudes.

Throughout the 1980s the Northern Hemisphere failed to show an effect comparable to that observed in the Antarctic. In recent years however, relatively large depletion events have been reported during the Arctic spring. The reason for this slower onset of

a less extensive ozone hole is thought to be a consequence of the more moderate dynamical behaviour at the Arctic. The Arctic vortex is somewhat less stable than its southern counterpart and as a result is less isolated and warmer, hence conditions are not so favorable for PSC formation.

Reaction (31) does not play a significant role in ozone chemistry when isolated from these meteorlogical effects, since ClO enrichment never occurs to a significant level without the aid of heterogeneous chemistry. Lower ClO concentrations reduce the flux through the cycle (since (31) is the rate determining step during sunlit hours and its rate is proportional to $[ClO]^2$) and higher temperatures induce thermal dissociation of Cl_2O_2 to 2ClO, no longer liberating free chlorine.

Other catalytic cycles are thought to supplement that described above. Most prominent is a similar cycle governed by the ClO + BrO reaction:

(1.34a) $ClO + BrO \rightarrow Cl + Br + O_2$

(1.34b) $\rightarrow Br + OClO$

(1.34c) $\rightarrow BrCl + O_2$

The important distinction between the ClO self reaction and the mixed ClO + BrO reaction is the lack of adduct formation in the latter. Direct production of halogen atoms from channels (34a) and (34b) promotes catalytic ozone loss without the requirement of a secondary photolytic process. However, channel (34b) produces OClO which photolyses to give an O atom, offsetting the importance of this channel in O_3 depletion. Subsequent photolysis of the interhalogen species generated via (34c) leads to further O_3 destruction.

As a consequence of the Montreal Protocol, the severity of these annual events is expected to decrease in the future.[15] However, the restrictions only curb production of the critical species, not usage. Thus current stocks of these species could ultimately be released into the atmosphere. It is consquently difficult to predict with great certainty when polar ozone depletion will begin to abate. To further complicate matters it has

been suggested that stratospheric cooling associated with global warming could lead to the formation of more stable polar vortices and enhance the rates of radical/radical reactions such as (31). Modelling studies have indicated that this phenomenon could delay the recovery of polar ozone by 10-15 years beyond an anticipated peak in stratospheric halogen loading.[16]

1.8.7 Midlatitude Stratospheric Ozone

Ozone trends at midlatitudes are far less dramatic than those observed in polar regions. Nevertheless the SAGE (Stratospheric Aerosol and Gas Experiment) campaign conducted over the period 1979-1996 suggests that erosion of the stratospheric ozone is occurring at non-polar latitudes[17].

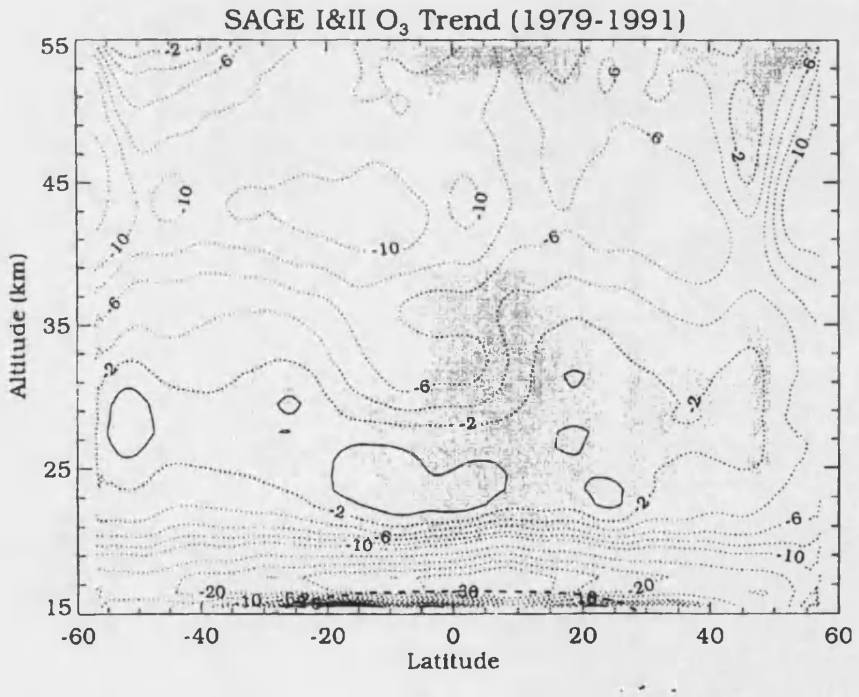

Figure 1.11: Spatial mapping of ozone trend (% loss per decade) at midlatitudes over the period 1979-1991[17].

Midlatitude ozone loss has been attributed to out mixing of polar ozone depleted air and to *in situ* free radical chemistry. Since halogen activation does not occur at midlatitudes, elevated concentrations of ClO and BrO radicals are not generated. As a

consequence, reactions between free radical families are the primary routes to chemical ozone loss in the midlatitude stratosphere, e.g.(35, 35a):

(1.35a) $ClO + HO_2 \rightarrow HOCl + O_2$

(1.35b) $\rightarrow HCl + O_3$

Provision of kinetic and mechanistic data on such processes is consequently a priority for atmospheric modelling purposes. It should be noted that in carrying out studies of the free radical cross-reactions, the self-reactions will also occur. Thus full characterisation of halogen oxide self-reactions is also a priority for other laboratory investigations of XO chemistry.

1.9 References

[1] Brasseur, G.; Solomon, S. *Aeronomy of the Middle Atmosphere 2nd Edition, D. Reidel Pub. Co. Dordecht*, **1986**.

[2] Madronich, S. *Environmental UV Photobiology, Plenum Press* **1993**.

[3] Dobson, G. M. B. *Proc. Roy. Soc. London, Sec. A* **1930**, 129, 411.

[4] Chapman, S. *Phil. Mag.* **1930**, 10, 369.

[5] DeMore, W.B.; Sander, S.P.; Golden, D.M.; Hanson, R.F.; Kurylo, M.J.; Howard, C.J.; Ravishankara, A.R.; Kolb, C.E.; Molina, M.J. *Chemical Kinetics and Photochemical Data for use in Stratospheric Modeling;* JPL publication **97-4**; California Institute of Technology, Pasadena.

[6] Hanson, D. R. and Ravishankara *J Geophys. Res. – Atmos.* **1993**, 98, 22931.

[7] Crutzen, P. J.; Boutron, C. Ed. *An Overview of Atmospheric Chemistry, Topics in atmospheric and Interstellar Physics and Chemistry*, Les editions de Physique, Les Ulis, **1994**, Boutron, C. Ed.

[8] Scientific Assessment of Ozone Depletion **1994**, World Meteorological Organisation Report no. 37.

[9] Lovelock, J. E.; Maggs, R. J.; Wade, R, J. *Nature* **1973**, 241, 194.

[10] Molina, M. J.; Rowland, F. S. *Nature* **1974**, 249, 810.

[11] Farman, J. C.; Gardiner, B. G.; Shanklin, J. D. *Nature* **1985**, 315, 207.

[12] Anderson, J. G.; Brune, W.H.; Proffitt, M. H. *J Geophys. Res. – Atmos.* **1989**, 95 15129.

[13] Crutzen P. J.; Arnold, F. *Nature* **1986** 324, 651.

[14] Fahey, D. W.; Solomon, S.; Kawa, S. R.; Loewwnstein, M.; Podolske, J. R.; Strahan, S. E.; Chan, K. R. *Nature* **1990**, 345, 698.

[15] Scientific Assessment of Ozone Depletion **2002**, World Meteorological Organisation Report no. 47.

[16] Shindell, D. T.; Rind, D.; Lonergan, P. *J. of Climate* **1998**, 11, 895.

[17] Scientific Assessment of Ozone Depletion **2002**, World Meteorological Organisation Report no. 47.

Chapter 2: Photochemistry and Gas Kinetics

2.1 Photochemistry

2.1.1 Absorption

A molecule may absorb a photon if its energy levels engender a transition whose energy is equal to that of the incident photon. Absorption of the photon by a species AB gives rise to an excited molecule, AB*, the fate of which is discussed in section 2.1.2:

$$AB + h\nu \rightarrow AB^*$$

The extent of absorption through a sample is determined by the absorption cross section, σ of the absorbing species at a given photon energy (wavelength). This process is described by the Beer-Lambert law where incident (I_0) and transmitted (I_t) light intensities through a sample of length l are related to the concentration of the absorbing species, c:

(2.i) $$A = \sigma c l = \ln\left(\frac{I_0}{I_t}\right)$$

UV/visible photon energies associated with solar radiation in the lower atmosphere correspond to electronic transition energies for many atmospheric constituents. If the upper state of an electronic transition is bound then structural features may be observed in the absorption spectrum. These features arise from vibrational and rotational excitation accompanying electronic excitation. In addition to providing fundamental information on the absorbing species, structural spectral features facilitate identification and quantification of such molecules. Many small molecules including halogen monoxide radicals such as BrO exhibit this phenomenon, as shown in figure 2.1.

With a knowledge of appropriate absorption cross sections, the Beer-Lambert law can be applied to measure concentrations of absorbing species in the laboratory. Absorption cross sections can vary as a function of both temperature and pressure. Furthermore the dispersing element instrument function and resolution can also affect values of σ, these issues are discussed in appendix 1. Given the factors affecting σ, a degree of caution must be exercised to ensure that any cross sections used are appropriate to the experimental conditions under which absorption measurements were taken.

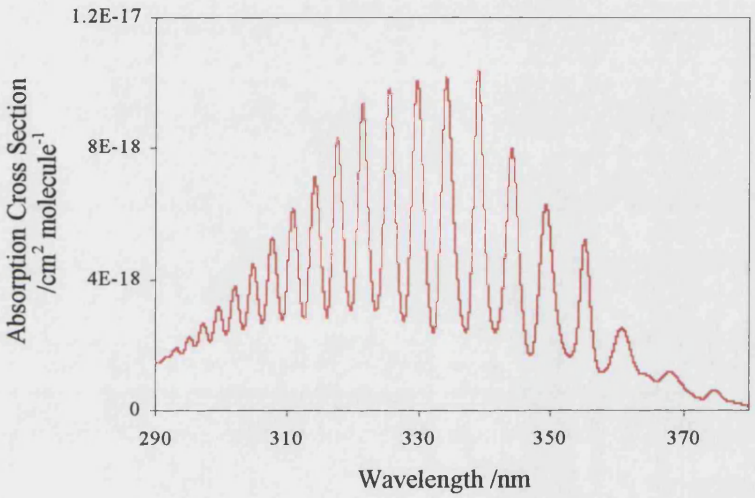

Figure 2.1: The BrO absorption cross section reported by Wilmouth et al.[1]

2.1.2 Fate of Excited Species

A number of fates are possible for the photo-generated excited state, AB*. For example it may re-emit radiation *via* fluorescence or phosphoresence. Alternatively AB* may redistribute its energy internally *via* non-radiative transitions or transfer its energy to another molecule during a collision. Of particular interest in atmospheric science is a dissociative pathway following absorption:

(2.1) $\quad AB^* \rightarrow A + B$

This process gives rise to fragments which may be highly reactive and thus play an important role in the chemistry of the atmosphere. Two principal mechanisms for this

process can operate: direct dissociation or pre-dissociation. Direct dissociation arises when fragmentation occurs directly from the upper state of the transition. This state might be unbound, thus the spectrum at this wavelength is essentially continuous and any excess energy beyond the dissociation threshold can be dissipated in the translational energies of the daughter fragments. Alternatively a bound upper state could be populated above the dissociation limit. Dissociation can also occur from bound upper states populated below the dissociation limit, albeit indirectly. If excitation occurs from the absorption of a photon in the structured region of the spectrum (at lower energies than the observation of a diffuse continuum, hence *pre*-dissociation) then the molecule does not have sufficient energy to dissociate directly. However if a crossing point exists between this excited state and a repulsive, unbound state, then a radiationless transition can give rise to population of the latter and dissociation follows.

The rate coefficient, J for a photodissociation process is given by the sum over all wavelengths, of the product of local light intensity (I_λ), the absorption cross section (σ_λ) and the quantum yield for the specified process (ϕ_λ):

(2.ii) $$J = \int_0^\lambda I_\lambda \sigma_\lambda \phi_\lambda \, d\lambda$$

2.2 Theory of Gas Phase Kinetics

Consider the general reaction in the gas phase:

(2.2) $$aA + bB = cC + dD$$

The extent of reaction, $\delta\xi$ is given by $\delta\xi = \delta n_Q / \nu_Q$. ν_Q, the stoichiometric number for any species in the reaction, is defined as negative for any reactant and positive for any product species:

(2.iii) $$\delta\xi = \frac{\delta n_A}{-a} = \frac{\delta n_B}{-b} = \frac{\delta n_C}{+c} = \frac{\delta n_D}{+d}$$

Thus the rate of reaction for any species Q is defined as:

(2.iv) $$\tilde{r} = \frac{d\xi}{dt} = \frac{1}{\nu_Q}\frac{dn_Q}{dt}$$

However, it is often convenient to consider the intensive quantity (rate/volume), and refer to this as the rate of reaction, r:

(2.v) $$r = \frac{1}{\nu_Q}\frac{d(n_Q/V)}{dt} = \frac{1}{\nu_Q}\frac{d[\mathrm{Q}]}{dt}$$

Experimentally it is observed that the rate of reaction is given by:

(2.vi) $$r = k_{obs}[\mathrm{A}]^{\alpha}[\mathrm{B}]^{\beta}$$

The observed rate constant, k_{obs} and the respective orders of the reaction, α and β are only determined experimentally and cannot be predicted from the overall reaction.

However, if the overall reaction proceeds *via* a series of known steps, termed elementary reactions, then a predicted rate equation can be derived. An elementary chemical reaction proceeds at a rate which is determined by the product of its rate constant, k and reactant concentrations raised to some power given by the stoichiometric number of the respective reactant.

(2.3) $$\mathrm{A} + \mathrm{B} \rightarrow \mathrm{AB}$$

(2.4) $$\mathrm{AB} \rightarrow \mathrm{C} + \mathrm{D}$$

(2.ii) $$-\frac{d[\mathrm{A}]}{dt} = -\frac{d[\mathrm{B}]}{dt} = k_3[\mathrm{A}][\mathrm{B}]$$

(2.iii) $$\frac{d[\mathrm{AB}]}{dt} = k_3[\mathrm{A}][\mathrm{B}] - k_4[\mathrm{AB}]$$

(2.iv) $$\frac{d[C]}{dt} = \frac{d[D]}{dt} = k_4[AB]$$

Often AB is a reactive intermediate. A result of this is that [AB] never reaches a significant value and $d[AB]/dt \approx 0$. By making the steady state approximation for AB, the rate equation can be expressed in terms of the original reactant concentrations [A] and [B]:

(2.v) $$\frac{d[C]}{dt} = \frac{d[D]}{dt} = k_3[A][B]$$

2.2.1 Bimolecular Reaction Rate Theory

Several theories have been developed to quantitatively rationalise the behaviour of bimolecular rate coefficients as a function of temperature. The simplest of these is Simple Collision Theory (SCT) which treats the reactant molecules as incompressible spheres which only interact upon collision. The theory essentially calculates the collision frequency between molecules and assumes that for a reactive collision the translational energy along the reaction coordinate exceeds some critical value (the activation energy, E_a). SCT gives rise to an expression for the bimolecular rate coefficient, k_{bi} of the form:

(2.vi) $$k_{bi} = A \exp(-E_a/RT)$$

A is termed the pre-exponential factor and represents the collision frequency given by the product of the collision diameter (πd^2, where d is the sum of the reactant radii) and the relative mean speed of the reactant molecules ($\{8k_BT/\pi\mu\}^{1/2}$ where k_B is the Boltzmann constant, T is the temperature and μ is the reduced mass of the reactants). In practice this theory often overestimates the experimentally measured rate coefficient. This weakness can be viewed as a failure of SCT to treat spatial requirements of reactive collisions (steric factors) and the internal energy distribution within reactant and product species. Clearly these concepts are not compatible with a hard sphere model and a more sophisticated level of theory is required.

Transition State Theory (TST, or Activated Complex Theory) assumes that an equilibrium is established between the reactant molecules and a transition state ($ABC^{\ddagger}$), hence the overall rate of reaction is effectively determined by the notional concentration of transition states and rate of decomposition of the transition state into the daughter fragments, such as AB and C.

(2.5) $A + BC \leftrightarrow ABC^{\ddagger}$

(2.6) $ABC^{\ddagger} \rightarrow AB + C$

(2.vii) $$\frac{d[AB]}{dt} = k_5[A][BC] = k_6[ABC^{\ddagger}]$$

(2.iix) $$[ABC^{\ddagger}] = K_5[A][BC]$$

The equilibrium constant between reactants and the transition state can be expressed in terms of the total partition functions, Q_n for A, BC and $ABC^{\ddagger}$ with k_B representing the Boltzmann constant and $\Delta\varepsilon_0$, the difference between the lowest energy levels in the reactants from those in the activated complex:

(2.ix) $$K_5 = k_5 \left(\frac{Q^{\ddagger}_{ABC}}{Q_A Q_{BC}}\right) exp\left(-\frac{\Delta\varepsilon_0}{k_B T}\right)$$

Combining equations (vii-ix) gives rise to an expression for the bimolecular rate constant, k_{bi}:

(2.x) $$k_{bi} = k_5 \left(\frac{Q^{\ddagger}_{ABC}}{Q_A Q_{BC}}\right) exp\left(-\frac{\Delta\varepsilon_0}{k_B T}\right)$$

Complexities arising from the number of vibrational modes associated with the transition state modify expression (x) to yield the following:

(2.xi) $$k_{bi} = \frac{\kappa k_B T}{h} \left(\frac{Q^{\ddagger}_{ABC}}{Q_A Q_{BC}} \right) exp\left(-\frac{\Delta\varepsilon_0}{k_B T}\right)$$

where Q_A and Q_{BC} represent the total partition functions for the reactant species A and BC respectively and $Q^{\ddagger}_{ABC}$ refers to the total partition function for the transition state excluding the term which represents one dimensional motion along the reaction coordinate, which has been factored out. h denotes Planck's constant and κ is the transmission coefficient which accounts for the fraction of activated complexes that lead to products rather than fragment back to the reactant species. Spectroscopically determined rotational and vibrational constants permit the calculation of Q_n *via* statistical mechanics. However, in reality these parameters are rarely available for the polyatomic activated complexes of interest to atmospheric chemists and assumptions must be made.

For the most simple case where both reactants are monatomic and thus can be considered to behave as hard spheres, SCT and TST treatments reduce to the same algebraic expression despite the differences in underlying theory. It has been shown empirically that many bimolecular rate coefficients can be described by a temperature dependence embodied in the Arrhenius expression:[2]

(2.xii) $$k_{bi} = A\ exp\ (-E_a/RT)$$

where E_a and A are the experimentally parameterised activation energy and pre-exponential factor respectively. The expression clearly takes an algebraic form similar to those derived from SCT and (simple) TST. As predicted by these theories the exponential term generally dominates the temperature dependence of the measured rate coefficient, k. In some cases the experimentally observed temperature dependence is found to deviate from the Arrhenius form, (xii). Referring once again to TST and expressing the temperature dependence of each partition function as a power law gives rise to a modification of (xii):

(xiii) $$k_{bi} = A' T^n\ exp\ (-E_a/RT)$$

Where the pre-exponential factor exhibits a strong experimental temperature dependence (since A is proportional to $T^{1/2}$) or where large extrapolations are required, (xiii) may give a more satisfactory parameterisation of the temperature dependent rate coefficients.

2.2.2 Unimolecular and Termolecular Theory

The rates of many gas phase unimolecular chemical reactions are often pressure dependent, suggesting a mechanism for dissociation which is not truly unimolecular. Moreover, at sufficient pressures these reactions tend to exhibit a change from second order to first order kinetics. This behaviour was first explained by Lindemann who proposed that unimolecular decomposition involved three elementary steps:[3]

(2.7)	AB + M	→	AB* + M
(2.-7)	AB* + M	→	AB + M
(2.8)	AB*	→	A + B

where M is any surrounding molecule such as AB or more typically in the atmosphere, N_2. The theory assumes that reaction proceeds through the energised molecule AB*. Making the steady state approxiation for the reactive AB* gives rise to an expression for the rate of product formation:

$$\text{(2.xiv)} \qquad \frac{d[\mathrm{A}]}{dt} = \frac{d[\mathrm{B}]}{dt} = \frac{k_7 k_8 [\mathrm{AB}][\mathrm{M}]}{(k_{-7}[\mathrm{M}] + k_8)}$$

The theory qualitatively accounts for the observed change in reaction order. At low pressures ($k_{-7}[\mathrm{M}] << k_8$), hence the rate of formation of A is second order and pressure dependent. Conversely at higher pressures ($k_{-7}[\mathrm{M}] >> k_8$) and the rate tends to a limiting, first order value with rate coefficient, ($k_7 k_8 / k_{-7}$).

A similar mechanism can be invoked to explain the pressure dependence of termolecular association reactions:

(2.9) $A + B \rightarrow AB^*$

(2.-9) $AB^* \rightarrow A + B$

(2.10) $AB^* + M \rightarrow AB + M$

Putting AB* into steady state once again leads to the following expression for the rate of AB formation:

(2.xv) $$\frac{d[AB]}{dt} = \frac{k_9 k_{10}[A][B][M]}{(k_{-9} + k_{10}[M])}$$

(2.xvi) $$\frac{d[AB]}{dt} = \frac{k_0[A][B][M]k_\infty}{(k_0[M] + k_\infty)} \qquad \text{where } k_0 = \frac{k_9 k_{10}}{k_{-9}} \text{ and } k_\infty = k_9$$

As with unimolecular dissociation, the rate of AB formation is pressure dependent at low pressures ($k_0[M] << k_\infty$) but tends to a limiting value at higher pressures ($k_0[M] >> k_\infty$).

In practice this level of theory does not perfectly replicate experimentally derived values of k'. In reality, the rates of decomposition and formation of the activated AB* species depend upon the internal degrees of freedom associated with AB*. Strictly the rate coefficients should be defined for each vibrational and rotational level of the activated species and the overall rate constant summed from these coefficients, weighted according to population. Various extensions of the Lindemann mechanism have led to the development of RRKM theory (named after its developers Rice, Ramsperger, Kassel and Marcus) which does consider the internal energy distribution of the activated species.[4] Where reliable thermodynamic data is available RRKM theory can often reproduce experimental data well.

Once again a lack of relevant thermodynamic data for excited atmospheric species precludes the prediction of many rate coefficients *via* RRKM theory. Troe[5] has shown that multiplying expression (xvi) by a broadening factor, F which is itself a function of k_0 and k_∞, can adequately parameterise pressure dependent rate coefficients obtained from experimental studies.

(2.xvii) $$k_{ter}' = \frac{k_0[\mathrm{M}]k_\infty}{(k_0[\mathrm{M}]+k_\infty)} \times F$$

(2.xviii) $$F = F_c^{\left\{1+\left(\log_{10}\{k_0[\mathrm{M}]/k_\infty\}\right)^2\right\}^{-1}}$$

The value which F_c takes is specific to the particular reaction under consideration but in practice a value of 0.6 provides a satisfactory description of termolecular rate coefficients for atmospherically relevant processes.[6]

2.3 References

[1] Wilmouth, D. M.; Hanisco, T. F.; Donahue, N. M.; Anderson, J. G. *J. Phys. Chem. A.* **1999**; 103(45); 8935-8945.

[2] Arrhenius, S. *Zeitschrift fur Physikalische Chemie* **1889**, 4, 226.

[3] Lindemann, F. A. *Transactions of the Faraday Society* **1992**, 17, 598.

[4] Rice, O. K.; Ramsperger, H. C. *J. Am. Chem. Soc.* **1927**, 49, 1617.

[5] Troe, J. *J. Chem. Phys.* **1977**, 66, 4745.

[6] DeMore, W.B.; Sander, S.P.; Golden, D.M.; Hanson, R.F.; Kurylo, M.J.; Howard, C.J.; Ravishankara, A.R.; Kolb, C.E.; Molina, M.J. *Chemical Kinetics and Photochemical Data for use in Stratospheric Modeling;* JPL publication **97-4**; California Institute of Technology, Pasadena.

3. Flash Photolysis with UV/Visible Absorption Spectroscopy Incorporating CCD Detection

3.1 The Flash Photolysis Technique

Flash photolysis is a technique which employs an intense but short lived pulse of light to generate a particular chemical species photolytically within a mixture. The species may be generated from direct photodissociation or by further chemistry following photochemical initiation. Either way it is essential to produce the desired species on a timescale that is much shorter than the subsequent chemistry. This requirement essentially decouples the formation and decay kinetics of the reactive species of interest. This allows the decay kinetics to be investigated. Concentrations of transient species - both reactants and products are monitored by a variety of techniques and their temporal behaviour analysed to provide kinetic data.

Flash photolysis is a particularly powerful tool when investigating the kinetics of highly reactive gaseous free radicals which dominate the chemistry of the lower atmosphere. Flash photolysis overcomes many of the problems associated with flow techniques which generally require low pressures - typically a few Torr. Premixing of gas mixtures enables kinetic measurements to be undertaken over a wide pressure regime, incorporating that range which is characteristic of the lower atmosphere.

Real time monitoring of transient absorbers is reliant on the availability of detection techniques with response times short enough to cope with rapid changes in concentration. Indeed it is the response time of the detection system coupled with the duration of the photolytic pulse which proves limiting when selecting an experimental timescale.

Detection systems also need to be sensitive enough to monitor very small changes in concentration and suitably specific to ensure that species are monitored unequivocally. Absorption spectroscopy satisfies these criteria and in particular absorption

spectroscopy in the UV / visible spectral region - exciting electronic transitions in small gas phase molecules - is especially convenient. Time resolved UV / visible absorption spectroscopy was historically the original detection technique applied to flash photolysis. A brief history of the technique is given below.

3.2 History of the Flash Photolysis Technique

The flash photolysis technique was originally developed by Porter, Norrish and co-workers in Cambridge in the late 1940s.[1,2] These pioneering experiments employed ex Royal Navy submarine capacitors charged to high voltage to power flashlamps. Gas phase species were monitored by absorption recorded on glass photographic plates The photographic plate was aligned in the dispersive plane of a spectrograph and wavelength resolved light from a second flashlamp, whose intensity was transmitted through the reacting gas mixture, was recorded. This second light pulse provided the time resolution of the technique as it was initiated at a known delay time after the photolysis flashlamp. The recorded intensities were converted to absorptions by measuring the degree of darkening across the photographic plates compared to an exposure collected with no photolysis flash. Repeated experiments with varied delay times gave rise to temporally resolved absorption profiles. An example of a set of flash photolysis spectra, reported for a study of CN radical kinetics by Dr David Husain (Cambridge)[3] is shown in figure 3.1.

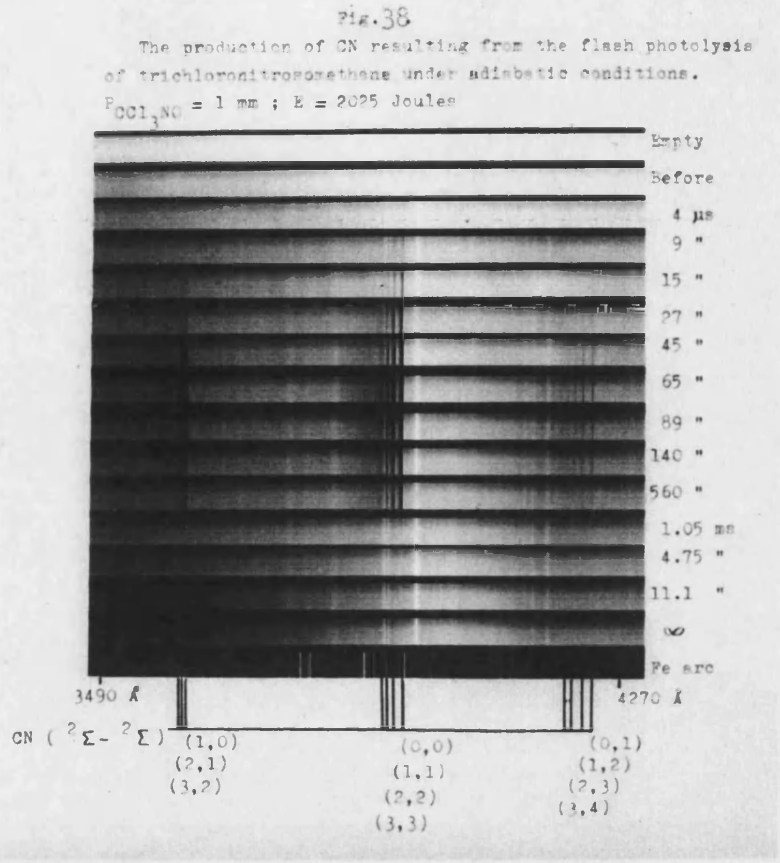

Figure 3.1: Photographic plate recorded transmission spectra of flash photolysed CCl_3NO (After D. Husain[3], reproduced with kind permission)

The availability of photomultiplier tubes (PMTs) in the 1960s enabled the continuous, rapid real time monitoring of transmitted light intensities for the first time.[4] Hence a single experiment could generate an entire decay profile, drastically reducing the experimental workload. However the inability of a PMT to distinguish photons arriving at different positions on the detector window, coupled with the physical size of the window and the dispersion of available spectrographs prevented the simultaneous measurement of wavelength resolved absorption. As a result, PMT experiments were limited to a single wavelength which was selected with a monochromator. The use of a single wavelength compromised the ability to distinguish between absorbing species. Nevertheless the advent of PMTs gave rise to significant advantages over photographic plate methods and they are still widely employed to this day.[5]

More recently, the development of photodiode arrays has permitted simultaneous monitoring of light intensity in both temporal and wavelength regimes. Such an array consists of a series of small, discrete light sensitive pixels which can be aligned in the dispersive plane of a spectrograph. Readout of the electronic signal limits the time resolution of the device. This is typically on the millisecond timescale which restricts the effectiveness of the photodiode array in studying rapid kinetic processes. This can be alleviated by coupling the array to a fast gating system, such that time resolved 'snapshots' of the spectrum are recorded in successive repeated experiments. However this arrangement necessitates carrying out multiple experiments to build up the temporal profile of absorbance. Nonetheless, diode array detection of absorbance in flash photolysis confers advantages. First, wavelength resolved measurements offer the possibility of monitoring multiple absorbing species in the reaction. Secondly, the improved signal to noise ratio associated with the monitoring of a whole absorption band gives rise to much more accurate determination of species concentration and thus better constrained kinetic data.

Experiments described in this thesis have utilised a two dimensional, light sensitive array to overcome the limitations associated with both PMT and photodiode techniques and to maximise the amount and quality of information recorded in an experiment.[6] The array, a charge coupled device (CCD) consists, once again, of a series of discrete pixels which convert incident light to photocharge. However, unlike the photodiode array, the device provides rapid and efficient transfer of charge across the device to a storage region. The rate of this charge transfer defines the time resolution of the CCD and is on the microsecond timescale. The data is not read out until the entire storage region has been filled. As a consequence, this can take place on a slower timescale without compromising the efficiency of data collection. The experimental set up is described in detail below.

3.3 Flash Photolysis Incorporating a 2-Dimensional Array

3.3.1 Principles of CCD Operation

A detailed description of the theory underlying CCD operation is beyond the scope of this thesis. However a brief summary is given here.

The CCD device consists of a grid of metal oxide semiconductor pixels embedded in a silicon substrate. Each of these pixels converts incident light to photocharge which is stored in an electrically generated potential well within the pixel. The quantum efficiency (QE) of the light to charge conversion peaks at incident wavelengths near 700 nm, with a value of approximately 60%. To enhance efficiency at wavelengths less than 400 nm, the pixels are coated with a thin layer of phosphor which fluoresces at visible wavelengths, giving rise to an effective QE of about 20%. The fluorescence lifetime is of the order of nanoseconds and therefore does not distort the time resolution of the device. Furthermore, the phosphor coating is thin (0.3 μm) in comparison with the pixel size (22.5 μm square), so the extent of cross talk between pixels is negligible.

Transfer of photocharge from one pixel to another is induced by the application of suitably phased voltages to a series of electrodes aligned perpendicular to the axis of transfer. This process is indicated schematically in figure 3.2. Charge transfer is efficient and typically exceeds 99.9999% per transfer. Transfer rates of up to 1 MHz (corresponding to a 1μs time resolution) are readily attainable.

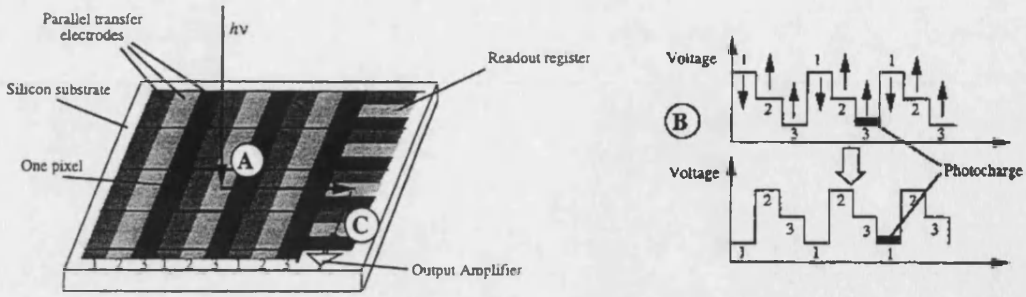

Figure 3.2: Principles of CCD operation and charge transfer. Incident light is converted to photocharge (A). Three sets of parallel transfer electrodes are charged cyclically to maintain a potential gradient across the device, moving charge. Finally, when the charge has traversed the entire device, the charge is read out via the output amplifier. Taken from Rowley et al.[6]

There are two major noise sources associated with the device. The first arises from the 'dark' current produced by the CCD, which is minimised by Peltier cooling the CCD to 200 K. Thermal insulation is provided by housing the entire device within a vacuum. Nevertheless this dark current is measured at each pixel prior to exposure and subtracted from the experimental intensities. The other significant noise source is photonic noise, a property inherent to the incident light intensity. Since photon flux typically exhibits a Poisson distribution, photonic noise is related to the square root of the number of incident photons at a given pixel. For a typical full pixel capacity of 2×10^6 photoelectrons, the associated photonic noise is ±0.07%.

3.3.2 CCD Detection Applied to Flash Photolysis

In the time honoured fashion, for flash photolysis with UV/visible absorption spectroscopy experiments, analysis lamp output is directed through the reaction vessel into a spectrograph which disperses the light onto a detector. In the experiments described below, the CCD effectively replaces a photographic plate or diode array detector and is oriented with the axis of charge transfer perpendicular to the dispersive plane of the spectrograph. The top few (31) rows of the CCD are illuminated by the wavelength resolved light, while the rest of the CCD is optically masked. The CCD affords light to charge conversion and charge transfer routines rapidly and efficiently

shift the photocharge down successive rows of the CCD, continuously permitting further acquisition of spectral data, until the entire length of the CCD has been traversed. The shift time or clocking rate is selected prior to the experiment, hence the clocking axis represents the time resolved axis of the detector. This setup is illustrated schematically in figure 3.3 below.

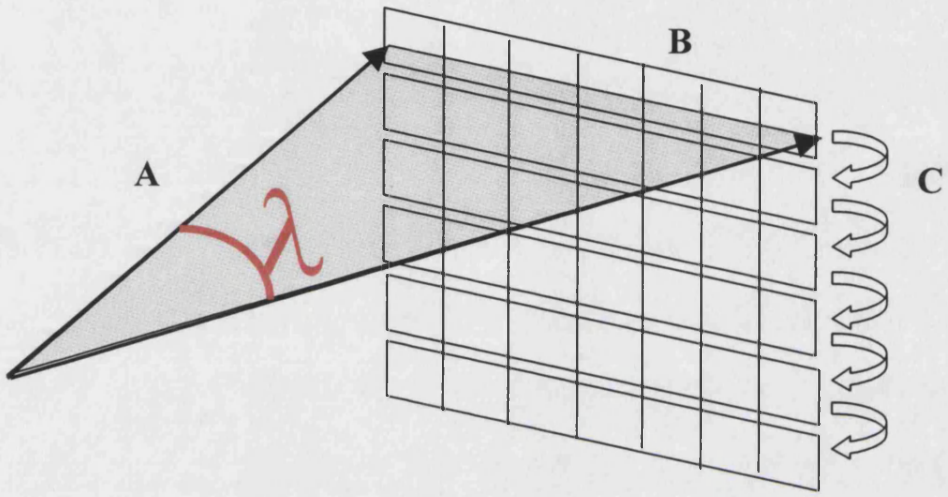

Figure 3.3: Application of the CCD in kinetic experiments. ***A****: Wavelength resolved light from the spectrograph is imaged across the top of the CCD array axis;* ***B****: incident light generates photocharge at the device;* ***C****: rapid and efficient charge transfer allows recording of sequential spectra.*

3.4 Description of the Apparatus

3.4.1 Gas Handling

Precursor gases were mixed in a carrier gas flow in a Pyrex mixing line equipped with Teflon taps (Young and Co.) prior to their arrival at the reaction cell. The mixing line consisted of a cylindrical carrier gas vessel punctuated at regular intervals by gas injectors aligned against the carrier gas flow to promote efficient mixing. Non corrosive gases were routed to the mixing line *via* mass flow controllers (MKS). The flowrates of corrosive gases were monitored by channelling their paths through glass ball-meters. All flow controllers and meters were regularly calibrated by monitoring the flow rate of a bubble through a burette attached to the upstream end of the given

mass flow controller. In those instances where precursor reagents existed in the liquid or solid phase at ambient temperatures, appropriate bubblers or traps were employed to entrain a vapour of the reagent in an inert gas flow.

Premixed gases were supplied to the reaction vessel *via* a Teflon line. The reaction cell consisted of a spectrosil quartz tube of 1 m in length and was double jacketed. The inner jacket was connected to a thermostatting unit (Huber CC180) which recirculated an inert temperature regulated liquid (Galden, HT110). The outer jacket was connected to a rotary pump and evacuated to prevent condensation of atmospheric humidity on the cell walls at low temperatures. Similarly, the windowed end pieces of the reaction vessel were double walled and evacuated to thwart condensation on the optical windows. The internal temperature of the vessel was measured using a ceramically enclosed, platinum resistance thermometer (Farnell, PT100) which resided in the gas flow. Hence the gaseous temperature in the cell could be regulated in the range 206 to 373 K as described in appendix 4.

During experiments, gases were continuously and slowly flowed through the apparatus, hence a fresh mix of gas was supplied to the reaction cell for each flashed experiment. This slow flow of gas took place on a timescale much longer then the kinetic timescale of kinetic processes under study. Experiments were conducted over a pressure range of 25 to 760 Torr by connecting the cell exit to a rotary pump. The pressure at the cell input was continuously monitored with a capacitance manometer (MKS Baratron). Experiments were undertaken to investigate the extent of any pressure gradient along the cell length. No measurable gradient was observed.

3.4.2 Radical Generation

Free radicals and atoms were generated within the reaction vessel by flash photolysis. The photolysis source was a 1 m long xenon arc lamp (Perkin Elmer, QDX66) filled to a pressure of 50 Torr which was situated adjacent and parallel to the reaction vessel. Power was supplied to the lamp from a 25 kV, 2.6 μF rapid discharge capacitor (NWL Ltd.). The capacitor was typically charged to 20 kV by a high voltage power supply (Glassman High Voltage Ltd., EH100). This high voltage causes spontaneous

breakdown in the lamp thereby flashing it. To prevent uncontrolled firing, a spark gap (EG&G, GP12B) isolated the flashlamp from the capacitor until triggering was required. The spark gap was ionised by a trigger module (EG & G, TM11A) which itself was initiated by a TTL pulse, generated by the control computer and connected *via* an isolated fibre optic cable. The pulse energy of the flashlamp, approximately 500 J, was completely discharged within 20 μs.

The reaction cell and flashlamp were housed within an opaque box to minimise the escape of light. The box was constructed from aluminium and earthed to a point remote to the CCD electronics, to minimise radiofrequency interference. A similar box, constructed from steel, enclosed the flashlamp circuit and was earthed to the same point. All electrical leads into these boxes were screened and integrity maintained with the earthed boxes at the interfaces. Mains power was supplied from a filtered unit.

The effective flashlamp light intensity at the cell could be varied by adjusting the separation of the lamp and the cell over a range of 3 to 18 cm. When short wavelength ($\lambda < 280$ nm) photolysis was not required, the flashlamp was enclosed within a Pyrex jacket.

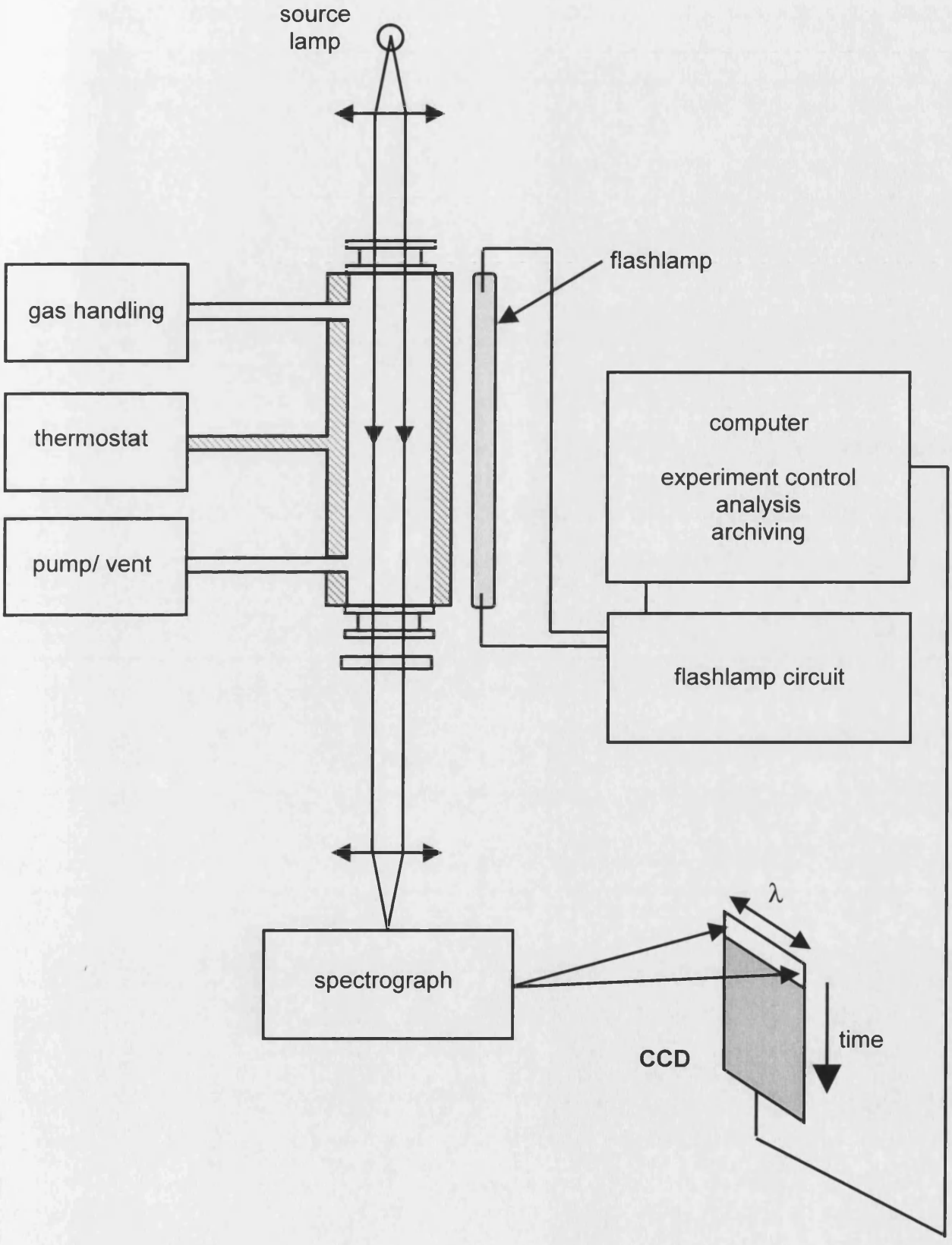

Figure 3.4: Schematic diagram of the flash photolysis apparatus employing CCD monitoring.

3.4.3 Species Monitoring

Transient molecules and radicals within the reaction vessel were identified and monitored by UV/visible absorption spectroscopy. The source was either a 30 W high-brightness deuterium lamp (Hamamatsu L5499) for work in the UV (λ = 200-300 nm) or a 70 W continuous xenon arc lamp (Hamamatsu L2174) where output in the UV/visible was required. In both cases, the lamp output was collimated along the length of the cell and subsequently focused, using a pair of spectrosil quartz lenses, onto the entrance slit of a 25 cm focal length astigmatic Czerny-Turner spectrograph, which imaged the dispersed light onto the CCD.

The spectrograph was fitted with three interchangable diffraction gratings, ruled at 600, 300 and 150 grooves/mm respectively. These gratings, coupled with the detector size, gave rise to spectral coverages of approximately 30, 60 and 120 nm respectively. Increasing the spectral coverage compromised resolution, hence limiting resolutions of the spectra associated with the respective gratings were approximately 0.11, 0.22 and 0.45 nm. The instrument function of the spectrograph was measured for each grating over a range of spectrograph entrance slit widths from 10 to 1000 μm. In each experiment the diffraction grating in use was dispersion and wavelength calibrated relative to the known spectral lines of a mercury pen-ray lamp.

The principle of operation of the CCD has been described above. The CCD employed in this work consisted of a 298 × 1152 array of light sensitive pixels mounted in a Peltier cooled camera head (Wright Instruments Ltd.). The short axis of the array was aligned in the dispersive plane of the spectrograph, representing the wavelength resolved axis of the array. The camera head was fixed to the spectrograph *via* a flange which facilitated linear translation in the focussing and vertical (time) axes. The wavelength resolved light from the spectrograph illuminated the 31 non-masked rows of the CCD. The distortion of the temporal resolution arising from the simultaneous illumination of 31 rows of the CCD is discussed in appendix 2. An optical shutter was integrated within the optical line to prevent the accumulation of photocharge between experiments.

3.5 Operating Procedure

The CCD and flashlamp were controlled from a personal computer. The course of a typical experiment is indicated by the flow chart in figure 3.5. To improve the signal to noise ratio each experiment typically incorporated 5-100 co-added photolysis runs. The repetition rate of these co-added runs was limited by the cell flow out time (dependent on total flow rate and pressure) and the high voltage capacitor recharge time (15 s). Following co-addition, data files of light intensity versus wavelength versus time were transferred to a separate PC for analysis.

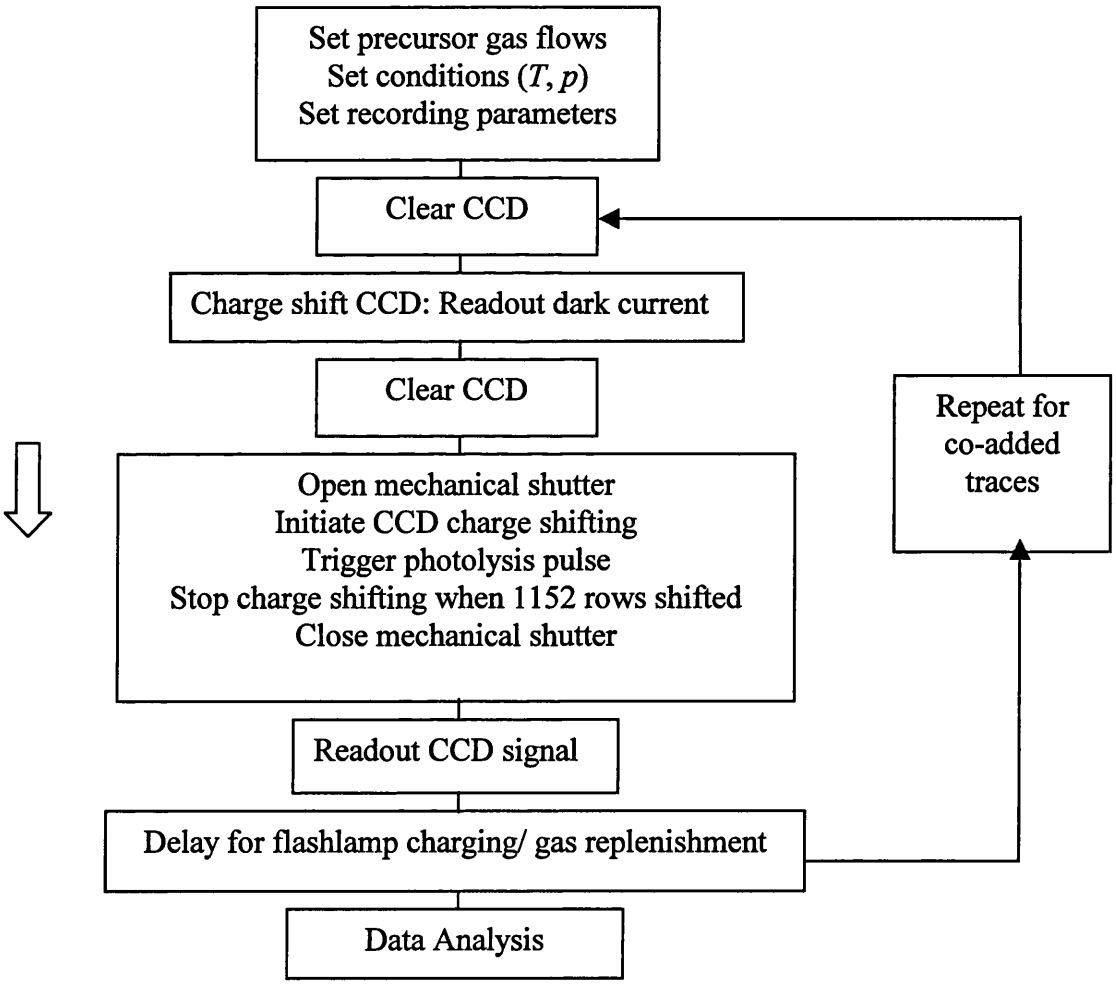

Figure 3.5: Flowchart indicating operation of a typical flash photolysis experiment.

3.6 Analytical Procedures

The recorded light intensity for a given pixel on the CCD was converted to the time and wavelength resolved absorbance of the cell contents by applying Beer's law:

(3.i) $$A_\lambda = \ln (I_{o,\lambda} / I_{t,\lambda})$$

The nature of the experiment affected the method by which (i) was applied. Both basic spectroscopy of non-flashed precursor gas mixtures and time resolved spectroscopy of photolysed gas mixtures was carried out, discussed in turn below.

3.6.1 Non-Kinetic Experiments

For a non-kinetic (non-flashed) experiment, the transmitted light intensity through the reaction vessel was recorded in both the presence and absence of the absorbing gas mixture. Time resolved rows of intensity were co-added, since no temporal information was gathered, and Beer's law was applied to each pair of intensities recorded in each column (wavelength point), giving rise to the absorption spectrum.

3(ii) $$A_\lambda = \ln (\langle I_0(\lambda,t)\rangle / \langle I_t(\lambda,t)\rangle)$$

$\langle I_0(\lambda,t)\rangle$ and $\langle I_t(\lambda,t)\rangle$ denote the time averaged wavelength (CCD column) resolved light intensities recorded in the absence and presence of the absorbing species respectively.

3.6.2 Kinetic Experiments

For kinetic (flashed) experiments, a wavelength resolved spectrum was recorded for every row (time point) on the CCD. Absorbances were calculated for each row relative to time averaged light intensities recorded during the pre-flash (non-kinetic) period, according to iii. Thus the absorption spectrum generated for any row on the CCD represented the *change* in absorbance resulting from the photolysis pulse and

subsequent chemistry. Sequential spectra show time evolution of these absorbance changes.

(3.iii) $$A_\lambda = \ln (\langle I_0(\lambda,t)\rangle / I_t(\lambda,t))$$

In practice a complication arose from the charge shifting routine executed by the CCD. As a row of signal (charge) was transferred down the non-illuminated region of the CCD, a small amount of additional charge was acquired. This effect was cumulative so that data recorded from early times in a given run, which traversed the entire length of the CCD, accumulated more of this charge than later rows which were shifted a shorter distance across the array. If left uncorrected, this phenomenon led to a spurious increase in absorption as a function of time. Correction was performed by running identical, but non-flashed experiments in conjunction with kinetic experiments and subtracting the absorptive contribution resulting from this phenomenon by modifying (iii):

(3.iv) $$A_\lambda = \ln (\langle I_0(\lambda,t)\rangle / I_t(\lambda,t))_{\text{flashed}} - \ln (\langle I_0(\lambda,t)\rangle / I_t(\lambda,t))_{\text{nonflashed}}$$

3.6.3 Determination of Species Concentration

The absorbance of a gaseous mixture is related to the concentrations of its components $x, y, z\ldots$ by the Beer-Lambert law:

(3.v) $$A_\lambda = \sigma_x(\lambda).[x].l + \sigma_y(\lambda)\,[y].l + \sigma_z(\lambda).[z].l + \ldots$$

Thus, in these experiments, the concentrations of transient absorbers were determined by fitting reference cross sections to the experimental absorption spectra. In many cases, spectral regions could be chosen where absorbers did not overlap and simple scaling allowed determination of absorber concentration. However, in cases where the absorption cross sections of transient absorbers overlapped, multiple equations could be constructed from (v) and solved simultaneously. For example, the two absorber (x and y) system gives rise to a Beer-Lambert expression of the form (vi):

(3.vi) $$A(\lambda) = l(\sigma_x(\lambda)[x] + \sigma_y(\lambda)[y])$$

Since the CCD recorded 298 wavelength resolved absorbances at each time point, in principle, 298 wavelength resolved equations could be constructed from the experimental data in which the quantities $A(\lambda)$, l, $\sigma_x(\lambda)$ and $\sigma_y(\lambda)$ were all known. Any two of these equations could then be solved to yield the concentrations $[x]$ and $[y]$. In practice, summation routines were used to generate the two required expressions to prevent data wastage and maximise the signal to noise ratio. A more detailed account of the spectral fitting routines is given in appendix 3.

Where the absorption cross sections of monitored species exhibited spectral structural features, differential fitting was used to identify and determine the concentration of those absorbers. Essentially, this technique employed high-pass filtering of the structured regions of both the reference cross section and the recorded absorption spectrum. This could be achieved by the fitting and subsequent subtraction of a low order polynomial function or a sliding average routine. Spectral fitting of the remaining structural features could then be implemented to yield the concentration of the spectrally structured absorber unequivocally and accurately. An example of this technique is illustrated by figures 3.6 and 3.7 which depict low order polynomial fitting to an experimental absorption spectrum and subsequent fitting of the differential structure. Since absorption cross-sections of structured spectral features are critically dependent upon spectrograph instrument function, care must be taken to match the resolutions of the reference and experimental spectra (see appendix 1).

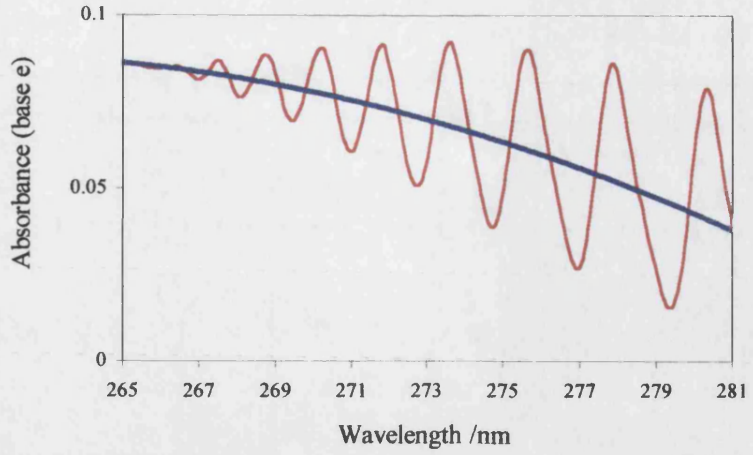

Figure 3.6: High-pass filtering of a typical ClO spectrum. Subtraction of the smooth function (blue) from the experimental spectrum (red) gives rise to the differential spectrum (see figure 3.7).

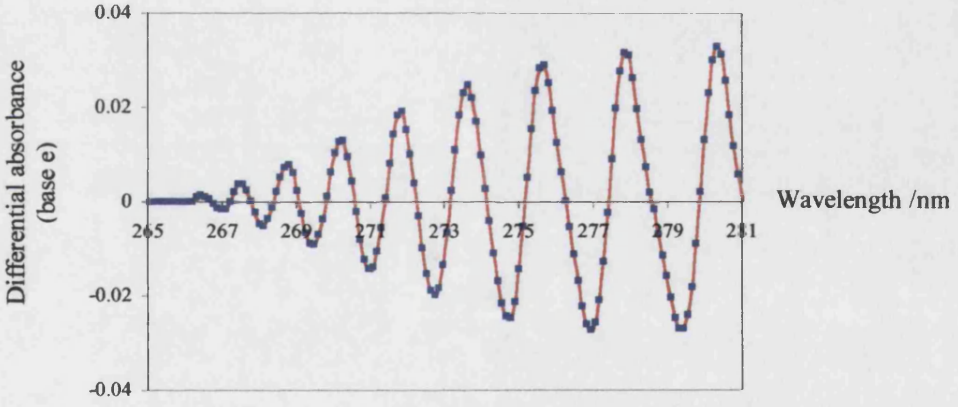

Figure 3.7: Differential fit of the ClO cross section (blue squares) to the experimental ClO absorption spectrum (red).

Differential spectroscopy is a powerful technique which gives rise to unequivocal identification and accurate quantification of an absorber exhibiting spectrally structured features in a manner which is unaffected by other species with overlapping absorption bands. Furthermore, this technique facilitates spectral deconvolution *via* subtraction of this quantified structured absorbance and further fitting can be applied to quantify any underlying spectrally smooth absorbers. The strength of this technique is shown in figure 3.8 which compares the concentration profiles of 3 absorbers (one structured

(ClO), two featureless (Cl_2O_2 and Cl_2O) fitted simultaneously to those obtained by differential fitting to the ClO and subsequent fitting to the two underlying absorption. It is particularly evident that the signal to noise ratio is greatly improved by differential fitting.

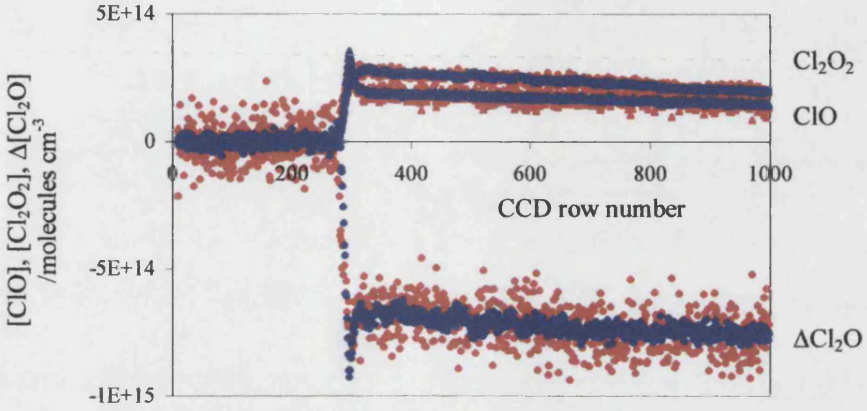

Figure 3.8: Comparison of concentration versus time profiles derived from the simultaneous three absorber fit (red) and the differential σ_{ClO} fit followed by two absorber fits to the residual (blue).

Temporal evolution of transient absorbers in the flash photolysis experiment was monitored by applying the chosen fitting routine to each row of CCD data, giving rise to concentration versus time profiles such as those shown in figure 3.8.

3.6.4 Kinetic Analysis of Concentration -Time Profiles

Wherever possible, classical solutions to the governing kinetic (differential) equations were derived, linearised and fitted to the experimental kinetics. For more complex systems, such as multiple reaction systems, the ensemble of differential equations was insoluble and numerical integration techniques were used to simulate temporal evolution of species concentration. Least squares fitting of simulated to observed concentration versus time profiles was used to optimise kinetic parameters. One problem with simple numerical integration routines, known as 'stiffness', results from the wide variety of timescales adopted by different reactions taking place. Efficient

algorithms built into commercial numerical integration programs accounted for this problem. The commercial package FACSIMILE[7] was used to simulate temporal profiles and fit these to experimental traces, extracting kinetic parameters. The model incorporated into FACSIMILE included all known gas phase chemical reactions and other subroutines specifically developed to account for flow in/out of the reaction vessel and distortions imparted to the experimental kinetics by the inherent time averaging associated with CCD detection (discussed in appendix 2).

Each kinetic analysis carried out using numerical integration was accompanied by a sensitivity study to ensure that the derived kinetic parameter was correctly and independently derived from the experimental data. Sensitivity studies were also used to determine the effect of secondary reaction rate coefficients included in the model on the kinetic parameter under study, and to exclude non-participating or unimportant reactions from the model. Typically, the study involved reanalysis of a representative experimental trace using a slightly modified model. Other types of sensitivity study involved examining the goodness of fit of simulated to experimental traces as a function of the kinetic parameter under investigation. Details of each sensitivity analysis carried out are given in the appropriate chapters, below.

3.7 References

[1] R.G.W. Norrish and G. Porter, *Nature* **1949**, 164, 658.

[2] G. Porter, *Proc. R. Soc. (London)*, **1950**, **A200**, 284.

[3] D. Husain; *PhD Thesis, University of Cambridge*, **1962.**

[4] G. Porter and P. West, *Proc R. Soc Ser. A.*, 1964, 279, 302.

[5] See, for example, P.D. Lightfoot; R. Lesclaux and B. Veyret, *J. Phys. Chem.*, **1999**, 94, 700.

[6] D.M. Rowley, M. H. Harwood, R.A. Freshwater and R.L. Jones, *J. Phys. Chem.*, **1996**, 100, 3020.

[7] A.R. Curtis and W.P. Sweetenham, FACSIMILE, *AERE Harwell Publication R12805*, Computer Science and Systems Division, Harwell Laboratory, Oxfordshire, **1987**.

4. The Absorption Cross Section and Self-Reaction of the ClO Radical

4.1 Introduction

The pivotal role of the ClO radical in human-induced polar ozone depletion is well established[1]. The catalytic cycle incorporating the ClO self-reaction and ClO dimer photolysis is thought to be the principal route to ozone destruction within the polar vortices:[2]

(4.1)		$2(Cl + O_3$	$\rightarrow$	$ClO + O_2)$
(4.2a, -4.2a)		$ClO + ClO + M$	$\leftrightarrow$	$Cl_2O_2 + M$
(4.3)		$Cl_2O_2 + h\nu$	$\rightarrow$	$ClOO + Cl$
(4.4)		$ClOO + M$	$\rightarrow$	$Cl + O_2 + M$
	net:	$2O_3$	$\rightarrow$	$3O_2$

In the sunlit stratosphere, forward reaction (2a) is the rate determining step in this cycle and therefore an accurate determination of its rate coefficient is critical in the simulation and hence quantification of polar ozone depletion. The current NASA recommendation for $k_{0,2a}$ at 200 K is $(7.7^{+2.2}_{-3.4}) \times 10^{-32}$ cm^6 molecule^2 s^{-1} for atmospheric modelling purposes[3] , giving considerable relative errors of +31% and – 47%.

In addition to the termolecular dimerisation indicated by reaction (2a), three competing bimolecular channels of the ClO self-reaction are known to exist:

(4.2b)	$ClO + ClO$	$\rightarrow$	$Cl_2 + O_2$
(4.2c)		$\rightarrow$	$ClOO + Cl$
(4.2d)		$\rightarrow$	$OClO + Cl$

However the rates of these bimolecular processes are slow in comparison to dimer formation ($k_{2b+2c+2d} = 0.03k_{2a}$ at 298 K and 760 Torr). Furthermore, the rate constants

which characterise the bimolecular channels show a positive temperature dependence in contrast to the negative temperature dependence exhibited by k_{2a}. As a result channels (2b-d) exert a negligible effect on the chemistry of ClO radicals under stratospheric conditions.

This chapter presents the results of a temperature and pressure dependent study of the termolecular dimerisation reaction channel (2a). Since ClO was monitored by UV absorption spectroscopy, quantification of ClO concentrations required a determination of the ClO absorption cross section. Moreover, since the absorption spectrum of the ClO radical exhibits vibronic structure at wavelengths in excess of 265 nm, the ClO absorption cross section is both instrument and temperature dependent. Thus it was necessary to determine the ClO cross section under all experimental conditions. This, in turn required detailed understanding and careful design of the radical generation chemistry, which is discussed below.

4.2 Radical Generation

ClO radicals were produced by flash photolysis of $Br_2/Cl_2O/Cl_2/N_2$ gas mixtures. Photolytic generation of bromine atoms and their subsequent reaction with excess Cl_2O represented the dominant source of ClO in the reaction vessel:

(4.5) $Br_2 + h\nu \rightarrow 2Br$

(4.6) $Br + Cl_2O \rightarrow ClO + BrCl \qquad k_{298} = 4.3 \times 10^{-12}$

{Unless stated otherwise all rate constants are quoted from the JPL-97 evaluation[3] and expressed in bimolecular units of molec^{-1} cm^3 s^{-1} at 760 Torr.}

In addition, some Cl_2 photolysis gave rise to ClO production *via* reactions (7), (8), (6) and (9):

(4.7) $Cl_2 + h\nu \rightarrow 2Cl$

(4.8)	$Cl + Br_2$	→	$Br + BrCl$	$k_{298} = 3.6 \times 10^{-10}$[4]
(4.9)	$Cl + Cl_2O$	→	$ClO + Cl_2$	$k_{298} = 9.6 \times 10^{-11}$

A third source of ClO was from direct Cl_2O photolysis. Given that Cl_2O photolysis is a multichannel process, this raised the possibility of complicating Cl, $O(^3P)$ and $O(^1D)$ chemistry in the gas mixture:

(4.10a)	$Cl_2O + h\nu$	→	$Cl + ClO$	($\lambda_{thresh} = 840$ nm)
(4.10b)		→	$2Cl + O(^3P)$	($\lambda_{thresh} = 292$ nm)
(4.10c)		→	$Cl_2 + O(^3P)$	($\lambda_{thresh} = 710$ nm)
(4.10d)		→	$Cl_2 + O(^1D)$	($\lambda_{thresh} = 335$ nm)

Despite the energy thresholds for all four channels of Cl_2O photolysis being accessible to the broadband flashlamp, recent experiments[5] have indicated that channel (10a) is the only active channel at wavelengths of 308 nm and above. Thus in these experiments, the flashlamp was enclosed in a Pyrex jacket to prevent short wavelength photolytic radiation ($\lambda < 280$ nm) entering the reaction vessel. A small amount of ClO production *via* (10a), (8), (6) and (9) was however, inevitable.

Br_2 was introduced to the gas mixing line by continuously bubbling a slow flow (typically 10 sccm) of N_2 (BOC, > 99.98% purity) through liquid bromine (Acros, > 99.8%). The bubbler was held at 273 K to ensure that a constant and known vapour pressure of Br_2 was entrained within the N_2 carrier gas flow.

Cl_2O was produced *in situ* in these experiments. Details of the synthetic scheme are given below. Taking into account the incomplete conversion of Cl_2 to Cl_2O associated with the synthesis (discussed below), typical precursor species concentrations are given in table 4.1 below.

Precursor Species	Pre-flash Concentration
Br_2	$(0.5 - 3) \times 10^{16}$
Cl_2O	$(2 - 8) \times 10^{15}$
Cl_2	$(1 - 5) \times 10^{15}$
N_2	Balance to 1 atmosphere

Table 4.1: Typical precursor concentrations in molecules cm^{-3} at 298K, 760 Torr.

Under these conditions, flash photolysis of the precursor gas mixture led to prompt generation of ClO radicals in comparison to the timescale of their subsequent decay. Calculation of *pseudo* first order loss rates for the photolytically produced atomic species confirmed that the sole fate of Br atoms was reaction with Cl_2O and that the principal fate of Cl atoms was reaction with Br_2, liberating Br. Any excited $O(^1D)$ atoms produced by Cl_2O photolysis would be rapidly and efficiently quenched to $O(^3P)$. Moreover, the sole fate of any $O(^3P)$ was calculated to be reaction with Br_2. As discussed below however, no evidence for O atom production was obtained.

4.2.1 Cl_2O Synthesis

Gaseous Cl_2O was produced in a trap upstream from the gas mixing line by the method of Hinshelwood and Pritchard (1923).[6] Chlorine (BOC, 5% in N_2, purity >99.9%) was passed through a trap containing dried yellow mercuric (II) oxide (Sigma Aldrich, >99%) interspersed with glass beads to allow a flow of gas:

(4.11) $$2Cl_{2(g)} + nHgO_{(s)} \rightarrow Cl_2O_{(g)} + HgCl_2.(n\text{-}1)HgO_{(s)}$$

The yield of Cl_2O was measured spectroscopically by fitting reference Cl_2O cross sections[3] to recorded absorption spectra of the Cl_2/Cl_2O mixture suitably diluted in N_2. The conversion efficiency of Cl_2 to Cl_2O was calculated by comparison with the known Cl_2 flow through the HgO trap and the subsequent dilution factor in the mixing line, coupled with the 2:1 stoichiometry associated with reaction (11). This efficiency

was typically 70%, a figure consistent with spectroscopically determined residual Cl_2 concentrations in the diluted mixture. Once again, Cl_2 cross sections were taken from the NASA evaluation.[3] This unreacted Cl_2 represented the only source of chlorine in the pre-flash mixture.

4.3 Determination of the Differential ClO Cross Section

Quantification of ClO concentrations in the kinetic experiments required a knowledge of the ClO absorption cross section, σ_{ClO}. As discussed in chapter 3, differential spectroscopy was used to fit reference cross sections to sequential time resolved spectra. This method makes use of the vibronic structure of the ClO spectrum, giving an unambiguous and accurate measure of $[ClO]_t$. However, since structured cross sections are both instrument resolution and temperature dependent, accurate determination of σ_{ClO} was essential. Four separate approaches to measure σ_{ClO} were attempted to characterise this key parameter.

4.3.1 σ_{ClO} Determination - Method 1

ClO radicals were generated by the $Br_2/Cl_2O/Cl_2/N_2$ photolysis scheme described above. The experimental settings are indicated in table 4.2. Each recorded data set was the result of 50 co-added flashed experiments recorded under identical conditions.

Source for UV absorption	D_2 lamp
Spectrograph diffraction grating	300 grooves /mm
Entrance slit width	75 μm
Resolution	1.1 nm (FWHM)
Wavelength regime	235 - 300 nm
CCD clocking rate	50 μs

Table 4.2: Experimental settings used in ClO cross section measurements (method 1)

A typical time averaged (for 10 ms directly following photolysis) post-flash absorption spectrum relative to pre-flash is shown in figure 4.1. The spectrum contains positive absorbance contributions from ClO (structured at $\lambda > 265$ nm) and Cl_2O_2 together with a negative contribution from the removal of the parent molecule, Cl_2O. In addition a small negative contribution arises from Cl_2 photolysis but this was negligible due to the small value of its cross section over the monitored wavelength region ($\sigma_{Cl2,300\ nm} = 1.2 \times 10^{-19}$ cm^2 molecule^{-1}).

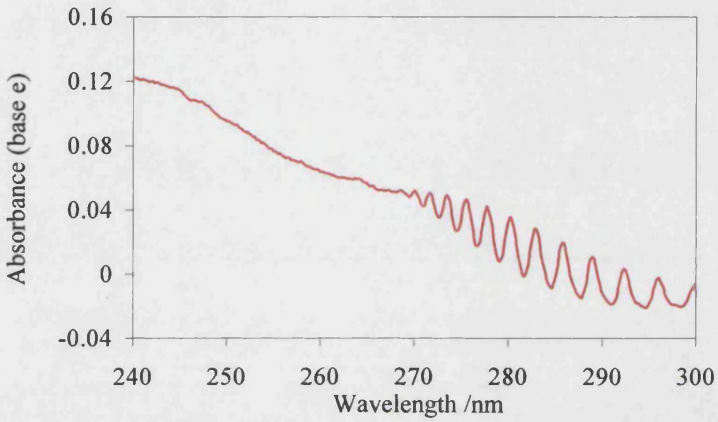

Figure 4.1: Typical post-flash absorption spectrum of $Br_2/Cl_2O/Cl_2/N_2$ gas mixture.

The essence of the first method attempted to determine σ_{ClO} relied upon the fact that at wavelengths below 265 nm, all three of the significant absorbers (ClO, Cl_2O_2 and Cl_2O) exhibit broad, featureless spectra and are thus independent of instrument resolution. Thus in principle it was possible to fit the sequential time resolved spectra with reference cross sections attributed to all 3 absorbers simultaneously. The provenance of the reference absorption cross sections is given in the next section. An example of the fit of the three unstructured absorption cross sections to a single observed post-flash spectrum is given at $\lambda < 265$ nm in figure 4.2.

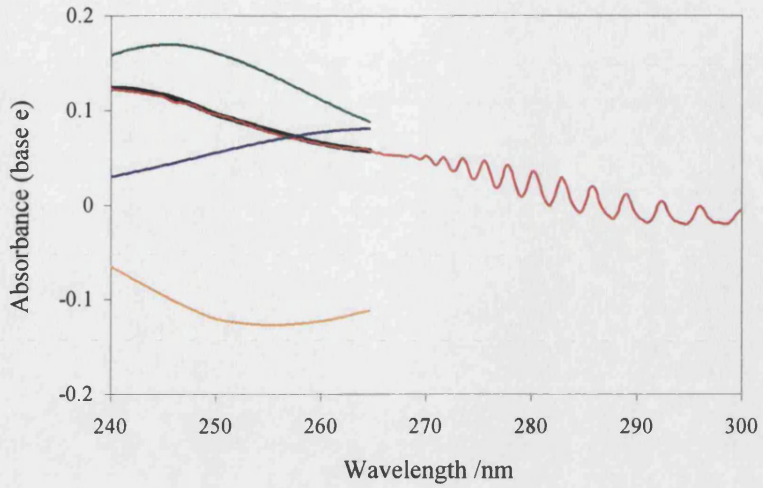

Figure 4.2: Cross section determination. The calculated absorption (black) is a composite of the three individual absorptions (ClO, Cl_2O_2 and ΔCl_2O shown in blue, green and orange respectively) determined by simultaneous fiiting of the three reference cross section to the data (red) at $\lambda < 265$ nm.

The spectrum shows, as expected, positive contributions from ClO and Cl_2O_2 absorbances and a negative contribution from Cl_2O, destroyed by photolysis and reaction with halogen atoms. Repeating this fitting to the respective spectrum recorded at each time point generated concentration versus time profiles for the three species such as that indicated in figure 4.3.

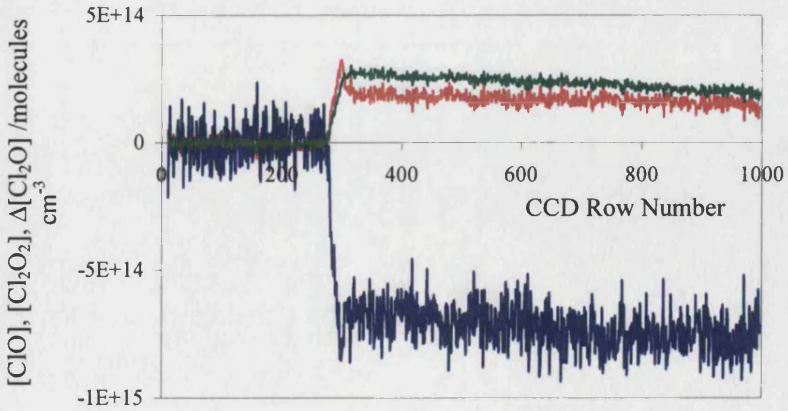

Figure 4.3: Concentration versus CCD row number (effectively time) profiles of the three transient absorbers, ClO (red), Cl_2O_2 (green) and Cl_2O (blue) determined by simultaneous fitting of the three reference cross sections to the time resolved absorbance data over the regime $240 < \lambda < 265$ nm.

The time resolved concentration data obtained from spectral fitting could then be used to simulate the individual absorptions comprising the time averaged composite spectra. Hence subtracting the simulated Cl_2O and Cl_2O_2 absorption contributions from the time averaged experimental spectrum over the entire wavelength regime gave rise to a spectrum attributed solely to ClO. Further application of the Beer-Lambert law, incorporating the known concentration of ClO associated with the spectrum, allowed calculation of the ClO cross section. Multiple experiments, conducted over a range of precursor concentrations (see table 4.1) displayed no systematic dependence of the ClO cross section on the initiation chemistry. Figure 4.4 shows the average ClO cross section obtained in this way from 16 determinations.

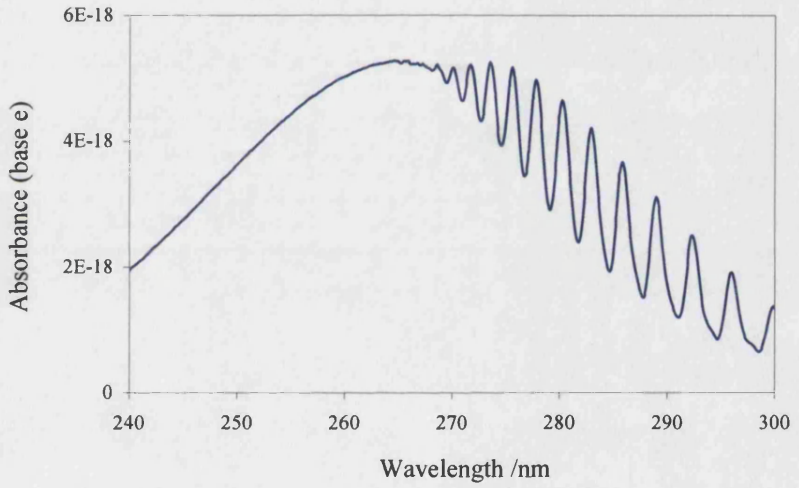

Figure 4.4: ClO absorption cross section determined by method 1. See text for details.

4.3.2 Reference Cross Sections

Figures 4.5, 4.6 and 4.7 illustrate previous determinations of the ClO, Cl_2O_2 and Cl_2O absorption cross sections available in the literature. In all cases the quoted values have been interpolated and error bars are omitted for clarity. Agreement between the Cl_2O spectra is strong across all four studies. Knauth's determination[7] was employed in this investigation in accordance with the recommendation by DeMore *et al.*[3]

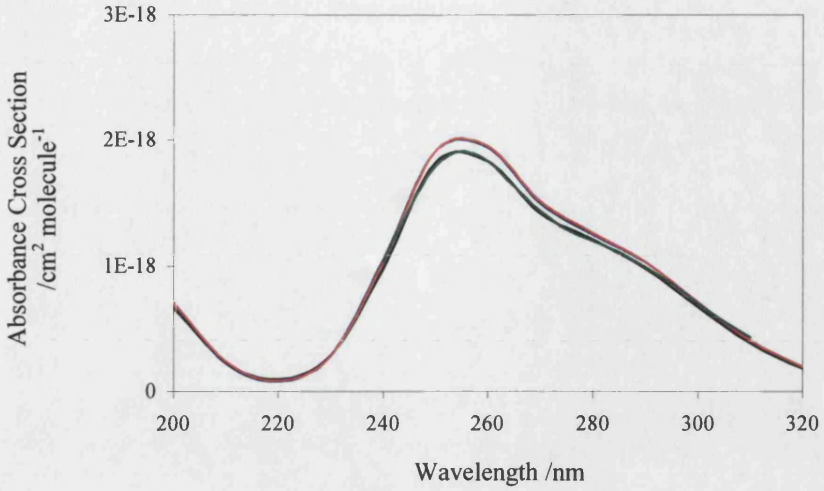

Figure 4.5: Comparison of the literature Cl_2O cross sections reported by Knauth et al.[7] (shown in red), Molina and Molina[8] (blue), Lin[9] (black) and Simon et al.[10] (green).

Similarly the reported unstructured (λ < 265 nm) ClO cross sections show good agreement. The mean of the determinations by Sander and Friedl[11], Simon *et al.*[10], Mandelman and Nicholls[13] and Trolier *et al.*[15] was used in this work.

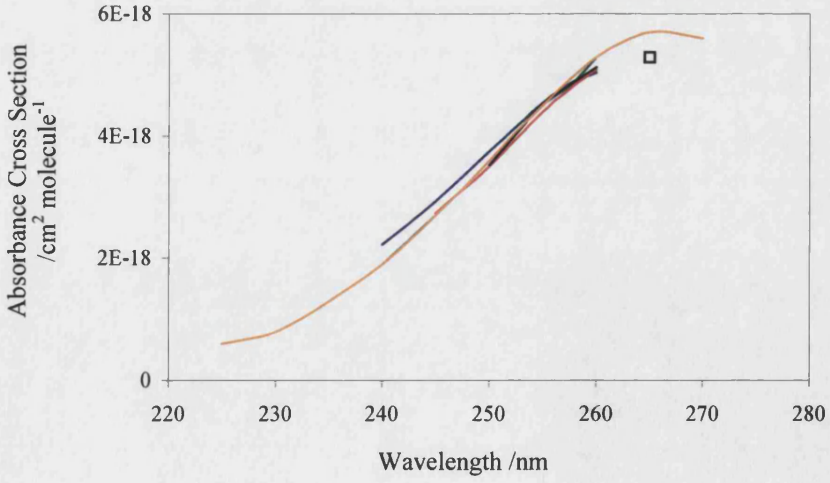

Figure 4.6: Comparison of the literature ClO cross sections reported by Simon et al.[10] (shown in blue), Sander and Friedl[11] (red), Porter et al.[12] (green), Mandelman and Nicholls[13] (black), Johnston et al.[14] (orange) and Trolier et al.[15] (open square).

There is, however, a significant degree of discrepancy between the reported Cl_2O_2 cross sections. These discrepancies may have arisen from the existence and unique spectroscopy of different isomers of the ClO dimer, which could have been produced in different ratios under the different conditions (notably temperature, pressure and experimental timescale) employed between the three studies.[21]

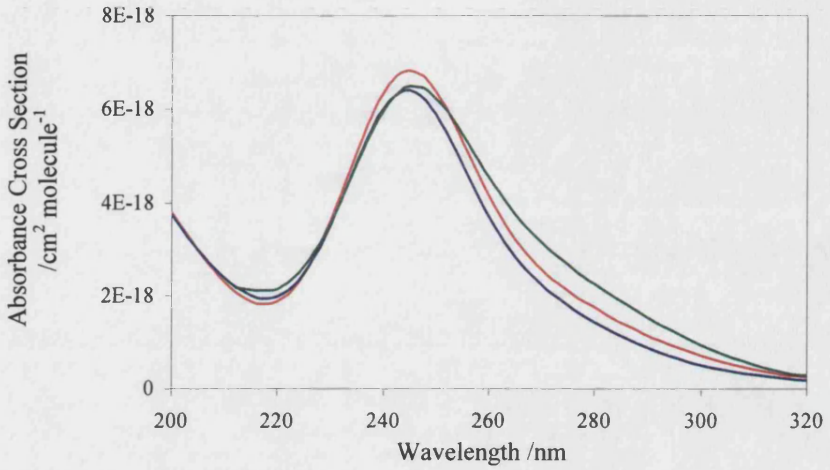

Figure 4.7: Comparison of the literature Cl_2O_2 cross sections reported by DeMore and Tschuikow-Roux[16] (shown in red), Huder and DeMore[17] (blue) and Burkholder et al.[18] (green)

The most recent study, by Huder and DeMore[17] concluded that previous measurements of the ClO dimer cross section had improperly corrected for the underlying Cl_2O absorption. On this basis the ClO dimer spectrum reported by Huder and DeMore was employed in this work. This choice is supported by a recent publication from Avallone and Toohey.[19] These authors measured the photolysis rate of Cl_2O_2 as a function of solar zenith angle (SZA) from observations of ClO mixing ratios in the Arctic stratosphere and compared their results with photolysis rates calculated from laboratory determined Cl_2O_2 cross sections. Avallone and Toohey's results are in accord with values derived from the determination by Huder and DeMore. By contrast their observations are in poor agreement with those calculated from the remaining literature studies and indeed the NASA evaluation[3] which represents an average of all the published spectra.

4.3.3 Differential σ_{ClO} Fitting

Having measured the ClO cross section at 298 K, differential spectroscopy, as discussed in section 4.3, could be implemented to quantify temporally resolved ClO concentrations. Software was developed to remove the contribution of ClO from each experimental absorption spectrum, leaving a residual spectrum comprising a positive absorption from Cl_2O_2 and a negative contribution from Cl_2O removal. An example of this spectral deconvolution is shown in figure 4.8.

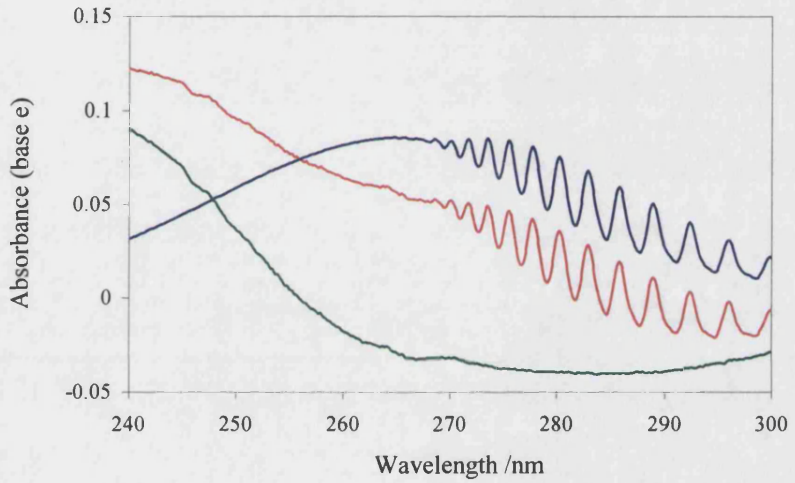

Figure 4.8: Typical experimental absorbance spectrum (red) shown with simulated ClO absorbance (blue) arising from the differential fit of the measured ClO cross section and the residual (green) after subtraction of the simulated ClO absorbance, a composite of ΔCl_2O and Cl_2O_2 absorptions.

Subsequent fitting of the literature cross sections to the residual absorption across the entire wavelength range adopted generated the concentration versus time profiles of the remaining two absorbers. Since the short wavelength absorptions were used to generate the ClO cross section, these were consistent with the temporal concentration profiles from fits to the low wavelength data only. However, signal to noise ratios associated with the three traces were vastly improved over those generated from the same data by employing a simultaneous three absorber fit in the smooth spectral region (see figure 4.9).

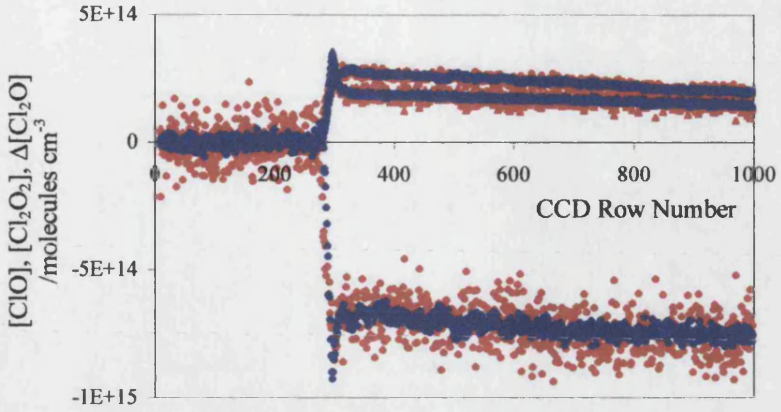

Figure 4.9: Comparison of concentration versus time profiles derived from the simultaneous three absorber fit (red) and the differential σ_{ClO} fit followed by two absorber fits to the residual (blue).

The ability to monitor all three chlorine oxide species in the reaction vessel gave rise to an internal check on the mass balance of the system. Given that there are no significant loss routes for these species on the experimental timescales, merely processes which interconvert them, summation of the concentrations of the three absorbers and accounting for the stoichiometry according to (i) should yield a zero residual. An example of a trace exhibiting mass balance is shown in figure 4.10.

(4.i) Mass balance(t) = $[ClO]_t + 2[Cl_2O_2]_t + [Cl_2O]_t = 0$

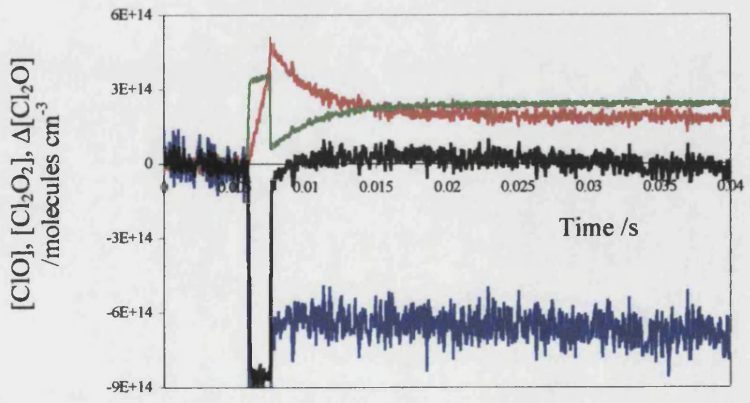

Figure 4.10: Temporally resolved $[ClO]_t$, $[Cl_2O_2]_t$, $[Cl_2O]_t$ (shown in red, green and blue respectively). Mass balance, calculated according to (i) is indicated in black.

Whilst figure 4.10 shows an unprecedented degree of constraint on the chlorine oxide species monitored, in practice mass balance calculations applied to the concentration profiles generally returned a positive residual such as that shown in figure 4.11. Moreover, figure 4.11 is one example of many recorded concentration profiles which exhibited an apparent regeneration of Cl_2O in the post-flash region, on the timescale of ClO decay. No known gas phase chemistry could account for this observation and it is therefore unlikely to be a real effect. Under the experimental conditions employed, recombination of Cl with ClO would not compete with other Cl atom loss routes even if it were collisionally fast.

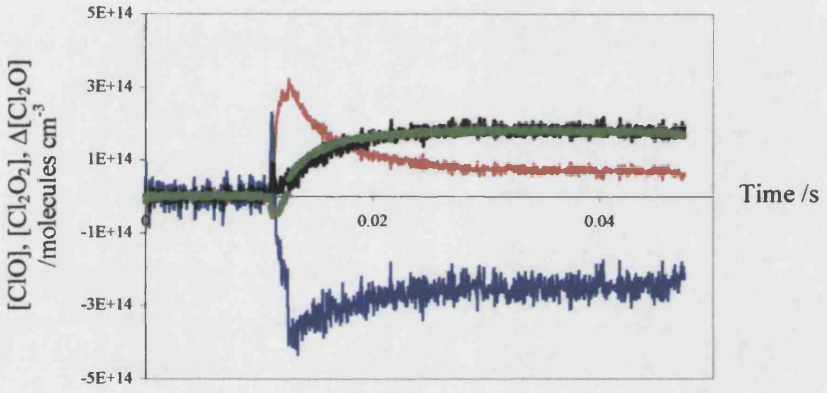

Figure 4.11: ClO self-reaction concentration versus time profile where mass balance is indicated in black and $[Cl_2O]_t$ shows spurious kinetic behaviour.

The most likely explanation of this problem suggests an error in the subtraction of the smooth ClO absorption at short wavelengths, giving rise to a residual which consists not only of Cl_2O and Cl_2O_2, but also some ClO absorbance. Subsequent fitting of this tainted residual most likely attributes the remaining kinetic ClO signal to Cl_2O (whose absorption spectrum is similar in shape to that of ClO), giving rise to spurious values of $[Cl_2O]_t$.

The most probable source of this spurious subtraction is a problem with the measured ClO absorption spectrum. This problem, in turn, could be a manifestation of the uncertainties associated with the literature cross sections for ClO or Cl_2O_2 in the diffuse spectral region. Indeed there is some discrepancy between the reported ClO

dimer cross sections, and to a lesser extent the reported ClO spectra, as described in section 4.3.2. Alternatively the simultaneous fit of the 3 smooth absorbers (at $\lambda < 265$ nm) to any one data set may be an under-determined system, irrespective of uncertainties in literature spectra, especially given the similarities in the shapes of $\sigma_{ClO}(\lambda)$ to $\sigma_{Cl2O}(\lambda)$ and $\sigma_{Cl2O2}(\lambda)$ to $\sigma_{Cl2O}(\lambda)$. These similarities are illustrated graphically in figure 4.12.

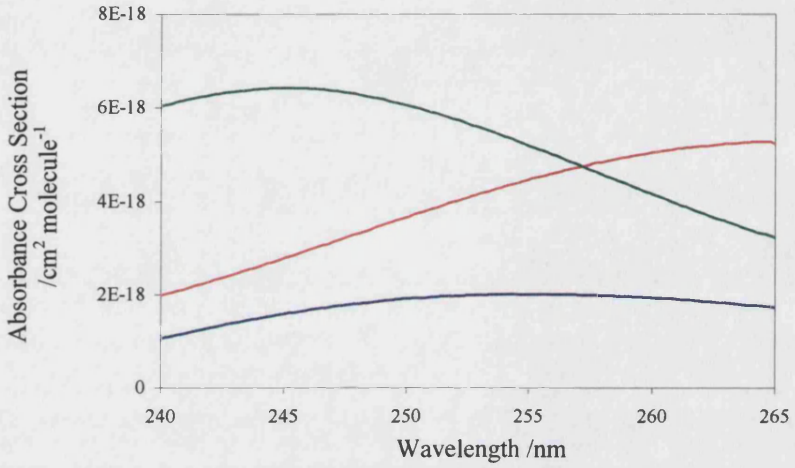

Figure 4.12: Absorption cross sections for ClO (red), Cl_2O_2 (green) and Cl_2O (blue) over the wavelength range used to measure the entire ClO cross section and also to fit the $[Cl_2O_2]_t$ and $[Cl_2O]_t$ following differential subtraction of the fitted ClO absorbance contribution.

It was clear that the temporally resolved concentration profiles derived by this method were of limited value in determining the kinetic parameters which describe ClO dimerisation (2a). With this in mind, alternative methods of measuring σ_{ClO} were undertaken.

4.3.4 σ_{ClO} Determination - Method 2

Any method which reduced the effective number of absorbers present during the fitting procedure could potentially facilitate the accurate determination of σ_{ClO} by reducing the propensity of the fitting routine to confuse the absorbers. Thus a viable extension to the determination of σ_{ClO} based upon method 1 could be developed if

independent spectral characterisation of an absorber concentration were possible. Both half life calculations and numerical integration of the rate equations involved in the $Br_2/Cl_2O/Cl_2/N_2$ system indicated that the $[Cl_2O]_t$ profile was effectively a step function (i.e. $d[Cl_2O]/dt = 0$) following initiation. Hence independent quantification of the magnitude of this step function ($\Delta[Cl_2O]$) and the subsequent removal of A_{Cl2O} from the post-flash spectra would reduce the fitting routine to a two absorber (ClO, Cl_2O_2) problem. In principle back to back experiments could be undertaken to monitor $\Delta[Br_2]$ at higher wavelengths (also a step function, $\sigma_{Br2,max}$ occurs at approximately 415 nm) and infer $\Delta[Cl_2O]$ from their stoichiometric relationship. This $\Delta[Cl_2O]$ value could then be used to analyse the composite spectra recorded at shorter wavelengths.

			net $-[Br_2]$: $-[Cl_2O]$
$Br_2 + h\nu$	→	2Br	
$2(Br + Cl_2O$	→	$ClO + BrCl)$	1 : 2
$Cl_2O + h\nu$	→	ClO + Cl	
$Cl + Br_2$	→	Br + BrCl	
$Br + Cl_2O$	→	ClO + BrCl	1 : 2

However this method was compromised by the incomplete conversion of Cl_2 to Cl_2O through the mercuric oxide column. Photolysis of residual Cl_2 in the gas mixture gave rise to a ClO production channel with a different $-[Br_2]$:$-[Cl_2O]$ stoichiometry to those channels described above:

			net $-[Br_2]$: $-[Cl_2O]$
$Cl_2 + h\nu$	→	2Cl	
$2(Cl + Br_2$	→	$Br + BrCl)$	
$2(Br + Cl_2O$	→	$ClO + BrCl)$	2 : 2

Since the ultimate products of photolysis and subsequent chemistry are BrCl and ClO it was not possible to independently quantify the fractions of Cl_2 and Cl_2O photolysed in the reaction cell. Therefore it was impossible to determine the overall stoichiometric ratio of -[Br_2]:-[Cl_2O] encompassing all three photolytic channels, hence $\Delta[Cl_2O]$ could not be inferred confidently from this chemical system.

In an attempt to improve the Cl_2 to Cl_2O conversion efficiency, longer columns of HgO were employed to maximise the contact time between the Cl_2 gas and mercuric oxide powder, but spectroscopic quantification indicated that conversion efficiency was always less than 100%. Thus to obtain a pure source of Cl_2O, the gaseous mixture downstream of the mercuric oxide column was collected in a trap held at liquid nitrogen temperature, under reduced pressure to prevent condensation of carrier N_2. Over a period of hours, a mixture of red/brown and yellow residues was deposited on the walls of the cold trap. Reduced pressure distillation in a gradually warmed dry ice/acetone bath removed the yellow species (Cl_2), leaving a red/brown residue attributed to pure Cl_2O. However, despite repeated freeze/thaw distillations, spectroscopic investigation continuously revealed a significant Cl_2 impurity. Whilst Cl_2O may have been collected and purified appropriately during the distillation procedure, subsequent Cl_2O decomposition to Cl_2 may have occurred during use. Cl_2O is known to be unstable with respect to decomposition to its elements (often explosively).[20]

4.3.5 σ_{ClO} Determination - Method 3

Having established that the spectral fitting routine was confusing the three transient absorbers, either as a result of errors in the literature cross sections or simply by underdetermination of a complex system, the problem was approached from a different angle. Accepting that the absorption spectrum data quality from the CCD system was good, emphasis was placed upon addressing these key weaknesses in the fitting procedure, rather than manipulating the chemistry, as a route to the differential ClO absorption cross section. In order to overcome the first problem: that involving uncertainties in the shapes and absolute magnitudes of the reference cross sections in the continuum region, a numerical model was developed where these properties were

parameterised and allowed to vary. In an attempt to surmount the second problem (underdetermination), the model was constructed in a form which permitted the fitting of multiple spectra (data sets) simultaneously.

The ClO, dimer and Cl_2O cross sections were each parameterised by fitting Gaussian functions of the form (ii) to the literature spectra.

(4.ii) $$\sigma_\lambda = \beta \, exp\{-\alpha(\lambda-\gamma)^2\}$$

Each Gaussian function incorporated into the model added three degrees of freedom: α, effectively defining the width of the function; β, the absolute magnitude and γ, the centre in the wavelength axis . The spectrally smooth region of the ClO cross section could be fitted with one Gaussian function whereas the more complex shapes of the σ_{Cl2O2} and σ_{Cl2O} each required composites of two such functions The combination required to parameterise the ClO dimer cross section is illustrated in figure 4.13.

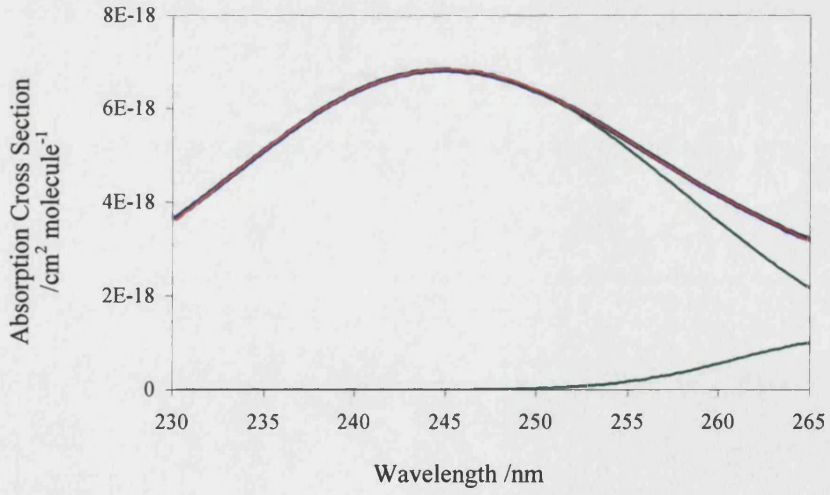

Figure 4.13: Least squares fit (red) of a linear combination of two Gaussian functions (green) to the literature Cl_2O_2 cross section (blue).

With the parameterised absorption cross sections in the model a simulated spectrum was readily constructed by applying the Beer-Lambert law:

$$A_{sim,total}(\lambda) = A_{sim,ClO}(\lambda) + A_{sim,Cl2O2}(\lambda) + A_{sim,Cl2O}(\lambda)$$

$$= \{\sigma_{ClO}(\lambda)\, c_{ClO} + \sigma_{Cl2O2}(\lambda)\, c_{Cl2O2} + \sigma_{Cl2O}(\lambda)\, c_{Cl2O}\} l \quad \text{(4.iii)}$$

In any given experimental spectrum the three species concentrations, c_x are unknown and the three cross sections, $\sigma_x(\lambda)$ can be defined by the Gaussian parameters (3 and 6 parameters for ClO and Cl_2O_2 or Cl_2O respectively. Given n sets of experimental absorbance data (*i.e.* n separate time resolved spectra) the number of degrees of freedom (*i.e.* the number of adjustable parameters), μ within the model is given by $\mu_n = 15 + 3n$, where 15 arise from the Gaussian parameters defining the reference cross sections, and $3n$ represents the three concentration parameters associated with each data set (one for each species x).

Given that each of the experimental spectra typically consists of 298 data points, 140 of which are used in the fitting procedure (where $\lambda < 265$ nm and the spectra are featureless) then, since $140 > 15 + 3n = 18$ for a single spectrum, the problem is overdetermined and in principle all 18 adjustable parameters can be evaluated.

In practice, prior to analysing experimental spectra in this way, simulated three absorber data sets (*i.e.* zero noise) were generated and reanalysed as a test of the model. Least squares fitting was used to minimise the differences between the initially artificial test spectra and simulated spectra simultaneously. Each of the $(15 + 3n)$ parameters were systematically varied until a minimum residual was identified. Output cross sections regenerated from the optimised parameters could be checked against several data sets to ensure the same minimum was consistently located and thus confidently determined. Furthermore, the ouput cross sections could be compared with the parameters used to generate the test data sets and conclusions drawn on the basis of errors associated with respective literature spectra.

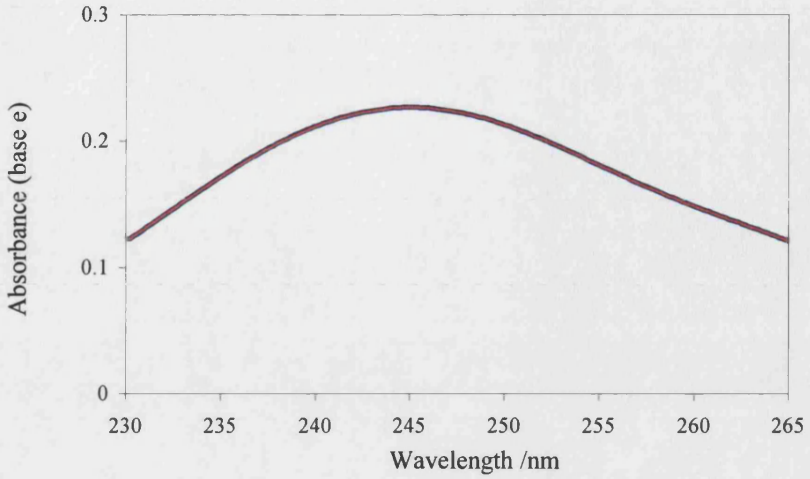

Figure 4.14: Artificial spectrum (thin red line) and simulated spectrum (thick blue line) determined by the model (n = 1).

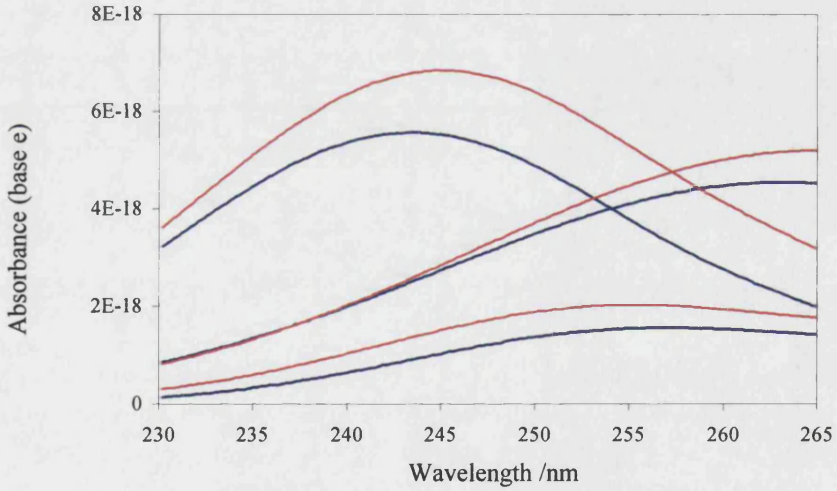

Figure 4.15: Output (red) and test (blue) cross sections associated with the fitting routine illustrated in figure 4.14.

Running a model with a single (n = 1) artificial data set rapidly returned a simulated spectrum which fitted the artificial spectrum well, but whose output cross sections bore little resemblance to the test parameters. An example of such a fit and the corresponding output cross sections are given in figures 4.14 and 4.15 respectively. Moreover, the output parameters were strongly dependent on the trial values used.

Potentially this problem could be resolved by increasing n. The number of degrees of freedom associated with the model is shown as a function of n in table 4.3.

n	μ_n	μ_n/n
1	18	18
2	21	10.5
3	24	8
6	33	5.5
12	51	4.25
24	87	3.625

Table 4.3: Number of degrees of freedom, μ associated with the model as a function of n experimental data sets (spectra). Also tabulated is the normalised number of degrees of freedom, μ_n/n.

Inevitably, it can be seen that whilst the number of degrees of freedom increases as more data sets are included, the normalised number of degrees of freedom, μ_n/n decreases with increasing n. In simplistic terms this is merely a manifestation of the number of additional data points (140 per spectrum) increasing more rapidly than the number of adjustable parameters (3 per spectrum) as additional spectra are included in the global fit. Figure 4.16 graphically illustrates the dependence of the normalised number of degrees of freedom on n.

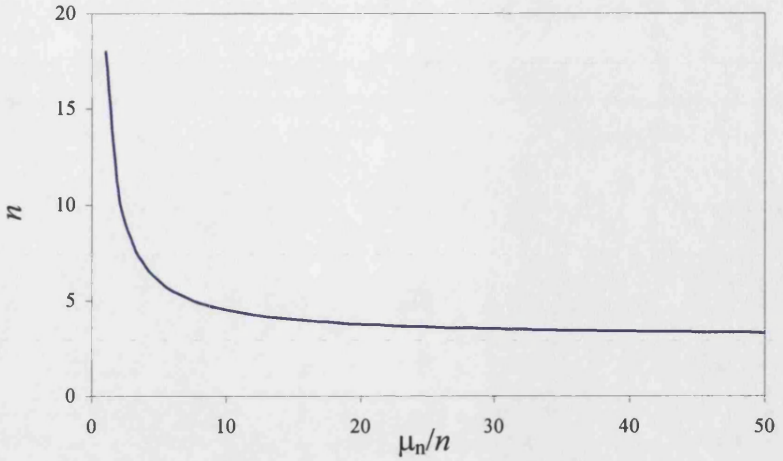

Figure 4.16: Dependence of the normalised number of degrees of freedom, μ_n/n on the number of spectra, n.

Up to twelve experimental data sets (spectra) were incorporated into the model without successfully determining the three cross sections according to the criteria described above. Figure 4.16 reveals that even vast increases in n beyond 12 lead to small decreases in μ_n/n, which asymptotes at a value of 3. Therefore it was necessary to conceive alternative methods for reducing the value of μ_n/n. The following methods and assumptions to constrain the model were considered and their influence on spectral fitting is discussed in turn:

(A) Since Cl_2O is a closed shell molecule its absorption cross section is, in principle, easier to record than those of the other two transient absorbers and might be expected to be well characterised (see section 4.3.2). Examination of figure 4.5 supports this assumption since all four of the determinations of the Cl_2O absorption cross section are in excellent agreement. Consequently the 6 Gaussian parameters governing the Cl_2O spectrum were no longer optimised by the model and they were held at values which described the NASA recommendation. This reduced the value of μ_n by 6.

(B) Although the absolute [ClO] associated with a given experimental spectrum could not be independently determined without knowledge of the differential ClO cross section, relative [ClO] could be evaluated. By differentially fitting the vibronic ClO structure of one recorded spectrum to that of another, the [ClO] of the latter spectrum was evaluated relative to the [ClO] associated with the former, since the Beer-Lambert

law states that A_{ClO} is linearly proportional to [ClO]. Formally, the value of $[ClO]_n/[ClO]_1$ could be derived from $A_{diff,n}/A_{diff,1}$. As a result only one ClO concentration parameter, $[ClO]_1$ was included explicitly within the model and the other ClO concentrations were coded in the form $[ClO]_n = \{[ClO]_n/[ClO]_1\} \times [ClO]_1$, where the value of the $\{[ClO]_n/[ClO]_1\}$ term was obtained from differential fitting. Hence the number of degrees of freedom for n data sets was reduced by a value of $(n-1)$.

(C) A similar argument can be used to reduce the number of $[Cl_2O_2]$ parameters in the model. Despite the problems inherent to the traces shown in figure 4.2, it is clear that there is no significant net chemistry proceeding after $t = 0.02$ s, since ClO has reached equilibrium with its dimer. Indeed numerical modelling of the system using NASA recommended rate coefficients supports this. Therefore the $[Cl_2O_2]$ associated with a spectrum recorded after equilibrium has been established can be related to [ClO] *via* the equilibrium constant for reaction (2a):

(4.iv) $[Cl_2O_2] = K_{2a}[ClO]^2$

The NASA recommendation for $K_{2a,298K}$ is 7.1×10^{-15} molecules^{-1} cm^3 and this was included as a fixed parameter in the model.[3] Applying this constraint to the model reduced μ_n by a value of n, since no $[Cl_2O_2]$ parameters were explicitly included in the model. However, it was recognised that applying this constraint could compromise the reliability of any subsequently derived k_{2a} and k_{-2a} values, since $K_{2a} = k_{2a}/k_{-2a}$. Indeed in some instances K_{2a} was also introduced as a variable parameter to the model.

(D) Finally, a mass balance constraint was considered, recognising the stoichiometry of the system:

(4.i) Mass balance$(t) = [ClO]_t + 2[Cl_2O_2]_t + [Cl_2O]_t = 0$

where the concentration of any species could be expressed in terms of the remaining two absorber concentrations. Once again this constraint reduced μ_n by a value of n. This was a potentially powerful constraint if applied in conjunction with (B) and (C),

since this would have reduced the number of concentration parameters from $3n$ to just 1. However, it was once again recognised that a degree of circularity was being introduced, since successful conformation to the mass balance algorithm was one of the key tests in validating the absorption cross sections used to generate the kinetic traces.

Table 4.4 shows how combinations of the four constraints (A-D) listed above serve to reduce the number of degrees of freedom available to the model for spectral deconvolution. Examples are shown for the $n = 12$ model employed in this study.

Constraint	μ_n	μ_{12}	$\mu_{12}/12$
none	$15 + 3n$	51	4.25
A	$9 + 3n$	45	3.75
B	$16 + 2n$	40	3.33
C	$15 + 2n$	39	3.25
D	$15 + 2n$	39	3.25
A, B	$10 + 2n$	34	2.83
A, B, C	$10 + n$	22	1.83
A, B, C, D	10	10	0.83

Table 4.4: Variation in the number of degrees of freedom available to the model by incorporating combinations of the constraints. Example calculations are shown for the model used in this study, where the number of analysed data sets (spectra) was 12.

However, despite the reduction in μ_n which accompanied the incorporation of these constraints into the model, no combination proved to be successful even with noiseless (artificial) data. Once again the model failed to consistently return a set of parameters which were consistent with the artificial parameters. Despite the large data sets and constraints incorporated into the model, it seems that the multidimensional χ^2 hypersurface over which the fitting routine scans is peppered with multiple minima and remains underdetermined. The most likely origin of these multiple minima is the

similarity between the three absorbing species in the region of their continua. This problem was compounded by adding random noise to the simulated data and hence precluded the analysis of experimental spectra in this way.

4.3.6 σ_{ClO} Determination - Method 4

It is clear that a method of calibrating the differential ClO cross section was required which was not marred by the presence of the other two absorbing chlorine oxide species. A new method was therefore devised, taking advantage of the time resolution associated with the CCD data. By extracting the calibration data in the period immediately following photolysis (hereafter referred to as t_0) the problem is reduced to a two absorber system: A_{ClO} and $-A_{Cl2O}$.

The immediate post photolysis (t_0) absorbance in the spectral continuum could therefore be expressed as:

(4.v) $$A_{\lambda,0} = (\sigma_{ClO,\lambda}[ClO]_0 + \sigma_{Cl2O,\lambda}\Delta[Cl_2O])l$$

Moreover, at t_0, where ClO has yet to undergo any decay, $-\Delta[Cl_2O] = [ClO]_0$ by stoichiometry, thus:

(4.vi) $$A_{\lambda,0} = [ClO]_0.l(\sigma_{ClO,\lambda} - \sigma_{Cl2O,\lambda})$$

Hence the initially generated ClO concentration, $[ClO]_0$ could be expressed in terms of the t_0 absorbance, the optical path length and the ClO and Cl_2O continuum cross sections:

(4.vii) $$[ClO]_0 = \frac{A_{\lambda,0}}{(\sigma_{ClO,\lambda} - \sigma_{Cl2O,\lambda}) \times l}$$

Similarly, at longer wavelengths where ClO absorption exhibited vibronic structure, the differential absorbance, A_{diff} is independent of $\Delta[Cl_2O]$:

(4.viii) $A_{diff,0} = \sigma_{ClO,diff}[ClO]_0.l$

Thus using the expression for $[ClO]_0$ from equation (vii), the differential absorption could be expressed as:

(4.ix) $$A_{diff,0} = \frac{\sigma_{ClO,diff}}{(\sigma_{ClO,\lambda} - \sigma_{Cl2O,\lambda})} \times A_{\lambda,0}$$

This relationship between the differential absorbance and the absorbance at the calibrating wavelength could be readily used to determine the ClO differential cross section provided that the (difference between the) ClO and Cl_2O cross sections were known at the calibrating wavelength. A plot of $A_{diff,0}$ versus $A_{\lambda,0}$ from experiments with differing initial ClO concentrations, $[ClO]_0$ should be linear and pass through the origin according to (ix).

A series of experiments was undertaken to generate ClO in differing initial concentrations by varying $[Br_2]$. Nominal instrument settings employed in the 298 K differential ClO cross section determination are indicated in table 4.5.

Spectrograph diffraction grating	600 grooves /mm
Entrance slit width	112 μm
Resolution	0.8 nm (FWHM)
Wavelength Regime	249-282 nm
CCD clocking rate	50 μs

Table 4.5: Experimental settings used in the ClO cross section measurements (method 4) at 298 K

The differential absorbance at the (12,0) band of the ClO absorption spectrum at t_0 ($A_{diff,0}$) versus $[Br_2]$ is shown in figure 4.17. This shows that, as designed, the

principal source of ClO was from Br_2 photolysis with a minor contribution from Cl_2 and Cl_2O photolysis manifested as an intercept.

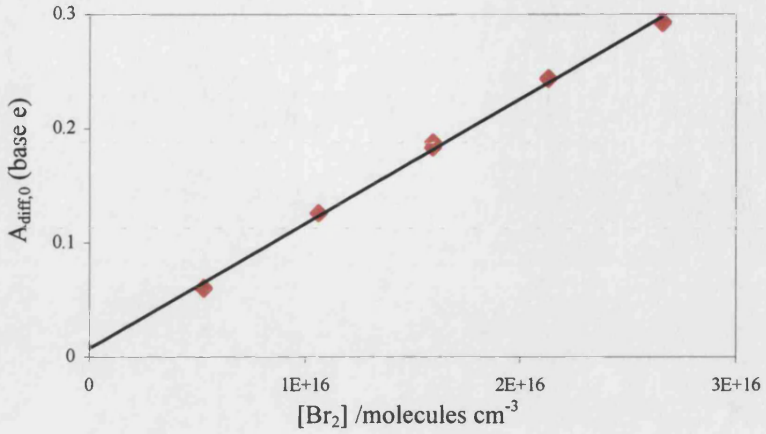

Figure 4.17: $A_{diff,0}$ from experiments performed as a function on $[Br_2]$ at 298 K. The data points are shown in red with a linear parameterisation in black.

A differential spectrum of ClO was generated by high-pass filtering the post-flash absorption spectrum as described in chapter 3. The resulting spectrum, shown in figure 4.18 was fitted to each time resolved spectrum in the kinetic trace (fit also shown in figure 4.14), giving a trace showing time resolved relative ClO concentration. This trace (figure 4.15) could be readily converted into a differential absorbance trace at any pair of wavelengths by scaling to the differential absorbance in the reference spectrum at those wavelengths ($A_{diff(ref)}$). Arbitrarily, the absorbance difference between the peak of the (12,0) band of the (A ← X) vibronic transition at 275.7 nm and the adjacent trough to higher wavelengths (277.2 nm) was chosen. The $A_{diff(ref)}$ trace obtained in this way was back extrapolated to obtain $A_{diff(ref)}$ at t_0. This quantity was used in the determination of $\sigma_{ClO,diff}$.

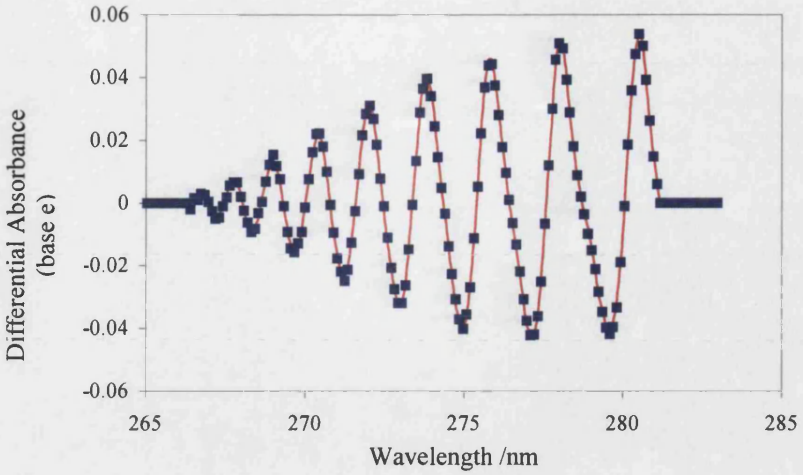

Figure 4.18: Differental fit of the reference spectrum (blue squares) to a time resolved experimental spectrum (red), evaluating $A_{diff(rel),t}$.

The back extrapolation was necessary due to the the inherent temporal averaging of the experimental data associated with the CCD system (see appendix 2). Since the signal from differentially fitting the vibronic structure was unequivocally due to ClO, extrapolation was achieved by fitting the trace with a time resolved classical solution to the kinetic scheme describing reactions (2a) and (–2a), the details of which are described in section 4.4.

(2a, -2a) $\quad ClO + ClO + M \quad \leftrightarrow \quad Cl_2O_2 + M$

A least squares fitting routine was applied during which $A_{diff,0}$, k_{2a} and k_{-2a} were varied. The fit quality was, without exception, extremely high (figure 4.19 is typical) and the fitted function was subsequently back-extrapolated to t_0, yielding $A_{diff,0}$. This quantity was converted to an absolute value by multiplying by $A_{diff,ref}$.

This process was repeated using the same reference spectrum over a range of pre-flash $[Br_2]$ values, effectively giving rise to a range of $[ClO]_0$ and hence $A_{diff,0}$ values. Despite the indisputable fit quality, these calibration experiments generally employed a faster timebase than those used in subsequent kinetic experiments, to minimise any error introduced by the extrapolation. The high quality of the fit to the differential absorbance trace confirms the successful decoupling of ClO formation and decay

chemistry, since the classical solution assumes ClO is discretely *injected*, and any overlapping of timescales would lead to a poor fit in the early decay data. The fitted values of k_{2a} and k_{-2a} are effectively meaningless in this instance, since the kinetic fitting utilises relative quantities only.

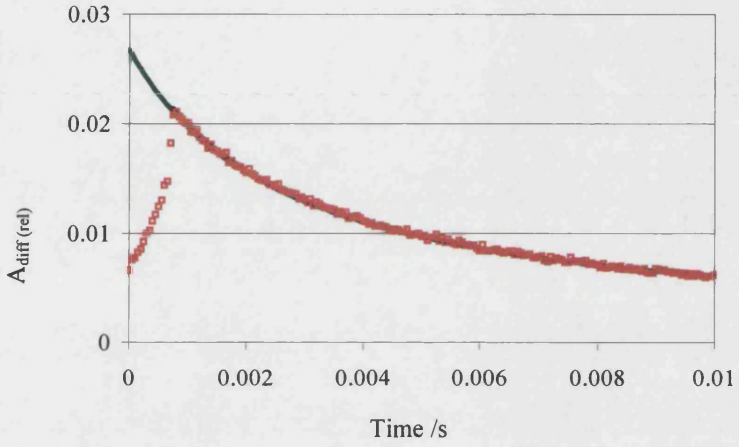

Figure 4.19: Least squares fit of modelled $A_{diff(rel)}$ (blue) to the time resolved data (red). The back extrapolation to t_0 (in the absence of time averaging) is indicated in green.

In a similar fashion $A_{\lambda,0}$, the absolute absorbance value at the calibrating wavelength in the smooth absorbance regime was determined at t_0 for each experimental data set. Having wavelength calibrated the data, the CCD column which corresponded with the desired calibration wavelength was identified. The time resolved absorption at this pixel in the wavelength axis of the CCD data was evaluated by applying Beer's law relative to a time averaged period in the pre-flash. This procedure was repeated for the adjacent pixel on either side (light dispersion across a given pixel was a nominal 0.11 nm) and a mean of the three calculated absorptions was evaluated to improve the associated signal to noise ratio, giving $A_{cal\lambda,t}$.

Examination of the literature data describing the absorption cross sections of ClO and its dimer (see section 4.3.2) suggests the isosbestic point for this equilibrium system occurs at approximately 248 nm. Near the isosbestic point $\sigma_{Cl2O2} \approx 2\sigma_{ClO}$ and very little overall change in absorbance results from ClO dimerisation. Therefore using a calibrating wavelength near to this value gave rise to a time resolved $A_{cal\lambda,t}$ trace with

a considerably longer half life than the analogous $A_{diff,t}$ trace (comparing figures 4.19 and 4.20). As a result the nature of the function fitted to the $A_{cal\lambda,t}$ trace was less critical in back extrapolating accurately to $A_{cal\lambda,0}$. Once again, however, least squares fitting of a numerical solution to the differential equations, taking account of multiple contributions to absorbance was used to determine this value. In this fashion $A_{cal\lambda,0}$ values were evaluated under the same initial $[Br_2]$ and hence $[ClO]_0$ as the measured $A_{diff,0}$ values.

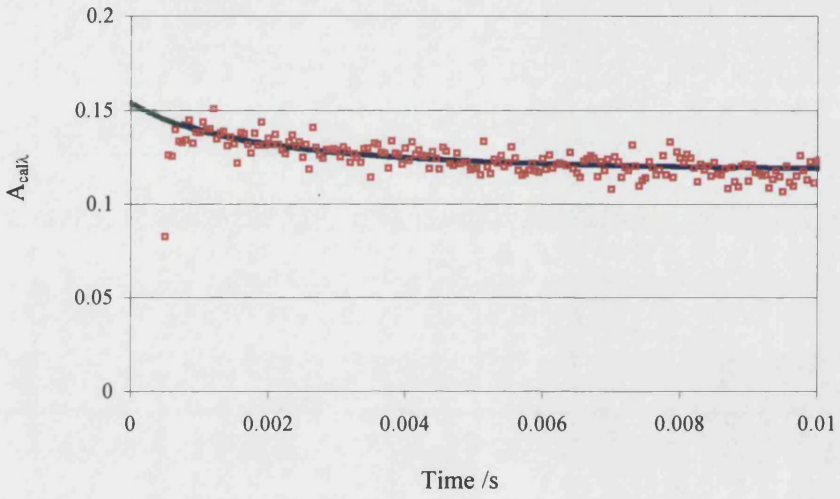

Figure 4.20: Least squares fit of modelled $A_{cal\lambda}$ (blue) to the time resolved data (red). The back extrapolation to t_0 (in the absence of time averaging) is indicated in green.

Having evaluated $A_{diff,0}$ and $A_{cal\lambda,0}$ for each data set, these values were plotted against one another. Typically two experiments were carried out at each of five different precursor Br_2 concentrations to generate a calibration plot whose gradient gave rise to σ_{diff} *via* expression (ix). In all cases plots were linear and posessed near zero intercepts An example using three different calibration wavelengths is shown in figure 4.21.

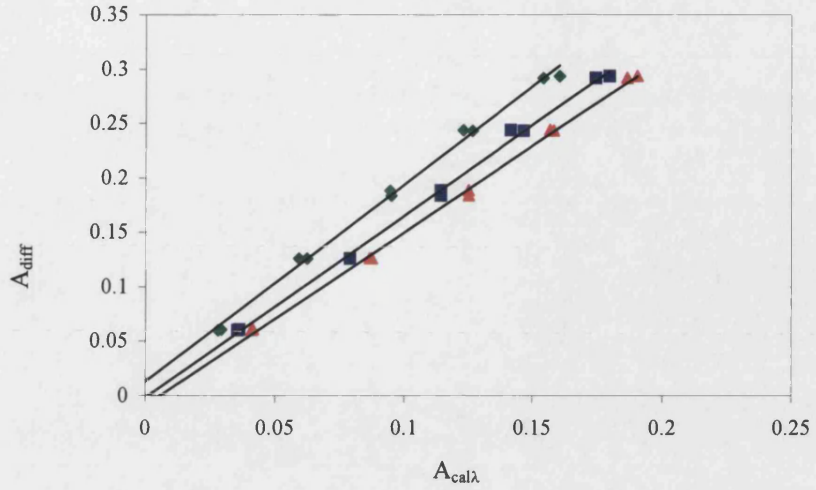

Figure 4.21: Calibration plot to determine σ_{diff} at 298 K. Data shown for calibration wavelengths of 250, 255 and 260 nm.

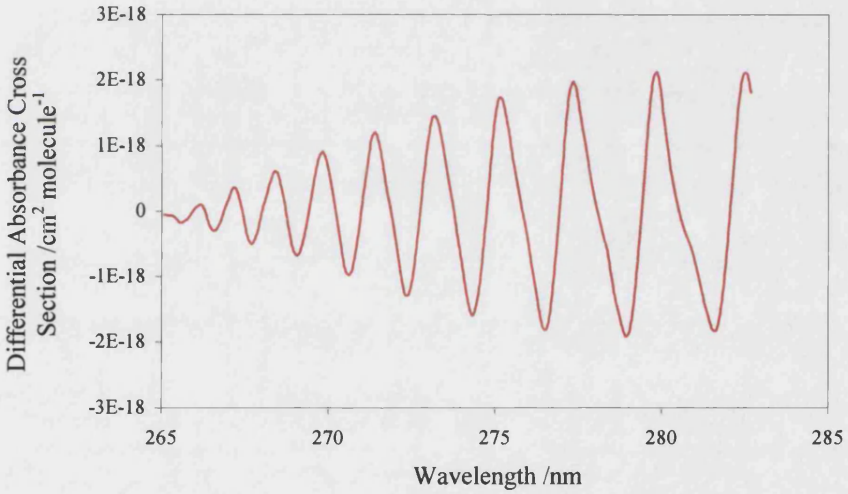

Figure 4.22: Measured differential cross section at 298 K.

The reference spectrum could then be converted to a wavelength resolved, differential ClO cross section by multiplying by ($\sigma_{diff}/A_{diff,ref}$), where the denominator represents the difference in peak to trough absorption at the (12,0) band in the reference spectrum. The differential ClO cross section at 298 K, calibrated relative to the 255 nm continuum is shown in figure 4.22.

This procedure was carried out as a function of calibrating wavelength over the region 250 nm to 265 nm at 2.5 nm intervals at 298 K, 253 K and 235 K. The literature ClO

and Cl_2O cross sections employed were those described above in section 4.3.2. Figure 4.23 shows the final calculated σ_{diff} values ((12,0) peak - trough), at the three temperatures as a function of calibrating wavelength. The error bars are at the 95 % confidence limits associated with the linear regression fits to the calibration plots.

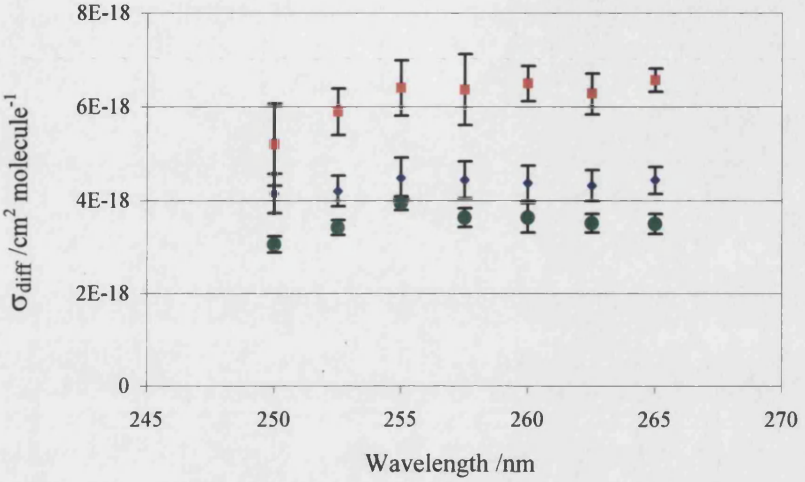

Figure 4.23: Measured σ_{diff} values (12,0) as a function of calibrating cross section wavelength at 298 K (green), 253 K (blue) and 235 K (red).

No systematic dependence of σ_{diff}(ClO) on calibration wavelength was observed for calibration wavelengths at 255 nm or greater. However, when 250 nm and 252.5 nm were used as reference wavelengths, the returned value of σ_{diff} was consistently lower than the mean value. This suggests that one or both of the reference cross sections (σ_{ClO} and σ_{Cl2O2}) are unreliable at wavelengths below 255 nm. As a result, the subsequent temperature dependent study of the differential cross section confidently employed a wavelength of 255 nm for calibrating cross sections.

It is interesting to note that the slight inconsistency in σ_{diff}(ClO) as a function of calibrating wavelength implies inconsistencies in the continuum cross section values for ClO and Cl_2O. This problem with the literature cross sections almost certainly contributed to the difficulties encountered when fitting the low wavelength continua to spectra during the σ_{ClO} determination methods 1 and 2, highlighting the need for reliable reference spectra.

A recent study of the ClO + ClO reaction by Bloss *et al.*[21] employed two photomultiplier tubes, each coupled to a monochromator to measure the differential cross section of ClO at the (12,0) band/trough. The method employed by Bloss *et al.* was similar to that employed in this work and the dual wavelength 'differential' ClO cross section obtained by Bloss *et al.* can be compared with this work by selecting the appropriate wavelengths from the calibrated spectrum. Whilst the work reported here has advantages over that of *Bloss et al.* insofar as the *entire* spectrum is calibrated, a corollary of this is that measurements reported here are at lower spectral resolution than those of Bloss *et al.* To enable comparison, $\sigma_{diff}(ClO)$ was therefore investigated as a function of experimental resolution by varying the entrance slit width of the spectrograph. Figure 4.24 shows the results of this study at 298 K in comparison with the determination by Bloss *et al.* No parameterisation was invoked to facilitate extrapolation of the resolution dependent differential cross section, since the resolution range was not broad enough to unequivocally constrain an arbitrary fit to any particular function. However brief inspection shows that any reasonable extrapolation of $\sigma_{diff}(ClO)$ reported in this work will give rise to a slightly larger differential cross section than that measured by Bloss *et al.*

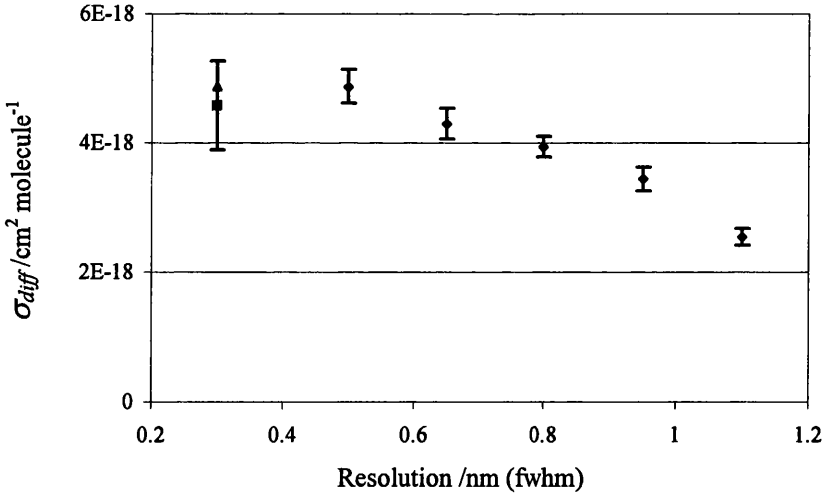

Figure 4.24: Comparison of measured σ_{diff} (blue) with determinations by Bloss et al. (2001). Shown are their 298 K parameterised value (red) and the adjusted value (green, see text). Error bars have been omitted from the latter point for clarity.

The study of Bloss *et al.* employed different chemical systems to generate ClO, whilst using a similar method to that employed here as a route to the differential cross section. One of the systems adopted by Bloss *et al.* involved monitoring BrCl and returned an anomalously low value by comparison to other systems. BrCl is a weak UV absorber, and the authors recognised that this could be the source of the anomaly although their calibration plots appeared well constrained. Thus, whilst recognising the potential anomaly, the authors could find no rationale for omitting these data from their parameterisation of of $\sigma_{diff}(ClO)$.

Unfortunately, Bloss *et al.* do not independently parameterise the results from their remaining three systems. However the authors do quote $\sigma_{diff}(ClO)$ values of 4.92×10^{-18} (calibrating cross section: σ_{ClO}-σ_{Cl2O}, recorded at 296 K), 5.14×10^{-18} (σ_{OClO}, 294 K) and 4.39×10^{-18} (σ_{ClNO}, 296 K) cm^2 $molecule^{-1}$ for various chemical systems. Furthermore, it appears that Bloss *et al.* failed to interpolate the reference cross section data, critically failing to account for the turning point in the Cl_2O cross section at ~255 nm, since the value of σ_{Cl2O} employed in their first system was too small. This would give rise to a 4% underestimation of their measured value for $\sigma_{diff}(ClO)$. Accounting for this error, the mean of these three determinations leads to a value of $\sigma_{diff} = 4.88 \times 10^{-18}$ cm^2 $molecule^{-1}$. This value is also indicated on figure 4.24 and should be treated as an upper limit for comparison with results extrapolated from this study, due to the slightly lower temperatures employed in their work. The 298 K $\sigma_{diff}(ClO)$ determination from this study is in reasonable agreement with this value reported by Bloss *et al.*

The temperature dependence of the differential cross section was investigated in the range 206-320 K using the same instrument settings given in table 4.5. At temperatures below 220 K however, the vapour pressure of bromine limited the maximum [Br_2] that could be introduced to the reaction cell without exceeding the saturated vapour pressure (*i.e.* condensing Br_2 in the reaction vessel). Thus it became impractical to perform experiments as a function of this quantity in order to produce the calibration plots. Consequently Br_2 was removed from the precursor mixture and the Pyrex jacket removed from the flashlamp. Cl_2O photolysis was the dominant

source of ClO under these conditions (and to a lesser extent Cl_2 photolysis and subsequent reaction of Cl atoms with Cl_2O). Despite the emergence of three new photolysis channels (10b-d) at these lower wavelengths, the 1:1 stoichiometry of $[ClO]_0:\Delta[Cl_2O]$ was preserved since the sole fate of any O atoms generated by Cl_2O photolysis was reaction with further Cl_2O. Hence these low temperature experiments were carried out as a function of pre-flash $[Cl_2O]$, giving rise to the calibration plots. The need to preserve effective decoupling of ClO formation and decay timescales effectively provided a lower limit to the pre-flash $[Cl_2O]$ that could be employed. Moreover, the weakness of the Cl_2O absorption cross section in comparison to that of Br_2 resulted in the generation of fewer radicals. Consequently, the experiments were carried out over a smaller $A_{diff,0}$ range. Nevertheless the method proved successful and the calibration plots exhibited well constrained linear behaviour such as that shown in figure 4.25.

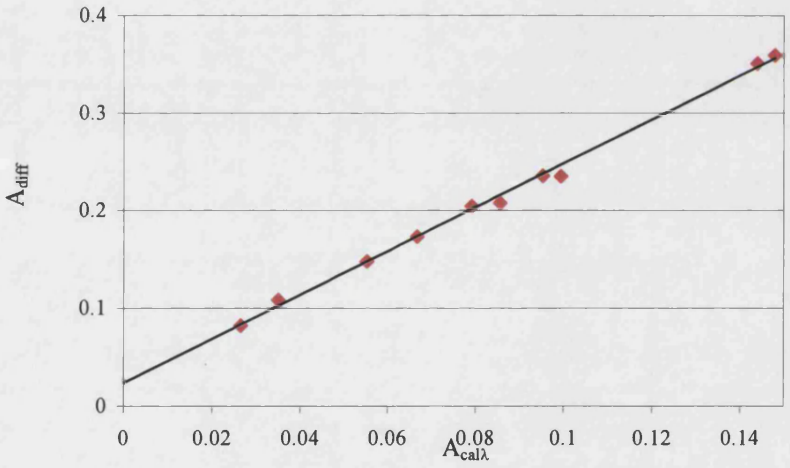

Figure 4.25: Calibration plot obtained by varying pre-flash $[Cl_2O]$ under Br_2 free conditions at 206 K.

The temperature dependence of the differential cross section between the (12,0) band and its high wavelength trough is indicated in figure 4.26.

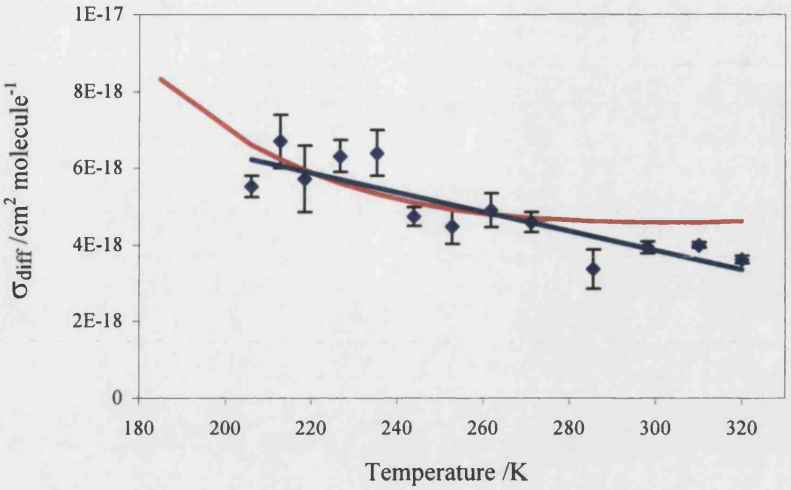

Figure 4.26: Measured temperature dependence of σ_{diff} at a spectral resolution of 0.8 nm (FWHM) and linear parameterisation (blue). Also shown is the parameterisation reported by Bloss et al.[21] at higher resolution (red).

The parameterisation is given by the equation:

(4.x) $\sigma_{diff}(T) = (-2.52 \times 10^{-20} T) + 1.14 \times 10^{-20}$ cm^2 molec^{-1}

The uncertainty associated with the temperature dependent cross section was calculated from the root mean square deviation of the experimental data from the parameterisation. Expressing the error relative to the 320 K σ_{diff} parameterised value gives rise an uncertainty of 13%. Since at 320 K $\sigma_{diff}(T)$ reaches its smallest value over the temperature range investigated, 13% represents an upper limit on the relative error associated with $\sigma_{diff}(T)$.

Also shown on figure 4.26 is the parameterisation of of σ_{diff}(ClO) quoted by Bloss *et al.* It has already been explained that the instrumental resolutions from the two studies differ so the results are not directly comparable. However, given that the differential cross sections are similar in magnitude but those measured in this work are at lower resolution, our determinations would inevitably lead to higher σ_{diff}(ClO) values if a basis for comparison was assumed. In the absence of a suitable basis for quantitative comparison, it is interesting to reflect upon the relative shapes of the two data sets. Bloss *et al.* fitted their data with a quadratic function after Nickolaisen *et al.*[22] By their

own admission, the original authors' (1994) 'use of a quadratic equation dependent on inverse temperature was somewhat arbitrary and was chosen because it provided the best visual interpolation of the data'. The data from this study can be satisfactorily parameterised by a linear function and there was no clear justification for adopting a more complex scheme. Indeed other differential cross sections have been shown to follow linear temperature dependencies (*e.g.* that of BrO reported by Gilles *et al.*[23]).

4.4 Kinetic Analysis

Having successfully parameterised the temperature dependence of the differential ClO cross section, experiments were undertaken to determine the kinetics of ClO dimerisation as functions of both temperature (206-320 K) and pressure (25-760 Torr). These experiments employed identical instrument settings to those used in the section 4.3.6, since the differential cross sections are a strong function of instrumental resolution. The only key difference invoked for kinetic experiments over those described in the previous section is the implementation of a longer timebase, since short timescale extrapolations to t_0 were no longer required. Moreover, monitoring $[ClO]_t$ over several half-lives facilitated the measurement of the equilibrium ClO concentration, $[ClO]_{eq}$. In conjunction with the extrapolated $[ClO]_0$ value, this provided an additional route to the characterisation of the equilibrium constant K_{2a} (over $K_{2a} = k_{2a}/k_{-2a}$) at appropriate temperatures ($T > 270$ K).

The typical composition of the precursor gas mixture at 298 K is shown in table 4.7. Typical concentrations at other temperatures were based upon these 298 K values having applied the appropriate thermal expansion/contraction factors given by the perfect gas law. Similarly, low pressure experiments employed the same ratio of component gases, whose absolute number densities were also dictated by the perfect gas law. Reactions (6) and (9) which were responsible for ClO generation exhibited very weak temperature dependencies, therefore it was unnecessary to adjust the precursor conditions to maintain rapid radical generation at low temperatures. As with the cross section measurements at temperatures below 220 K, Br_2 was removed from the pre-flash mixture to prevent condensation on the walls of the reaction cell.

Similarly, the Pyrex jacket was removed from the flashlamp and short wavelength Cl_2O photolysis was the dominant route to ClO production at these low temperatures.

Precursor Species	Pre-flash Concentration
Br_2	$(0.5\text{-}2) \times 10^{16}$
Cl_2O	$(2\text{-}7) \times 10^{15}$
Cl_2	$(2\text{-}6) \times 10^{15}$
N_2	Balance to 1 atmosphere

Table 4.7: Typical precursor concentrations at 298 K, 760 Torr

As described previously, Beer's Law was applied to the post-flash data relative to the pre-flash data, giving rise to 1000 time resolved absorbance spectra. Automated routines were developed and implemented to fit these spectra to the differential cross section, as described in chapter 3, giving rise to temporally resolved ClO profiles, $[ClO]_t$ by satisfying the Beer-Lambert law.

An example of such a $[ClO]_t$ profile is shown in figure 4.26, which was recorded at 298 K and 760 Torr. The temporal trace clearly shows prompt formation of ClO, and subsequent decay to a non-zero, equilibrium concentration.

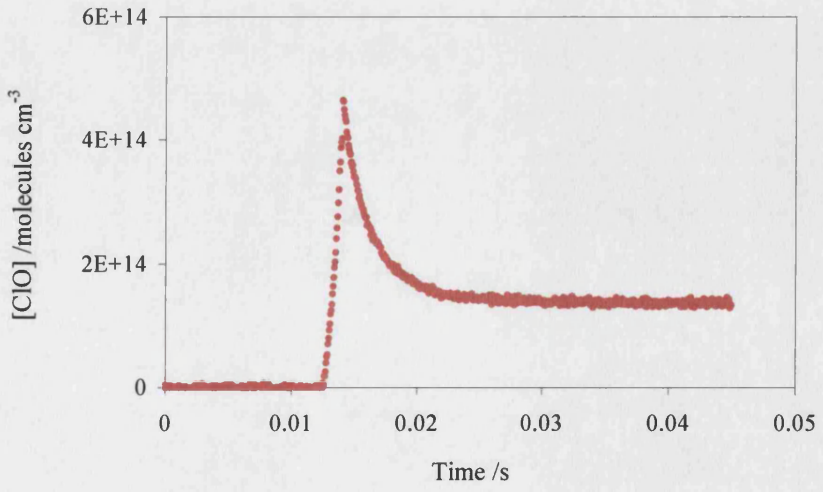

Figure 4.27: Typical $[ClO]_t$ decay trace at 298 K.

The differential equation describing the temporal behaviour of ClO decay is:

$$-\frac{1}{2}\frac{d[\mathrm{ClO}]}{dt}=\frac{d[\mathrm{Cl_2O_2}]}{dt}=k_{2a}[\mathrm{ClO}]^2-k_{-2a}[\mathrm{Cl_2O_2}] \quad \text{(4.xi)}$$

The solution to this differential equation is complex and as a result most studies have either focused on low temperature studies (T < 250 K) where k_{-2a} becomes negligible, and the dimer is effectively stable. Hence the kinetics can be adequately described by a simple second order solution. Alternatively, at higher temperatures, numerical modelling (e.g. FACSIMILE) has been used to overcome these mathematical complexities. However, an exact solution to the differential equation *can* be evaluated by substitution:

$$[\mathrm{ClO}]=[\mathrm{ClO}]_{eq}+2x \quad \text{(4.xii)}$$

where $2x$ is the concentration of ClO radicals in excess of the equilibrium concentration of ClO, $[\mathrm{ClO}]_{eq}$. Secondly, by stoichiometry:

$$[\mathrm{Cl_2O_2}]=[\mathrm{Cl_2O_2}]_{eq}-x \quad \text{(4.xiii)}$$

where $[Cl_2O_2]_{eq}$ is the concentration of Cl_2O_2 at equilibrium. Since $[Cl_2O_2]_{eq}$ is constant the rate equation can be simplified to:

$$\frac{d[\mathrm{Cl_2O_2}]}{dt}=-\frac{dx}{dt}=k_{2a}[\mathrm{ClO}]^2-k_{-2a}[\mathrm{Cl_2O_2}] \quad \text{(4.xiv)}$$

Substituting (xii) and (xiii) into (xiv) yields:

$$-\frac{dx}{dt}=k_{2a}([\mathrm{ClO}]_{eq}-2x)^2-k_{-2a}([\mathrm{Cl_2O_2}]_{eq}-x) \quad \text{(4.xv)}$$

However, by definition, the equilibrium constant is given by the following expression:

(4.xvi) $$K_{2a} = \frac{k_{2a}}{k_{-2a}} = \frac{[Cl_2O_2]_{eq}}{[ClO]_{eq}^2}$$

Which can be conveniently rearranged:

(4.xvii) $$k_{2a}[ClO]_{eq}^2 = k_{-2a}[Cl_2O_2]_{eq}$$

Expanding (xv) and substituting (xvii) into the resulting expression gives:

(4.xviii) $$-\frac{dx}{dt} = 4k_{2a}[ClO]_{eq}x + 4k_{2a}x^2 + k_{-2a}x$$

Hence,

(4.xix) $$\frac{dx}{x(4k_{2a}[ClO]_{eq} + 4k_{2a}x + k_{-2a})} = -dt$$

This is a differential equation of the form:

$$\frac{dx}{x(a+bx)} = -dt$$

where:

$$a = 4k_{2a}[ClO]_e + k_{-2a} \qquad \text{and} \qquad b = 4k_{2a}$$

Integrating gives:

$$\int_{x_0}^{x_t} \frac{dx}{x(a+bx)} = -\int_0^t dt$$

$$-\frac{1}{a}\ln\left(\frac{a+bx_t}{x_t}\right)+\frac{1}{a}\ln\left(\frac{a+bx_0}{x_0}\right)=-t$$

$$\ln\left(\frac{a+bx_0}{x_0}\cdot\frac{x_t}{a+bx_t}\right)=-at$$

Thus,

(4.xx) $$x_t=\frac{ax_0\exp(-at)}{a+bx_0-bx_0\exp(-at)}$$

and (xii) converts x_t to the experimental quantity, $[ClO]_t$.

(4.xii) $$[ClO]_t=[ClO]_{eq}+2x_t$$

This solution to the temporal behaviour of $[ClO]_t$ was used to simulate ClO decay. Least squares fitting was employed to minimise the residuals between the temporally resolved experimental and simulated ClO traces by allowing the values of $[ClO]_0$, k_{2a} and k_{-2a} to vary.

4.5 Results

4.5.1 Results at 298 K, 760 Torr

k_{2a}	k_{-2a}	Resolution	Notes
5.62E-13	31.20	0.95	f([Br$_2$])
5.60E-13	30.83	0.95	f([Br$_2$])
4.76E-13	32.11	0.95	f([Br$_2$])
4.77E-13	32.48	0.95	f([Br$_2$])
5.14E-13	30.83	0.95	f([Br$_2$])
5.11E-13	30.74	0.95	f([Br$_2$])
4.72E-13	33.03	0.95	f([Br$_2$])
4.74E-13	32.85	0.95	f([Br$_2$])
4.82E-13	31.84	0.95	f([Br$_2$])
4.91E-13	31.66	0.95	f([Br$_2$])
4.96E-13	31.84	0.65	f([Br$_2$])
4.95E-13	31.11	0.65	f([Br$_2$])
4.63E-13	31.47	0.65	f([Br$_2$])
4.65E-13	31.66	0.65	f([Br$_2$])
5.43E-13	31.47	0.65	f([Br$_2$])
5.40E-13	31.20	0.65	f([Br$_2$])
4.54E-13	32.39	0.65	f([Br$_2$])
4.59E-13	31.93	0.65	f([Br$_2$])
4.80E-13	30.83	0.65	f([Br$_2$])
4.80E-13	30.92	0.65	f([Br$_2$])
4.40E-13	32.30	1.1	f([Br$_2$])
4.41E-13	32.20	1.1	f([Br$_2$])
4.61E-13	31.47	1.1	f([Br$_2$])
4.68E-13	31.02	1.1	f([Br$_2$])
5.47E-13	32.66	1.1	f([Br$_2$])
5.40E-13	32.48	1.1	f([Br$_2$])
4.58E-13	31.56	1.1	f([Br$_2$])
4.58E-13	31.47	1.1	f([Br$_2$])
4.86E-13	30.56	1.1	f([Br$_2$])
4.93E-13	30.65	1.1	f([Br$_2$])
5.57E-13	31.47	0.8	f([Br$_2$])
5.61E-13	31.38	0.8	f([Br$_2$])
4.79E-13	32.66	0.8	f([Br$_2$])
4.79E-13	32.57	0.8	f([Br2])
4.93E-13	32.11	0.8	f([Br2])
4.91E-13	32.11	0.8	f([Br2])
4.72E-13	33.30	0.8	f([Br2])
4.72E-13	33.30	0.8	f([Br2])
5.10E-13	32.30	0.8	f([Br2])
5.09E-13	31.84	0.8	f([Br2])
4.84E-13	26.72	0.5	f([Br2])
4.71E-13	29.73	0.5	f([Br2])
4.99E-13	31.02	0.5	f([Br2])
4.98E-13	31.66	0.5	f([Br2])
4.54E-13	33.85	0.5	f([Br2])
4.56E-13	33.12	0.5	f([Br2])
4.81E-13	32.66	0.5	f([Br2])
4.81E-13	32.02	0.5	f([Br2])
5.72E-13	32.75	0.5	f([Br2])
5.58E-13	31.38	0.5	f([Br2])
4.87E-13	29.37	0.8	f([Cl2])
4.84E-13	29.83	0.8	f([Cl2])
5.02E-13	32.20	0.8	f([Cl2])
4.83E-13	33.67	0.8	f([Cl2])
4.80E-13	32.39	0.8	f([Cl2])
4.80E-13	32.02	0.8	f([Cl2])
5.38E-13	36.32	0.8	f([Cl2])
5.24E-13	34.03	0.8	f([Cl2])
5.09E-13	25.43	0.8	f([Cl2])
5.06E-13	25.43	0.8	f([Cl2])
4.95E-13	29.28	0.8	f([Cl2])
4.95E-13	29.37	0.8	f([Cl2])
4.53E-13	43.4	0.8	f([Br2])
4.55E-13	43.3	0.8	f([Br2])
4.34E-13	45.4	0.8	f([Br2])
4.32E-13	44.7	0.8	f([Br2])

Table 4.8: Determinations of k_{2a} and k_{-2a} at 298 K and 760 Torr where the associated units are cm^3 $molecules^{-1}$ s^{-1} and s^{-1} respectively. Also indicated is the parameter which was systematically varied during a set of experiments at a given spectral resolution.

These data give rise to 298 K and 760 Torr values of $k_{2a} = (4.92 \pm 0.66) \times 10^{-13}$ cm^3 molecules^{-1} s^{-1} and $k_{-2a} = (31.5 \pm 5.00)$ s^{-1}, where errors are statistical only at the 95% confidence limits. No systematic variation of k_{2a} or k_{-2a} on experimental resolution or initial reactant concentration was observed.

4.5.2 Pressure Dependence at 298 K

Consistent with previous work and with theory describing termolecular reactions, the dimerisation of the ClO radical exhibits a pressure dependence, where at low pressures the apparent bimolecular rate coefficient is proportional to pressure but falls off toward some limiting value at higher pressures. This phenomenon is qualitatively illustrated by the two $[ClO]_t$ traces displayed in figure 4.28, both recorded at 298 K but with respective pressures of 760 and 200 Torr.

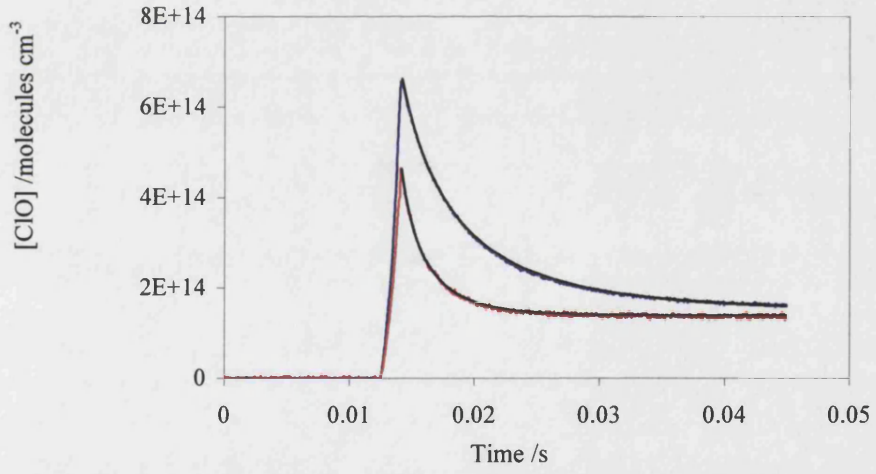

Figure 4.28: Classical fits (black) to $[ClO]_t$ at 298 K and pressures of 760 Torr (red) and 200 Torr (blue).

Troe has successfully developed a method for the parameterisation of this falloff behaviour as a function of increasing pressure, as described in section 2.2.2[24]. A Troe parameterisation of the 298 K data evaluated as a function of pressure is shown in figure 4.29. The error bars represent precision at the 95% confidence limits, where appropriate *Student's t factors* have been applied.

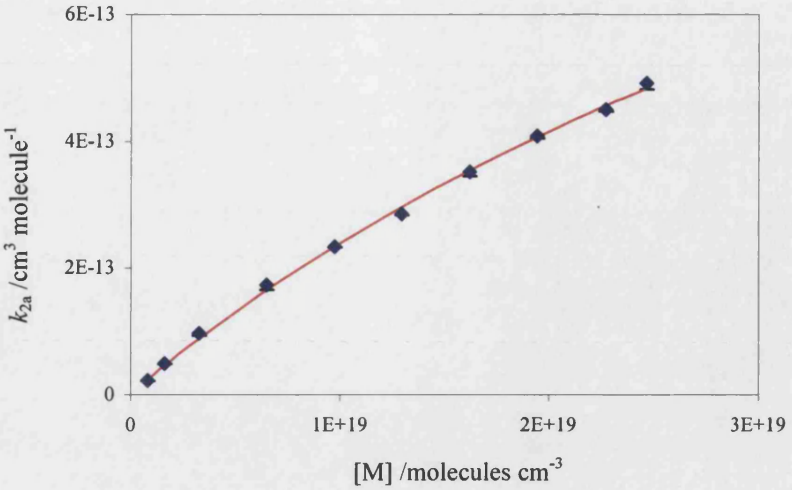

Figure 4.29: Pressure dependence of the 298 K rate coefficient k_{2a} (blue) and the associated Troe fit (red). The error bars represent 95% confidence limits, where the 760 Torr error bar has been divided by $n^{1/2}$, to account for non-equivalence of samples size.

The falloff expression defining this fit is of the form (2.xvii), where the fitted kinetic parameters are:

$$k_0 = (3.22 \pm 0.12) \times 10^{-32} \text{ molecules}^{-2} \text{ cm}^6 \text{ s}^{-1}$$
$$k_\infty = (4.39 \pm 0.51) \times 10^{-12} \text{ molecules}^{-1} \text{ cm}^3 \text{ s}^{-1}$$

and the value of F_c was held at 0.6 as recommended in the NASA evaluation[3].

The reaction only begins to enter the falloff regime at the higher pressures so the fitting routine is largely insensitive to k_∞, and this parameter is poorly characterised.

4.5.3 Temperature Dependence

The experimental data were extremely well reproduced by the simulated $[ClO]_t$ traces, returning k_{2a} and k_{-2a} with two small complications:

At temperatures below 250 K sensitivity to the value of k_{-2a} vanished and the kinetics effectively reduced to a second order system. The model was given an arbitrarily small

value for k_{-2a} and this parameter was no longer varied within the fitting routine. A typical fit to the data in this temperature regime is shown in figure 4.30.

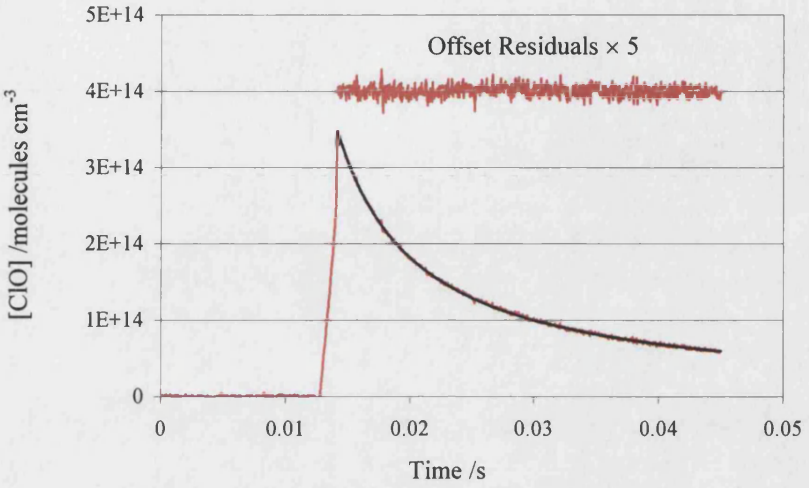

Figure 4.30: Fitted $[ClO]_t$ decay trace recorded at 218 K and magnified residuals, offset by 4×10^{14} molecules cm^{-3}.

Conversely, at temperatures in excess of 320 K the equilibrium concentration of ClO underwent a small but noticeable long timescale decay as indicated in figure 4.31. Literature data indicated that whilst the dimerisation channel (2a) of the ClO self-reaction exhibited a negative temperature dependence, the competing bimolecular processes increased with temperature. As a result, at $T \geq 320$ K, the sum of the bimolecular processes began to compete effectively with the dimerisation channel and the contribution of the former channels could no longer be neglected from the model in the search for a satisfactory fit. Thus, since data associated with these high temperatures is not relevant to the stratosphere further experimentation was restricted to temperatures below 320 K.

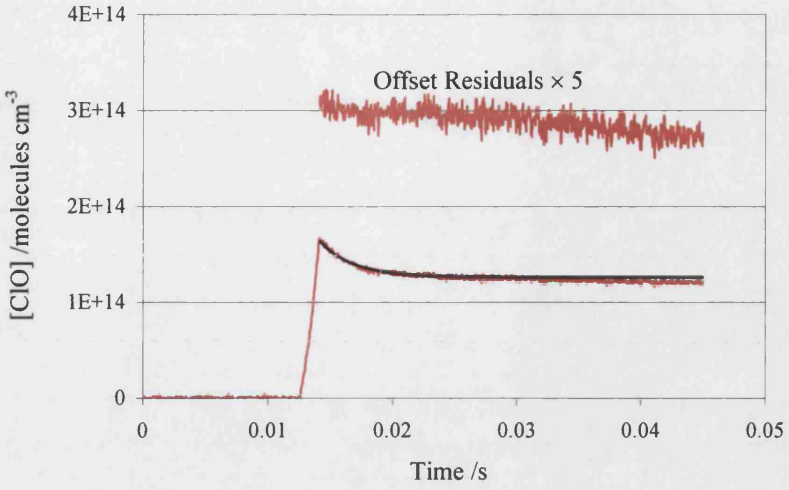

Figure 4.31: Fitted $[ClO]_t$ decay trace recorded at 320 K and magnified residuals, offset by 3×10^{14} molecules cm^{-3}.

Trolier *et al.*[15] reported an unexpectedly high third body efficiency for Cl_2 in the ClO + ClO dimerisation. Nickolaisen *et al.*[22] observed a similar phenomenon when employing high $[Cl_2]$ conditions ($0.5 - 1.8 \times 10^{17}$ molecules cm^{-3}), which manifested an unusual temperature dependence. The degree of enhancement reached a minimum at 300-310 K, increasing dramatically to both lower and higher temperatures. They attributed the low temperature enhancement to a chaperone effect involving $ClO\text{-}Cl_2$ formation, facilitating subsequent reaction with ClO:

(4.11) $ClO + Cl_2 \rightarrow ClO\text{-}Cl_2$

(4.12) $ClO\text{-}Cl_2 + ClO \rightarrow ClOOCl + Cl_2$

This effect was investigated over and above the range of precursor Cl_2 concentrations employed in this work. Figure 4.32 shows the fitted rate constants from investigations at 760 Torr and temperatures of 298 K and 206 K. No systematic dependence on the fitted values of k_{2a} and k_{-2a} on $[Cl_2]$ was observed, even at the lower temperature where thermal contraction enhanced the intracellular number densities. These results are consistent with the recent study by Bloss *et al.*[21] who reported the absence of such a dependence over a similar range of precursor conditions.

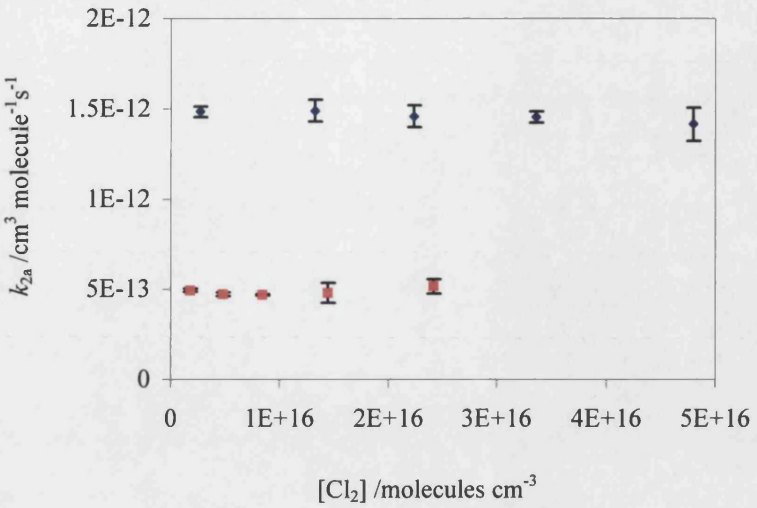

Figure 4.32: Fitted rate constants from experiments performed as a function of pre-flash [Cl_2] at 298 K (red) and 206 K (blue).

Previous studies of the ClO + ClO reaction have generally employed Cl_2 rather than Br_2 as a radical source. Therefore a similar role for Br_2 was investigated over the range (0.5-2) × 10^{16} molecules cm^{-3} at 760 Torr, 298 K. No low temperature study was undertaken since the kinetic experiments performed in this regime utilised Br_2 free conditions, as described above. Once again no systematic influence was observed on the fitted values of k_{2a}. It can be concluded that no significant chaperone or third body effects arising from the presence of either halogen compound were operating during the course of these experiments at 760 Torr.

Figure 4.33 shows the pressure dependent rate coefficient k_{2a} measured at 298.0 K, 271.2 K, 252.8 K, 235.2 K 218.2 K and 206.0 K. The falloff behaviour as the dimerisation kinetics tended from third to second order was once again analysed by least squares fitting to the Troe formalism at each temperature.

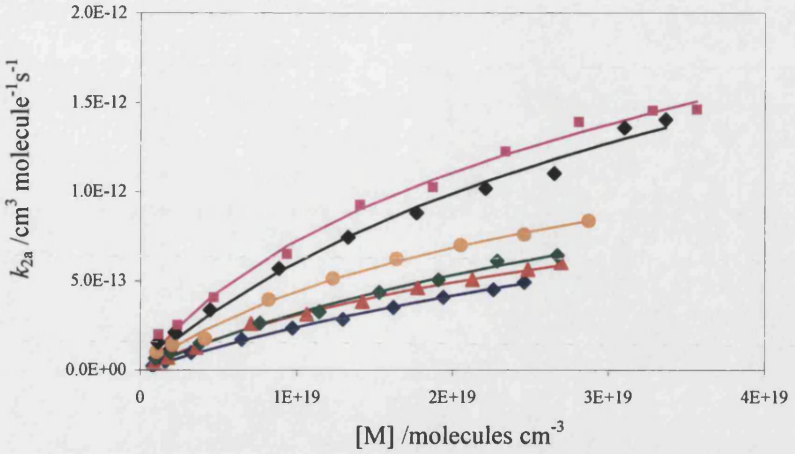

Figure 4.33: Pressure dependence of k_{2a} at 298 K (blue), 271.2 K (red), 252.8 K (green), 235.2 K (orange), 218.2 K (black) and 206 K (pink) fitting to all data points at a given temperature. Data is denoted by a marker associated Troe fit at a given temperature is denoted by the identically coloured line.

The optimised k_0 and k_∞ parameters are given in table 4.9. There is a clear increase in k_0 with decreasing temperature, in keeping with previous observations.[3] Conversely k_∞ shows no systematic trend as a function of temperature since the measurements were taken at pressures considerably lower than the limiting second order regime. As a result the fitting routine is largely insensitive to the value of k_∞ and this parameter is poorly characterised by the data.

At low temperatures (T < 271.2 K) the fitted curves were consistently lower than the k_{2a} measurements at low pressures. To quantify this phenomenon an intercept, k_{int} was incorporated into the Troe formulism and the data refitted. This intercept does not correspond to any specific theoretical or mechanistic process although possible origins of this phenomemon are discussed below. The results of this analysis are presented in table 4.10.

Temperature /K	k_0 /10^{-32}	k_∞ /10^{-12}
298	3.22 ± 0.12	4.39 ± 0.51
271.2	4.94 ± 0.29	2.98 ± 0.30
252.8	4.56 ± 0.43	4.38 ± 0.91
235.2	7.53 ± 0.78	3.66 ± 0.53
218.2	9.13 ± 1.04	7.03 ± 1.30
206	13.03 ± 1.45	5.42 ± 0.73

Table 4.9: Temperature dependence of k_0 and k_∞ values from least squares fitting to the Troe formalism. Respective units associated with k_0 and k_∞ are cm^6 $molecule^{-2}$ s^{-1} and cm^3 $molecule^{-1}$ s^{-1}.

Temperature /K	k_0 /10^{-32}	k_∞ /10^{-12}	k_{int}/10^{-14}
298	3.02 ± 0.21	5.00 ± 0.92	0.65 ± 0.59
271.2	4.84 ± 0.62	3.04 ± 0.48	0.22 ± 1.24
252.8	3.44 ± 0.43	7.42 ± 2.92	3.71 ± 1.34
235.2	6.45 ± 1.31	4.17 ± 0.97	2.58 ± 2.86
218.2	6.13 ± 0.91	12.4 ± 4.46	10.1 ± 3.40
206	9.65 ± 1.71	6.87 ± 1.29	7.98 ± 4.36

Table 4.10: Temperature dependence of k_0, k_∞ and k_{int} values from least squares fitting to the Troe formalism incorporating an intercept. Units associated with k_0 are are cm^6 $molecule^{-2}$ s^{-1}, whereas cm^3 $molecule^{-1}$ s^{-1} for k_{int} and k_∞

The magnitude of the intercept broadly follows an inverse relationship with temperature. Comparison with table 4.9 reveals that the manifestation of this intercept is, unsurprisingly, correlated with a decrease in the fitted value of k_0. The dependence of k_0 on temperature from both analytical procedures is parameterised below using the formalism adopted by NASA:[3]

(4.xxi) $k_0(T) = k_0(300)(T/300)^{-n}$

Least squares fitting to the intercept free parameterisation of the k_0 data gives:

$k_0(300) = (2.78 \pm 0.41) \times 10^{-32}$ cm^6 molecule^{-2} s^{-1}

$n = 3.99 \pm 0.47$

Whilst using the k_0 data obtained from the Troe formalism incorporating an intercept, k_{int} yields:

$k_0(300) = (2.78 \pm 0.66) \times 10^{-32}$ cm^6 molecule^{-2} s^{-1}

$n = 3.07 \pm 0.79$

4.6 Thermochemistry and Equilibrium Constant

At temperatures in excess of 270 K, the ClO dimerisation data provided sufficient sensitivity to evaluate k_{-2a} in addition to k_{2a} by optimising these parameters within the classical model of the equilibrium kinetics (xx). The pressure dependence of k_{-2a} at 298 K was well described by the Troe formulism and showed qualitative consistency with the simultaneously evaluated values of k_{2a}, as indicated by figure 4.34.

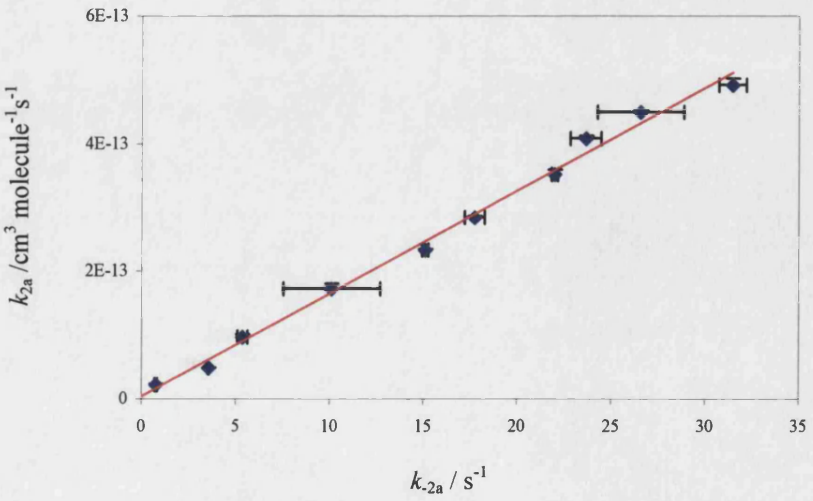

Figure 4.34: k_{2a} plotted against k_{-2a} from the 298 K experimental data.

Further experiments were undertaken at pressures of 760 Torr and temperatures of 271.2, 285.0, 290.0, 298.0, 305.0, 310.0, 315.0 and 320.0 K to investigate the thermochemistry of the ClO dimer. The equilibrium constant, K_{2a} was evaluated by two methods at each experimental temperature. The first method simply required the calculation of the ratio of fitted k_{2a}/k_{-2a} values. At 320 K where contributions from the bimolecular channels exert a small but non-negligible ClO loss route, the fitting routine was restricted to the ClO decay and very early equilibrium data, minimising the influence of these channels on the optimised values of k_{2a} and k_{-2a}. The second method assumed $[Cl_2O_2]$ on the basis of stoichiometric arguments incorporating experimentally determined values of $[ClO]_0$ and $[ClO]_{eq}$. As with the previous method, the 320 K evaluation of $[ClO]_{eq}$ was restricted to the early dimerisation in an attempt to minimise systematic error arising from bimolecular decay.

(4.xxii)
$$K_{2a} = \frac{k_{2a}}{k_{-2a}} = \frac{[Cl_2O_2]_{eq}}{[ClO]_{eq}^2} = \frac{([ClO]_0 - [ClO]_{eq})/2}{[ClO]_{eq}^2}$$

Good agreement between the two methods was observed at all temperatures. It is notable that this level of consistency provides confidence in the extrapolated values of $[ClO]_0$ and hence the extrapolated values of $A_{diff,0}$ used in the determination of the ClO differential cross section. The temperature dependent K_{2a} values evaluated from the two procedures were averaged prior to utilisation in the following analyses.

The K_{2a} values (strictly $K_{2a,c}$, expressed in concentration units) were converted to to $K_{2a,p}$ (expressed in pressure units, given in table 4.11) before performing a Second Law analysis whose output data could be compared to the literature expressed in standard states of 1 atmosphere for an ideal gas. The relationship given by (xxiii) defines this conversion for a stoichiometric reaction of the form:

$$aA + bB + ... \leftrightarrow \quad xX + yY + ...$$

(4.xxiii)
$$K_p = K_c(RT)^{\Delta n}$$

where Δn is the mole change in reaction, in this case -1, given by:

(4.xxiv) $$\Delta n = (x + y + ...) - (a + b + ...)$$

T/K	$K_{2a,p}$ /atm^{-1}	k_{-2a}/s^{-1}
271.2	$(2.00 \pm 0.94) \times 10^7$	1.3 ± 3.7
285	$(3.22 \pm 2.99) \times 10^6$	4.58 ± 3.12
290	$(7.72 \pm 0.47) \times 10^5$	16.6 ± 1.6
298	$(3.79 \pm 0.95) \times 10^5$	31.5 ± 5
305	$(1.42 \pm 0.05) \times 10^5$	67.9 ± 6.1
310	$(8.47 \pm 1.36) \times 10^4$	94.7 ± 2.9
315	$(5.19 \pm 0.22) \times 10^4$	144 ± 13
320	$(3.51 \pm 0.42) \times 10^4$	195 ± 15

Table 4.11: Averaged values of $K_{2a,p}$ determined from two methods on the temperature dependent data. Also indicated are the k_{-2a} values obtained from the classical fits to the $[ClO]_t$ data. Errors are expressed at the 95% confidence level.

A van't Hoff plot of $\ln(K_{2a,p})$ versus $1000/T$ is shown in figure 4.35. The enthalpy of reaction (2a) calculated from the slope of the van't Hoff plot is $\Delta H° = -80.0 \pm 4.0$ kJ mol^{-1} and the intercept derived from the intercept in the $\ln(K_{2a,p})$ axis is $\Delta S° = -172 \pm 13$ J mol^{-1} K^{-1}. The fit was weighted on the basis of the 95% confidence error bars associated with each K_{2a} value at a given temperature. This was considered necessary since the uncertainties associated with the two lowest temperature evaluations of K_{2a} were large, reflecting the insensitivity of the kinetic model to k_{-2a} at these temperatures, where the kinetics tended toward second order behaviour. Also shown in figure 4.35 are van't Hoff plots from previous studies of the Cl_2O_2 thermochemistry derived from kinetic analyses.

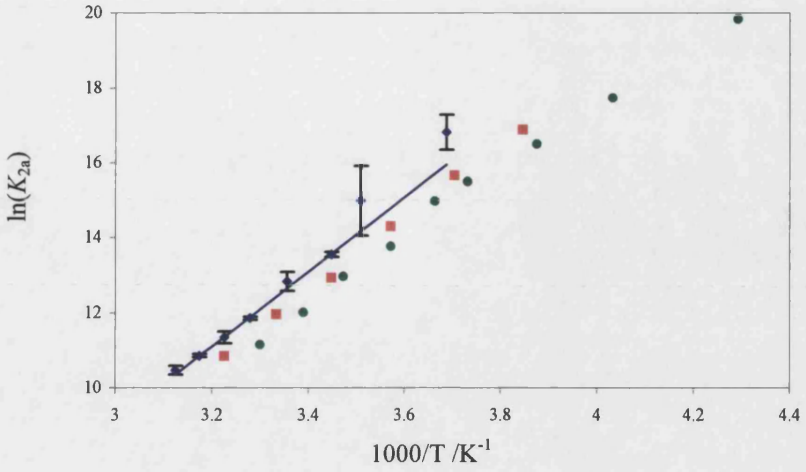

Figure 4.35: Van't Hoff plot and weighted parameterisation of the K_{2a} data expressed in pressure units (blue). Previous data reported by Nickolaisen et al.[22] and Cox and Hayman[25] are shown in red and green respectively.

The thermochemistry of Cl_2O_2 can also be determined from the Third Law.

(4.xxv) $$\Delta H° = \Delta G° + T\Delta S°$$

Where $\Delta S° = -151$ Jmol^{-1}K^{-1}, evaluated using tabulated entropy[3], $S°_{298K}(ClO) = 227$ J mol^{-1} K^{-1} and $S°_{298K}(Cl_2O_2) = 303.2$ J mol^{-1} K^{-1}. ΔG can be calculated directly from the experimental values of K_{2a}:

(4.xxvi) $$\Delta G° = -RT \ln(K_{2a})$$

Thus $\Delta H°$ was calculated at each temperature by invoking the third law analysis. These values were generally in good agreement except those utilising the two lowest temperature K_{2a} evaluations. Once again this reflects the insensitivity to k_{-2a} in the lower temperature experiments which is propagated through to the calculated K_{2a} values. Hence an average of the calculated $\Delta H°$ values over the range 290 K $\leq T \leq$ 320 K gave rise to a $\Delta H° = -76.3 \pm 0.8$ kJ mol^{-1}.

The thermochemical results are presented and compared to existing data in table 4.11. The measured $\Delta H°$ and $\Delta S°$ values are in excellent agreement with those reported by Nickolaisen *et al.*[22] These authors reported values of $\Delta H°$ from the third law analysis which were approximately 5% lower than those derived from the second law analysis. This small but consistent discrepancy may arise from weaknesses associated with the literature values of $S°_{298K}(ClO)$ and $S°_{298K}(Cl_2O_2)$, since Nickolaisen *et al.* employed the same sources utilised in this study. A potential drawback with the Second Law analysis is that $\Delta H°$ is itself a temperature dependent quantity. However, the temperature dependence of $\Delta H°$ is often weak[26] which appears to be the case here, since the van't Hoff plot is exhibits good linear behaviour (except to the lowest temperatures, although this is likely to be a manifestation of insensitivity to k_{-2a} and hence K_{2a} at these temperatures and not related to $\Delta H°$. In any case the weighted fit to the data removed any bias in the parameterisation of the van't Hoff plot.) For these reasons the Second Law determination of $\Delta H°$ is considered to be the more reliable method.

Reference	$\Delta H°$ (Third Law)	$\Delta H°$ (Second Law)	$\Delta S°$ (Second Law)
This work	-76.3 ± 0.8	-80.0 ± 4.0	-172 ± 13
Nickolaisen *et al.*[22]	-76.0 ± 0.8	-81.9 ± 2.9	-174 ± 10
Cox *et al.*[25]		-72.5 ± 3.0	-144 ± 11

Table 4.12: Evaluated thermochemical data from the kinetic experiments and comparison with previous results. Units of $\Delta H°$ and $\Delta S°$ are $kJmol^{-1}$ and $Jmol^{-1}K^{-1}$ respectively.

4.7 Discussion

4.7.1 Literature Cross Sections

The procedure used to measure the ClO differential cross section indicated a systematic dependence of $\sigma_{ClO,diff}$ on the value of the calibrating cross sections (σ_{ClO}-σ_{Cl2O}) at wavelengths below 255 nm. This strongly points to a problem with one or both of the two cross sections. This is most likely an error associated with σ_{ClO}, since ClO is a transient species, readily undergoing self-reaction, whereas Cl_2O is a closed shell molecule with a long lifetime in the gas phase. Indeed the database on the absorption cross section of Cl_2O shows excellent agreement across all of the investigations as discussed in section 4.3.2.

4.7.2 ClO Differential Cross Section

This work presents the first broad band investigation into the temperature dependence of the ClO differential cross section. The only comparable results are those reported by Bloss *et al.*[21] whose study at higher resolution employed dual wavelength monitoring at 275.2 and 276.4 nm to measure the temperature dependence of this *pseudo*-differential ClO cross section. Their results are not directly comparable since Bloss *et al.* worked at higher spectral resolution. However, Bloss *et al.* reported a quadratic dependence of $\sigma_{ClO,diff}$ on decreasing temperature. By contrast, this investigation reports a linear dependence of $\sigma_{ClO,diff}$ on decreasing temperature. The importance of this discrepancy is paramount in the subsequent investigation into the kinetics of the ClO radical undertaken by both groups, given the linear dependence of k_{2a} on σ_{ClO} under the second order loss conditions which characterise ClO dimerisation at stratospheric temperatures.

(4.xxvii) $$k_{2a} = \frac{\sigma l}{2t}\left(\frac{1}{A_t} - \frac{1}{A_0}\right)$$

Bloss *et al.* cite a key advantage of their *pseudo*-differential monitoring technique over previous, single wavelength, studies of reaction (2). Differential spectroscopy removes the need to account for baseline fluctuations arising from other transient absorbers at the monitored wavelengths. Strictly, for a two wavelength analysis, this is only true if the magnitude of any underlying absorbance spectrum is identical at the two wavelengths. In this instance, Cl_2O_2 and Cl_2O are not flat between 275.2 and 276.4 nm, so a small correction is still required to account for the transience of absorbers underlying the *pseudo*-differential ClO absorption monitored by Bloss *et al.*

Broad band differential spectroscopy *entirely* removes the need to account for fluctuations in baseline absorbance. Moreover, broad band monitoring of the differential ClO cross section provides a vast improvement in the signal to noise ratio associated with the spectral fitting which evaluates $[ClO]_t$. Thus any kinetic data obtained from differentially evaluated $[ClO]_t$ is better constrained than that obtained from experiments incorporating dual wavelength monitoring. Furthermore a gradual drift in the wavelength axis of the spectrograph over the course of a set of experiments was observed from the need to shift the ClO differential cross section by small increments to optimise the fit to the experimental absorption data, readily removing this source of systematic error. Both observation of this effect (presumably arising from external forces within the laboratory, *e.g.* fluctuations in ambient temperature, pump vibration) and accounting for it is less trivial when utilising the dual wavelength technique. The high spectral resolution associated with the monochromators used by Bloss *et al.* ensures that even a very small degree of migration in the wavelength domain would lead to a very large systematic error in inferred [ClO].

4.7.3 ClO Dimerisation Kinetics

Troe parameterisation of the experimentally determined temperature and pressure dependent rate coefficients, k_{2a} and k_{-2a} was performed. At low temperatures the Troe model consistently underestimated the measured values of k_{2a} at low pressures. An intercept, k_{int} was included in the model to investigate the temperature dependence of this effect. The general trend was an increase in the value of k_{int} with decreasing temperature. The phenomenon has been observed previously by Trolier *et al.*[15] who

also incorporated an intercept into the Troe parameterisation of their data. The authors reported values of k_{int} which are of the same order of magnitude as those observed in this study. Futhermore they reported an inverse relationship between k_{int} and temperature, which is at least qualitatively consistent with the dependence measured in this study.

Trolier *et al.* suggest that the observed rate enhancement under conditions of low temperature and pressure could be a consequence of an additional dissociative channel from the excited Cl_2O_2* complex, most likely yielding Cl_2 and O_2. This channel would be indistinguishable from bimolecular ClO decay in a flash photolysis experiment and reduced Cl_2O_2 yields would be anticipated as the proposed pathway became increasingly significant. However, Trolier *et al.* themselves performed some experiments to monitor Cl_2O_2 and ClO simultaneously using a diode array setup. They observed no such decrease in Cl_2O_2 yields although their results were marred by the apparent production of physically unreasonable $[Cl_2O_2]$ limited by [ClO] decay. Similarly the study by Bloss *et al.* monitored Cl_2O_2 evolution at 210 nm where the other transient species exerted no significant absorption. No such anomalies were observed in the Cl_2O_2 yields in their experiments either, although their simultaneous optimisation of $[ClO]_0$, k_{2a} (their experiments were undertaken at T < 250 K where k_{-2a} is negligible) *and* σ_{Cl2O2} casts doubt over the use of $[Cl_2O_2]$ as a quantitative tool. As a result the possibility of an additional dissociative pathway from Cl_2O_2* remains a possible explanation for the non-zero intercepts observed on the low temperature falloff plots from this work and that of Trolier *et al.*

Alternatively the intercept could be a manifestation of more complex falloff behaviour characterising reaction (2a). If more than one isomer of Cl_2O_2 existed then it follows that these isomers could exert different falloff behaviour. The literature investigating production of multiple Cl_2O_2 isomers from (2a) is somewhat conflicting. Rotational spectroscopy carried out Birk *et al.*[27] suggested that ClOOCl was the sole product. However, calculations by Lee *et al.*[28] have indicated that $ClClO_2$ would lie just (3.8 ± 8.2) kJ mol^{-1} higher in energy than ClOOCl, whereas ClOClO would lie (42 ± 17) kJ mol^{-1} higher in energy than the symmetric isomer. Direct formation of $ClClO_2$ from two ClO radicals is unlikely but it has been suggested that it could form from

isomerisation following mechanistically plausible ClOClO production.[29] Indeed $ClClO_2$ has been observed, although not from reaction (2a), and its absorption cross section recorded.[30] The absorption cross section of ClClO2 overlaps that attributed to ClOOCl and is significantly larger. Indeed unexpected formation of this isomer could be responsible for the considerable discrepancies between reported absorption cross sections of ClOOCl. The three key studies of this spectrum were carried out under different temperature and pressure regimes which may have been conducive to different isomer yields. Once again production of multiple Cl_2O_2 isomers could be responsible for the observed intercepts on the low temperature falloff data.

However another possible explanation for the unusual falloff behaviour involves complexities arising from the presence of Cl_2. Trolier *et al.*[15] reported an enhancement of $k_{0,200K}$ by a factor of 7 when N_2 was replaced by Cl_2 as the bath gas. Moreover, Nickolaisen *et al.*[22] observed a similar phenomenon, noting enhancement in the rate of ClO loss in the presence of molecular chlorine. These authors reported a temperature dependent effect which minimised around 300 K and increased to both higher and lower temperatures, although they could not explicitly quantify this dependence. They attributed the low temperature enhancement of k_{obs} to a chaperone mechanism involving the formation of a ClO-Cl_2 complex, as described above.

Investigation during the course of this work revealed no manifestation of any chaperone phenomenon at 206 K and at 298 K. These investigations were undertaken at 760 Torr where formation of a significantly long lived ClO-Cl_2 complex was considered to be most plausible. During the pressure dependent experiments, the pre-flash [Cl_2O] was deliberately held constant to ensure rapid production of ClO and hence no overlapping of radical formation and decay timescales. However, due to the decrease in absolute number densities at low pressure this involved reducing the carrier N_2 flow and hence the dilutant factor for Cl_2O and unreacted Cl_2. As a result as the total pressure was reduced, the relative amount of Cl_2O and hence unreacted Cl_2 within the cell increased. It was not possible to perform a low pressure determination of k_{obs} as a function of [Cl_2] since Cl_2 flow was already at the upper limit permitted by the flow meter and significant decrease in [Cl_2] would have prevented rapid ClO formation, reducing k_{obs}. However, calculations employing the 200 K value of k_0 in

the Cl_2 bath gas reported by Trolier *et al.* and the known precursor gas concentrations indicated that the experimental k_{obs} values at 25 and 50 Torr would be only 10% and 3% larger than hypothetical points recorded under these conditions in a bath gas consisting purely of N_2. These enhancements cannot quantitatively account for the large value of k_{int} observed at 206 K.

It was not possible to quantify the effects of Cl_2 on k_{obs} at other temperatures since Trolier *et al.* report this effect at 200 K. However, the decrease in the measured k_{obs} values as the temperature approached 300 K is qualitatively consistent with the temperature dependence of the chaperone effect alluded to by Nickolaisen *et al.* Even if ClO-Cl_2 formation did not exert a pressure dependence of its own, its manifestation would exert a pressure dependence in our experiments, due to its dependence on $[Cl_2]/[N_2]$ which itself was systematically (although not for this reason) changed as a function of pressure. As a result, if this phenomenon were responsible for the rate enhancement at low temperatures, it would not be manifested as a simple intercept on the falloff plots. This may account for the large relative errors associated with optimised values of k_{int}, which exceed even those of k_∞ which is poorly characterised by the data.

The evidence presented above suggests that the chaperone effect involving Cl_2 is at least partially responsible for the low temperature, low pressure enhancement of k_{obs}. However the available data on this process cannot quantitatively account for this effect and it is not possible to entirely discount the mechanistic explanations described beforehand. A low pressure study ($p < 50$ Torr) as a function of $[Cl_2]$ could potentially resolve these uncertainties, although these experiments were not possible using the flash photolysis apparatus. As a result the inclusion of the low pressure points in the low temperature parameteristaion of the falloff data most likely leads to an overestimation of k_0 at these temperatures. As a result, the falloff data was refitted excluding the 25 and 50 Torr (lowest pressures). Even at the lowest temperature, where Nickolaisen *et al.* report the most significant rate enhancement, the Cl_2 becomes so heavily diluted at a pressure of 100 Torr that the chaperone effect contributes less than 1.5% of the measured k_{obs}. Table 4.13 shows the results of these

parameterisations in comparison to the optimised k_0 values obtained from fitting all the pressure dependent data, previously given in table 4.8.

Temperature /K	k_0 /10^{-32} (entire data set)	k_0 /10^{-32} ($p \geq 100$ Torr)
298	3.22 ± 0.12	3.21 ± 0.15
271.7	4.94 ± 0.29	4.92 ± 0.36
252.8	4.56 ± 0.43	4.34 ± 0.37
235.2	7.53 ± 0.78	7.11 ± 0.70
218.2	9.13 ± 1.04	8.57 ± 0.95
206	13.03 ± 1.45	12.10 ± 1.27

Table 4.13: Comparison of k_0 values obtained by fitting: (i) to the entire data set at a given temperature, (ii) to the data at $p \geq 100$ Torr only. Units associated with k_0 are are cm^6 $molecule^{-2}$ s^{-1}. Also included for completeness are the k_∞ values associated with the $p \geq 100$ data, expressed in units of cm^3 $molecule^{-1}$ s^{-1}. Errors from the fits are statistical at the 95% confidence limits.

It is interesting to note that the statistical error bars are, in the main, not significantly increased by excluding the low pressure data from the fitting procedure, despite the fact that, in principle, the low pressure observations constrain k_0 most effectively. This can be interpreted as another manifestation of the non-Troe behaviour of these low pressure k_{obs} determinations. This last parameterisation of the pressure dependent data is considered to represent the most accurate of the 3 methods used to fit the falloff data. Once again the temperature dependence of k_0 was fitted by adopting the formulism given by (2.xvii).

$k_0(300) = (2.79 \pm 0.43) \times 10^{-32}$ cm^6 molecule^{-2} s^{-1}

$n = 3.78 \pm 0.79$

Comparison of the temperature dependent k_0 values with previous studies is shown in figure 4.36. The k_0 values determined in this study are consistently larger than those

from previous studies over the entire temperature range. The temperature dependence of k_0 from this study is consistent with that measured by Bloss *et al.* and Trolier *et al.* when the latter authors did not incorporate an intercept into their falloff parameterisations. The most likely origin of the discrepancy in the magnitude of the k_0 values determined here in comparison to those determined by Bloss *et al.* is the differential cross section. It has already been shown that k_{2a} is proportional to σ_{ClO} under the second order loss conditions observed at low temperature. The differential cross section measured by Bloss *et al.* was smaller than that determined in this study if the resolution dependence is factored out (Bloss *et al.* report similar values of $\sigma_{ClO,diff}$ to those recorded in this study but worked at higher spectral resolution).

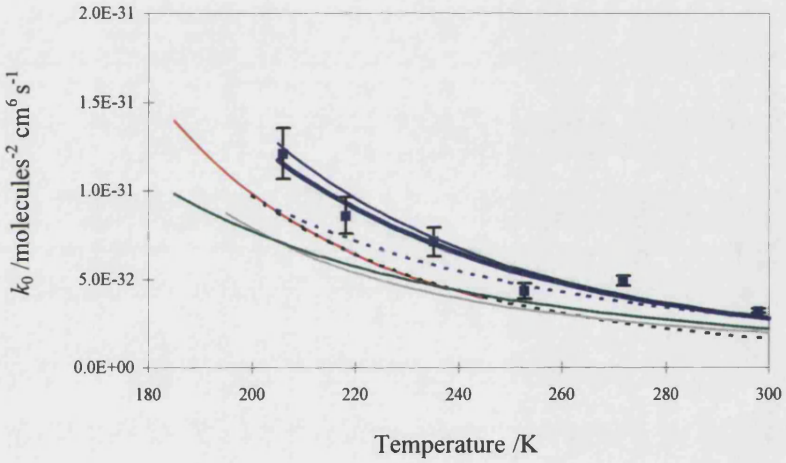

Figure 4.36: Experimentally determined temperature dependence of k_0 by fitting to $p \geq 100$ Torr data only (blue squares, heavy blue line). The temperature dependence of k_0 derived from Troe parameterisations to all the data ($25 \leq p \leq 760$ Torr) excluding and incorporating an intercept are shown by the weak blue line and the broken blue line respectively. The data by Bloss et al. (red), Trolier et al. (broken black), Nickolaisen et al. and the most recent NASA evaluation (solid black) are included for comparative purposes.

Given the improved signal to noise ratio and the other advantages associated with broad band spectroscopy over single (and dual) wavelength monitoring of transient absorbers (described above), it is asserted here that this determination of the ClO differential cross section is less prone to both systematic and random errors than that

reported by Bloss *et al.* As such kinetic measurements from this work, critically sensitive to $\sigma_{ClO,diff}$ are more reliable. It is interesting to note that the quadratic dependence of $\sigma_{ClO,diff}$ reported by Bloss *et al.* is not manifested as a discrepancy in the temperature dependence of k_0 in comparison to that measured in this work, which reports a linear dependence of $\sigma_{ClO,diff}$ on temperature. However, the quadratic dependence "arbitrarily chosen" by Bloss *et al.* manifests a deviation from linearity most strongly at temperatures below 206 K, which could not be achieved in this laboratory. It is not possible to compare the ClO cross sections employed by the other groups with that measured here since they did not utilise the differential cross section. Instead they monitored temporal ClO absorbances in the continuum region where baseline fluctuations can represent a significant source of systematic error. However it is interesting to note that the k_0 data obtained by Troe parameterisation with an artificial intercept follows a temperature dependence akin to that reported by Nickolaisen *et al.* However, the authors did not fit their data with the Troe formulism so it was not possible to investigate this similarity in detail.

The determination of higher k_0 values than previously reported over the entire temperature range has profound consequences on the current understanding of stratospheric ozone loss, particularly in the polar vortices where ClO mixing ratios reach the highest levels. To a first approximation, the k_0 values reported here would lead to an enhancement in polar ozone depletion over current estimates. It is worth noting that the most recent NASA evaluation[3] of the k_0 data describing (2a) is much lower and exerts a weaker inverse temperature dependence than that suggested here and by Bloss *et al.*, the only other investigation of ClO + ClO kinetics which supersedes this evaluation. For atmospheric modelling purposes, quantifying the enhancement in polar ozone depletion expected on the basis of these experiments, the k_0 values must be corrected for the different third body efficiencies associated with N_2 and O_2. The relative efficiency on ClO dimerisation for M = O_2 to M = N_2 has been investigated by Nickolaisen *et al.* and Trolier *et al* who reported ratios of 0.62 and 0.82 respectively. The mean of these two values and an atmospheric abundance ratio $0.21O_2/0.79N_2$ gives rise to a 6% reductive correction in the measured k_0 values, which to a first approximation yields:

(4.xxviii) $$k_0(\text{atm}) = (2.6 \pm 0.4) \times 10^{-32} \times (T/300)^{-(3.8 \pm 0.8)}$$

Once again errors represent precision only and are quoted at the 95% confidence limits. For atmospheric modelling purposes at a given stratospheric pressure, the k_{2a} values evaluated from expression (xxvii) should be combined with a further 13% error arising from potential error in the ClO differential cross section. This compares with the NASA recommendation:[3]

$$k_0(\text{atm}) = (2.2 \pm 0.4) \times 10^{-32} \times (T/300)^{-(3.1 \pm 0.5)}$$

4.8 References

[1] Molina, L.T.; Molina, M.J. *J. Phys. Chem.* **1987**, 91, 433.

[2] Scientific Assessment of Ozone Depletion **2002**, World Meteorological Organisation Report no. 47.

[3] DeMore, W.B.; Sander, S.P.; Golden, D.M.; Hanson, R.F.; Kurylo, M.J.; Howard, C.J.; Ravishankara, A.R.; Kolb, C.E.; Molina, M.J. *Chemical Kinetics and Photochemical Data for use in Stratospheric Modeling;* JPL publication **97-4**; California Institute of Technology, Pasadena.

[4] Bedjanian,Y.; Laverdet,G.; Le Bras,G. *J. Phys. Chem. A* **1998**, 102, 953.

[5] Smith, G.D.; Tablas, F.M.G.; Molina, L.T.; Molina, M.J. *J. Phys. Chem. A* **2001**, 105, 8658.

[6] Hinshelwood, C.N.; Pritchard, C. R. *J.C.S.* **1923**, 123, 2730.

[7] Knauth, H.D.; Alberti, H.; Clausen, H. *J. Phys. Chem.* **1979**, 83, 1604.

[8] Molina, L.T.; Molina, M.J. *J. Phys. Chem.* **1978**, 82, 2401.

[9] Lin, C.L. *J. Chem Eng. Data* **1976**, 21, 411.

[10] Simon, F.G.; Schneider, W.; Moortgat, G.K.; Burrows, J.P. *J Photochemistry and PhotoBiology A: Chem* **1990**, 55, 1.

[11] Sander, S.P.; Friedl, R.R.; Yung, Y.L. *Science* **1989**, 245, 1095.

[12] Porter, G.; Wright, F.J. *Disc. Faraday Soc.* **1953**, 14, 23.

[13] Mandelman, M.; Nicholls, R.W. *J. Quant. Spectrosc. Rad. Transfer* **1977**, 17, 483.

[14] Johnston, H.S.; Morris, E.D.; Van den Bogaerde, J. *J. Atm. Chem. Soc.* **1969**, 91, 7712.

[15] Trolier, M.; Mauldin III, R.L.; Ravishankara, A.R. *J. Phys. Chem.* **1990**, 94, 4896.

[16] DeMore, W.B.; Tschuikow-Roux, E. *J. Phys. Chem.* **1990**, 94, 5856.

[17] Huder, K.J.; DeMore, W.B. *J. Phys. Chem.* **1995**, 99, 3905.

[18] Burkholder, J.B.; Orlando, J.J.; Howard, C.J. *J. Phys. Chem.* **1990**, 94, 687.

[19] Avallone, L.M.; Toohey, D.W. *J. Geophys. Res. – Atmos.* **2001** 106 (D10): 10411.

[20] Greenwood, N.N.; Earnshaw, A. *Chemistry of the Elements, Pergamon Press*, **1990**.

[21] Bloss, W.J.; Nickolaisen, S.L.; Salawitch, R.J.; Friedl, R.R.; Sander, S.P. *J. Phys. Chem. A* **2001**, 105, 11226.

[22] Nickolaisen, S.L.; Friedl, R.R.; Sander, S.P. *J Phys. Chem.* **1994**, 98, 155.

[23] Gilles, M.K.; Turnipseed, A.A.: Burkholder, J.B. *J. Phys. Chem. A* **1997**, 101, 5526.

[24] Troe, J. *J. Chem. Phys.* **1977**, 66, 4745.

[25] Cox, R.A.; Hayman, G.D. *Nature* **1988**, 332, 796

[26] Atkins, P.W. *Physical Chemistry (Fifth Edition), Oxford University Press* **1994.**

[27] Birk, M.; Friedl, R.; Cohen, E.; Pickett, H.; Sander, S.P. *J. Chem. Phys.* **1989**, 91, 6588.

[28] Lee, T.J.; Rohlfing, C.M.; Rice, J.E. *J. Chem. Phys.* **1992**, 97, 6593.

[29] McGrath , M.P.; Clemitshaw, K.C.; Rowland, F.S.; Hehre, W.J. *J. Phys. Chem.* **1990**, 94, 6126.

[30] Jacobs, J.; Kronberg, M.; Muller, H. S. P.; Willner, H. *J Am. Chem. Soc.* **1994**, 116, 1106.

Chapter 5 :The BrO + BrO Reaction

5.1 Introduction

The important role played by BrO radicals in the destruction of atmospheric ozone is well documented. Catalytic cycles involving the BrO radical have been show to play a crucial role in the destruction of stratospheric ozone in both polar and midlatitude regions.[1] In the troposphere, elevated BrO mixing ratios show distinct anticorrelation with simultaneous ozone measurements in the Arctic Marine Boundary Layer (MBL).[2]

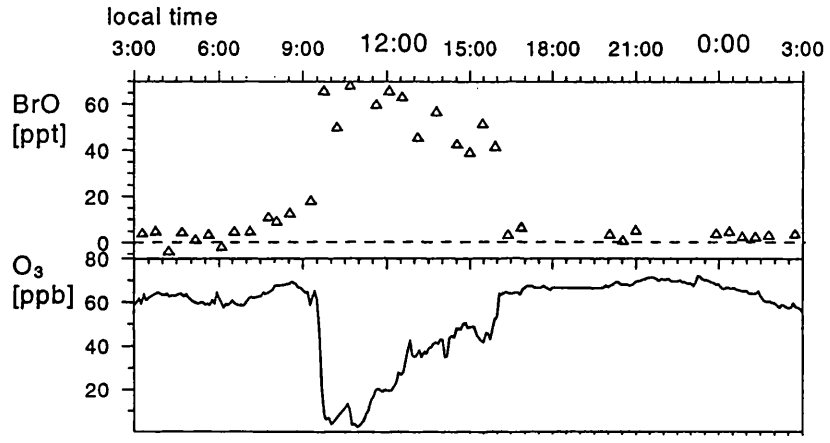

Figure 5.1: Time series of tropospheric mixing ratios of BrO (in parts per trillion, top panel) and ozone (in parts per billion, bottom panel). Taken from reference 2.

Several mechanisms involving heterogeneous chemistry have been proposed to explain these high gas phase BrO concentrations observed in the MBL,[3,4,5,6] each sharing sea salt Br^- as the source of inorganic bromine. One such example involves the night-time uptake of HOBr onto sea-salt aerosol particles, which produces Br_2. Subsequent release of Br_2 back into the gas phase, followed by the solar photolysis of Br_2 liberates bromine atoms, which generate BrO radicals at the expense of ozone:

(5.1)	HOBr(g) + aerosol	↔	HOBr (aq)
(5.2)	HOBr (aq) + Br^- (aq) + H^+ (aq)	↔	Br_2 (aq) + H_2O
(5.3)	Br_2(aq)	↔	Br_2 (g)

(5.4)		$Br_2(g) + h\nu$	→	2 Br
(5.5)		2 (Br + O_3	→	BrO + O_2)
	Net:	HOBr + Br^- + H^+ + $2O_3$	→	2BrO + $2O_2$ + H_2O

The resulting enrichment in local BrO mixing ratio gives rise to further ozone loss through a catalytic cycle involving the BrO self-reaction:

(5.6a)		BrO + BrO	→	2Br + O_2
(5.5)		2 (Br + O_3	→	BrO + O_2)
	Net:	$2O_3$	→	$3O_2$

Similar effects have recently been observed in the midlatitude marine boundary layer, notably at the Dead Sea where salinity can reach levels twelve times that found in typical ocean water.[7] This increased salinity enhances the rate of heterogeneous release of Br_2 (and indeed BrCl) in reactions such as (1-4) above.

It is instructive to note that the BrO self-reaction, occurring during episodes of elevated BrO mixing ratios, leads to surface ozone depletion in an analogous fashion to the ClO + ClO reaction in the stratosphere. The enhanced importance of the heavier halogens Br, and indeed I in the troposphere is a result of their reduced propensity to form, and reduced stability of halogen reservoir species. By contrast, Cl atoms react rapidly with many species in the lower atmosphere, forming stable reservoir species such as HCl. Consequently chlorine is a much less efficient agent for surface ozone loss than its heavier counterparts.

Given the importance of the BrO radical self-reaction in surface ozone depletion events, any channel of this reaction which does not lead to the production of Br atoms could significantly alter the atmospheric impact of this process. Furthermore, accurate knowledge of the kinetic data describing the BrO self-reaction allows determination of the extent to which other reactions (e.g. BrO + HO_2, BrO + NO_2) can compete with the self-reaction, facilitating more accurate model description of surface O_3 chemistry

and partitioning between active and inactive bromine species.

Numerous studies of the BrO self-reaction have been undertaken during the last three decades. These studies have employed flash photolysis / UV absorption (FP/UV),[8-15] discharge flow / mass spectrometry (DF/MS),[16-18] discharge flow / UV absorption (DF/UV)[19] and molecular modulation/ UV absorption (MM/UV)[20,21] techniques to generate and monitor BrO and deduce the rate constants describing its removal. Strong evidence has been gathered to support the existence of a 2 channel mechanism:

(5.6a) $BrO + BrO \rightarrow 2Br + O_2$

(5.6b) $BrO + BrO \rightarrow Br_2 + O_2$

An early study observed the formation of Br_2 by emission from the electronically excited molecular product.[19] Direct measurement of the branching ratio by time resolved monitoring of BrO decay and Br_2 evolution was not accomplished until the 1990s by FP/AS[13] and DF/MS.[18]

Indirect attempts to distinguish channel branching in the BrO self-reaction achieved success by employing different chemical systems. Channel (6a) could be effectively masked by carrying out experiments under conditions of excess ozone. Under such conditions the reconversion of bromine atoms formed in channel (6a) to BrO is rapid, and channel (6a) does not contribute to the observed decay of BrO. Thus, analysis of the BrO decay allows determination of the rate coefficient of reaction channel (6b) alone, k_{6b}.

(5.5) $Br + O_3 \rightarrow BrO + O_2$

Conversely, experiments carried out under ozone free conditions precluded any regeneration of BrO. Therefore, under these conditions, the observed BrO decays along both reaction channels (6a) and (6b) and an analysis of this decay allows determination of the overall rate coefficient $k_6 = k_{6a} + k_{6b}$. Comparison of results from the two chemical systems allows direct calculation of the branching ratio for the non-terminating channel, defined as $\alpha = (k_{6a}/(k_{6a}+k_{6b}))$. Similarly, experiments monitoring

both BrO and O_3 have been undertaken to provide simultaneous monitoring of both channels. BrO decay provides k_{6b} whilst k_{6a} could be inferred from the degree of ozone consumption.[12]

Table 5.1 summarises previous studies of the kinetics and product branching ratios for the BrO self-reaction at ambient temperature. It is clear that both the overall rate coefficient and the product branching ratio are reasonably well established at 2.9×10^{-12} molec^{-1} cm^3 s^{-1} and 0.85 respectively. The reported values of the 298 K rate coefficient do however range between $(2.17\text{-}3.4) \times 10^{-12}$ molec^{-1} cm^3 s^{-1}.

In this study, the unique advantage of the CCD detector set up, giving accurate and unequivocal monitoring of structured absorbers such as BrO was ideally suited to constraining the kinetics of the BrO decay. Moreover the ability of the CCD detector to monitor multiple species simultaneously allowed direct measurement of the product branching ratio and the investigation of potential secondary chemistry involving molecules such as OBrO, discovered subsequent to many of the kinetics studies reported in table 5.1.

$k_{6a+6b}/10^{-12}$	$\alpha = k_{6a}/k_{6a+6b}$	Reference	Experimental Technique
2.90 ± 0.28	0.89	Harwood *et al.* (1998)[15]	FP/UV
3.4 ± 0.5		Gilles *et al.* (1997)[14]	FP/UV
2.8 ± 0.5		Laszlo *et al.* (1997)[13]	FP/UV
2.98 ± 0.42	0.84	Rowley *et al.* (1996)[12]	FP/UV
2.78 ± 0.25	0.85	Mauldin *et al.* (1993)[11]	FP/UV
3.1 ± 0.4		Bridier *et al.* (1993)[10]	FP/UV
3.2 ± 0.5	0.85	Lancar *et al.* (1991)[18]	DF/MS
2.49 ± 0.26	0.88	Turnipseed *et al.* (1990)[17]	DF/MS
2.17 ± 0.68	0.84	Sander and Watson (1981)[9]	FP/UV
3.2 ± 0.7		Clyne and Watson (1975)[16]	DF/MS

Table 5.1: Comparison of the literature data on the BrO self-reaction at 298 K.

5.2 Experimental

Two distinct chemical sources of BrO radicals were used to investigate the kinetic behaviour of the BrO self-reaction at 298 K. The first system employed the short wavelength ($\lambda < 200$ nm) photolysis of molecular oxygen ($[O_2] = 2.4 \times 10^{19}$ molecules cm^{-3}) and the subsequent reaction of oxygen atoms with molecular bromine ($[Br_2]$ = $(0.5\text{-}1) \times 10^{17}$ molecules cm^{-3}):

(5.7) $O_2 + h\nu \rightarrow 2O$

(5.8) $O + Br_2 \rightarrow BrO + Br$

The absence of any route to secondary BrO formation in this system ensured that analysis of kinetic BrO concentrations gave rise to $k_6 = k_{6a} + k_{6b}$.

The second chemical system utilised the longer wavelength ($\lambda \approx 400$ nm) photolysis of molecular bromine ($[Br_2] = (1\text{-}5) \times 10^{16}$ molecules cm^{-3}) in the presence of ozone ($[O_3] = (0.05 - 5) \times 10^{17}$ molecules cm^{-3}). In this system, long wavelength photolysis radiation was selected by encasing the flashlamp in a Pyrex jacket which absorbed flashlamp emission at wavelengths below 280 nm:

(5.9) $Br_2 + h\nu \rightarrow 2Br$

(5.5) $Br + O_3 \rightarrow BrO + O_2$

Ozone was produced upstream of the gas mixing line by flowing molecular oxygen through a commercial ozoniser (*Ozonia*). Where low ozone concentrations were required, upstream production was accomplished by flowing oxygen through a cell incorporating a mercury pen-ray lamp which effected O_2 photolysis *via* its 184.9 nm emission line:

(5.7) $O_2 + h\nu \rightarrow 2O$

(5.10) $O + O_2 + M \rightarrow O_3 + M$

Ozone production efficiency was periodically calibrated by fitting reference O_3 cross sections[22] in the Hartley band to non-flashed absorption spectra. Outputs from both the ozoniser and the Hg emission cell were found to be stable and highly reproducible. Ozone concentrations in the reaction cell were calculated from these known production efficiencies, along with calibrated gas flow rates.

Br_2 vapour was introduced to the reaction cell by bubbling nitrogen through an upstream bubbler of liquid bromine, as described in chapter 4.

Providing an excess of ozone was maintained during the course of experiments using the second chemical system, any bromine atoms produced by channel (6a) were rapidly reconverted back to BrO *via* reaction (5). As a result this channel was effectively masked and analysis of BrO temporal profiles provided sensitivity to the value of k_{6b} only. Therefore, coupling the kinetic data extracted from both chemical systems gave rise to k_{6b}, $(k_{6a}+k_{6b})$ and hence the branching ratio, $\alpha = k_{6a}/(k_{6a}+k_{6b})$.

Time resolved BrO absorption spectra were recorded at 298 K using the instrument settings detailed in table 5.2. Where necessary the signal to noise ratio was improved by the co-addition of up to 50 flashed experiments.

Source for UV absorption	Xe/D_2 lamps
Diffraction grating	300 grooves/mm
Entrance slit width	75 μm
Resolution (FWHM)	1.1 nm
Wavelength regime	290 - 355 nm
CCD clocking rate	50-100 μs/ spectrum

Table 5.2: Nominal instrument settings employed during kinetic BrO monitoring experiments.

Temporally resolved BrO concentration profiles were generated by differentially fitting the structured absorption spectra with the BrO cross sections recently measured

by Wilmouth *et al.*[23] The 298 K spectrum obtained from these authors was convolved to the experimental instrumental resolution employed in this work by applying a sliding average routine which incorporated a Gaussian kernel matching the experimental instrument function (see appendix 1). Figure 5.2 shows this convolved BrO cross section in conjunction with those of any other transient absorbers within the monitored wavelength regime. Wilmouth *et al.* discuss discrepancies in the absolute wavelength calibration of recently reported BrO absorption spectra. However, any miscalibration associated with the cross sections would exert no effect on the quality of the fitting employed here since software routines were used to shift the spectra by small increments (typically < 0.2 nm) in the wavelength axis, in order to maximise the overlap of experimental and reference spectra and optimise the fit quality.

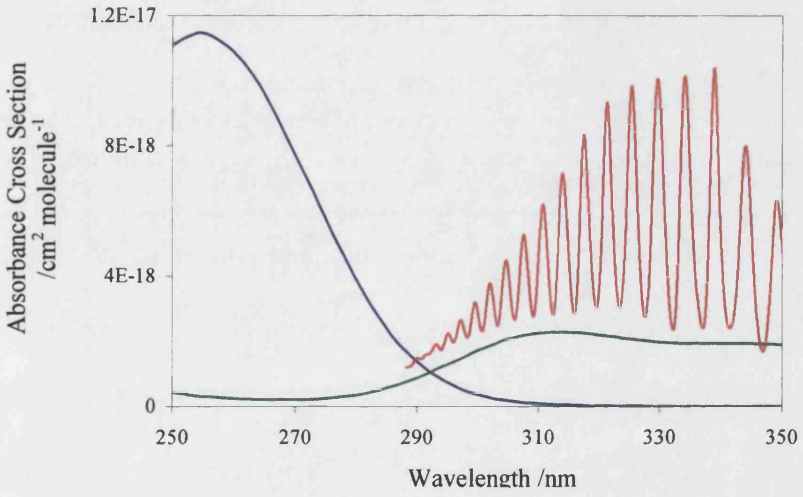

Figure 5.2: Absorption cross sections of O_3 (blue, DeMore et al.[22]), BrO (red, Wilmouth et al.[23]), Br_2O (green, Orlando et al.[24])

5.3 Results

5.3.1 System 1: $O + Br_2 \rightarrow BrO + Br$

BrO concentration versus time traces were recorded under conditions where pre-flash $[Br_2]$ was varied within an O_2 carrier flow. The resulting high $[O_2]$ ensured that a significant number of O atoms were liberated upon flashing, typically of the order of 10^{13} molecules cm^{-3}. In all cases the BrO radicals were generated promptly and the BrO decays were well described by a second order kinetic scheme whose timescale was effectively decoupled from that of the BrO formation chemistry.

(5.i) $$-\frac{d[BrO]}{dt} = 2k_{6a+6b}[BrO]^2$$

Integrating this differential equation generates a linear solution:

(5.ii) $$\frac{1}{[BrO]_t} = \frac{1}{[BrO]_0} + 2k_{6a+6b}t$$

Thus a plot of $1/[BrO]_t$ versus t gave rise to a gradient of $2k_{6a+6b}$. A typical BrO decay trace with its associated reciprocal plot is shown in figure 5.3.

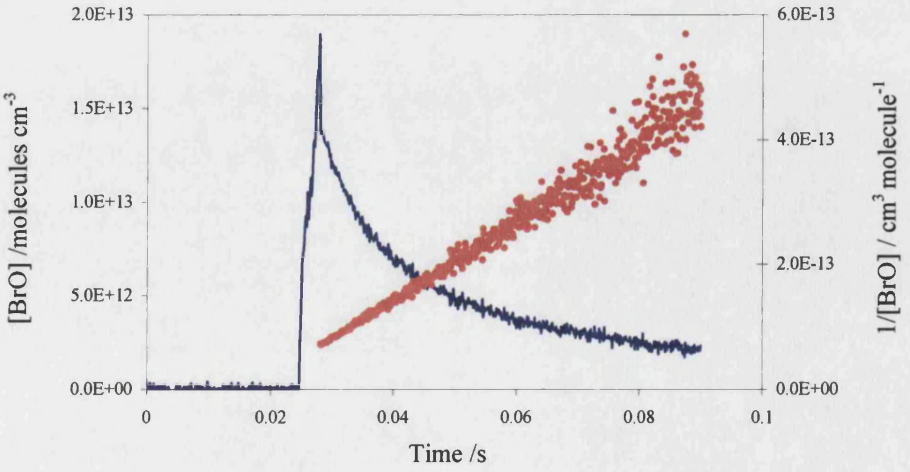

Figure 5.3: Typical experimental BrO build up and decay trace (blue) with associated reciprocal plot (red) from the O + Br_2 chemical system..

However, taking the reciprocal of the concentration data magnifies the noise in an asymmetric manner which becomes increasingly significant at long times where $[BrO]_t$ tends toward zero. As a result the apparent gradient of the reciprocal plot is enhanced as a function of time. Whilst more co-added traces improved the signal to noise ratio, it was not possible to improve the signal to noise ratio by working under higher $[BrO]_0$ conditions since $[O_2]$ was already at its limit as the carrier gas. Thus, to minimise the systematic error associated with the gradient of the asymmetric reciprocal plots, the gradient was measured as a function of the number of time points (CCD rows) included in the linear regression since the flashlamp fired at t_0. Figure 5.4 shows a typical plot of the $k_{obs} = k_{6a+6b}$ obtained from these data. The figure shows a small but consistent increase in the k_6 evaluation as successive time resolved data are included in the gradient evaluation routine. Hence the value of k_{6a+6b} was back extrapolated to t_0 in order to determine its true value in the absence of asymmetric noise resulting from the reciprocal plot.

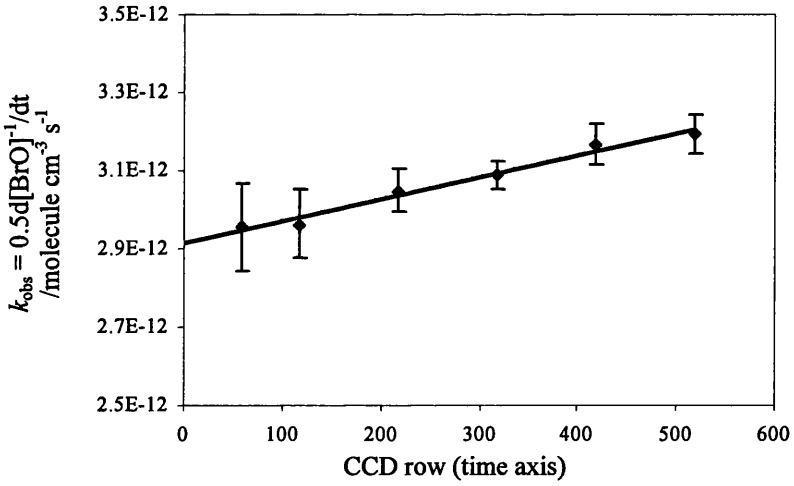

Figure 5.4: k_{6a+6b} back-extrapolation from the time dependent gradient of a typical reciprocal plot of the $[BrO]_t$ data.

As a result of 11 determinations at 298 K, $k_{6a+6b} = (2.92 \pm 0.14) \times 10^{-12}$ cm^3 molecule^{-1} s^{-1} where the quoted errors represent precision only at the 95% confidence limit. However since the BrO cross section used in the analysis exerts a linear dependence on the evaluated rate constant, an additional 11% uncertainty as quoted by Wilmouth *et al* lends a systematic influence to the uncertainty in k_{6a+6b}.

5.3.2 System 2: $Br + O_3 \rightarrow BrO + O_2$

Flashed experiments monitoring the time evolution of the BrO radical were carried out over a range of precursor gas concentrations ($[Br_2] = (0.7\text{-}2) \times 10^{16}$ molecules cm^{-3} and $[O_3] = (0.003\text{-}2) \times 10^{17}$ molecules cm^{-3}). Evaluation of k_{obs} from reciprocal plots of the $[BrO]_t$ data obtained over the extent of these precursor ranges revealed a dependence of this quantity on $[O_3]/[BrO]_0$ as illustrated by figure 5.5. A broad plateau exists under moderate conditions ($100 < [O_3]/[BrO]_0 < 300$) where this ratio exerts no significant effect on the extracted k_{obs} values. However this plateau is straddled at both extremes by enhancement in the rate of BrO loss, particularly at low $[O_3]/[BrO]_0$ ratios. These enhancements in k_{obs} were accompanied by deviations from second order loss and the BrO kinetics under three regimes of $[O_3]/[BrO]_0$ are discussed in turn below.

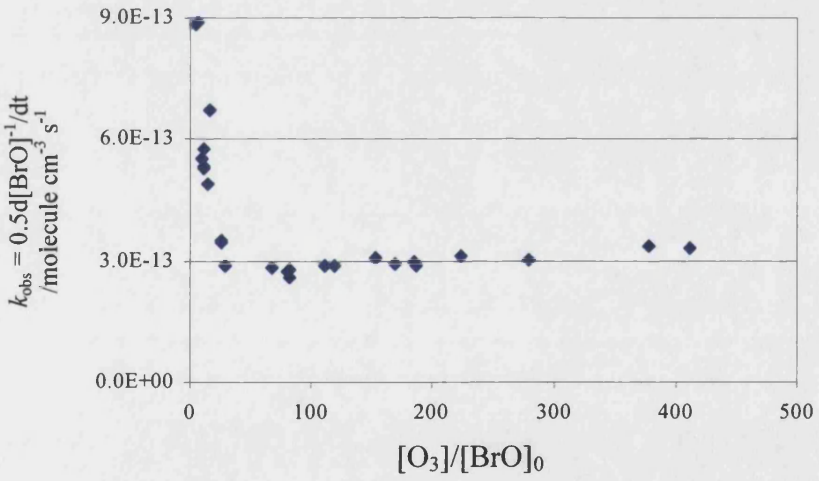

Figure 5.5: k_{obs} obtained from classical second order analysis, plotted as a function of preflash $[O_3]/[BrO]_0$.

5.3.2.1 Moderate $[O_3]/[BrO]_0$ conditions: $100 < [O_3]/[BrO]_0 < 300$

Over the intermediate range of precursor conditions employed, all $[BrO]_t$ traces produced well constrained, linear reciprocal plots such as that shown in figure 5.6. As a result k_{obs} was once again determined from the gradient of these plots according to

the classical solution to a second order decay scheme. As with the O_2/Br_2 system the asymmetric noise generation associated with the reciprocal plots grew increasingly significant at longer times, leading to a positive bias in the gradient. Hence, as above, the time dependent gradient was to back-extrapolated to t_0 in order to remove this artefact from the determination of k_{6b}.

16 determinations of k_{6b} in this manner gave rise to $k_{6b} = (3.01 \pm 0.17) \times 10^{-13}$ $cm^3 molecule^{-1} s^{-1}$. Once again, the error bars reflect precision at the 95% level and the BrO cross sections[23] exert a further influence of ± 11% uncertainty on the rate coefficient. In conjunction with the value of k_{6a+6b} determined above, this leads to a branching ratio for the non-terminating channel, $\alpha = 0.90 \pm 0.03$.

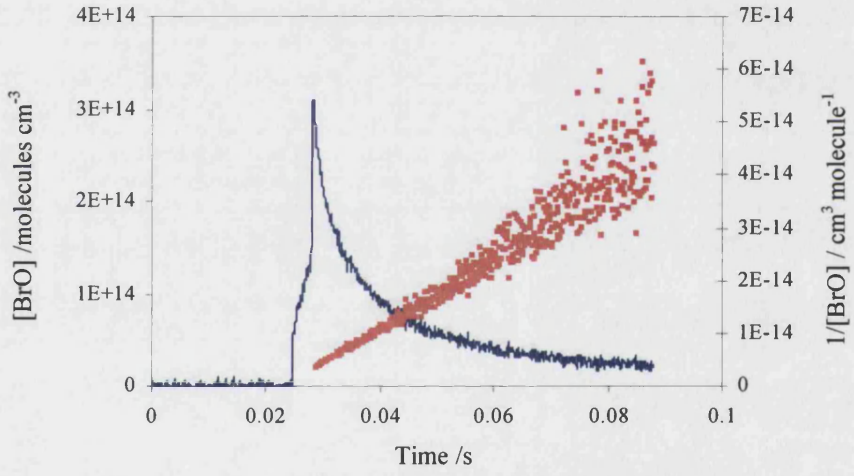

Figure 5.6: Typical experimental BrO build up and decay (blue) with associated reciprocal plot (red) under moderate $[O_3]/[BrO]$ conditions.

5.3.2.2 High $[O_3]/[BrO]_0$ conditions: $[O_3]/[BrO]_0 > 300$: Observation of OBrO

Preliminary experiments employing the Br_2/O_3 system at high $[O_3]$ revealed the presence of a transient absorber in the spectral region 400 to 600 nm. The absorbance exhibited strong coarse spectral structure and was attributed to OBrO. A comparison between the observed post- relative to pre-flash spectrum and the OBrO cross sections recently reported by Knight *et al.*[25] is given in figure 5.7.

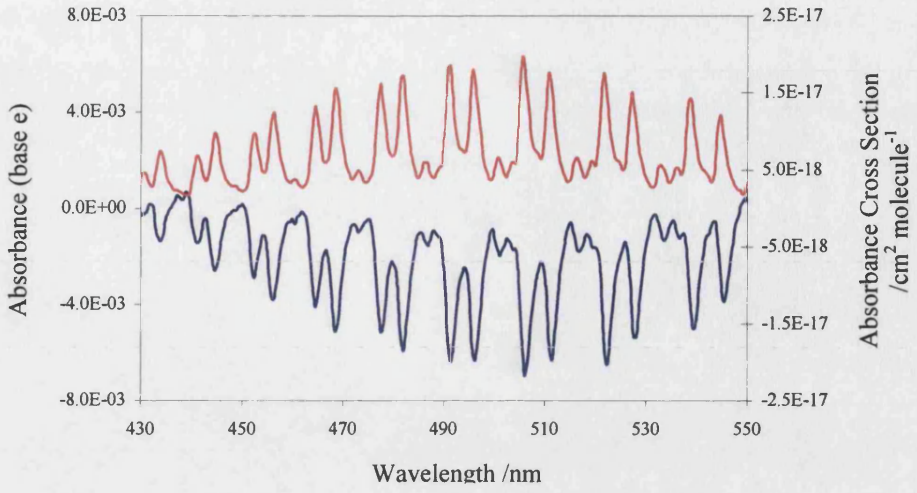

Figure 5.7: Typical postflash absorption spectrum (blue) compared to the OBrO cross section reported by Knight et al. (red).

What is most interesting about the postflash spectrum is that it is negative, indicating that OBrO has been *consumed* upon flashing. Naturally this observation demonstrates that some OBrO was present in the pre-flash period, although the only gaseous components flowed into the reaction cell were Br_2, O_3, O_2 and N_2. The post-flash evolution of OBrO (relative to pre-flash) was monitored by differential fitting of the OBrO cross section reported by Knight *et al.* to time resolved absorption spectra recorded by the CCD. The fit quality was generally excellent and a typical example of the observed $[OBrO]_t$ behaviour is shown in figure 5.8. The reference OBrO cross section measured by Knight *et al.* was recorded at a spectral resolution of 1.28 nm (FWHM). In this investigation the width of the entrance slit to the spectrograph was selected to match this resolution, precluding the need to convolve the OBrO cross sections.

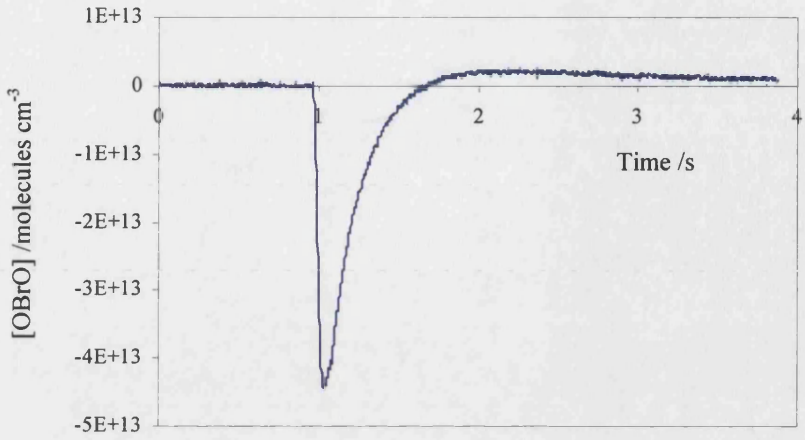

Figure 5.8: OBrO consumption and subsequent regeneration following flash photolysis of $Br_2/O_3/O_2/N_2$ mixtures.

Clearly OBrO removal occurs immediately upon flashing. This may arise directly from OBrO photolysis or reaction with Br or O atoms produced by the flashlamp photolysis of Br_2 and O_3 respectively. OBrO then grows back on long timescales and interestingly reaches a positive value after approximately 0.7 s, indicating that postflash [OBrO] eventually exceeds preflash [OBrO]. This suggests that the flashlamp initiates some chemistry which produces OBrO in addition to that produced under *dark* (non-flashed) conditions. At very long timescales (> 1 s post flash) the $[OBrO]_t$ decays in a linear fashion, suggesting that zeroth order flow out of the reaction vessel dominates the transient OBrO behaviour as the gaseous mixture returns toward preflash [OBrO].

Rowley *et al.*[12] observed similar OBrO evolution observed in back to back experiments monitoring OBrO and BrO respectively. This was attributed to the slow reaction of BrO with excess O_3 at long timescales, where [BrO] was small and competition of the BrO + O_3 reaction with the BrO self-reaction was most effective.

Given the observed rate of OBrO regeneration following its removal upon photolysis, these results indicate that OBrO is unlikely to be a direct product of the BrO self-reaction, and the BrO + O_3 reaction is the likely source of OBrO. Several possible

sources exist for the BrO precursor to preflash OBrO . Firstly, source lamp (Xe) photolysis of Br_2, and subsequent reaction of liberated Br atoms with O_3 could lead to OBrO production *via* reactions (9), (5) and (11).

(5.9) $Br_2 + h\nu \rightarrow 2\,Br$

(5.5) $2\,(Br + O_3 \rightarrow BrO + O_2)$

(5.11) $2\,(BrO + O_3 \rightarrow OBrO + O_2)$

Alternatively a similar route to OBrO *via* source lamp photolysis of O_3 could exist:

(5.12) $O_3 + h\nu \rightarrow O + O2$

(5.8) $O + Br_2 \rightarrow BrO + Br$

(5.5) $Br + O_3 \rightarrow BrO + O_2$

(5.11) $2\,(BrO + O_3 \rightarrow OBrO + O_2)$

Another possibility is that thermal decomposition of either Br_2 or O_3 could initiate OBrO production *via* channels similar to those described above. Indeed spontaneous explosion of bromine/ozone mixtures incorporating high O_3 concentrations is well established.[26]

In order to investigate the source of BrO and hence OBrO, non-flashed OBrO concentrations (hereafter $[OBrO]_{dark}$)were recorded as functions of both $[Br_2]$ and $[O_3]$ with the xenon lamp as the analytical source. The system was left flowing for 2 hours before any spectral data was recorded for reasons which are described below. OBrO concentrations were evaluated by applying Beer's law to the non-flashed Br_2/O_3 mixtures relative to data recorded with an intracellular presence of N_2 only. Once again differential routines were used to fit the reference OBrO cross section to the non-flashed absorbance spectra, eliminating spurious contributions from underlying spectrally smooth absorbers such as Br_2.

Figure 5.9 shows no significant systematic dependence of non-flashed $[OBrO]_{dark}$ on $[Br_2]$. Instinctively this tends to suggest that Br_2 is not primarily responsible for non-

flashed OBrO production through photo- or thermally- induced channels. However it cannot be ruled out entirely since any increase in $[OBrO]_{dark}$ arising from increased $[BrO]_{dark}$ could be mitigated by an increase in the rate of BrO loss *via* self-reaction (which is proportional to $2[BrO]^2$) over the rate of the BrO + O_3 reaction.

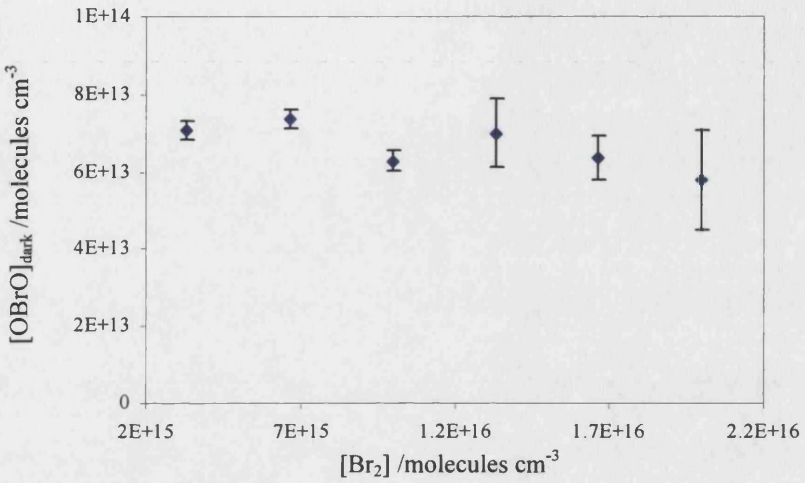

Figure 5.9: $[OBrO]_{dark}$ measured as a function of $[Br_2]$. $[O_3]$ held constant at 3 × 10^{17} molecules cm^{-3}.

By contrast, it is clear from figure 5.10 that observed $[OBrO]_{dark}$ correlates with $[O_3]$. This strongly suggests that O_3 is the source of the observed OBrO. However, once again it should be noted that this could be a manifestation of increasingly successful competition of the BrO + O_3 reaction with the BrO loss through self-reaction. However, this seems unlikely since the dependence is linear to a first approximation and a more complex relationship would be expected if there were any significant competition from the quadratic term:

$$\text{(5.iii)} \qquad \frac{-d[BrO]}{dt} = 2k_{6a}[BrO]^2 + k_{11}[BrO][O_3]$$

However this competition between the two BrO loss processes could qualitatively account for the non-zero intercept observed in figure 5.10.

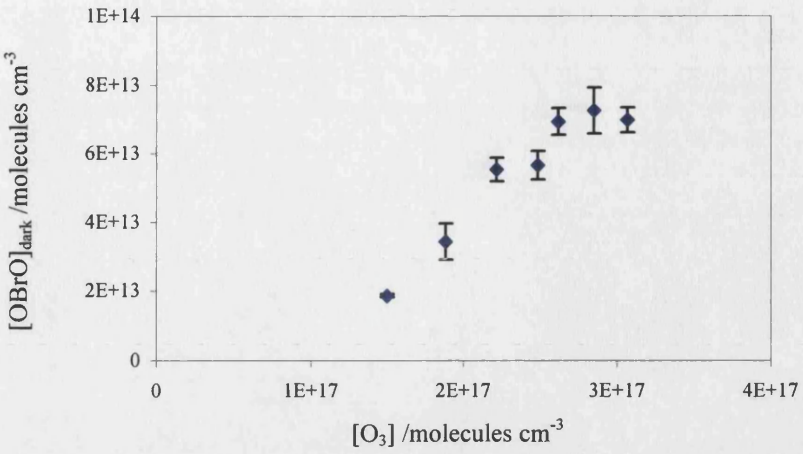

Figure 5.10: $[OBrO]_{dark}$ measured as a function of $[O_3]$. $[Br_2]$ held constant at 1 × 10^{16} molecules cm^{-3}.

In addition to this complex, uninitiated chemistry it was observed that $[OBrO]_{dark}$ exhibited a time dependence over a period of approximately two hours. No known gas phase chemistry could account for this, so prior to investigation the reaction cell was heated to 350 K and flushed out with N_2 for 16 hours to attempt to remove any gaseous or adsorbed OBrO from the cell. Following this period, the cell was returned to a thermostatted temperature of 298 K and a spectrum was recorded in the presence of N_2 only. Flows of Br_2, O_3 (and residual O_2) in an N_2 carrier were subsequently introduced and OBrO spectra recorded every few minutes. The resulting time resolved $[OBrO]_{dark}$ data and a first order fit are shown in figure 5.11.

The observed trend in $[OBrO]_{dark}$ suggests wall effects are responsible for this long timescale phenomenon. It is possible that a heterogeneous equilibrium is established between gaseous and adsorbed OBrO on the internal walls of the reaction cell:

(5.13) OBrO (g) ↔ OBrO (ads)

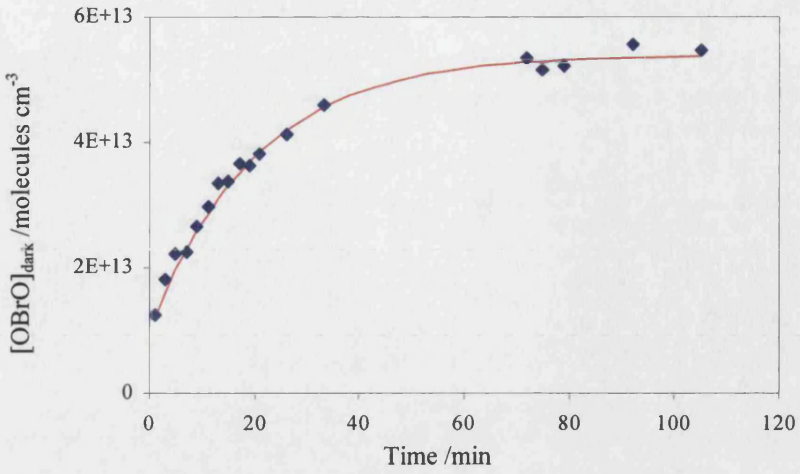

Figure 5.11: $[OBrO]_{dark}$ measured as a function of time following introduction of $O_3/O_2/Br_2$ into the N_2 flow.

The [OBrO] data were well described by a first order rate scheme, where least squares fitting yielded a rate coefficient $k_{13} = 8.3 \times 10^{-4}$ s^{-1}. Such a first order scheme would be consistent with a Langmuir adsorption isotherm. Alternatively, it may be that the reaction cell walls are progressively passivated over the course of two hours, and that OBrO does not readily desorb in a manner consistent with the isotherm. However, attempts to repeat this experiment observed similar qualitative behaviour on a comparable timescale but the absolute magnitude of the limiting $[OBrO]_{dark}$ at the plateau tended to vary. This non-reproducibility of this data prevented any further investigation into the nature of this heterogeneous phenomenon. Similarly non-reproducible heterogeneous behaviour of OBrO was reported by Rattigan *et al.* in the original paper detailing the first observation of the OBrO absorption spectrum.[27] These authors found that OBrO could be observed in a reaction cell previously exposed to Br_2/ O_3 mixtures flushed with pure nitrogen.

On account of the non-reproducible behaviour of OBrO, further attempts to investigate the source of the dark BrO and hence OBrO were not carried out. In principle photo- and thermally induced O_3 and Br_2 decomposition could have been investigated by filtering the radiation from the xenon source lamp. Inclusion of a Pyrex filter (cut off at approximately $\lambda < 300$ nm) could distinguish between Br_2 and O_3 photolysis. This would cut off absorption at the Hartley band of ozone, which

photodecomposition but would leave any Br_2 photolysis, which occurs at longer wavelengths, unaffected. Similarly, reducing the intracellular irradiation with a series of neutral density filters could distinguish between thermal and photo-effects generally. In fact these experiments were undertaken but subsequent discovery of the heterogeneous effect and the associated non-reproducibility negated the reliability of these data and they are not presented in this thesis. On the evidence presented here it is not possible to unequivocally assign initiation of the OBrO producing chemistry to any particular source. However in an attempt to minimise these effects, subsequent experiments at the ozone concentrations where dark OBrO has been observed have employed a deuterium lamp as an analytical source, which is less intense and narrower in output wavelength range than its xenon counterpart.

In addition to the observation of OBrO, at very high ozone concentrations - in excess of 1×10^{17} molecules cm^{-3} - small but consistent positive curvature from linearity was observed in the $1/[BrO]_t$ plots as shown in figure 5.12. This effect was most strongly manifested at long timescales where [BrO] reached its smallest values. Moreover, the effect was significantly more pronounced than the apparent curvature imparted to the $1/[BrO]_t$ traces by the asymmetric noise of the reciprocal plot. The degree of non linearity of the reciprocal plot was also increased at the highest ozone concentrations. This was attributed to the reaction between BrO and O_3 under conditions where it could effectively compete with the BrO self-reaction. It was not possible to monitor the $[OBrO]_t$ kinetics in these experiments due to the long wave cut off associated with the deuterium analysis lamp ($\lambda_{cut} \approx 360$ nm). In any case even with the deuterium lamp replacing the xenon lamp, the anticipated $[OBrO]_t$ kinetics may have been distorted by heterogeneous chemistry arising from pre-existent OBrO as described above.

The numerical integration and fitting package FACSIMILE[28] was used to study the temporal behaviour of BrO under conditions of elevated $[O_3]$. The reaction scheme is given in table 5.3 and routines to simulate flow out and the inherent temporal averaging associated with the CCD were included in the model. Rate coefficients k_{6b} and k_{11} were allowed to vary in optimising the model fit to the experimental BrO temporal traces. In all cases the fit quality was excellent - an example is given in figure

5.12. A sensitivity study was also carried out which showed that the returned values of k_{6b} and k_{11} were unaffected by changes in other rate coefficients used in the model. (This was an unsurprising result as, under conditions of very high $[O_3]$, the exclusive fate of Br atoms is reaction with O_3 and channel (6a) of the BrO self-reaction does not affect the BrO decay).

Reaction	k at 298 K	Source
$Br + O_3 \rightarrow BrO + O_2$	$k_5 = (1.16 \pm 0.23) \times 10^{-12}$	DeMore *et al.*[22]
$BrO + BrO \rightarrow 2Br + O_2$	$k_{6a} = (2.92 \pm 0.14) \times 10^{-12}$	This work
$BrO + BrO \rightarrow Br_2 + O_2$	$k_{6b} = (3.01 \pm 0.17) \times 10^{-13}$	Optimised
$BrO + O_3 \rightarrow OBrO + O_2$	$k_{11} = (4.8 \pm 0.6) \times 10^{-17}$	Optimised
$Br + Br + M \rightarrow Br_2 + M$	$k_{17} = (2.07 \pm 0.17) \times 10^{-13}$	Baulch *et al.*[29]

Table 5.3: Chemical reactions coded into the FACSIMILE model used to fit the $[BrO]_t$ data where $[O_3]/[BrO]_0 > 300$,. All units are $cm^3 molecule^{-1} s^{-1}$, where the termolecular Br association rate coefficient is reported at 760 Torr.

It has been suggested that a Br_2O_3 adduct may form in the mutual presence of BrO and OBrO by analogy to observed Cl_2O_3 chemistry[12].

(5.14) $\quad BrO + OBrO + M \quad \leftrightarrow \quad Br_2O_3 + M$

However, high quality fits were obtained without having to incorporate this process into the model and its inclusion was rejected. Fitting 8 individual data sets gave rise to $k_{6b} = (3.12 \pm 0.13) \times 10^{-13}$ cm^3 molecule^{-1} s^{-1} and $k_{11} = (4.8 \pm 0.6) \times 10^{-17}$ cm^3 molecule^{-1} s^{-1}, where error bars reflect precision at the 95% limits. The value of k_{6b} obtained under these conditions was not factored into the recommended value for k_{6b} from this study, since a small degree of correlation was observed between k_{6b} and k_{11} when simultaneously fitted in this manner. Nevertheless the value of k_{6b} is in good agreement with that obtained under moderate $[O_3]/[BrO]_0$ conditions, thereby emphasising confidence in the fitted value of k_{11}.

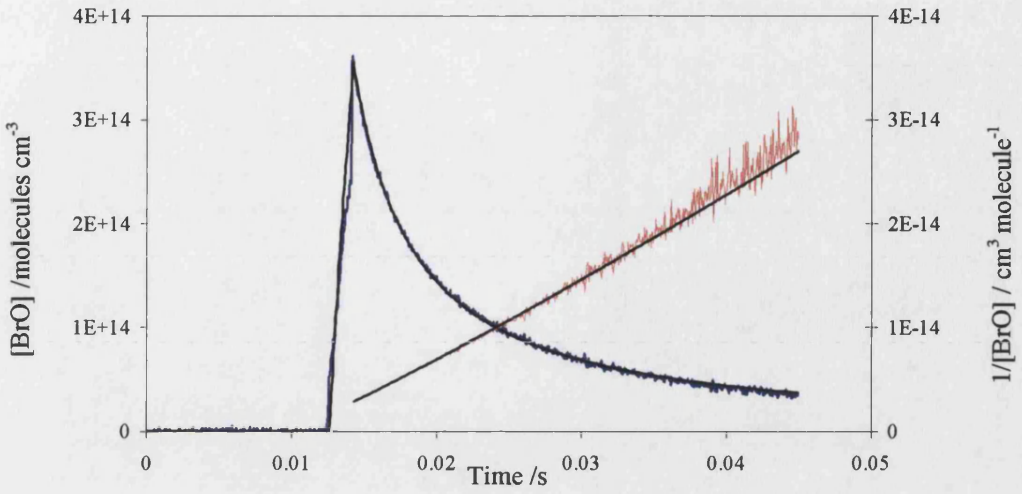

Figure 5.12: Typical experimental $[BrO]_t$ trace (blue) and reciprocal plot (red) recorded under high $[O_3]/[BrO]$ conditions. The optimised FACSIMILE model is indicated in black. The weak positive curvature on the reciprocal plot is accounted for by inclusion of reaction (11).

5.3.2.3 Low $[O_3]/[BrO]_0$ conditions: $[O_3]_0/[BrO]_0 < 100$

Under conditions of low (but still excess) ozone concentrations, different distortions in the BrO temporal behaviour were observed. Figure 5.13 illustrates a typical $[BrO]_t$ decay and associated reciprocal plot recorded under these precursor gas conditions. At long timescales the second order plots were essentially linear and evaluating the gradient yielded a value of k_{obs} which is consistent with the $k_{6b} = (3.01 \pm 0.17) \times 10^{-13}$ cm^3 $molecule^{-1}$ s^{-1} obtained at moderate $[O_3]/[BrO]_0$ ratios. However, the initial BrO reciprocal plot exhibited curvature and a gradient which was markedly higher than that at later times, gradually reducing toward slower, second order behaviour.

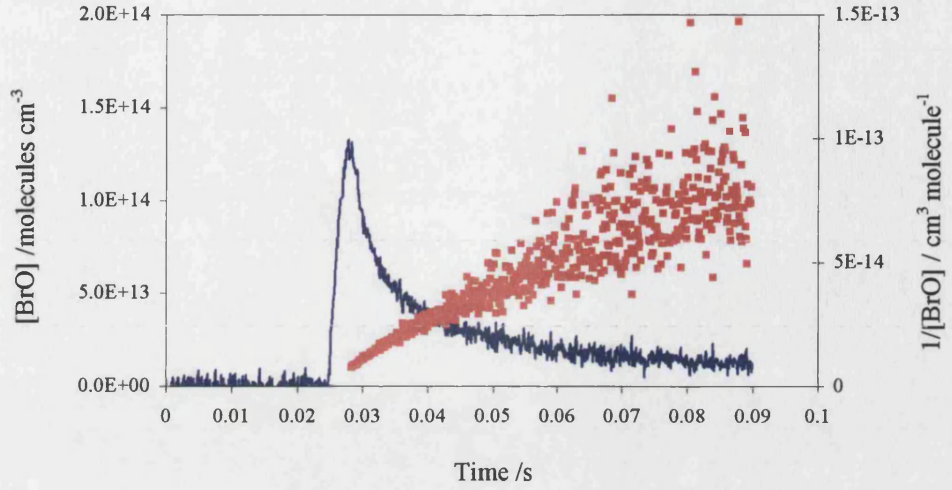

Figure 5.13: Typical experimental BrO build up and decay (blue) with associated reciprocal plot (red) under low $[O_3]/[BrO]$ conditions.

This behaviour was attributed to the formation and subsequent chemistry of Br_2O by analogy to its chlorine counterpart[10]:

(5.15) $Br + BrO + M \rightarrow Br_2O + M$

(5.16) $Br + Br_2O \rightarrow Br_2 + BrO$

net: $Br + Br + M \rightarrow Br_2 + M$

At low excess ozone concentrations, where $[O_3]/[BrO] < 100$, BrO competes effectively with O_3 in reacting with Br atoms (15). Moreover, subsequent reaction of Br_2O with further Br atoms (16) also competes with (5) and (15), since this reaction is extremely fast ($k_{16,298K} = 2 \times 10^{-10}$ cm^3 molecule^{-1} s^{-1}).[30] The net effect of (15) and (16), potentially in conjunction with (17) is to reduce the number of Br atoms from channel (6a) available for reconversion to BrO.

(5.17) $Br + Br + M \rightarrow Br_2 + M$

This loss of Br atoms effectively introduced a small contribution to the BrO decay from reaction (6a) despite the presence of ozone; accounting for the increase in the phenomenological rate coefficient. This deviation from BrO decay along reaction channel (6b) alone was most significant at the start of the BrO decay. This is

unsurprising, since flux through reactions (15) and (16) is most significant where [BrO] is high enough to compete with ozone for reaction with Br atoms and ensure some formation of Br_2O. At longer timescales [BrO] reduces and reaction (15) cannot compete with (5), thus the kinetics revert toward a second order scheme.

It is interesting to note that processes (15) and (16) would have been occuring readily in the O_2 photolysis system. However, the measurement of k_{6a+6b} was unaffected by this chemistry since these channels provided no net change in BrO concentration under these ozone free conditions, where there was no independent sensitivity to k_{6b}.

There is a paucity of kinetic data describing reactions (15) and (16) in the open literature. Only one quantitative investigation of $k_{15,298K}$ exists at 760 Torr,[12] which reports this parameter in the range (2-4) $\times$ 10^{-12} cm^3 $molecule^{-1}$ s^{-1}. Similarly only one study of reaction (16) is available in the open literature by Burkholder[30], who reported $k_{16,298K} = (2 \pm 0.5) \times 10^{-10}$ cm^3 $molecule^{-1}$ s^{-1}. Moreover, this determination of k_{16} incorporates the average of the range of k_{15} values measured by Rowley *et al.*[12] in a complex numerical analysis. Indeed the author asserts that if k_{15} were any faster than that reported by Rowley *et al.*, then the reported value of k_{16} would be overestimated. In response to these weaknesses in the current database, attempts were made to constrain the kinetic parameters which describe Br_2O chemistry.

Numerical integration of the reaction scheme given in table 5.3 was used to simulate and fit to BrO temporal profiles recorded under low excess ozone concentration. Whilst excellent fitting to the BrO temporal profiles could be achieved by allowing k_{15} to vary, a sensitivity study showed that the value of k_{15} returned was strongly affected by the precise values for the other kinetic parameters employed in the model. Thus k_{15} was not independently determined by the BrO traces alone, and further constraint of the model was sought.

A particular advantage of the CCD monitoring is the recording of a wide spectral window of UV absorption as a function of time. Since ozone is a strong absorber of UV/ visible radiation, simultaneous monitoring of O_3 and BrO was attempted. This

was made possible in these experiments due to the relatively low ozone concentrations. This had not been possible at higher ozone concentrations (where $[O_3] > 1 \times 10^{16}$ molecules cm^{-3}) since the strong absorption cross section at the Hartley band ensured the gaseous mixture became optically thick at these wavelengths, precluding $[O_3]_t$ monitoring on signal to noise grounds.

Differential routines were used to determine $[BrO]_t$ and remove the contribution of BrO, A_{BrO}, from the post flash absorption spectra. This subtraction left a residual absorption potentially consisting of A_{O3} (negative, due to ozone consumption) and A_{Br2O} (positive). Numerical modelling incorporating NASA recommended data in conjunction with the k_{15} and k_{16} values reported by Rowley *et al.*[12] and Burkholder[30] respectively, indicated that under the conditions employed, $[Br_2O]_t$ would never exceed 2×10^{12} molecules cm^{-3}. At these concentrations, given the low absorption cross sections of Br_2O, the absorbance due to Br_2O was well below the detection limits, hence its contribution to the residual absorption was negligible. Furthermore, $[O_3]_t$ was quantified by fitting a reference O_3 cross section[22] to the Hartley band at wavelengths below 280 nm only, where σ_{O3} becomes overwhelmingly large compared to other absorbers. Thus the wavelength region 260-325 nm was imaged onto the CCD and the simultaneous evolution of BrO and O_3 could be monitored unequivocally . Figure 5.14 shows a typical fit of the reference ozone cross section to the experimental absorbance data having subtracted the BrO contribution. The fit quality is high and the residual following the removal of this ozone absorption (and the BrO absorption) is negligible. This provides strong confirming evidence that no significant Br_2O build up occurred during these experiments and Br_2O decay *via* (16) was rapid enough to be effectively decoupled from its production through (15).

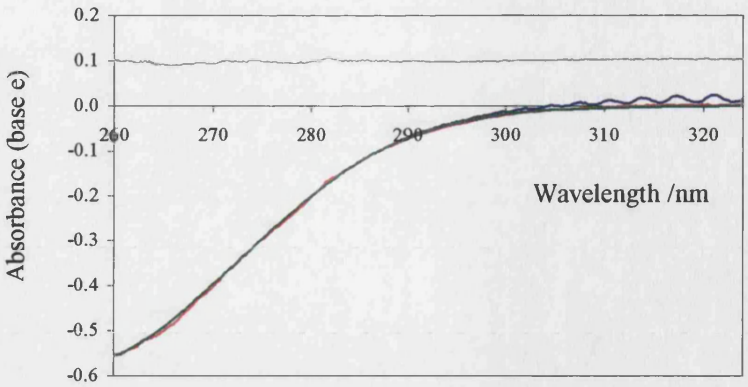

Figure 5.14: Early time-averaged postflash absorption spectrum (blue). Also shown is the residual following A_{BrO} subtraction (red), the fitted O_3 absorption (green) and the residual following subtraction of both absorbers (grey, offset by +0.1 for clarity).

Once again a sensitivity study was undertaken to assess the ability to constrain the value of k_{16} by simultaneously fitting to the $[BrO]_t$ and $\Delta[O_3]_t$ data. This study revealed no sensitivity to k_{16} until its value in the model was increased by a factor of 5 over that reported by Burkholder[30], whose error bars are significantly smaller at 25%. Whilst this precluded the extraction of any kinetic data describing (16), it effectively decoupled the kinetics of reaction (16) from those of (15), simplifying the attempts to measure k_{15}. Similarly the sensitivity of the optimised k_{15} value on the secondary chemistry was systematically investigated. An experimental $[BrO]_t$ and $\Delta[O_3]_t$ data set was fitted with numerically modelled traces by incorporating the literature data indicated in table 5.4, whilst allowing k_{15} and the fraction of Br_2 photolysed (effectively defining $[Br]_0$) to vary. Both data sets were well fitted by the experimental data, as shown in figure 5.17.

Reaction	k at 298 K	Source
$BrO + BrO \rightarrow 2Br + O_2$	$k_{6a} = (2.92 \pm 0.14) \times 10^{-12}$	This work
$BrO + BrO \rightarrow Br_2 + O_2$	$k_{6b} = (3.01 \pm 0.17) \times 10^{-13}$	This work
$Br + Br + M \rightarrow Br_2 + M$	$k_{17} = (2.07 \pm 0.17) \times 10^{-13}$	Baulch *et al.*[29]
$Br + O_3 \rightarrow BrO + O_2$	$k_5 = (1.16 \pm 0.23) \times 10^{-12}$	DeMore *et al.*[22]
$Br + Br_2O \rightarrow BrO + Br_2$	$k_{16} = (2 \pm 0.5) \times 10^{-10}$	Burkholder[30]
$BrO + O_3 \rightarrow OBrO + O_2$	$k_{14} = (4.8 \pm 0.6) \times 10^{-17}$	This work

Table 4: Secondary rate coefficients which were systematically varied during sensitivity study undertaken to assess the validity of fitted k_{15} values.

The secondary rate constants in the model were then varied, in turn by a factors of 0.5 and 2. Each time the data were reanalysed by allowing the model to refit the data, by varying k_{15} and the fractional photolysis of Br_2. In this way the fitted values of k_{15} under each set of conditions provided an indication of the sensitivity of this fitted parameter to each of the secondary rate coefficients independently. The results of this sensitivity analysis are presented in figure 5.15.

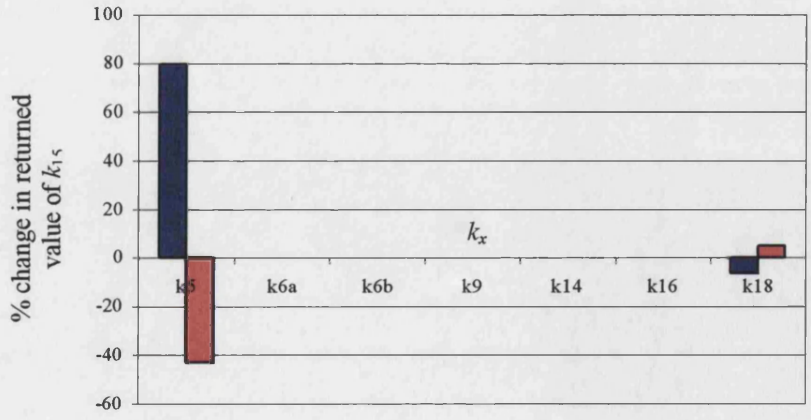

Figure 5.15: Percentage change in the returned values of k_{15} following manipulation of a given secondary rate coefficient k_x. The blue bars represent the % change when $2k_x$ was applied to the model, and the red where $k_x/2$ was applied. Where no bar is displayed, the sensitivity was either negligible or no satisfactory fit to the data was attainable (see below).

As anticipated there is no sensitivity of k_{15} to either k_{14} (which exerts no influence on either $[BrO]_t$ or $\Delta[O_3]_t$ at low preflash ozone concentrations) or k_{16}. Moreover, whilst the values of both k_{6a} and k_{6b} exert a profound influence on the shapes and magnitudes of the modelled $[BrO]_t$ or $\Delta[O_3]_t$ traces, no satisfactory fit to both data sets simultaneously could be identified with perturbed values of the rate coefficients. This demonstrated the advantage of fitting to both $\Delta[O_3]_t$ and $[BrO]_t$ data, over the fit to $[BrO]_t$ alone, where multiple combinations of k_{15}, k_{6a} and k_{6b} would readily optimise to fit the single data set. Indeed figure 5.16 shows how the sensitivity to k_{15} is enhanced by the ability to simultaneously monitor $[BrO]_t$ and $\Delta[O_3]_t$.

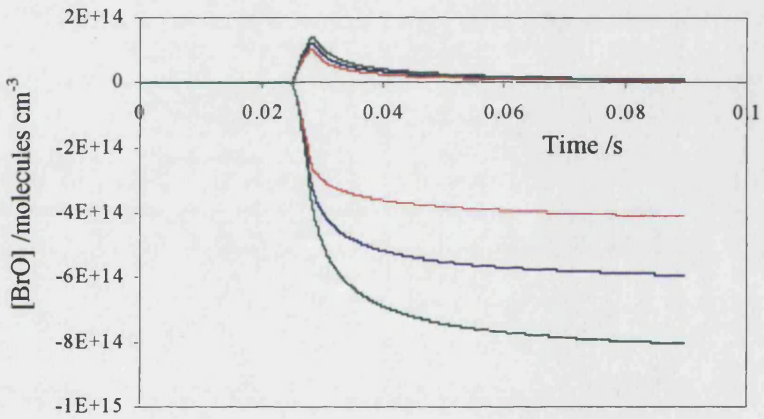

Figure 5.16: Modelled $[BrO]_t$ and $\Delta[O_3]_t$ using the kinetic data given in table 5.3 (blue). Red and green show modelled traces where k_{15} has been halved and doubled respectively.

The sensitivity analysis summarised in figure 5.15 exposes a considerable sensitivity of k_{15} to the value of k_5 (for the Br + O_3 reaction) and to a lesser extent, k_{17}. (for the Br + Br reaction). However, the impact of these parameters on any uncertainties associated with fitted k_{15} values would only become significant if these secondary rate coefficients were poorly characterised. The (Br + O_3) rate coefficient is well known at 298 K with all five of the most recent determinations in very good agreement[22]. The uncertainty associated with the 298 K value of k_5 is ±20%. Incorporation of these error bars into

the numerical model leads to an uncertainty of ±16% on the optimised value of k_{15}. Similarly the error associated with k_{17} is just 8%, which would exert no significant influence on the fitted k_{15} values, given the weak sensitivity to this parameter as indicated in figure 5.15 at the +100% and –50% limits.

The O_3 concentration present in the reaction cell influenced the fate of Br atoms in the same manner as k_5, since Br atom loss *via* reaction 5 is given by (iv).

$$\text{(5.iv)} \qquad \frac{-d[Br]}{dt} = k_5[Br][O_3]$$

O_3 was produced by the O_2 photolysis (Hg lamp) cell and the yields of ozone were found to be highly reproducible. Consequently the error associated with this quantification was small and exerted a negligible influence on k_{15}.

k_{15} was therefore unequivocally evaluated at 298 K by simultaneously fitting the $[BrO]_t$ and $\Delta[O_3]_t$ data by varying k_{15} and the fractional Br_2 photolysis. All secondary rate coefficients were held at the values detailed in table 5.4. Numerical fits to data sets from 6 separate experiments (each consisting of 20 co-added experiments) at three different $[O_3]/[BrO]_0$ ratios (by varying $[O_3]$) gave rise to a well constrained value of $k_{15} = (3.15 \pm 0.34) \times 10^{-12}$ cm^3 molecule^{-1} s^{-1} , where the quoted errors are statistical only at the 95% confidence limits.

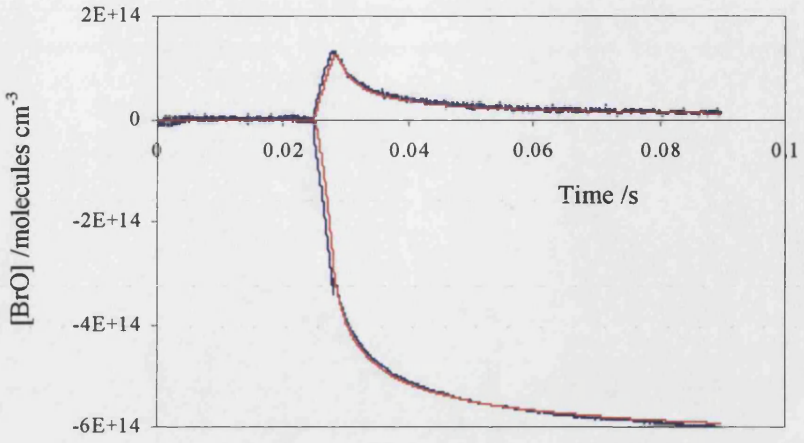

Figure 5.17: Temporal [BrO] and [O_3] (blue) behaviour and FACSIMILE fits (red), optimising k_{15}.

5.4 Discussion

Table 5 shows the kinetic data derived from previous studies of the BrO self-reaction at 298 K along with the results of this study. The value of k_{6a+6b} reported in this work is in excellent agreement with the literature values with the slight exception of those reported by Gilles *et al.*[14], Turnipseed *et al.*[17] and Sander and Watson[9].

k_{6a+6b} /10^{-12}	$\alpha = k_{6a}/k_{6a+6b}$	Reference	Experimental Technique	Reference σ_{BrO} employed
2.92 ± 0.14	0.90	This work	FP/UV	Wilmouth *et al.* (2000)[23]
2.90 ± 0.28	0.89	Harwood *et al.* (1998)[15]	FP/UV	Wahner *et al.* (1988)[31]
3.4 ± 0.5		Gilles *et al.* (1997)[14]	FP/UV	Gilles *et al.* (1997)[14]
2.8 ± 0.5		Laszlo *et al.* (1997)[13]	FP/UV	Laszlo *et al.* (1997)[13]
2.98 ± 0.42	0.84	Rowley *et al.* (1996)[12]	FP/UV	Wahner *et al.* (1988)
2.78 ± 0.25	0.85	Mauldin *et al.* (1993)[11]	FP/UV	Wahner *et al.* (1988)
3.1 ± 0.4		Bridier *et al.* (1993)[10]	FP/UV	Wahner *et al.* (1988)
3.2 ± 0.5	0.85	Lancar *et al.* (1991)[18]	DF/MS	
2.49 ± 0.26	0.88	Turnipseed *et al.* (1990)[17]	DF/MS	
2.17 ± 0.68	0.84	Sander and Watson (1981)[9]	FP/UV	Sander and Watson (1981)[9]
3.2 ± 0.7		Clyne and Watson (1975)[16]	DF/MS	

Table 5.5: Comparison of kinetic data describing the BrO + BrO reaction (6) at 298 K. All rate coefficients are quoted in units of molecules cm^{-3} s^{-1}. The study by Laszlo et al. was conducted at 295 K but is included for completeness.

Rate coefficients for second order reactions require knowledge of absolute concentrations of reactants or products. Thus, those determined from UV spectroscopy methods are not strictly sensitive to k, but to k/σ. This investigation into the self-reaction kinetics of the BrO radical is the first to employ the BrO spectrum recently reported by Wilmouth *et al.*[23] They included within their paper describing the BrO cross section an extensive review of previous σ_{BrO} measurements and assigned an absolute cross section to their FTUV absorption cross section on the basis of this review. As a result, values of k/σ evaluated using the reference BrO spectrum reported by Wilmouth *et al.* are considered to have been subjected to the smallest systematic error. The BrO cross section measured by Laszlo *et al.* is in good agreement with the review of Wilmouth, and their value of k_6 is in good agreement with that reported in this work. The BrO absorption cross section measured by Gilles *et al* is approximately 14% larger than that reported by Wilmouth *et al.* However, when the measured k_{6a+6b} reported by Gilles is scaled relative to the recommended cross section of Wilmouth *et*

al., $k_{6a+6b} = 2.96 \times 10^{-12}$ molecules cm^{-3} s^{-1}, and becomes consistent with the result presented in this study. Similarly, the BrO cross section reported by Sander and Watson[9] is 48% smaller than the recommendation of Wilmouth *et al.*, scaling the rate coefficient reported by Sander and Watson gives $k_{6a+6b} = 3.20 \times 10^{-12}$ molecules cm^{-3} s^{-1}, again improving agreement with this work.

Wilmouth *et al.* also compare their absolute and differential BrO cross sections with those reported by Wahner *et al.*[31] at the (7,0) peak (and the adjacent trough to lower wavelengths) at a resolution of 0.40 nm. The absolute and differential cross-sections of Wahner *et al.* are respectively 2% and 8% smaller than those of Wilmouth. However, Wilmouth *et al.* also note that no consistent multiplicative factor could fit the either the differential or the absolute cross sections across the entire wavelength range. The BrO + BrO kinetics studies performed by Harwood *et al.*[15], Rowley *et al.*[12] and Bridier *et al.*[10] all used differential (or *pseudo*-differential) fitting methods to determine $[BrO]_t$ in their experiments from the cross sections reported by Wahner *et al.* As a result it is not possible to scale their rate coefficients, since the scaling factor required over the entire fitted wavelength region is unknown and in any case could vary with wavelength. By contrast, Mauldin *et al.*[11] determined their $[BrO]_t$ relative to the (7,0) peak of the Wahner *et al.* cross section, allowing scaling to the value of the recommended cross section at this single wavelength. This scaling gives rise to a corrected $k_{6a+6b} = 2.83 \times 10^{-12}$ molecules cm^{-3} s^{-1}. Once again, this becomes more consistent with the rate coefficient measured in this study.

The low value of k_{6a+6b} published by Turnipseed *et al.*[17] was obtained from a DF/MS study and thus independent of absorption cross section. As a result their value remains a discrepancy which cannot be reconciled.

The branching ratio for the non-terminating channel of BrO + BrO evaluated in this study at $\alpha = 0.90 \pm 0.03$ is consistent with previous determinations, which show spread of values between 0.84 and 0.89. The branching ratio is independent of σ_{BrO}, so the use of different spectral resolutions cannot account for the spread of values across studies

employing UV spectroscopy as a quantitative tool. Moreover, the studies utilising discharge flow/mass spectrometry techniques show a similar spread of values[16,17,18].

The measured value of k_{11} = (4.8 ± 0.6) × 10^{-17} molecule^{-1} cm^3 s^{-1} is in excellent agreement with the only other measurement, that reported by Rowley et al.[12] at (2.1 ± 0.7) × 10^{-17} molecule^{-1} cm^3 s^{-1}.

The value of k_{15} = (3.15 ± 0.34) × 10^{-12} molecule^{-1} cm^3 s^{-1} reported at 298 K and 760 Torr is in good agreement with the range approximated by Rowley *et al.*[12] as (2-4) × 10^{-12} molecule^{-1} cm^3 s^{-1}. A lower pressure study at 200 Torr by Laszlo *et al.*[13] evaluated k_{15} = (1.5 ± 0.4) × 10^{-12} molecule^{-1} cm^3 s^{-1}. Without undertaking a full pressure dependent study of k_{15} it is not possible to reconcile their smaller value against a termolecular, pressure dependent mechanism, although this is a plausible hypothesis since reaction (15) is an association process. If reaction (15) is found to be pressure independent, the k_{15} values reported in this work are arguably subject to less uncertainty than those of Laszlo *et al.* Firstly, Laszlo *et al.* evaluate k_{15} by simultaneously fitting to $[BrO]_t$ and $[Br_2]_t$. Both of these data sets show only a weak sensitivity to k_{15}. However, the catalytic loss of ozone (mitigated by chain termination arising from (6b)) is highly sensitive to the value of k_{15} (as discussed above, see figure 5.16). Therefore simultaneously monitoring $[BrO]_t$ and $[O_3]_t$ in these experiments provided a higher precision route to k_{15} evaluation than that employed by Laszlo *et al.* Moreover the inherent signal to noise ratios associated with the $[BrO]_t$ and $[O_3]_t$ data recorded and analysed in this study were considerably higher than the $[BrO]_t$ and $[Br_2]_t$ data recorded by Laszlo *et al.*

5.5 References

[1] Scientific Assessment of Ozone Depletion **2002**, World Meteorological Organisation Report no. 47.

[2] Platt, U. Private Communication, 2002.

[3] Fan S.M.; Jacob D.J. *Nature* **1992**, 359, 522

[4] Mozurkewich, M. *J. Geophys. Res-Atmos* **1995**, 100, 14199.

[5] Sander, R.; Crutzen, P.J. *J. Geophys. Res.-Atmos.* 1996, 101, 9121.

[6] Vogt, R.; Crutzen, P.J.; Sander, R. *Nature* **1996**, 383, 327.

[7] Mateev, V.; Peleg, M.; Rosen, D.; Tov-Alper, D.S.; Hebestreit, K.; Stutz, J.; Platt, U.; Blake, D.; Luria, M. *J. Geophys. Res.-Atmos.* **2001**, 106, 10375.

[8] Basco, N.; Dogra, S.K. *Proc. R. Soc. London A* **1971**, 323, 417.

[9] Sander, S.P.; Watson, R.T. *J. Phys. Chem.* **1981**, 85, 4000.

[10] Bridier, I.; Veyret, B.; Lesclaux, R. *Chem. Phys. Lett.* **1993**, 201, 563.

[11] Mauldin, R.L., III; Wahner, A.; Ravishankara, A.R. *J. Phys. Chem.* **1993**, 97, 7585.

[12] Rowley, D.M.; Harwood, M.H.; Freshwater, R.A.; Jones, R.L. *J. Phys. Chem.* **1996**, 100, 3020.

[13] Laszlo, B.; Huie, R.E.; Kurylo, M.J. *J. Geophys. Res.-Atmos.* **1997**, 102, 1523.

[14] Gilles, M.K.; Turnipseed, A.A.; Burkholder, J.B.; Ravishankara, A.R.; Solomon, S *J. Phys. Chem. A* **1997** 101, 5526.

[15] Harwood, M.H.; Rowley, D.M.; Cox, R.A.; Jones, R.L. *J. Phys. Chem. A* **1998** 102, 1790.

[16] Clyne, M.A.A.; Watson, R.T. *Ber. Bunsenges. Phys. Chem.* **1975**, 71, 336.

[17] Turnipseed, A.A.; Birks, J.W.; Calvert, J.G. *J. Phys. Chem.* **1990**, 94, 7477

[18] Lancar, I.T.; Laverdet, G.; Le Bras, G.; Poulet, G. *Int. J. Chem. Kinet.* **1991**, 23, 37

[19] Clyne, M.A.A.; Cruse, H.W. *Trans. Faraday Soc.* **1970**, 66, 2214.

[20] Cox, R.A.; Sheppard, D.W.; Stevens, M.P. *J. Photochem.* **1982**, 19, 189.

[21] Jaffe, S.; Mainquist, W.K. *J. Phys. Chem.* **1980**, 84, 3277

[22] DeMore, W.B.; Sander, S.P.; Golden, D.M.; Hanson, R.F.; Kurylo, M.J.; Howard, C.J.; Ravishankara, A.R.; Kolb, C.E.; Molina, M.J. *Chemical Kinetics and Photochemical Data for use in Stratospheric Modeling;* JPL publication **97**-4; California Institute of Technology, Pasadena.

[23] Wilmouth, D. M.; Hanisco, T. F.; Donahue, N. M.; Anderson, J. G. *J. Phys. Chem. A.* **1999**; 103(45); 8935-8945.

[24] Orlando, J.J.; Burkholder, J.B. *J. Phys. Chem.* **1995**, 99, 1143.

[25] Knight, G.; Ravishankara, A.R.; Burkholder, J.B. *J. Phys. Chem.* **2000**, 104, 11121.

[26] Sidgwick, N.V. *Chemical Elements and their Compounds, Oxford Press* **1950**.

[27] Rattigan, O.V.; Jones, R.L.; Cox, R.A. *Chem. Phys. Lett.* **1994**, 230, 121.

[28] Curtis A. R.: Sweetenham W. P. *FACSIMILE*, AERE Harwell publication R 12805: Computer Science and Systems Division, Harwell Laboratory, Oxfordshire, U.K. **1987**.

[29] Baulch, D.L.; Duxbury, J.; Grant, S.J.; Montague, D.C. *J. Phys. Chem.* **1998,** Ref. Data 10.

[30] Burkholder, J. B. *Int. J. Chem. Kinetics* **1998**, 30, 571.

[31] Wahner, A.; Ravishankara, A. R.; Sander, S. P.' Friedl, R. R. *Chem. Phys. Lett.* **1988**, 152, 107.

Chapter 6: The BrO + ClO Reaction

6.1 Introduction

The reaction between BrO and ClO radicals couples the chemistries of bromine and chlorine, playing an important role in the chemistry of the stratosphere. By analogy with the halogen monoxide self-reactions, the BrO + ClO reaction can form part of a catalytic stratospheric ozone destruction cycle.[1] Three product channels are known to exist, as shown below, along with their 298 K branching ratios. The recommended 298 K rate coefficient for the sum of all three channels is $k_1 = (1.39 \pm 0.70) \times 10^{-11}$ molecule^{-1}cm^3 s^{-1} (2)

				Branching Ratio
(6.1a)	BrO + ClO	→	Br + OClO	0.49
(6.1b)		→	Br + ClOO	0.44
(6.1c)		→	BrCl + O_2	0.07

Atmospheric modelling studies indicate that the catalytic ozone destruction cycle incorporating the BrO + ClO reaction is responsible for between 25 and 50% of the total ozone depletion observed in the polar vortices.[3] Using the kinetic data from the NASA JPL-97 evaluation of kinetic data for atmospheric modelling purposes,[2] Cox *et al.*[4] quantified the individual contributions to stratospheric ozone depletion resulting from various chemical loss cycles as a function of latitude during the Northern hemisphere winter of 1994/95. The results from this model study are shown in Table 6.1 and clearly demonstrate the key role of reaction (1) in the stratospheric chemistry of ozone in both polar regions and midlatitudes.

Ozone loss cycle	Equivalent-latitude bands (°N)					
	90–70	70–60	60–50	50–40	40–30	90–30
Cycle I (Cl_2O_2 + $h\nu$)	18.5	12.7	9.1	6.2	4.4	10.6
Cycle II (ClO + BrO)	33.2	26.5	22.1	18.4	15.7	23.7
Cycle III (HO_2 + O_3)	14.5	21.8	27.0	31.3	35.3	25.3
Cycle IV (HO_2 + ClO)	6.1	6.8	7.2	7.5	7.5	7.0
Cycle V (HO_2 + BrO)	2.5	3.6	4.6	5.7	7.7	4.6
Cycle VI (ClO + O)	10.8	11.4	11.3	10.9	10.0	11.0
Cycle VII (BrO + O)	0.7	1.0	1.2	1.4	1.5	1.2
Cycle VIII (NO_2 + O)	3.6	6.7	8.2	9.7	10.0	7.5
Total ozone loss (DU)	60.3	49.2	37.9	28.7	17.3	34.1
Total ozone production (DU)	9.0	16.2	18.5	19.4	19.3	17.5
Model ozone (DU)	161.8	154.8	137.1	118.3	90.1	124.6
Passive ozone (DU)	212.6	187.4	156.1	127.4	88.0	141.0
Chemical change (DU)	−50.8	−32.5	−19.1	−9.1	2.2	−16.4
Alpha	73.4	59.8	53.1	49.8	48.3	54.6

Table 1: Percentage contribution to ozone loss using DeMore et al. recommended rate constants due to the main catalytic loss cycles as a function of latitude. Extracted from Coupled Bromine Chemistry Affecting Stratospheric Bromine report, 2000.[4]

Avallone *et al.*[5] undertook in-situ measurements of stratospheric BrO and ClO mixing ratios simultaneously during the Arctic winter of 1991/92. In conjunction with kinetic data from the literature, their results suggested that the ozone destruction cycle incorporating the ClO + BrO reaction was responsible for the destruction of up to 0.6% of total ozone per day at an altitude of 20 km. More recently the same group has reported anomalous ratios of BrO to total inorganic stratospheric bromine (Br_y) in the Arctic stratosphere, following measurements taken during the AASE missions of 1988/89 and 1991/92.[6] In this study, atmospheric modelling incorporating all the known Br_y chemistry evaluated a BrO lifetime of just 15 minutes in the absence of solar photolysis, since BrO reacts with NO_2 or ClO to form $BrONO_2$ or BrCl nighttime reservoirs respectively. However the associated measurements revealed significant BrO/Br_y ratios long after sunset, suggesting that the description of stratospheric bromine chemistry was incomplete. These observations were corroborated to some degree by Wahner *et al.*[7,8] who also reported non-zero nighttime BrO column abundances during the Arctic winter of 1989, although these authors were unable to determine confidently the altitude of the BrO radicals.

Avallone and Toohey[6] postulated that a weakly bound adduct in equilibrium with BrO could account for the anomaly between observed and modelled BrO abundances, in the same way that the ClO dimer is responsible for mitigating ClO loss *via* reservoir formation after sunset. This speculation is supported by theoretical studies of the BrO + ClO radical reaction which proposed the existence of an adduct between BrO and ClO.[9,10] In the latest theoretical studies of the BrO + ClO reaction,[11] the BrOOCl isomer was calculated to be the most stable form of the adduct between BrO and ClO, with a BrO-OCl bond strength of over 70 kJ mol^{-1}. This energetic stability exceeds the measured stability of the BrO dimer relative to 2 BrO radicals (60 kJ mol^{-1},[12]) and is nearly comparable to that of ClOOCl relative to 2 ClO radicals.[2] By analogy with the ClO and BrO self-reactions, and given the reported negative temperature dependence of the BrO + ClO rate coefficient, the BrO + ClO reaction is believed to proceed through an excited $BrClO_2$* intermediate. Formation and subsequent decomposition of a BrOOCl* species could certainly account for channels (1b) and (1c), whilst formation of BrOClO*, either directly or by isomerisation of BrOOCl*, could account for the OClO producing channel (1a). However no experimental evidence has ever been reported for the existence of any stabilised $BrClO_2$ adduct.

(1d) $\quad BrO + ClO + M \quad \leftrightarrow \quad BrClO_2 + M$

Considering the importance of the BrO + ClO reaction, relatively few kinetics studies exist and these have tended to focus on temperatures more relevant to the midlatitude stratosphere than to Polar Regions. The lowest temperature kinetic studies of BrO + ClO were undertaken at 220 K by Sander and Friedl[13] and Friedl and Sander.[14] Another investigation, at a lowest temperature of 234 K, was reported by Turnipseed *et al.*[15] Clearly the lack of a $BrClO_2$ adduct at these temperatures cannot be extrapolated to lower temperatures, where conditions could be themodynamically conducive to $BrClO_2$* stabilisation. It is notable that Avallone and Toohey assumed a temperature of 210 K in their Arctic model, although polar stratospheric temperature may fall as low as 185 K within the vortices associated with an extreme Antarctic winter.

Renard *et al.*[16] tentatively reported nightime observations of stratospheric OBrO, where mixing ratios reached 20 pptv. These levels would make OBrO the dominant nightime reservoir of stratospheric bromine. OBrO is produced in the reaction of BrO with O_3 (see chapter 5), which is too slow to account for the reported mixing ratios. It has also been suggested that OBrO formation can occur by self-reaction of vibrationally excited BrO radicals[17], however stratospheric BrO mixing ratios are too low to account for the reported OBrO abundances. However an additional channel of the BrO + ClO reaction, yielding OBrO can readily be envisaged by analogy to the OClO production channel (1a):

(6.1e) $\quad BrO + ClO \quad \rightarrow \quad OBrO + Cl$

All the existing studies of reaction (1) predate both the putative OBrO observations of Renard *et al.* and the gas phase detection of OBrO by Rattigan *et al.*[18] (1994). The existence of an OBrO producing channel of reaction (1) would profoundly influence the current understanding of stratospheric halogen chemistry, beyond the support lent to the observations by Renard *et al.* If the products of OBrO photolysis were BrO and O, such a channel would result in a null cycle for catalytic ozone depletion during sunlit hours, reducing the ozone depleting potential of the BrO + ClO reaction.

The following chapter describes experiments to determine the kinetics and products of the BrO + ClO reaction. Particular emphasis is placed upon investigation at temperatures (210-298 K) and pressures (100-760 Torr) where the results are applicable to the stratosphere over all altitudes. The fast timescale and broad band coverage afforded by the CCD was used to simultaneously monitor BrO, ClO and OClO, giving rise to an unprecedented degree of accuracy in studying this reaction.

6.2 Experimental

Flash photolysis of $Br_2/Cl_2O/Cl_2/O_2/O_3/N_2$ mixtures was used to investigate the kinetics of the BrO + ClO reaction. The following photolytic channels gave rise to radical production within the reaction cell:

(6.2)	$Br_2 + h\nu$	$\rightarrow$	2Br
(6.3)	$Cl_2 + h\nu$	$\rightarrow$	2Cl
(6.4a)	$Cl_2O + h\nu$	$\rightarrow$	Cl + ClO
(6.4b)		$\rightarrow$	$Cl_2 + O(^3P)$
(6.4c)		$\rightarrow$	$Cl_2 + O(^1D)$
(6.4d)		$\rightarrow$	$2Cl + O(^3P)$
(6.5a)	$O_3 + h\nu$	$\rightarrow$	$O(^1D) + O_2$
(6.5b)		$\rightarrow$	$O(^3P) + O_2$

Subsequent reaction of these photolytically produced species with reagent molecules gave rise to production of both BrO and ClO:

(6.6)	$Br + Cl_2O$	$\rightarrow$	$ClO + BrCl$
(6.7)	$Br + O_3$	$\rightarrow$	$BrO + O_2$
(6.8)	$Cl + Br_2$	$\rightarrow$	$Br + BrCl$
(6.9)	$Cl + Cl_2O$	$\rightarrow$	$ClO + Cl_2$
(6.10)	$Cl + O_3$	$\rightarrow$	$ClO + O_2$
(6.11)	$O(^1D) + N_2$	$\rightarrow$	$O(^3P) + N_2$
(6.12)	$O(^3P) + Br_2$	$\rightarrow$	$BrO + Br$
(6.13)	$O(^3P) + Cl_2O$	$\rightarrow$	$2ClO$
(6.14)	$O(^3P) + O_2 + N_2$	$\rightarrow$	$O_3 + N_2$

It is clear that multiple reactive partners existed for each photolytically generated radical, with the exception of $O(^1D)$, whose virtually exclusive fate was quenching to ground state $O(^3P)$ *via* collision with N_2 bath molecules. These multiple channels led to a complex reactive mixture, whose $[ClO]_0/[BrO]_0$ ratio was critically dependent on the relative precursor concentrations. Extensive numerical modelling using FACSIMILE was undertaken to design the experimental conditions and ensure that the flux of radicals through the complex network of reactions was understood and

optimised for the investigation of the BrO + ClO kinetics. The precursor gas concentrations employed are given in Table 6.2.

Precursor species	Pre-flash concentration
Br_2	$(1 - 3) \times 10^{16}$
O_3	$(0.5 - 1.0) \times 10^{15}$
Cl_2O	$(4 - 8) \times 10^{15}$
Cl_2	$(2 - 5) \times 10^{15}$
O_2	2×10^{18}
N_2	Balance to 1 atmosphere

Table 6.1: Typical precursor concentrations in molecules cm^{-3} at 298K, 760 Torr.

These conditions were specifically chosen so as to ensure that reaction (12) represented the only significant source of BrO. This criterion required that the reaction of bromine atoms with Cl_2O (6) rather than O_3 (7) was dominant, which was critically dependent upon the $[Cl_2O]/[O_3]$ ratio in the precursor mixture. The ratio was kept as high as possible, whilst keeping the absolute $[O_3]$ at a value high enough to produce a significant number of $O(^3P)$ atoms *via* O_3 photolysis (5) and subsequently BrO radicals *via* reaction of the former with molecular bromine (12). Hence no secondary regeneration of BrO could occur. By contrast, conditions were such that Cl atoms reacted to regenerate ClO directly through reactions (9) and (10) and indirectly *via* their reaction with molecular bromine and the subsequent exclusive reaction of the Br atoms with Cl_2O in reaction (6). Furthermore, the chosen reagent concentrations promoted rapid formation of ClO and BrO on a timescale that was largely decoupled from decay *via* reaction (1).

6.2.1 Production of Precursor Gases

Cl_2O was prepared by passing gaseous chlorine through a column of yellow mercuric (II) oxide.[19] The details of this procedure have been described in chapter 4. The

conversion efficiency of Cl_2 to Cl_2O was measured spectroscopically by fitting reference Cl_2O cross sections[20] to recorded absorption spectra from non-flashed experiments. The conversion efficiency of Cl_2 to Cl_2O was typically 70%, giving rise to the inclusion of Cl_2 in the precursor mixture described above.

O_3 production at the low concentrations required for these studies was effected *via* the flow of molecular oxygen through a cell incorporating a mercury pen-ray lamp. The 184.9 nm emission line of the mercury lamp gave rise to O_2 photolysis. Reaction of the liberated $O(^3P)$ atoms with molecular oxygen gave rise to O_3 production. The details of this procedure are described in Chapter 5. Ozone concentrations within the cell were taken from the known and reproducible generation efficiency of the mercury pen ray cell. These were also calibrated by fitting a reference cross section[2] to the Hartley Band of ozone absorption spectra recorded during non-flashed experiments.

Other precursor gases, nitrogen (>99.98%, BOC), oxygen (>99.99%, BOC) were used as supplied. Chlorine (BOC, 5% in N_2 >99.9%) was supplied in a 5% mixture diluted in nitrogen. Bromine (>99.8%, Aldrich) was introduced into the gas phase by flowing nitrogen through a bubbler containing liquid Br_2. The bubbler was kept in an ice/water bath to ensure a known and constant bromine vapour pressure.

6.2.2 Radical and Product Monitoring

The temporally resolved concentrations of reactant and product species were monitored by absorption spectroscopy. The CCD detector facilitated the simultaneous monitoring of BrO, ClO and OClO. The CCD and spectrograph settings used in monitoring these transient species are given in Table 6.3.

Source for UV absorption	Xe lamp
Spectrograph diffraction grating	300 grooves mm^{-1}
Entrance slit width	75 μm
Monitored wavelength range	270-335 nm
Spectral resolution	1.1 nm (FWHM)
CCD clocking rate	2-4 μs/ spectrum

Table 6.3: CCD and spectrograph settings employed during the investigation into the kinetics of the BrO + ClO reaction.

The absorption spectra of BrO, ClO and OClO all exhibit distinctive vibronic structure. Figure 6.1 shows two examples of temporally averaged, post-flash absorption spectra recorded during a typical flashed experiment on the gaseous $Br_2/Cl_2O/Cl_2/O_2/O_3/N_2$ mixture.

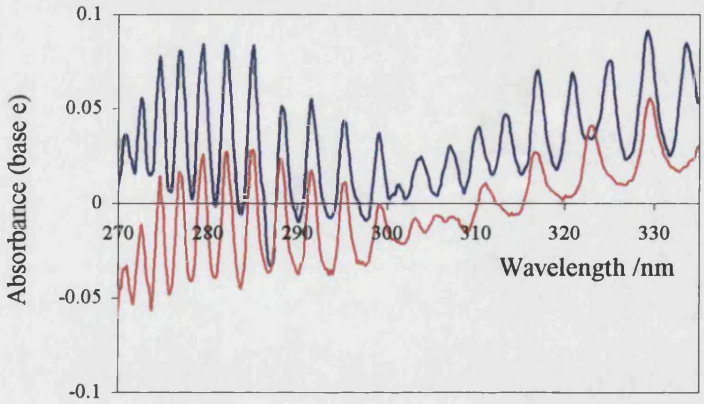

Figure 6.1: Temporally averaged spectra recorded in the immediate (blue) and late post-flash (red) following initiation of the $Br_2/Cl_2O/Cl_2/O_2/O_3/N_2$ gas mixture.

The blue spectum in Figure 6.1 was recorded in the period immediately following photolysis $(0.5\text{-}2.5) \times 10^{-5}$ s after flashing. It is dominated by ClO spectral structure at low wavelengths ($270 < \lambda < 310$ nm) and BrO structure to higher wavelengths ($300 < \lambda < 335$ nm). The red spectrum in Figure 6.1, recorded $(2.8\text{-}3.2) \times 10^{-3}$ s after flashing also shows intense ClO structure at low wavelengths, but by contrast, is dominated by

OClO vibronic structure at higher wavelengths. Since differential spectroscopy was used to analyse time-resolved spectra collected in each experiment, reference cross-sections of all three absorbing species were required. The provenance of the cross-sections used is discussed below.

6.2.3 Reference Cross Sections

6.2.3.1 ClO

Measurement of the ClO differential cross section was a major focus of chapter 4, in conjunction with a study of the ClO + ClO reaction. The temperature dependent cross section reported in chapter 4 was used to quantify ClO concentrations during these experiments. However, the differential cross section reported in chapter 4 was measured at a spectral resolution of 0.8 nm (FWHM), determined by the diffraction grating (600 grooves mm^{-1}) and the entrance slit width of the spectrograph. This spectral resolution was convenient for comparison to other measurements of σ_{ClO} and provided the most accurate determination of ClO concentrations due to the optimised signal to noise ratio associated with the highly resolved structure. However, in order to quantify [ClO] in conjunction with [BrO] and [OClO] simultaneously, it was necessary to monitor a wider wavelength regime at the expense of resolution. Therefore a less finely ruled grating (300 grooves mm^{-1}) was employed within the spectrograph to afford this extended wavelength coverage. This change of grating was accompanied by a decrease in spectral resolution. Consequently it was necessary to calibrate the ClO cross section at the lower resolution (1.1 nm (FWHM)) relative to that measured at a resolution of 0.8 nm (FWHM).

Back to back experiments were performed on $Br_2/Cl_2/Cl_2O/N_2$ mixtures at spectral resolutions of 0.8 nm and 1.1 nm. The first kinetic experiment was performed at the higher resolution, under which the differential ClO cross section was originally recorded and consisted of 20 co-added, flashed experiments. The experiment was then repeated but the spectrograph settings were altered to the new, lower resolution. Thus the chemistry within the cell was, in principle, unchanged but the monitoring

parameters deliberately altered. The entire procedure, incorporating both experiments was then repeated three times. The operating parameters employed in these two sets of experiments are given in Table 6.4 for the calibration at 298 K.

Operating parameter	High resolution expts.	Low resolution expts.
Diffraction grating	600 grooves mm^{-1}	300 grooves mm^{-1}
Entrance slit width	112 μm	75 μm
Wavelength regime	250 – 285 nm	270 – 335 nm
Spectral resolution	0.8 nm (FWHM)	1.1 nm (FWHM)
CCD clocking rate	50 μs	50 μs

Table 6.4 : Comparison of operating parameters employed in the experiments undertaken to calibrate the differential ClO cross section.

From each kinetic experiment a time averaged spectrum was developed by applying Beer's law over analogous temporally resolved data. Hence four spectra were obtained at each of two resolutions, each consisting of ClO exhibiting vibronic structure with underlying smooth absorbances arising from transient Cl_2O and Cl_2O_2 presences (as described in chapter 4). Comparisons of the four spectra obtained at each resolution are indicated in figures 6.2 and 6.3.

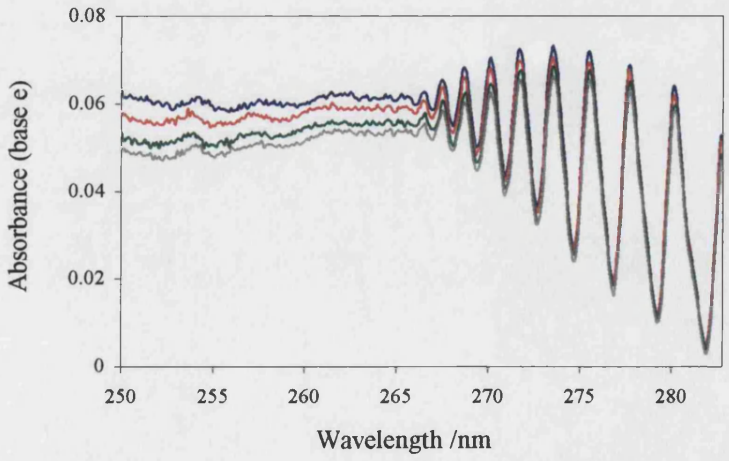

Figure 6.2: Comparison of the four ClO spectra recorded at a spectral resolution of 0.8 nm, used to determine the ClO concentration.

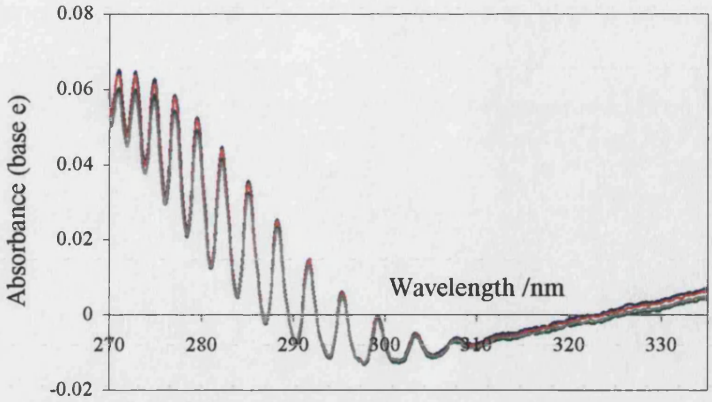

Figure 6.3: Comparison of the 4 ClO spectra recorded at a spectral resolution of 1.1 nm. These were converted to ClO cross sections by applying Beer's law with a knowledge of [ClO].

Some fluctuations in the baseline absorption are clearly evident between experiments but the magnitude of the differential structure used to determine the associated ClO concentrations was essentially constant, indicated by the fitting procedure described below.

The four spectra recorded at a resolution of 0.8 nm were fitted with the differential $\sigma_{ClO,298K}$ reported in chapter 4, giving rise to the [ClO] associated with each spectrum. The variation in the returned [ClO] values was less than 1%, indicating that no significant change in the kinetics of the ClO radical had been effected between experiments. These well constrained ClO concentrations were then used to convert the spectra recorded at 1.1 nm resolution to differential ClO cross sections by applying the Beer-Lambert law:

$$\sigma_{ClO,\lambda} = \frac{A_{ClO,\lambda}}{[ClO]l} \qquad (6.i)$$

The mean of these four ClO cross sections was used to quantify ClO concentration during the investigation of the ClO + BrO reaction. This entire process was repeated at 272 K, 228 K and 210 K to determine $\sigma_{ClO,T}$ for kinetic investigation at these lower temperatures.

By analogy to the cross sections reported in chapter 4, the ClO cross section determined *via* this calibration is not an absolute quantity. The underlying absorbances from Cl_2O and Cl_2O_2 have not been removed and only once these have been filtered out does the residual spectrum (the differential ClO spectrum) correspond solely to ClO absorption.

6.2.3.2 BrO

Several measurements of the absorption cross section of the BrO radical have been published.[21] However the vibronic spectral structure associated with the cross section is temperature dependent and the majority of these studies have focussed on the room temperature BrO spectrum alone.[22,23,24] Only two independent investigations into the temperature dependence of σ_{BrO} have been reported. Wahner *et al.*[25] recorded the wavelength resolved BrO cross section ($310 < \lambda < 390$ nm) at 223 K and at 298 K. Gilles *et al.*[26] reported a pseudo-differential cross section of BrO between the peak of the (7,0) band and the adjacent, blue shifted trough at nine temperatures between 204 K and 388 K. The most recent investigation of σ_{BrO} by Wilmouth *et al.*[21] incorporated an extensive literature review and reported the entire spectrum ($290 < \lambda < 390$ nm) at 228 K and 298 K. However, Wilmouth *et al.* explicitly measured the absorption spectrum only and subsequently converted it to an absolute cross section on the basis of the previous measurements. This operation was facile at 298 K, the focus of previous studies, but extrapolation techniques were employed at 228 K based on the temperature dependent studies described above.

The study of the BrO + ClO reaction reported here employed the BrO absorption cross section recently reported by Wilmouth *et al.* to determine experimental BrO concentrations. Cross sections were not explicitly available at each experimental temperature, so interpolation was employed after Wilmouth *et al.* The validity of the interpolation method is discussed below.

Gilles *et al.* reported linear temperature dependencies of both the absolute BrO cross section at the (7,0) peak and the pseudo-differential cross section associated with its adjacent blue-shifted minimum. These trends are illustrated graphically in figure 6.4.

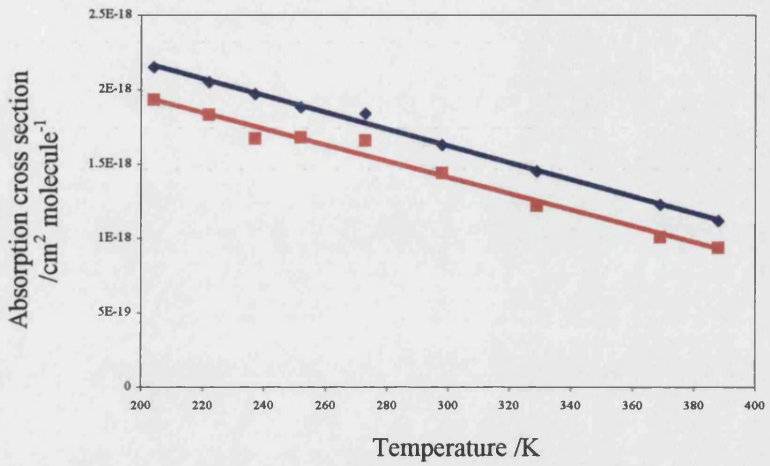

Figure 6.4: Temperature dependencies of the absolute and pseudo-differential BrO cross section about the (7,0) maximum. The solid lines represent linear parameterisations of the data.

For comparative purposes the 298 K measurements of the BrO cross-sections reported by Gilles *et al.* were converted to 228 K values by implementing the temperature dependencies illustrated in figure 6.4. Similarly, linear interpolation of the Wahner *et al.* data (reported at 223 K and 298 K) gave rise to the BrO cross section at 228 K based on their data alone. The ratios of the cross sections ($\sigma_{BrO,228K}/\sigma_{BrO,298K}$) were then inspected for both systems. For the absolute (7,0) band this ratio was found to be 1.242 (Gilles *et al.*[26]) and 1.248 (Wahner *et al.*[25]). For the pseudo-differential cross-section between the peak and the blue -shifted adjacent trough the ratio was found to be 1.232 (Gilles *et al.*[26]) and 1.259 (Wahner *et al.*[25]). Hence the temperature dependencies to the BrO cross-sections reported by Gilles *et al.* are extremely well supported by the Wahner *et al.* data, the only other temperature dependent study. Wilmouth *et al.* used this dependence to assign their absolute 228 K BrO cross section.

This study employed linear weighting of the Wilmouth *et al.* data to generate BrO cross sections at experimental temperatures between 228 K and 298 K. For

investigation outside of this range, linear extrapolation based on the temperature dependence reported by Gilles *et al.* was undertaken. Sliding average routines were used to convolve the highly resolved reference spectra to the experimental resolution of 1.1 nm. (as discussed in appendix 1)

6.2.3.3 OClO

The OClO absorption cross sections have been measured at 204 K and at 296 K by Wahner *et al.*[27] who showed that the vibronic bands are temperature dependent. The 296 K OClO spectrum reported by Wahner *et al.* is in excellent agreement with the room temperature OClO cross section reported by Harwood *et al.*[28] In the absence of any extensive temperature dependent studies of the OClO absorption cross section, linear interpolation routines were applied to construct spectra at temperatures between 204 K and 296 K using the spectra reported by Wahner *et al.* Experiments have shown that the temperature dependence of the vibronic structure associated with the spectra of other gas phase halogen oxide species follows linear behaviour. This is discussed above in relation to the BrO spectrum.[26] Furthermore, chapter 4 of this thesis measured the temperature dependence of the differential ClO absorption cross section and linear behaviour was also observed in this case. The OClO cross sections generated at each experimental temperature were smoothed with a Gaussian kernel to match the instrument resolution of 1.1 nm employed in this study.

6.2.3.4 Summary of Spectra used

The 298 K ClO, BrO and OClO absorption cross sections used to determine the temporal concentrations of the respective species during kinetic experiments, are shown, at a spectral resolution of 1.1 nm (FWHM) in figure 6.5. The uncertainties associated with the differential ClO, BrO and OClO absorption cross sections are 13%, 11% and 4% respectively.

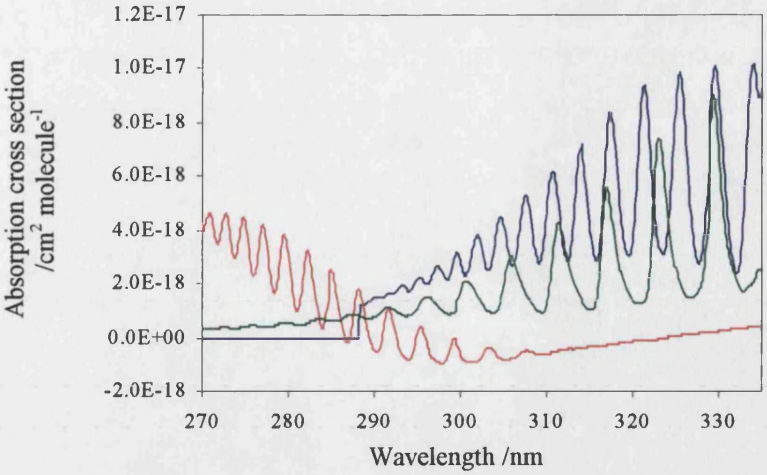

Figure 6.5: ClO (red), BrO (blue) and OClO (green) cross sections used to quantify the respective radical concentrations at 298 K, having been convolved to the experimental resolution. The negative σ_{ClO} values at intermediate wavelengths arise from the presence of underlying absorptions. As a result only the differential ClO cross section corresponds to a physically meaningful quantity.

6.3 Results

6.3.1 Obtaining Channel Specific Kinetics

The ability of the CCD detection system to monitor an entire window of UV absorption as a function of time enabled the differential fitting to all spectrally structured absorbers present. In this way, $[ClO]_t$, $[BrO]_t$ and $[OClO]_t$ were independently quantified. A typical concentration versus time profile from a kinetic experiment at 298 K is shown in figure 6.6.

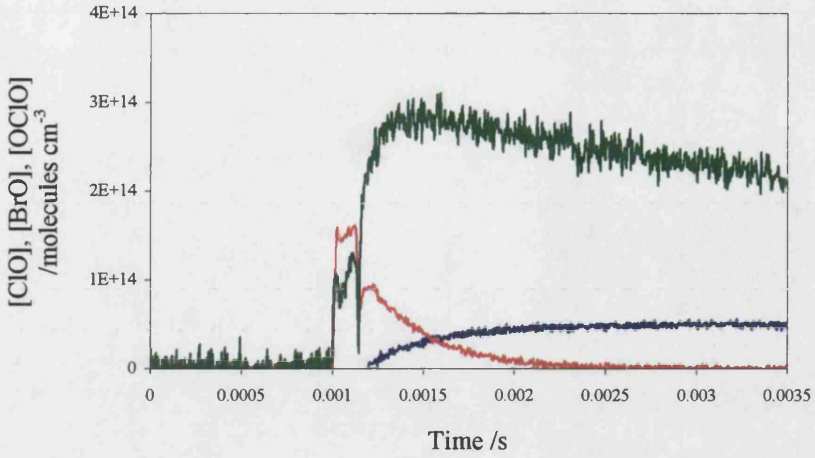

Figure 6.6: Typical concentration versus time profile. The measured BrO, ClO and OClO concentrations are indicated in red, green and blue respectively. The concentrations measured between 0.001 and 0.00115 s are spurious due to the collection of scattered flashlamp light at the CCD.

These temporally resolved concentration profiles provided, in principle, a route to the quantification of the kinetics and product branching between the ClO + BrO product channels:

(6.1a) $BrO + ClO \rightarrow Br + OClO$

(6.1b) $\rightarrow Br + ClOO$

(6.1c) $\rightarrow BrCl + O_2$

Since the nature of the reaction mixture ensured that, following initiation, no secondary regeneration of BrO radicals could take place, $[BrO]_t$ provided a direct quantification of the rate of BrO loss along all channels which operate. Consequently, analysis of the BrO decay determined $k_1 = k_{1a} + k_{1b} + k_{1c} + (k_{1d} + k_{1e})$. k_{1d} and k_{1e} represent the rate coefficients for the hypothetical channels proposed to explain the stratospheric observations reported by Avallone and Toohey[6] and Renard *et al.*[16] respectively:

(6.1d) $BrO + ClO + M \leftrightarrow BrClO_2 + M$

(6.1e) $BrO + ClO \rightarrow OBrO + Cl$

By contrast, since the reaction mixture was designed such that the secondary generation of any halogen atoms led to the prompt regeneration of ClO radicals *via* reactions (8), followed by (6), (6) directly and (9), several of the reaction channels were effectively masked in the ClO decay. Specifically, channel (1a) would not contribute to the ClO decay, channel (1b) would in fact lead to ClO production and channel (1c), forming BrCl would lead to loss of ClO. Similarly, putative channel (1d) would also contribute to ClO decay, whereas channel (1e), if it operated would not contribute to ClO decay. Specific experiments, discussed in detail below, were undertaken to confirm or deny the existence of reaction channels (1d) and (1e) in the BrO + ClO reaction. No evidence was found for the existence of either channel. Thus in principle, analysis of the ClO decay profile (and taking into account other loss chemistry of ClO, notably the self-reaction) should reveal sensitivity to the (difference between) rate coefficients for channels (1b) and (1c).

In similar fashion, the direct differential monitoring of OClO provided a direct channel specific quantification of the OClO producing channel (1a). No other significant sources of OClO were present in the photolysed reaction mixture (the bimolecular channel of the ClO self-reaction producing OClO has a 298 K rate coefficient of the order of 10^{-15} molec^{-1}cm^{3}s^{-1} [(2)]). Thus k_{1a} could be determined independently from the OClO temporal profile, and comparison of this result with the total rate constant obtained from the BrO decay gave $k_{1b} + k_{1c}$. Constraining this sum and analysing the ClO decay should then determine k_{1c} independently (the only reaction channel of the BrO + ClO reaction which actually removes ClO under the experimental conditions adopted.) In practice, numerical modelling of the full reaction system using FACSIMILE[29] indicated that channel (1c) was too slow to provide sufficient sensitivity to quantify this channel given the noise associated with the $[BrO]_t$ and especially the $[ClO]_t$ data. This is illustrated in figure 6.7 which shows a fitted $[ClO]_t$ decay trace using a k_{1b}:k_{1c} ratio of 6.3 : 1, in accordance with the JPL-97 evaluation[2]. Also shown is the modelled $[ClO]_t$ trace if k_{1c} is halved, giving rise to a k_{1b} : k_{1c} ratio of 12.6 : 1. The clear similarity of the two traces exposes the lack of sensitivity associated with the $[ClO]_t$ data to significant changes in k_{1c}.

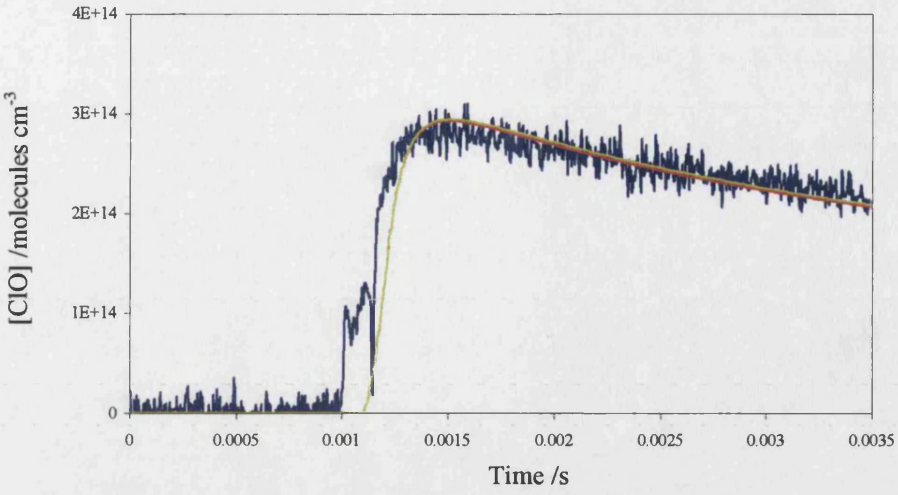

Figure 6.7: Experimental $[ClO]_t$ data (blue) and two modelled $[ClO]_t$ traces using k_{1b} : k_{1c} ratio of 6.3 :1 (red) and 12.6 : 1 (green), exposing the lack of sensitivity to k_{1c} associated with the $[ClO]_t$ data.

Furthermore, even if these small changes in the modelled temporal behaviour of ClO were reconcilable within the sensitivity limits they would also be critically dependent on any secondary chemistry exhibited by the ClO radical. This would become particularly problematic at lower temperatures where the poorly characterised reaction of ClO with OClO, (15) is expected to become increasingly significant, in addition to the self-reaction of the former (16).

(6.15) $ClO + OClO + M \leftrightarrow Cl_2O_3 + M$

(6.16) $ClO + ClO + M \leftrightarrow Cl_2O_2 + M$

Likewise, spectral monitoring of any BrCl absorption provided a potential means of quantifying the minor channel, (1c). However BrCl absorbs only weakly and its detection was hampered by an intense overlying Br_2 absorbance. Moreover several sources of BrCl exist in the complex reactive mixture, indeed numerical modelling showed that more than 95% of BrCl was generated through reactions (6) and (8), rather than (1c). These complexities eliminated any sensitivity to the quantification of the minor channel by this method. However, the overall rate coefficient k_1, along with that from the OClO producing channel, k_{1a} were determined as discussed in the following section.

6.3.2 Kinetics of the BrO + ClO Reaction

The kinetics of the BrO + ClO reaction were investigated at 298 K, 272 K, 228 K, and 210 K. A pressure dependent study of the reaction kinetics was undertaken at the lowest temperature, where the potential stabilisation of any $BrClO_2$* intermediate was likely to be most significant. At each temperature, the values of k_1 and k_{1a} were independently determined.

6.3.2.1 Kinetics at 298 K

Under the experimental conditions adopted, ClO radicals were produced and maintained in an excess over BrO. Thus the temporal behaviour of photolytically generated BrO radicals could be described by a pseudo-first order decay scheme:

$$\frac{-d[\mathrm{BrO}]}{dt} = k_1'[\mathrm{BrO}] \qquad \text{(6.ii)}$$

where $k_1' = k_1[\mathrm{ClO}]$. Integrating gives rise to a simple exponential solution for the time dependent BrO concentration, $[\mathrm{BrO}]_t$:

$$\ln[\mathrm{BrO}]_t = \ln[\mathrm{BrO}]_0 - k_1't \qquad \text{(6.iii)}$$

By applying the Beer-Lambert law:

$$\ln(A_{\mathrm{BrO},t}) = \ln(A_{\mathrm{BrO},0}) - k_1't \qquad \text{(6.iv)}$$

Hence k_1' can be determined without knowlege of the absolute time resolved BrO concentration. k_1 can then be determined providing $[\mathrm{ClO}]_t$ is known.

In similar fashion, since the $[\mathrm{OClO}]_t$ is determined readily by differentially fitting the ÓClO absorption cross sections, a classical solution to the OClO evolution kinetics can also be derived as follows:

(6.v) $$\frac{d[\mathrm{OClO}]}{dt} = k_{1a}'[\mathrm{BrO}]$$

Where $k_{1a}' = k_{1a}[\mathrm{ClO}]$ and substituting for [BrO] on the basis of (iii):

(6.vi) $$\frac{d[\mathrm{OClO}]}{dt} = k_{1a}'[\mathrm{BrO}]_0 e^{-k_1' t}$$

Integrating gives the following expression, where $[\mathrm{OClO}]_t = 0$ upon flashing at $t = 0$:

(6.vii) $$[\mathrm{OClO}]_t - [\mathrm{OClO}]_0 = \frac{k_{1a}'[\mathrm{BrO}]_0}{k_1'}(1 - e^{-k_1' t})$$

This solution defines k_1' and hence k_1 again from knowledge of the excess [ClO] present during the OClO buildup. Moreover, using the absolute value of $[\mathrm{BrO}]_0$ obtained from the fit to the BrO temporal data gives a direct determination of the branching ratio to channel (1a), k_{1a}/k_1. In practice, non-linear least squares fitting was employed to fit simulated decay traces to the $[\mathrm{BrO}]_t$ and $[\mathrm{OClO}]_t$ data *simultaneously* by optimising the k_1, k_{1a}, and $[\mathrm{BrO}]_0$ parameters and inputting the average $[\mathrm{ClO}]_t$ value into the model. The typical quality of this classical solution to the experimental data is shown in figure 6.8.

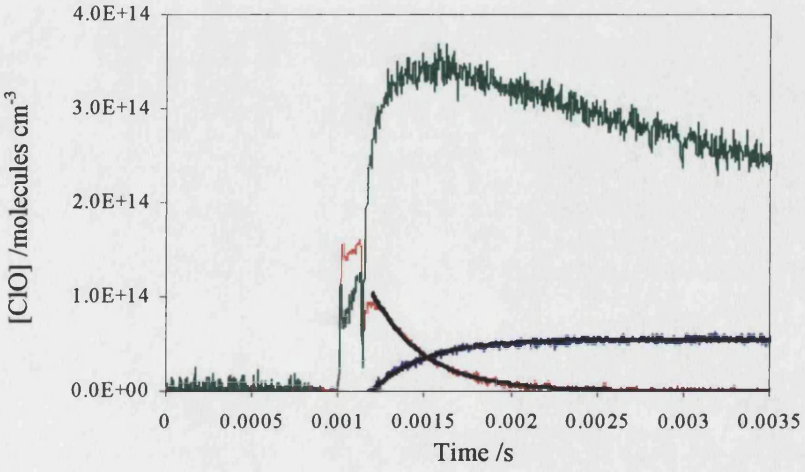

Figure 6.8: Classical first order fits to the $[\mathrm{ClO}]_t$ and $[\mathrm{BrO}]_t$ data recorded at 298 K.

In practice, the rapid decay timescales of both BrO and ClO radicals could not be completely decoupled from the timescales of their formation. This would lead to a systematic underestimation in the fitted values of both k_1 and k_{1a} in this simple analysis. Thus, to minimise this effect the immediate post-flash data was not included in the fitting scheme.

From 10 experiments over a range of precursor concentrations and hence $[BrO]_0$ values, the following kinetic parameters were determined for the BrO + ClO reaction at 298 K :

$$k_{1,298K} = (1.06 \pm 0.23) \times 10^{-11} \text{ cm}^3 \text{ molecule}^{-1} \text{ s}^{-1}$$

$$k_{1a,298K} = (5.33 \pm 0.47) \times 10^{-12} \text{ cm}^3 \text{ molecule}^{-1} \text{ s}^{-1}$$

The uncertainties are statistical only, quoted at the 95% confidence limits. These fitted rate coefficients gave rise to a branching ratio for the OClO production channel of the BrO + ClO reaction of $\alpha_{1a} = k_{1a}/k_1 = 0.50 \pm 0.12$.

In addition to the overlapping of radical formation and decay timescales, a small dependence of the returned kinetic parameters on the experimental $[Cl_2O]/[O_3]$ ratio was observed from this simple analysis. Specifically, the overall rate coefficient k_1 derived from the BrO decays exhibited a slight anticorrelation with $[Cl_2O]/[O_3]$, suggesting that a small amount of BrO regeneration was occurring *via* (7) rather than (6):

(6.6) $Br + Cl_2O \rightarrow ClO + BrCl$

(6.7) $Br + O_3 \rightarrow BrO + O_2$

Thus, in order to account for this deviation from pseudo-first order kinetics and to provide a more rigorous treatment of the formation/decay phenomenon and other secondary chemistry, numerical modelling was employed. A FACSIMILE[29] model was developed which incorporated all of the known precursor concentrations and all of the

recognised secondary chemistry. The kinetic data describing these processes is given in table 6.5.

Reaction	k(T)	Source
$Br + Cl_2O \rightarrow BrCl + ClO$	$k_6 = 2.1 \times 10^{-11} exp\ (-470/T)$	DeMore *et al.*[2]
$Br + O_3 \rightarrow BrO + O_2$	$k_7 = 1.7 \times 10^{-11} exp\ (-800/T)$	DeMore *et al.*
$Cl + Br_2 \rightarrow BrCl + Br$	$k_8 = 2.3 \times 10^{-10} exp\ (135/T)$	Bedjanian *et al.*[30]
$Cl + Cl_2O \rightarrow Cl_2 + ClO$	$k_9 = 6.2 \times 10^{-11} exp\ (130/T)$	DeMore *et al.*
$Cl + O_3 \rightarrow ClO + O_2$	$k_{10} = 2.9 \times 10^{-11} exp\ (-260/T)$	DeMore *et al.*
$O(^1D) + N_2 \rightarrow O(^3P) + N_2$	$k_{11} = 1.8 \times 10^{-11} exp\ (110/T)$	DeMore *et al.*
$O(^3P) + Br_2 \rightarrow BrO + Br$	$k_{12} = 5.1 \times 10^{-13} exp\ (989/T)$	Harwood *et al.*[12]
$O(^3P) + Cl_2O \rightarrow 2ClO$	$k_{13} = 2.7 \times 10^{-11} exp\ (-530/T)$	DeMore *et al.*
$O(^3P) + O_2 + N_2 \rightarrow O_3 + N_2$	$k_{14} = 5.1 \times 10^{-13} exp\ (989/T)$	DeMore *et al.*
$ClO + OClO + N_2 \rightarrow Cl_2O_3 + N_2$	$k_{15} = [M]\ 6.2 \times 10^{-32} exp\ (T/300)^{-1.5}$	DeMore *et al.*
$Cl_2O_3 + N_2 \rightarrow ClO + OClO + N_2$	$k_{-15} = k_{15}/\{[M]1.1 \times 10^{-24} exp\ (5455/T)\}$	DeMore *et al.*
$ClO + ClO + N_2 \leftrightarrow Cl_2O_2 + N_2$	See chapter 4	This work
$Cl_2O_2 + N_2 \leftrightarrow ClO + ClO + N_2$	See chapter 4	This work
$OClO_{(g)} \rightarrow OClO_{(ads)}$	Optimised (T < 272 K)	This work
$ClOO \rightarrow Cl + O_2$	$k_{19} = 2.8 \times 10^{-10} exp\ (-1820/T)$	DeMore *et al.*
$BrO + BrO \rightarrow 2Br + O_2$	$k_{20a} = 5.3 \times 10^{-12} exp\ (-211/T)$	Harwood *et al.*
$BrO + BrO \rightarrow Br_2 + O_2$	$k_{20b} = 1.1 \times 10^{-14} exp\ (983/T)$	Harwood *et al.*

Table 6.5: Kinetic data used in the FACSIMILE model to optimise k_1 and k_{1a}. Associated units are $cm^3\ molecule^{-1}\ s^{-1}$.

The chemical reactions given in table 6.6 were also considered for inclusion within the FACSIMILE model but brief investigation indicated that they exerted no observable influence on the concentrations of the ClO, BrO and OClO radicals.

Reaction	Source
$Br + BrCl \rightarrow Br_2 + Cl$	DeMore *et al.*2
$Cl + BrCl \rightarrow Br_2 + Cl$	DeMore *et al.*
$Br + Br + N_2 \rightarrow Br_2 + N_2$	Sander and Watson[31]
$Cl + OClO \rightarrow 2ClO$	DeMore *et al.*
$Br + OClO \rightarrow ClO + BrO$	DeMore *et al.*
$O(^3P) + BrO \rightarrow Br + O_2$	DeMore *et al.*
$O(^3P) + ClO \rightarrow Cl + O_2$	DeMore *et al.*
$Cl + BrO \rightarrow ClO + Br$	DeMore *et al.*
$Br + ClO \rightarrow ClO + Br$	DeMore *et al.*

Table 6.6: Reactions which exerted no significant influence on the modelled ClO, BrO and OClO concentrations.

For each experiment the $[BrO]_t$, $[OClO]_t$ and the $[ClO]_t$ data were fitted using numerically simulated traces, optimising k_1, k_{1a} and separate parameters accounting for the fractional photolysis of O_3 and Br_2, leading predominantly to the formation of BrO and ClO radicals respectively. A typical fit of the FACSIMILE model to the experimental data is shown in figure 6.9.

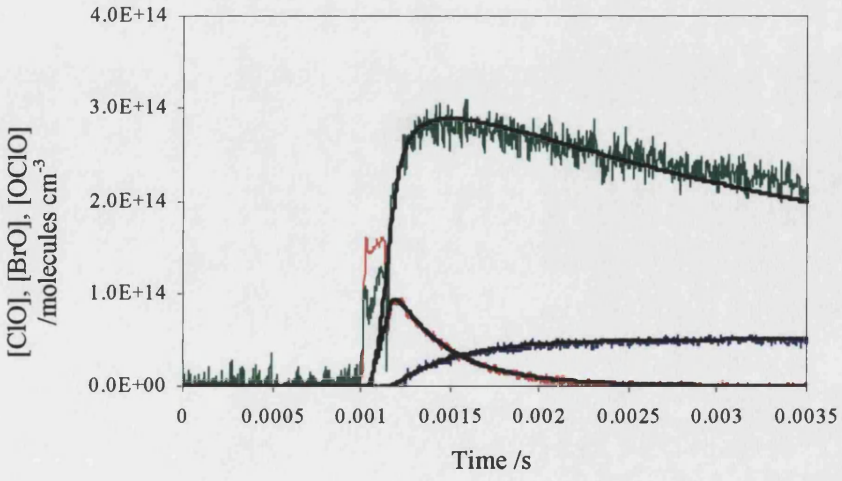

Figure 6.9: FACSIMILE fit to the three transient absorbers, optimising k_1 and k_{1a}.

Fitting the same 10 data sets as before, the following 298 K rate coefficients were determined, leading to a branching ratio for the OClO producing channel, $\alpha_{1a} = 0.46 \pm 0.07$.

$$k_{1,298K} = (1.15 \pm 0.16) \times 10^{-11} \text{ cm}^3 \text{ molecule}^{-1} \text{ s}^{-1}$$

$$k_{1a,298K} = (5.34 \pm 0.27) \times 10^{-12} \text{ cm}^3 \text{ molecule}^{-1} \text{ s}^{-1}$$

6.3.2.2 Temperature Dependence of the BrO + ClO Kinetics

Analogous experiments to those at 298 K were carried out to characterise the rate coefficient of the BrO + ClO reaction at reduced temperatures. However, at temperatures below 298 K, the $[OClO]_t$ data exhibited more complex kinetic behaviour. Numerical modelling suggested that formation of a Cl_2O_3 adduct between OClO and ClO was responsible for this phenomenon:

(6.15) $\quad ClO + OClO + M \leftrightarrow Cl_2O_3 + M$

The data recorded at 272 K were readily fitted by incorporating (15) into the numerical model, using kinetic data from DeMore *et al.*[2] However, at temperatures below 272 K incorporation of all the known gas phase chemistry could still not facilitate an adequate fit to the $[OClO]_t$ data. Figure 6.10 shows a typical experimental trace recorded at 228 K.

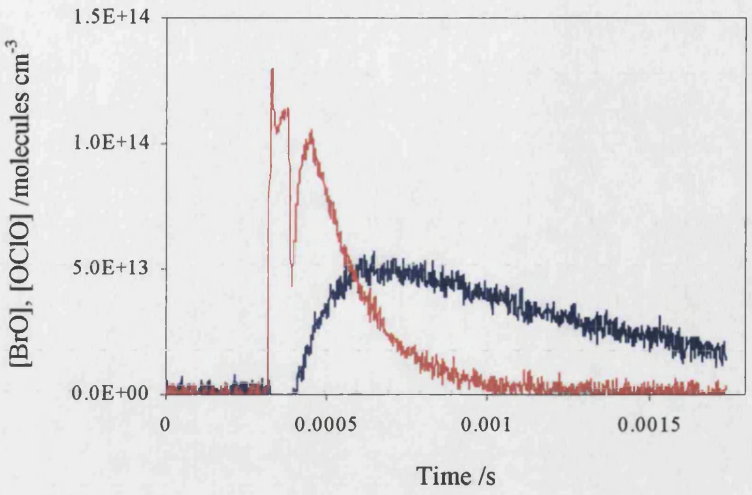

Figure 6.10: 228 K $[OClO]_t$ (blue) and $[BrO]_t$ (red) concentration versus time profile illustrating the zeroth order loss process.

It is clear from figure 6.10 that a process operates depleting $[OClO]_t$ which continues long after $[BrO]_t$ has reached zero. The linear nature of this $[OClO]_t$ decay on long timescales indicated that the decay kinetics were independent of the absolute $[OClO]_t$, *i.e.* a zeroth order effect. This was attributed to a heterogeneous process, during which OClO was adsorbed onto the walls of the reaction vessel:

(6.17) $\quad OClO_{(g)} \rightarrow OClO_{(ads)}$

For each data set at 228 K and at 210 K, the rate of OClO loss *via* this mechanism, k_{17} was determined from the gradient of the $[OClO]_t$ data at long timescales. However, this method provided only an approximation to k_{17} in the presence of other processes affecting $[OClO]_t$. FACSIMILE modelling indicated that reaction (15) operated on a similar timescale to (17). Since (15) represents a dynamic equilibrium, any influence on $[OClO]_t$ by (17) will have a systematic effect on the OClO flux through (15). As a result of this synergistic effect, it was not possible to independently measure k_{17}. Indeed the coupling of the two processes would be complicated further by the possible desorption of OClO molecules from the vessel walls (-17). The linear decay kinetics at long timescales suggested that this process was negligible under the experimental conditions adopted but further investigation was considered beyond the scope of this work.

The approximate k_{17} values were incorporated into, but not optimised within, the numerical model used to fit the $[BrO]_t$, $[OClO]_t$ and the $[ClO]_t$ data. However, the model could still not reproduce the experimental OClO kinetics at long timescales.

This poor fitting of the OClO temporal behaviour was attributed to the incorporation of both the literature k_{15} and k_{-15} parameters along with an estimated k_{17} value which would inevitably have been affected by k_{15} and k_{-15}. Moreover, it was not possible to investigate the Cl_2O_3 kinetics independently in this system since the absorption spectrum of Cl_2O_3 is overlapped strongly by that of ClO. Further, only the differential ClO cross section was measured in this study, thus it was not possible to remove the absolute ClO absorption in the search for residual Cl_2O_3. Nevertheless the ability to monitor ClO and OClO radicals simultaneously did provide a degree of sensitivity to the kinetics of (15), although this was limited given the competing processes involving both ClO and OClO.

Sensitivity of the OClO traces to k_{1a} tends to zero as $[BrO]_t$ tends to zero (and $[OClO]_t$ tends to a limiting value in the absence of secondary processes such as (15) and (17)). Thus fitting the long time $[OClO]_t$ data was not crucial in determining the value of k_{1a}. However in an attempt to reconcile the source of this long timescale issue with the assumed secondary OClO chemistry, k_{-15} was also optimised in fitting the three concentration versus time profiles. The first guess k_{-15} values were calculated from the NASA recommendations[2] of k_{15} and K_{eq} for reaction (15). The database for these parameters is sparse but those existing studies are in reasonable agreement.[32]

In this analysis, k_{-15} was chosen as the variable parameter rather than k_{15} or indeed K_{15}, since the former did not significantly influence the $[OClO]_t$ kinetics at short timescales, where sensitivity to k_{1a} was maximised. Figures 6.11 and 6.12 demonstrate this - showing modelled OClO concentrations under typical conditions where k_{15} and k_{-15} have been varied respectively.

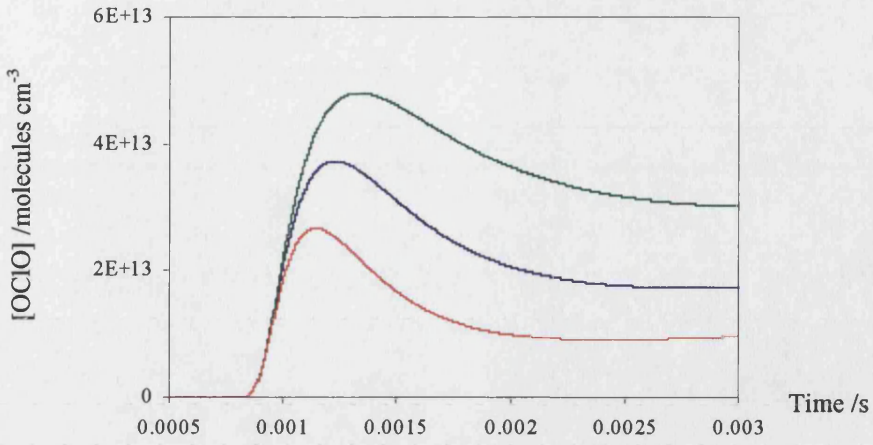

Figure 6.11: Modelled $[OClO]_t$ trace at 298 K and 760 Torr using the recommended k_{15} value of 9.8×10^{-12} cm^6 $molecules^{-2}$ s^{-1} (blue)[2]. Variations in k_{15} by factors of 0.5 and 2 lead to $[OClO]_t$ traces shown in green and red respectively.

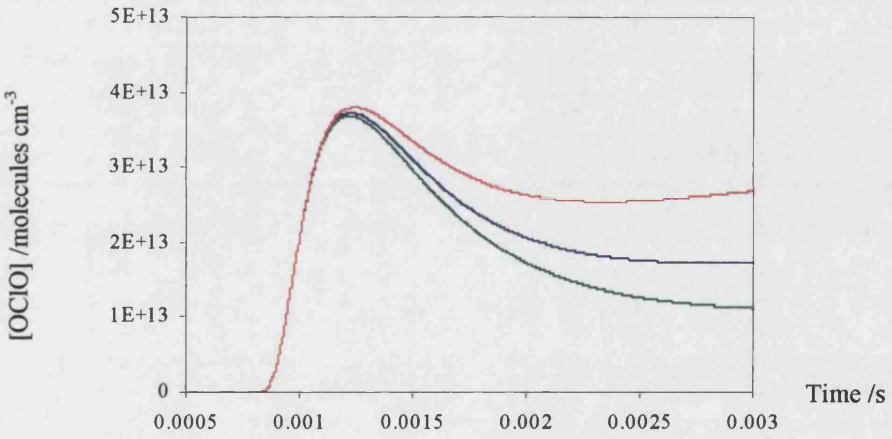

Figure 6.11: Modelled $[OClO]_t$ trace at 298 K and 760 Torr using the recommended k_{-15} value of 360 s^{-1} (blue)[2]. Variations in k_{-15} by factors of 0.5 and 2 lead to $[OClO]_t$ traces shown in green and red respectively.

It is clear that k_{15} exerts a significant influence on the OClO formation kinetics at short post-flash timescales and would exert a corresponding influence on the optimised value of k_{1a}. By contrast k_{-15} exerts a negligible effect on the OClO build up, but plays a key role at longer timescales, where the model has little or no sensitivity to k_{1a} but difficulty in reproducing the experimental $[OClO]_t$ data.

Thus k_1, k_{1a}, and k_{-15}, in addition to parameters determining the fractional photolysis of precursor Br_2 and O_3 were optimised in fitting the model to experimental traces at 228 K and 210 K. Typical fits to the experimental data recorded at 228 K and 210 K are shown in figures 6.13 and 6.14 respectively.

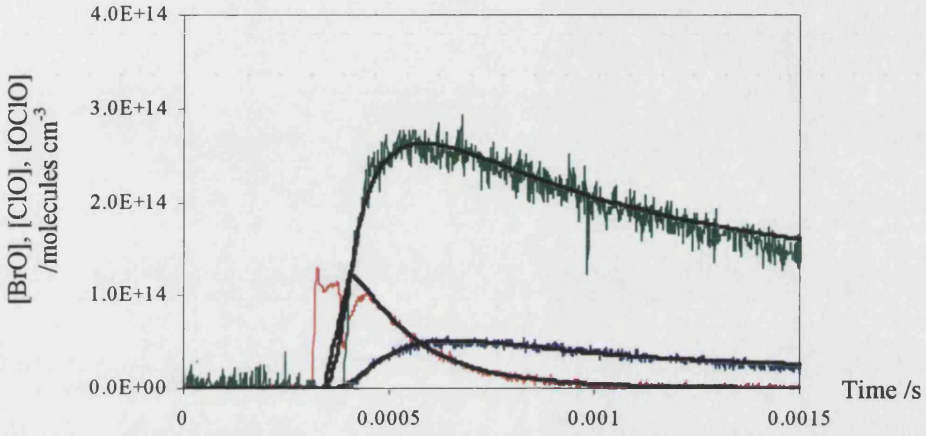

Figure 6.13: FACSIMILE fits to the temporally resolved concentrations of the three transient absorbers recorded at 228 K.

At 210 K both $[BrO]_0$ and $[ClO]_0$ were limited by the experimentally attainable Br_2 concentration in the precursor gas mixture. Br_2 flows were kept low enough to ensure that the saturated vapour pressure of Br_2 was never exceeded. This reduced signal led in turn to a reduced signal to noise ratio, and precluded experiments at lower temperatures.

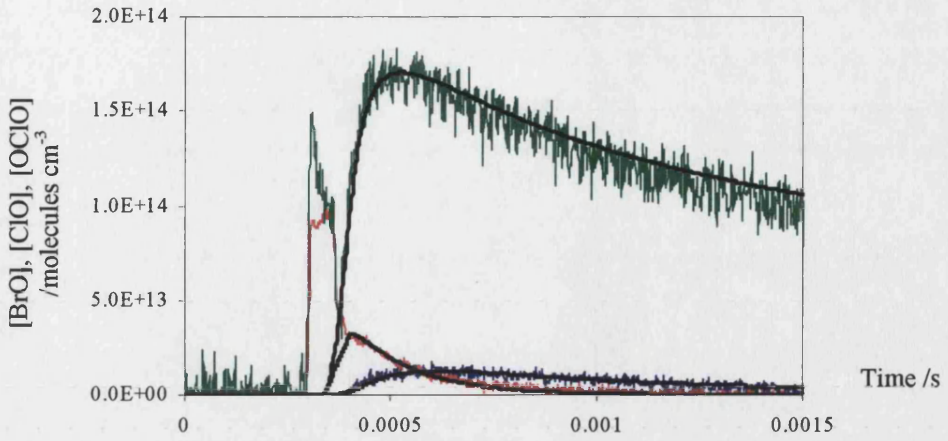

Figure 6.14: FACSIMILE fits to the temporally resolved concentrations of the three transient absorbers recorded at 210 K.

The temperature dependent determinations of k_1 and k_{1a} are summarised in Table 6.7. The optimised k_{-15} parameters are not quoted since they do not reflect an accurate determination of this parameter due to the systematic error imposed by the zeroth order loss of OClO. During the numerical fitting of the data, the deviation of the returned k_{-15} value from the NASA[2] value was typically 15%.

Temperature /K	k_1/cm^3 molec^{-1} s^{-1}	k_{1a}/ cm^3 molec^{-1} s^{-1}
298	$(1.15 \pm 0.08) \times 10^{-11}$	$(5.34 \pm 0.27) \times 10^{-12}$
272	$(1.58 \pm 0.08) \times 10^{-11}$	$(6.00 \pm 0.97) \times 10^{-12}$
228	$(1.59 \pm 0.34) \times 10^{-11}$	$(1.25 \pm 0.17) \times 10^{-11}$
210	$(2.86 \pm 0.32) \times 10^{-11}$	$(1.78 \pm 0.46) \times 10^{-11}$

Table 6.7: Kinetic parameters determined from FACSIMILE fits to the temperature dependent data.

Notwithstanding the determination of only four temperature dependent rate coefficients for k_1 and for k_{1a}, both parameters were well described by Arrhenius temperature dependencies, whereby:

$$k_1 = (2.1 \pm 1.6) \times 10^{-12} \exp\{(521 \pm 197)/T\}$$

$$k_{1a} = (2.5 \pm 0.8) \times 10^{-13} \exp\{(895 \pm 79)/T\}$$

Errors are quoted at the 95% confidence limits. These temperature dependencies are shown and discussed with regard to other determinations in section 6.4, below.

6.3.3 Sensitivity Study and Potential Sources of Error

A sensitivity study was conducted at 228 K to assess the dependence of the optimised k_1 and k_{1a} values on the secondary chemistry included in the numerical model. A representative set of experimental BrO, ClO and OClO concentration profiles were repeatedly reanalysed using a reaction scheme where each secondary rate coefficient was either increased or decreased in turn by a factor of 2. This study was performed at 228 K since it represented an intermediate temperature within the investigated range where the complex OClO chemistry, involving zeroth order loss and Cl_2O_3 formation was clearly evident. The percentage changes in the returned k_1 and k_{1a} from each FACSIMILE fit are shown in figure 6.15. Those secondary rate coefficients whose variation by a factor of two resulted in a change in the sum of residuals of less than 2% exerted no measurable influence on the optimised values of k_1 or k_{1a} and have been omitted from figure 6.15.

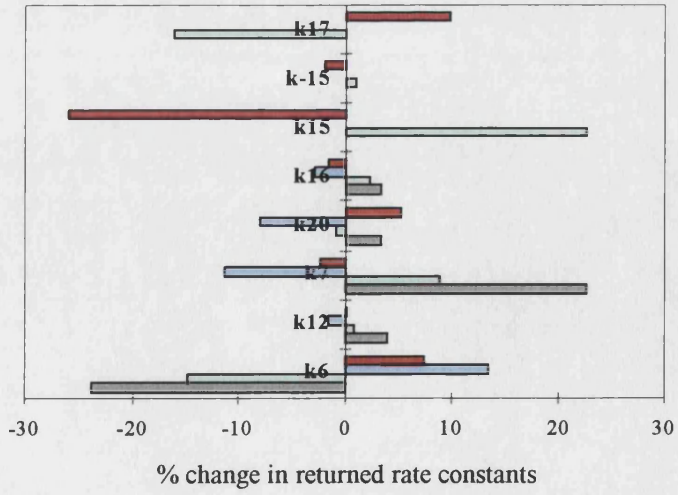

Figure 6.15: % changes in returned values of k_1 (blue, grey) and k_{1a} (red, green) as the value of a secondary rate constant is changed by a factor of 2 or 0.5 respectively.

Figure 6.15 shows a strong dependence of the optimised k_{1a} value on the forward rate coefficients k_{15} and k_{17}. Only two studies of k_{15} exist: Burkholder *et al.*[36] investigated the pressure dependence (40-250 Torr) of k_{15} between 220 and 260 K, observing falloff behaviour over the entire temperature range. Parr *et al.*[33] measured k_{15} at 226 K between pressures of 4 and 28 Torr. Their data do not overlap those of Burkholder et al. in the pressure domain, but extrapolation of the Parr *et al.* data is in good agreement with the data obtained by Burkolder *et al.* at higher pressures. In this study, modelling indicated that reaction 15 only exerted a significant effect on the OClO kinetics at the lowest two temperatures (210 and 228 K) investigated. Thus any significant error in the literature value of k_{15} employed could be manifested as systematic deviation of k_{1a} from Arrhenius behaviour over the temperature regime studied, as the contribution of k_{15} to the OClO kinetics increased with decreasing temperature. Since no such systematic deviation was observed this could indicate that reaction 15 was correctly accounted for in the numerical analysis of data reported here. In any case the uncertainty associated with k_{15} is certainly smaller than the factor of 2 adopted in the sensitivity study, and consequently is not considered a significant source of error in the reported k_{1a}.

The zeroth order loss process for OClO observed in this work has not been reported previously so there is no basis for comparison of the extracted k_{17} values. In any case, this parameter is probably dependent on the nature of the reaction vessel given the proposed heterogeneous mechanism. Since the $[OClO]_t$ data was essentially linear following BrO consumption at long timescales, extraction of the zeroth order rate coefficient in this time period was, to a first approximation, reliable. Inevitably some contribution of k_{-15} was inherently confused within this parameterisation of k_{17} given the role of (-15) at long timescales. During this period zeroth order OClO loss is mitigated by the release of OClO following the perturbation of the ClO+OClO/Cl_2O_3 equilibrium by ClO dimerisation, (16). This confusion probably gave rise to the need to optimise k_{-15} within the data fitting model, to account for OClO behaviour at long timescales. Nevertheless the sensitivity study clearly shows that k_{-15} exerts a negligible effect on the returned values of k_1 and k_{1a}, in corroboration with figures 6.11 and 6.12.

Figure 6.15 clearly illustrates the dependence of the returned k_1 and k_{1a} values on the the rates of the Br + Cl_2O (6) and Br + O_3 (7) reactions. Coupled with the concentrations of Cl_2O and O_3, k_6 and k_7 determine the extent of BrO regeneration:

(6.viii) Fractional BrO regeneration = k_6 [O_3] / k_7 [Cl_2O]

The concentrations of O_3 and Cl_2O were readily measured in the pre-flash period of each experiment by fitting the appropriate absorption cross sections. The error in determining these concentrations was negligible (< 5%). Moreover, several studies of the temperature dependence of k_6 are available in the literature, all of which are in good agreement. A best fit parameterisation incorporating all of these data was used in this investigation, in accordance with the NASA evaluation.[2] As a result k_6 is not considered to be a significant source of error within the numerical model.

By contrast, only two investigations into the temperature dependence of k_7 have been published. The Arrhenius parameterisation reported by Stevens and Anderson[34] gives rise to a k_7 value of 3.1×10^{-12} molecules^{-1} cm^3 s^{-1} at 228 K. However the parameterisation quoted by Sander and Friedl[13] yields a value of k_7 value of 2.1×10^{-12} molecules^{-1} cm^3 s^{-1} at the same temperature. The value used was the mean of these two figures, once again in line with the NASA evaluation. The use of the higher or lower literature value results in changes in the optimised k_1 value of +3% and -5% respectively.

In addition to the precision errors associated with the optimised k_1 and k_{1a} values (all quoted at the 95% confidence level) and the uncertainties imposed by the complex secondary chemistry, the absorption cross sections used to quantify ClO, BrO and OClO concentrations also exert a degree of uncertainty.

k_1, determined by the loss rate of BrO in the presence of a known ClO concentration is virtually insensitive to the value of the BrO cross section, since it is effectively a first order process in the absence of the minor distortion imparted by the overlapping of BrO formation and decay timescales. However the 13% uncertainty on the ClO cross

section exerts the same uncertainty on the extracted k_1 value and this should be combined with the precision error associated with the Arrhenius expression for k_1 when employing $k_1(T)$ measured during this study.

In similar fashion, the optimised values of k_{1a} are sensitive to the absolute concentrations and hence the cross sections of BrO, ClO and OClO. This more complex dependence arises from the measurement of k_{1a} relative to $[BrO]_0$. Combination of the uncertainties associated with these three cross sections gives rise to an additional 17% systematic error on the optimised k_{1a} values.

6.3.4 Pressure Dependence of the BrO + ClO Reaction at 210 K

The existence of termolecular channels of the ClO + ClO and BrO + BrO reactions have been described above and in previous chapters. By analogy it has been suggested that a $BrClO_2$ product channel may exist to the BrO + ClO reaction, although no conclusive laboratory evidence has ever been presented as proof or disproof. Avallone and Toohey[5] have published tentative evidence for the existence of a $BrClO_2$ adduct at 210 K, based on anomalous BrO/Br_y ratios in the Arctic stratosphere. Theoretical chemical studies have also proposed the existence of three isomers of $BrClO_2$, where BrOOCl is the most stable.[11]

The database on the BrO + ClO reaction is sparse in comparison to those of the respective self-reactions of the constituent radicals. Indeed no investigation into the kinetics of the BrO + ClO reaction has ever been undertaken at temperatures below 220 K. Pressure dependencies associated with termolecular adduct formation have been observed over a wide temperature range for the Cl_2O_2 species[2] and at temperatures below 250 K for the Br_2O_2 species.[12]

A pressure dependent investigation into the kinetics of the BrO + ClO reaction at 210 K was undertaken in an attempt to confirm or deny the existence of channel (1d) at this temperature. Whilst $[BrO]_t$, $[ClO]_t$ and $[OClO]_t$ were all monitored during the course of the experiments, *via* their vibronic signatures, two factors prevented the inclusion of the $[OClO]_t$ data in the numerical fit. First, any pressure dependence of the zeroth

order loss process for OClO, (17) was unknown and could not be characterised readily. Secondly, reaction (15) is termolecular and therefore exerts a pressure dependence of its own on the OClO kinetics. As a result, fitting to the $[BrO]_t$ and $[ClO]_t$ data provided sensitivity to the overall rate coefficient, k_1 only. The results of this pressure dependent study are illustrated in figure 6.16

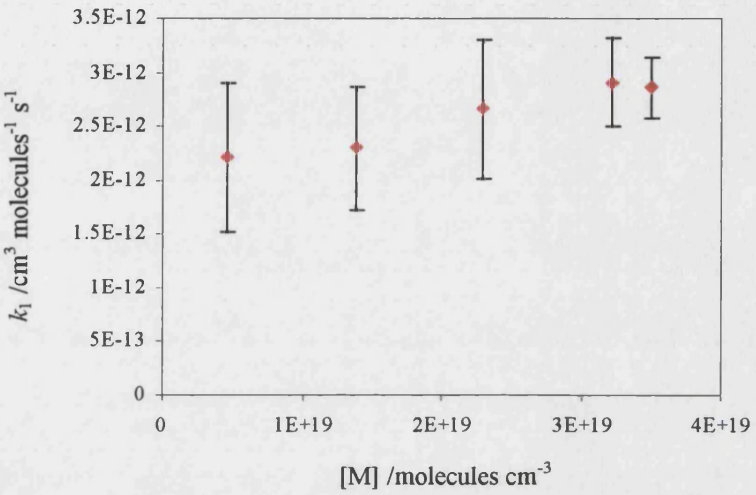

Figure 6.16: Pressure dependence of k_1 at 210 K.

The optimised values of k_1 show a small systematic dependence on the experimental pressure. However, given the large error bars associated with the data, no significant pressure dependence can be unequivocally assigned to the BrO + ClO reaction at 210 K.

It was not possible to reduce the uncertainty associated with low temperature k_1 measurements, since the absolute initial radical concentration was limited by the Br_2 vapour pressure, and subsequent BrO decay was rapid, on a timescale approaching the limit of CCD charge shifting. At low pressures a further restraint on $[BrO]_0$ was imposed by a decrease in precursor $[O_3]$ arising from pressure dependence of (14), following the mercury lamp photolysis of molecular oxygen:

(6.14) $\quad O(^3P) + O_2 + N_2 \quad \rightarrow \quad O_3 + N_2$

This reduced operational [O_3] led to a reduction in the concentration of photolytically generated O atoms and, correspondingly, $[BrO]_0$.

6.3.5 Spectroscopic Evidence for $BrClO_2$ and OBrO Production

Both the ClO and BrO dimers absorb strongly in the near UV spectral region. Several studies of the Cl_2O_2 absorption cross section exist,[35,36] each reporting a absorption maximum at 246 ± 1 nm. The Br_2O_2 spectrum, exerting a maximum at 305 nm, has been recorded by Harwood *et al*[12]. Figure 6.17 shows the Br_2O_2 absorption cross section in comparison with the Cl_2O_2 spectrum reported by DeMore *et al*[35].

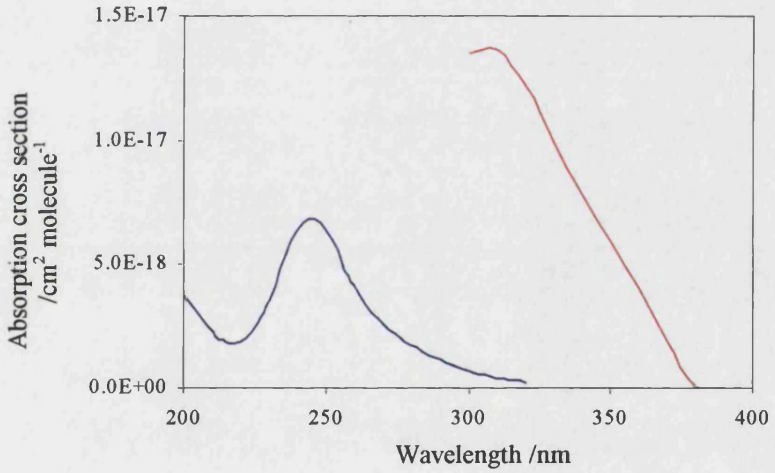

Figure 6.17: Reported Cl_2O_2, and Br_2O_2 spectra shown in blue and red respectively.

A similarity in the shape of the published spectra is evident. This similarity in spectral shape, in conjunction with a redshifted and increased spectral magnitude associated with successively heavier halogen atoms is a trend observed across many inorganic halogen families (eg. Cl_2/BrCl/Br_2/BrI/I_2 and ClO/BrO/IO). As a result, $BrClO_2$ might also be expected to absorb in the near UV, most likely with an absorption maximum near 275 nm, half-way between the spectra of Cl_2O_2 and Br_2O_2.Figure 6.18 compares two time resolved absorption spectra recorded following flashlamp initiation of the gaseous $Br_2/Cl_2/Cl_2O/O_3/O_2/N_2$ mixture at 210 K and 760 Torr, where termolecular $BrClO_2$ stabilisation is likely to be most efficient.

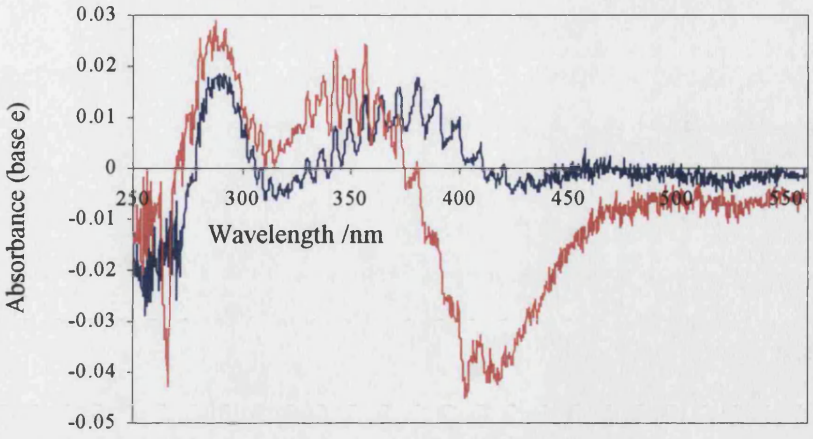

Figure 6.18: Spectra showing changes in absorption in the immediate (red) and late post-flash (blue).

The red spectrum in Figure 6.18 was recorded in the period immediately following the flash ((4.5–5.0) × 10^{-4}) s after flashing). The blue spectrum was recorded much later ((1.1–1.5) × 10^{-3}) s after flashing), when the BrO decay was complete and the concentration of any adduct would be maximised. Unfortunately the signal to noise ratio was not high enough to undertake a comprehensive spectral deconvolution process, given that ClO, Cl_2O_2, O_3, Cl_2O and Cl_2O_3 all absorb in this region. However, no clear evidence for significant absorption attributable to a $BrClO_2$ adduct is observed around 275 nm or elsewhere in the near UV/ visible spectral region monitored.

Knight *et al.*[37] have shown that OBrO exhibits very strong vibronic structure between 450 and 550 nm. Back to back experiments were therefore attempted, covering the short wavelength (270-335 nm) and long wavelength (470-535 nm) regions alternately. No such structure was observed in the 470-535 nm region over the entire temperature range of these experiments. Based on the detection limits associated with the differential OBrO cross section, an upper limit of $\alpha_{1e} = k_{1e}/k_1 < 0.02$ is placed upon the hypothetical OBrO producing channel, (1e) between 210 and 298 K.

6.4 Discussion

Figure 6.19 shows the measured temperature dependence of k_1 in comparison to those results available in the literature.

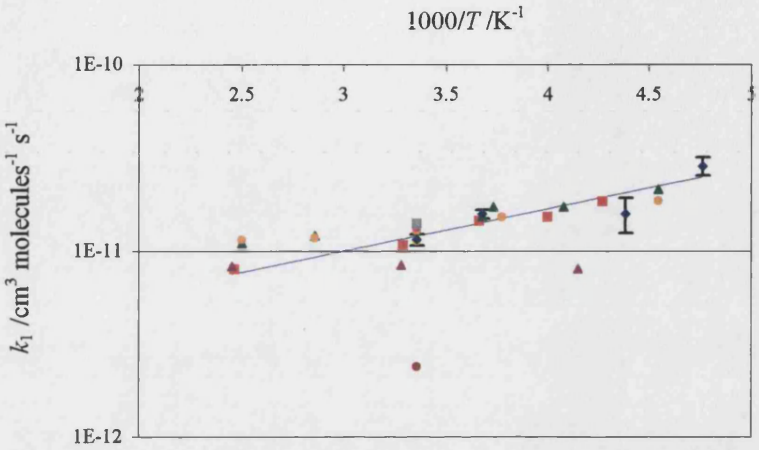

Figure 6.19: Temperature dependence of k_1 at 760 Torr (blue). Also shown for comaparison are the data by Hills et al.[38] (purple triangles), Basco and Hunt[39] (brown circle), Turnipseed et al.[15] (red squares), Sander and Friedl[13] (orange circles), Friedl and Sander[14] (green triangles), Toohey and Anderson[40] (grey square), Poulet et al.[41] (yellow circle), Clyne and Watson[42] (pink square).

With the exception of the data reported by Hills *et al.*[38], all the previous studies have reported that k_1 adopts well constrained Arrhenius behaviour incorporating a negative activation energy. The results from this study are in excellent agreement over the entire temperature range with the data reported by Turnipseed *et al.*[15] who employed discharge flow/mass spectrometry apparatus in their investigation. Furthermore the 298 K results are in good agreement with the k_1 measurements by Toohey and Anderson[40], Clyne and Watson[42] and Poulet *et al.*[41]

A stronger negative temperature dependence is reported here than was observed in both investigations by the co-authors Friedl and Sander which are in mutual agreement. The reason for this difference in observed temperature dependence is unclear, especially given any systematic error would be reduced by their use of different experimental techniques (DF/MS[14], FP/UV[13]). However, their UV/visible spectroscopy

are flawed by the monitoring of both BrO and ClO at single wavelengths, where multiple underlying absorbances are significant in both cases.

The k_1 measurements quoted by Hills *et al.* are in stark contrast to all the other data sets in that they suggest that the kinetics of the BrO + ClO reaction are independent of temperature. Friedl and Sander[14] have attributed these anomalous results to a distortion of the observed kinetics arising from secondary chemistry. In particular they cite regeneration of BrO radicals *via* the reaction of Br atoms with O_3 as the cause of this distortion, since Hills *et al.* failed to account for halogen atom production through channels (1a) and (1b) when evaluating their k_1 and k_{1a} coefficients.

Figure 6.20 shows an Arrhenius plot of the k_{1a} data alongside the results from existing studies.

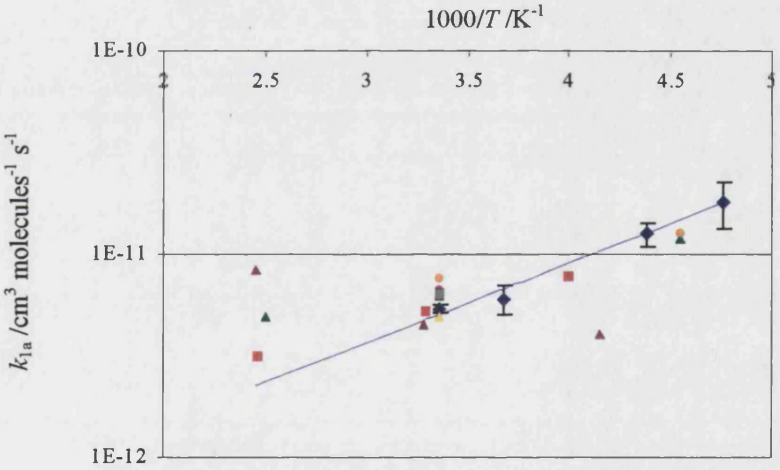

Figure 6.20: Temperature dependence of k_{1a} at 760 Torr (blue). Also shown for comaparison are the data by Hills et al.[38] (purple triangles), Turnipseed et al.[15] (red squares), Sander and Friedl[13] (orange circles), Friedl and Sander[14] (green triangles), Toohey and Anderson[40] (grey square), Poulet et al.[41] (yellow circle), Clyne and Watson[42] (pink square).

The results reported here are in reasonable agreement with the previously determined k_{1a} values, although a stronger temperature dependence is evident once again. The temperature dependence reported in this study is considered to provide the most accurate parameterisation of k_{1a}. None of the previous investigations were able to

measure the rate of k_{1a} at more than three, and in some cases, two temperatures. As a result their Arrhenius parameterisations are poorly constrained by the paucity of data. All of the studies employing the DF/MS technique[14,15,40,41,42,42] produced ClO by reacting Cl atoms with either Cl_2O or OClO. An equal (or in some cases excess) concentration of Cl atoms were employed with respect to OClO or Cl_2O, to ensure complete consumption of the respective precursor molecules, facilitating the subsequent monitoring of OClO following production *via* channel (1a). However, in the absence of excess Cl_2O concomitant halogen atom production from (1a) and (1b) gives rise to subsequent reaction with OClO:

(8) $Cl + Br_2 \rightarrow BrCl + Br$

(18) $Br + OClO \rightarrow BrO + ClO$

As a result the anticipated OClO formation kinetics describing channel (1a) are distorted. Poulet *et al.*[41] noted that (18) did proceed in their experiments and they corrected for it. Despite the large error associated with k_{18} (approximately 100% at the 1σ level) it is interesting to note that the 298 K value of k_{1a} reported by Poulet *et al.* is in closest agreement with the measurement from this study. No study of the temperature dependence of k_{18} has ever been published in the open literature. Failure to correct for this OClO loss route in the literature DF/MS experiments could give rise to the discrepancies in the temperature dependence of k_{1a} (and to some extent k_1) observed in comparison to that reported in this study.

The FP/UV study published by Sander and Friedl[13] would not be susceptible to this source of systematic error since they employed a similar chemical system to that of the present study, incorporating excess Cl_2O. Moreover, these the authors were only able to measure k_{1a} at two temperatures, the lower of which was at 220 K. However, they did not monitor the temporal evolution of OClO, but measured the "final" OClO concentration once the BrO decay was complete. As a result they would not have been able to observe any zeroth order OClO loss if it were occurring in their reaction vessel at low temperatures in the same way that it was observed at 228 K and 210 K during the course of these experiments. If this process were occurring in their system then

they would underestimate k_{1a} at 220 K, biasing their observed temperature dependence of k_{1a} further away from that reported here.

6.5 Conclusions

The temperature dependencies of k_1, the overall rate coefficient and k_{1a}, the OClO producing channel have both been measured. Both show good Arrhenius behaviour and follow a negative temperature dependence. This negative temperature dependence provides evidence for the formation of a metastable intermediate $BrClO_2$* with a subsequent barrier to product formation. At 210 K, the lowest temperature investigated in this study, a systematic dependence of k_1 on the total pressure was observed. However, given the large error bars associated with the low temperature data, the pressure dependence cannot be unequivocally assigned to a termolecular adduct formation channel (1d) and the apparent correlation may just represent scatter. The search for a pressure dependence of k_1 is particularly difficult given the fast competing bimolecular processes which would give rise to a positive intercept on any Troe type falloff data.

Assuming BrOOCl is the sole isomer of the adduct produced by the following mechanism (by analogy to the weight of the data regarding the BrO + BrO and ClO + ClO reactions), the emergence of such a channel (1d) at 210 K may be accompanied by some deviations from Arrhenius behaviour with respect to the kinetics at higher temperatures:

$$
\begin{array}{lcll}
 & k^*_f & \rightarrow & OClO + Br \quad (1a) \\
BrO + ClO & \leftrightarrow \quad BrClO_2^* & \rightarrow & ClOO + Br \quad (1b) \\
 & k^*_r & \rightarrow & BrCl + O_2 \quad (1c) \\
 & \downarrow [M] & & \\
 & BrClO_2 \ (1d) & &
\end{array}
$$

An overall enhancement in k_1, the observed loss coefficient obtained from the decay of BrO radicals, would be anticipated as channel (1d) competes (along with (1a-c)) with

k*r. This would be manifested as a positive deviation of k_1 from Arrhenius behaviour at 210 K. However, no such deviation was observed.

Similarly, the emergence of channel (1d) would be accompanied by a decrease in the rate of one or more of the competing channels, as BrO and ClO are deposited in the dimer at the expense of the bimolecular products (i.e. k_{1d} competes with $k_{1a\text{-}c}$). No corresponding negative deviation from Arrhenius behaviour was observed in the plot of the temperature dependent k_{1a} data. However this would not be anticipated if channel (1a) proceeded directly through a BrOClO* intermediate:

$$BrO + ClO \leftrightarrow BrOClO^* \rightarrow OClO + Br \quad (1a)$$

Channel (1b) is more likely to decrease in accompaniment to the emergence of channel (1d) since it would most likely proceed through the same BrOOCl* transition state, thus k_{1b} would be in direct competition with k_{1d}. Likewise if channel (1c) were to proceed through a four centre (square) rearrangement of the BrOOCl isomer, leading to Br-Cl bond formation, then channel (1c) might also suffer at the expense of competion with (1d). However neither of these channels could be quantified under the experimental conditions.

Experiments monitoring all three channels at low temperatures (210 K or below), may stand a better chance of evidencing channel (1d). Furthermore the existence of channel (1d) is likely to be more profound at lower temperatures, due to an increased thermal lifetime of any $BrClO_2$* adduct and hence an increased probablility of quenching to a stable state. Given that the polar stratosphere can reach temperatures as low as 185 K during an extreme winter, further investigation at such temperatures may prove important. However, the chemical system employed here prevented further cooling of the reaction vessel below 210 K, since the saturated vapour pressure of Br_2 precluded BrO concentrations that were above the detection limits.

No previous measurements of k_1 or k_{1a} have been reported below 220 K. Avallone and Toohey[5] have presented atmospheric evidence to tentatively support the existence of a $BrClO_2$ adduct at 210 K. No overwhelming evidence to support or deny the existence

of $BrClO_2$ adduct formation has been gathered from either spectroscopic or pressure dependent analysis. As a result these experiments cannot unequivocally confirm or refute the suggestion by Avallone and Toohey that a $BrClO_2$ isomer is responsible for the anomalous BrO/Br_y ratios which they observed in the Arctic stratosphere.

No spectral evidence for an OBrO formation channel, (1e) of the BrO + ClO reaction was uncovered. As such an upper limit of $\alpha_{1e} = k_{1e}/k_1 < 0.02$ is placed upon this hypothetical channel and the stratospheric OBrO concentrations reported by Renard *et al.* remain unaccountable.

6.6 References

[1] Yung, Y. L; Pinto, J. P.; Watson, R. T.; Sander, S. P. *J. atmos. Sci.* **1980**, 37, 339.

[2] DeMore, W.B.; Sander, S.P.; Golden, D.M.; Hanson, R.F.; Kurylo, M.J.; Howard, C.J.; Ravishankara, A.R.; Kolb, C.E.; Molina, M.J. *Chemical Kinetics and Photochemical Data for use in Stratospheric Modeling;* JPL publication **97**-4; California Institute of Technology, Pasadena.

[3] Scientific Assessment of Ozone Depletion **2002**, World Meteorological Organisation Report no. 47.

[4] Cox, R. A.; Rowley, D. M.; Percival, C. J.; Lee, A. M.; Hynes, R.; Bloss, W. J.; Mossinger, J. C. *Coupled Bromine Chemistry Affecting Stratospheric Ozone (COBRA) Report*, **2000**.

[5] Avallone, L. M.; Toohey, D. W.; Schauffler, S. M.; Pollock, W. H.; Heidt, L. E.; Atlas, E. L.; Chan, K. R. *Geophys. Res. Lett.* **1995**, 22, 831.

[6] Avallone, L. M. and Toohey, D. W. *J. Geophys. Res. – Atmos.* **2001**, 106, 10411.

[7] Wahner, A.; Callies, J.; Dorn H. P. *Geophys. Res. Lett.* **1990**, 17, 497.

[8] Wahner, A.; Schiller, C. *J. Geophys. Res. – Atmos.* **1992**, 97, 8047.

[9] Gleghorn, J. T. *Chem. Phys. Lett.* **1997**, 271, 296.

[10] Gomez, P. C. and Pacios, L. F. *J. Phys. Chem. A.* **1999**, 103, 739.

[11] Papayannis, D.; Kosmas, A. M.; Melissas, V. S. Chemical Physics **2001**, 243, 249.

[12] Harwood, M.H.; Rowley, D.M.; Cox, R.A.; Jones, R.L. *J. Phys. Chem. A* **1998** 102, 1790.

[13] Sander, S. P. and Friedl, R. R. *J. Phys. Chem.* **1989**, 93, 4764.

[14] Friedl, R. R. and Sander, S. P. *J. Phys. Chem.* **1989**, 93, 4756.

[15] Turnipseed, A. A.; Birks, J. W.; Calvert, J. G. *J. Phys. Chem.* **1991**, 95, 4356.

[16] Renard, J. B.; Pierre, M.; Robert, C. *J. Geophys. Res.* **1998**, 103, 25383.

[17] Li, Z. *J. Phys. Chem. A* **1999**, 103, 1206.

[18] Rattigan, O.V.; Jones, R.L.; Cox, R.A. *Chem. Phys. Lett.* **1994**, 230, 121.

[19] Hinshelwood, C.N.; Pritchard, C. R. *J.C.S.* **1923**, 123, 2730.

[20] Knauth, H.D.; Alberti, H.; Clausen, H. *J. Phys. Chem.* **1979**, 83, 1604.

[21] Wilmouth, D. M.; Hanisco, T. F.; Donahue, N. M.; Anderson, J. G. *J. Phys. Chem. A.* **1999**; 103(45); 8935-8945.

[22] Cox, R.A.; Sheppard, D.W.; Stevens, M.P. *J. Photochem.* **1982**, 19, 189.

[23] Orlando, J. J.; Burkholder, J. B.; Bopegedera, A. M. R. P.; Howard, C. J. *J. Mol. Spectrosc.* **1991**, 145, 278.

[24] Laszlo, B.; Huie, R.E.; Kurylo, M.J. *J. Geophys. Res.-Atmos.* **1997**, 102, 1523.

[25] Wahner, A.; Ravishankara, A. R.; Sander, S. P.' Friedl, R. R. *Chem. Phys. Lett.* **1988**, 152, 107.

[26] Gilles, M.K.; Turnipseed, A.A.; Burkholder, J.B.; Ravishankara, A.R.; Solomon, S *J. Phys. Chem. A* **1997** 101, 5526.

[27] Wahner, A.; Tyndall, G. S.; Ravishankara, A. R. *J. Phys. Chem. A* **1987**, 91, 2734.

[28] Harwood, M. H.; Rowley, D. M.; Freshwater, R. A.; Cox, R. A.; Jones, R. L. *J. Chem. Soc. Faraday Trans.* **1995**, 91, 3027.

[29] Curtis A. R.: Sweetenham W. P. *FACSIMILE, AERE Harwell publication R12805: Computer Science and Systems Division, Harwell Laboratory, Oxfordshire, U.K.* **1987**.

[30] Bedjanian,Y.; Laverdet,G.; Le Bras,G. *J. Phys. Chem. A* **1998**, 102, 953.

[31] Sander, S.P.; Watson, R.T. *J. Phys. Chem.* **1981**, 85, 4000.

[32] Burkholder, J. B.; Mauldin, R. L.; Yokelson, R. J.; Solomon, S.; Ravishankara, A. R. *J. Phys. Chem.* **1993**, 97, 7597.

[33] Parr, A. D.; Wayne, R. P.; Hayman, G. D.; Jenkin, M. E.; Cox, R. A. *Geophys. Res. Lett.* **1990**, 17, 2357.

[34] Stevens, P. S. and Anderson, J. G. *J. Phys. Chem.* **1992**, 96, 1708.

[35] DeMore, W.B.; Tschuikow-Roux, E. *J. Phys. Chem.* **1990**, 94, 5856.

[36] Burkholder, J.B.; Orlando, J.J.; Howard, C.J. *J. Phys. Chem.* **1990**, 94, 687.

[37] Knight, G.; Ravishankara, A.R.; Burkholder, J.B. *J. Phys. Chem.* **2000**, 104, 11121.

[38] Hills, A. J.; Cicerone, R. J.; Calvert, J. G.; Birks, J. W. *J. Phys. Chem.* **1988**, 92, 1853.

[39] Basco, N.; Dogra, S. K. *Proc. R. Soc. London A* **1971**, 323, 417.

[40] Toohey, D. W.; Anderson, J. G. *J. Phys. Chem.* **1988**, 92, 1705.

[41] Poulet, G.; Lancar, I. T.; Laverdet, G.; LeBras, G. *J. Phys. Chem.* **1990**, 94, 278.

[42] Clyne, M. A. A.; Watson, R. T. *J. Chem. Soc. Faraday Trans.* **1997**, 73, 1169.

Chapter 7: Summary and Concluding Remarks

The results reported in this thesis constitute the first comprehensive studies of the ClO + ClO and ClO + BrO reactions using broad band absorption spectroscopy. A study of the BrO + BrO reaction at ambient temperature is also reported. Wherever possible, full channel specific information on the different product channels has been investigated. Moreover, complicating secondary chemistry in all of these systems has been thoroughly investigated. In all of the halogen monoxide systems investigated, sensitivity analyses have been carried out to validate the uniqueness of the kinetic parameters obtained and to quantify the effect of secondary chemistry on the values reported. Specific issues such as the possible formation of OBrO in the BrO self reaction and in the BrO + ClO reaction have been addressed. The possibility of stabilised adduct formation in the BrO + ClO reaction has also been investigated, and tentatively rejected.

The results reported in this thesis, since they concern the principal ozone depleting reactions in the Springtime Polar Stratosphere have profound atmospheric implications, which are only properly quantifiable through modelling studies. However, the rate of the ClO + ClO reaction reported in this study is greater across the entire temperature range than those results reported in the most recent NASA evaluation[1] and the only other subsequent study.[2] Simplistically it would be expected that the incorporation of this data into an appropriate model would lead to enhanced ozone destruction with respect to simulated results using *any* previous kinetic data for the ClO + ClO reaction.

The atmospheric implications of the BrO + ClO kinetic parameters measured in this work are less clear. The BrO + ClO reaction plays a destructive role in atmospheric ozone chemistry at all latitudes since its overall rate coefficient is greater than those governing the XO self-reactions and the stratospheric abundances of ClO and BrO are lower at midlatitudes than those observed in polar regions. The NASA evaluation adopts the kinetic parameters measured by Friedl and Sander.[3] These authors reported a weaker negative temperature dependence of the overall BrO + ClO rate coefficient than that measured during the course of this study. The Arrhenius parameterisation of

Friedl and Sander intersects with that reported here at approximately 260 K. This suggests that the BrO + ClO reaction is responsible for less ozone depletion at higher temperatures and more depletion at lower temperatures than those figures calculated on the basis of the NASA evaluated BrO + ClO kinetic data. The implications of these findings are complex given the temperature profile across the three dimensional atmosphere. Simplistically this suggests ozone destruction *via* the BrO + ClO reaction is significantly underestimated during the polar winter. The implications at midlatitudes cannot be postulated readily given the variation in stratospheric temperature with altitude (typically ranging between 220 and 275 K).

These assertions are based upon crude approximations and sophisticated atmospheric modelling is required to assess the quantitative implications of the kinetic data reported in this thesis. However, to a first approximation, it appears that the current understanding of stratospheric chemistry may have led to underprediction of the true rate of polar ozone depletion, due to weakness in the database describing the ClO + ClO and BrO + ClO reactions. It has been suggested that the timescale of polar ozone recovery may have been underestimated, given the stratospheric cooling associated with global warming and the negative temperature dependencies of the key radical/radical reactions. The results presented here suggest that a further delay in the onset of polar ozone recovery may be anticipated.

The kinetic studies reported in this thesis demonstrate the immense power of time resolved UV visible spectroscopy in the investigation of halogen monoxide radical kinetics. Since the first investigation of the 'bimolecular disappearance of chloric oxide radicals' was reported using flash photolysis in 1952 by Porter and Wright, this thesis cannot justifiably claim precedence to this finding. Nonetheless, the subsequent development of detectors in flash photolysis has allowed the gradual increase in the amount of information to be gathered from a flash photolysis experiment, and the use of CCD detection of UV/ visible absorption is arguably a further step. Specifically, the acquisition of sequential, broad wavelength coverage spectra of a photolysed gas mixture - in many ways a direct automated analogue of the 'photographic plate' method of detection - confers many clear advantages.

The identification of absorbing species in the gas mixture is the most obvious of these, and instantly opens up the potential observation of unexpected absorbing species. The quantification of absorbing species is also vastly improved over single wavelength techniques, insofar as entire spectral fitting is adopted. In particular the use of 'differential' fitting of spectrally structured absorbers is a very powerful way of completely accounting for changes in time resolved absorption underlying structured spectra.

A subtle advantage of differential fitting is the incremental shifting of the wavelength scale of the high pass filtered experimental versus reference spectra in optimising this fit. Over the course of a day of experiments, small drifts (<0.1 nm) in the wavelength calibration of the spectrograph were noticed, and were completely accounted for in the spectral fitting routines used in this work. Since other studies have typically used single or dual wavelength temporal monitoring of UV absorbance to obtain kinetic information, and since the wavelengths in these studies were typically chosen to coincide with the maxima of highly resolved vibronic spectral features, the occurrence of analogous wavelength drifting could have profound consequences on the results obtained. Simple calculations show that even a 0.1 nm drift off the centre of a peak of 0.5 nm FWHM would reduce the effective peak maximum by 15%. Such a change in a reference absorption cross-section used for single or dual wavelength UV absorption spectroscopy would have profound implications for kinetic parameters obtained for non first order processes.

Indeed, the provision of high quality absorption cross sections for species of interest has been a strong focus of the work reported in this thesis. For ClO radicals in particular, this work constitutes the most comprehensive study of the differential cross section carried out to date. The calibrating of the ClO cross section in the structured region of the spectra with a variety of wavelengths in the spectral continuum demonstrates the arbitrary nature of choosing a single continuum wavelength. Indeed, the extraction of different ClO cross sections with the choice of different continuum wavelengths for calibration highlights the strong reliance of these ClO cross section measurements on previously reported spectral measurements. Ultimately this reliance probably explains why the most ambitious and exciting result in this thesis - the simultaneous monitoring of ClO, Cl_2O_2 and the parent molecule Cl_2O, showing the

mass balance of the system, was not repeatable. Despite this, the monitoring of the entire ClO differential spectrum as a function of time provided the most highly constrained measure of its time resolved concentration available to date.

The power of the broad band technique was particularly evident in the ClO + BrO study reported in chapter 6. Here the ability to monitor ClO, BrO and the OClO product simultaneously and accurately using differential spectroscopy was unique to this work. Moreover, careful manipulation of the radical source chemistry enabled the arrangement of effectively *pseudo*-first order conditions of BrO decay in excess ClO, greatly simplifying kinetic analysis. This simplicity of kinetic analysis is - in part - another advantage of the data quality obtained from the CCD monitoring. The analysis of broad band spectra returns time resolved concentrations, which are directly comparable with the kinetic model. Thus, returning to the ClO dimerisation kinetics, a trivial solution to the governing differential equations could be fit to the observed time resolved data.

The halogen monoxide self- and cross- reactions which have formed the focus of these studies show mechanistic similarities. All three combinations of reactions between ClO and BrO radicals (*i.e.* ClO + ClO; BrO + BrO and ClO + BrO) exhibit negative temperature dependencies (although the temperature dependence of BrO + BrO was not the focus of these studies) which is attributable to the initial formation of a radical association complex, with an energetic barrier to the product channels lying at lower energy than the entrance channel. The possibility of collisional stabilisation of the first formed X_2O_2 species was observed for the Cl_2O_2 species and has been reported at low temperatures for the Br_2O_2 species from the respective self-reactions.[4] The production of a $BrClO_2$ isomer from the BrO + ClO reaction at 210 K is tentatively rejected. The analytical advantages afforded by the CCD were pushed to the limit in the search for any stabilised adduct of the BrO + ClO reaction at the lowest temperature. No unequivocal evidence, denying the existence such an adduct has been presented, but together, the lack of any convincing pressure dependence, spectroscopic evidence and deviation from (higher temperature) Arrhenius behaviour, suggests it was not formed in the reaction vessel at 210 K.

Further work incorporating a new cooling facility in the laboratory would enable further investigation of halogen oxide radical chemistry at temperatures relevant to the polar stratosphere.

A pressure dependent investigation of the BrO + ClO at temperatures below 210 K may provide new information about the possible existence of an adduct between these radicals. A different chemical scheme (perhaps incorporating CH_3Br as a source) would need to be adopted, given the constraint imposed by the vapour pressure of Br_2 at low temperature.

Investigation of the termolecular ClO + ClO kinetics to a temperature of 185 K would provide an comprehensive understanding of the basic kinetics. The ability to monitor all three transient chlorine oxide absorbers simultaneously with the CCD apparatus was hampered by weaknesses in the reference cross sections (ClO, Cl_2O_2). The key advantage in measuring the differential ClO cross section accurately during this study was afforded by the high quality of time resolved ClO absorbance data. The precision and accuracy associated with this quantity facilitated the back extrapolation to the immediate post-flash, where the system was reduced from a three absorber (ClO, Cl_2O_2, Cl_2O) to a two absorber problem (ClO, and Cl_2O). The Cl_2O absorbance could not be independently quantified relative to the Br_2 absorption due to stoichiometric complexities arising from a Cl_2 impurity. However, the use of a different photochemical system (e.g. excess $Cl_2/OClO/N_2$) would preclude the need to account for the underlying Cl_2O absorption, facilitating the broad band measurement of the absolute (encompassing the differential structure) ClO cross section. Furthermore, this accurate determination of the smooth ClO cross section would facilitate a determination of the ClO dimer cross section. Undertaken as a function of temperature and pressure, this could reveal information about the nature of any Cl_2O_2 isomers formed and refine the associated solar photolysis rate(s).
Reliable reference cross sections for all three chlorine oxide absorbers may permit an accurate fit to the three spectra simultaneously, providing a mass balance check on the chemical system.

The advantages of the flash photolysis / CCD / UV absorption apparatus over pre-existing techniques are most evident when monitoring transient species whose

absorbance spectra show structural features. Hence future investigation into other gas phase reactions involving halogen oxide radicals (e.g. ClO + HO_2, ClO + IO) would be expected to extend and improve the current kinetic database. Similarly, investigation of other reactions involving structured absorbers such as NO_2 would play to the advantages of the CCD.

7.1 References

[1] DeMore, W.B.; Sander, S.P.; Golden, D.M.; Hanson, R.F.; Kurylo, M.J.; Howard, C.J.; Ravishankara, A.R.; Kolb, C.E.; Molina, M.J. *Chemical Kinetics and Photochemical Data for use in Stratospheric Modeling;* JPL publication **97-4**; California Institute of Technology, Pasadena.

[2] Bloss, W.J.; Nickolaisen, S.L.; Salawitch, R.J.; Friedl, R.R.; Sander, S.P. *J. Phys. Chem. A* **2001**, 105, 11226.

[3] Friedl, R. R. and Sander, S. P. *J. Phys. Chem.* **1989**, 93, 4756.

[4] Harwood, M.H.; Rowley, D.M.; Cox, R.A.; Jones, R.L. *J. Phys. Chem. A* **1998** 102, 1790.

Appendix 1: The Effect of Instrument Function on Cross Section

Observed radiation associated with any electronic transition has a natural line width governed by Heisenberg's uncertainty principle. However, the ability to detect monochromatic radiation using a dispersive detection system is subject to the instrument function of this system, which directly influences the observed line width. Even purely monochromatic light passed through a diffraction spectrograph will appear to be spread over a range of apparent wavelengths upon its detection. The extent of this spread is determined by the instrument function of the detection system which, in turn is dependent upon the spectral resolution. In the case of the spectrograph/CCD detection system employed in this work, the spectral resolution is a function of the entrance slit width and dispersion of the spectrograph.

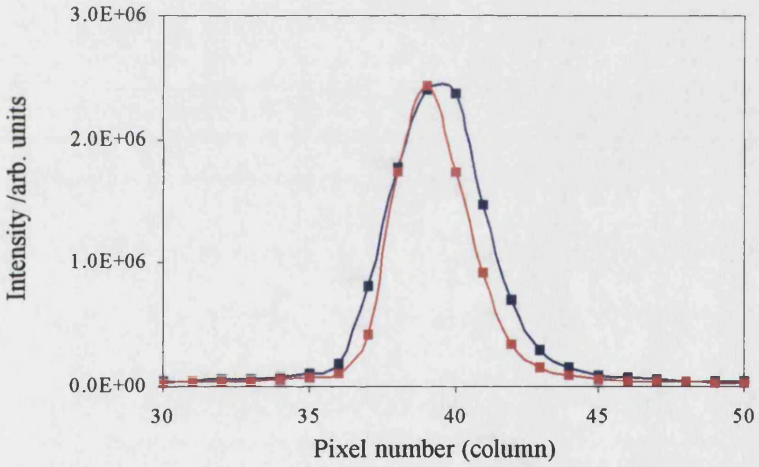

Figure A1.1: A mercury singlet recorded at the CCD employing entrance slit widths of 25 μm (red) and 50 μm (blue). The magnitude of the red data has been normalised to the peak of the blue data for ease of comparison.

The effect of the instrument function is illustrated by figure A1.1 which shows a singlet emission line from a mercury spectrum. The peak shown in red was recorded with a spectrograph entrance slit width of 25 μm whilst that shown in blue was recorded with a slit width of 50 μm. Both clearly show finite widths but the blue peak is clearly wider, showing a broader spread of value in the wavelength axis of the CCD. The blue

peak is said to be recorded at lower resolution and this resolution is estimated by the width of the singlet at half the value of the maximum intensity (full width half maximum, FWHM). Thus as the entrance slit width increases the spectral resolution decreases, giving rise to a larger FWHM value. The spectral resolution was observed to decrease smoothly with increasing entrance slit width, as shown by figure A1.2. The instrument function was readily parameterised by fitting a Gaussian function to the recorded mercury emission line associated with a given combination of spectral settings.

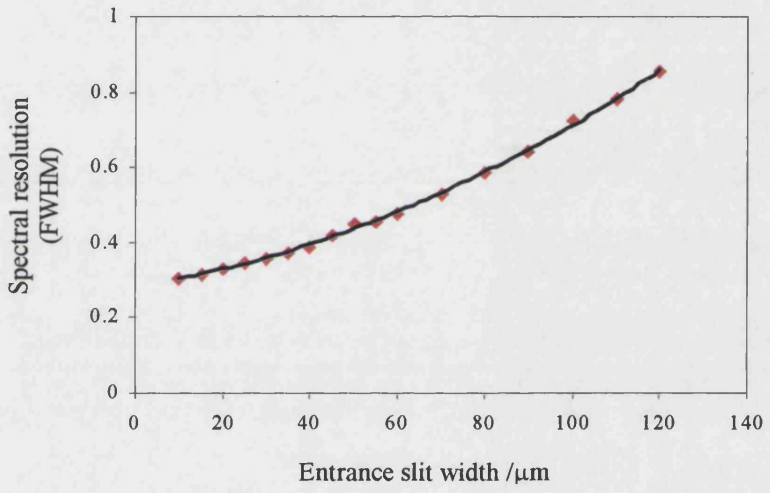

Figure A1.2: Effect of spectrograph entrance slit width on spectral resolution.

Decreasing the resolution associated with the detection system serves to broaden the apparent line widths of any spectral features upon observation at the CCD. In practice, the effect of this upon broad spectral features is negligible. However, small molecules frequently show distinct spectral features where a progression of 'separately' resolved peaks are observed corresponding to transitions to discrete vibrational states below the dissociation continuum threshold. The magnitude of such vibronic structure (and indeed rotational fine structure, although the spectral resolution was too low for such observation in these experiments) is readily affected by the instrument function, since the natural widths of these transitions maybe comparable or smaller than the spectral resolution (FWHM) dictated by the instrument function.

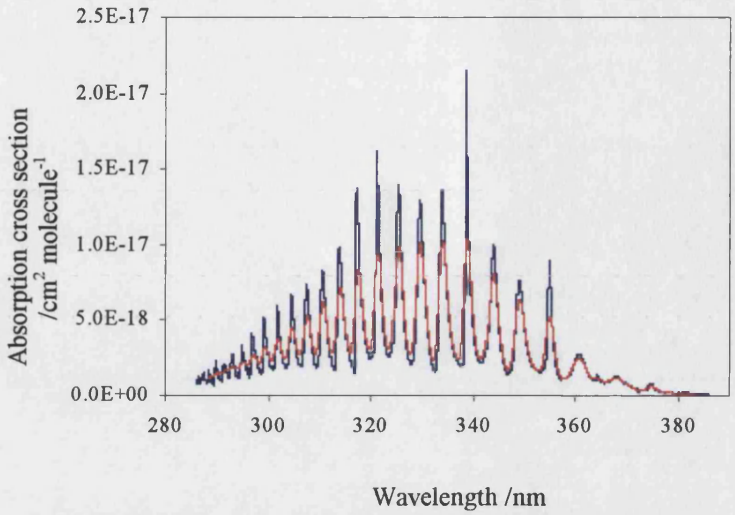

Figure A1.3: The effect of spectral resolution on strucured absorbance spectra. The blue and red spectra are associated with resolutions of 0.4 nm and 1.1 nm (FWHM).

This effect is illustrated by figure A1.3 which shows the 298 K BrO spectrum at spectral resolutions of 0.4 and 1.1 nm. Differential routines were employed to determine radical concentrations by fitting the structural magnitude of reference cross sections to that of recorded absorption spectra. Therefore it was imperative that the respective resolutions were matched to ensure accurate determination of radical concentrations and hence the kinetic parameters inferred from these temporally resolved concentrations.

Indeed many reference cross sections available in the open literature have been measured at higher spectral resolutions than those employed in this work. Hence smoothing routines were required prior to spectral fitting to ensure uniformity of resolution.

In theory appropriate smoothing must be applied to both the I_0 and I_t values used to generate the higher resolution spectrum, in order to calculate this absorption spectrum and subsequently the cross section at the lower resolution. However, in practice it is often possible to smooth the higher resolution cross sections directly:

(i) $$A_{smooth} = \ln\left(\frac{fI_0}{fI_t}\right) = \ln\left(\frac{fI_0 e^{-\sigma cl}}{fI_0}\right)$$

Generally the source lamps (xenon, deuterium) employed in making cross section measurements generate a smooth output across a broad wavelength regime. As a result f has a negligible effect on I_0 and smoothing affects only influences I_t. A_{smooth} is generally small hence $e^{-\sigma cl}$ can be approximated to $(1-\sigma cl)$ and the cross sections can be smoothed directly.

Sliding average routines were developed in FORTRAN to simulate these spectral smoothing procedures. The instrument function was well described by a Gaussian parameterisation (as described above) and this optimised function provided the basis for the smoothing kernel employed within the averaging procedure. In many cases the reference cross sections were recorded at much higher spectral resolutions than were employed in the kinetic studies described here. As a result the reference spectrum could be considered infinitely resolved with respect to the experimental spectra, and following smoothing, the resolutions were well matched. The quality of the resolution match could be investigated by spectral subtraction of fitted reference spectrum (by optimising the species concentration, satisfying the Beer-Lambert law) from the experimentally resolved spectrum. The absence of any systematic residual across the wavelength axis confirmed that the resolutions were commensurate.

In some cases the reference cross sections were not recorded at significantly higher resolution than employed in these kinetic experiemnts. In these instances the infinite resolution approximation was weak and systematic features were indeed observed in the residuals following spectral subtraction as illustrated by figure A1.4. The differential fit to the BrO structure appears reasonable, but a systematically structured residual is evident, where the structural features occur at half the oscillatory period of the original structure.

Weakness of the *infinite resolution* approximation ensured that the reference cross sections were oversmoothed. Thus the width parameter formalising the Gaussian kernel was incrementally increased (reducing the width of the function) and the smoothing routine was re-applied to the original reference spectrum and the residual quality re-analysed. This procedure was repeated until the appropriate Gaussian width was determined and no systematic residual was observed in the corresponding spectral deconvolution, indicating that the resolutions were uniform.

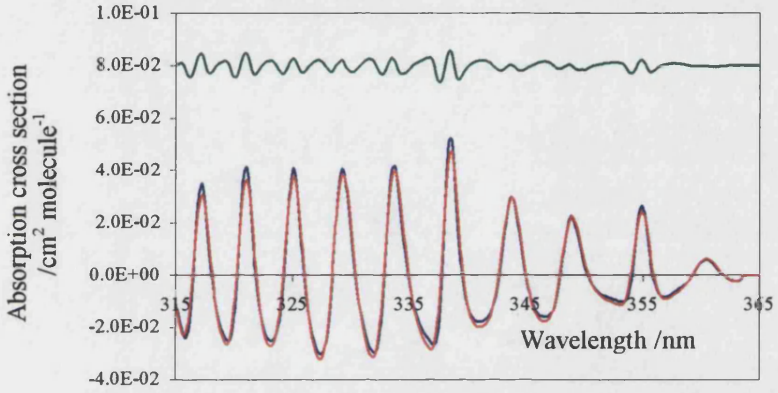

Figure A4.2: Differential fit of the BrO cross section (red) to the experimental absorption (blue). The residual spectrum (green) exhibits a distinct systematic feature, arising from oversmoothing of the reference BrO cross section.

Appendix 2: Temporal Resolution of the CCD Detection System

The temporal resolution of the CCD detection system is determined by the rate of row by row charge transfer (clocking rate) and the extent of illumination along the temporal axis. To ensure a good signal to noise ratio in the light intensity data 31 rows of the CCD are illuminated simultaneously. As a result each row on the CCD collects data for a time period defined by (number of illuminated rows) × (clocking rate). That is to say a 1MHz clocking rate gives rise to a 31 μs exposure time for any given CCD row. Hence any absorption spectrum generated from a row of CCD data represents an average of the true absortion spectrum over a finite time period defined by the parameters above. Since species concentrations are evaluated by fitting cross sections to this absorbance data at each row, a temporal distortion effect is imparted onto the resulting, temporally resolved concentrations. Figure A2.1 shows an example of this distortion in measured species concentration.

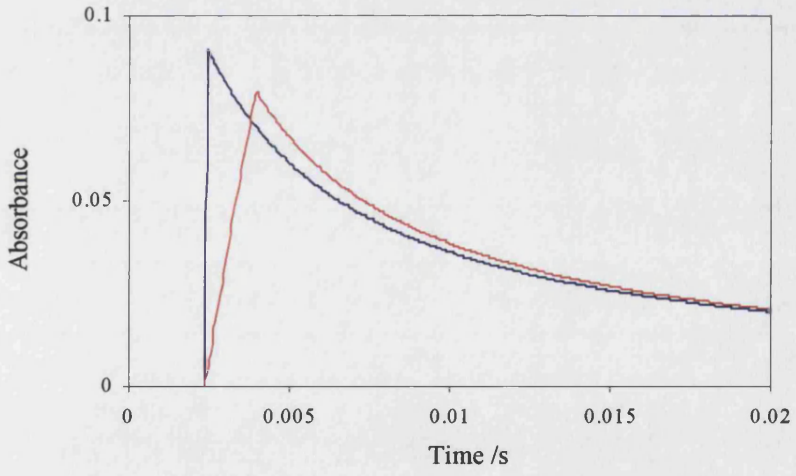

Figure A2.1: Effect of 31 row oversampling at the CCD. The red curve illustrates the temporal distortion to true data, shown in blue, imparted by the inherent temporal averaging.

Distortions in the kinetic parameters inferred from the temporally averaged concentration data are prevented by simulating the distortion within the model used to analyse a given data set. The true concentrations are simulated by classical or

numerical integration techniques according to the chemical system employed. The temporal distortion is then imparted to the simulated data by applying an averaging function. Finally the kinetic parameters under investigation are optimised by minimising the sum of squares of the residuals between the experimental data and this averaged simulation.

Appendix 3: Spectral Fitting Procedures

Concentrations of the absorbing species in the reaction cell are determined by numerically fitting appropriate reference cross sections to the experimental absorbance spectra, satisfying the Beer-Lambert:

(i) $A_\lambda = \sigma_\lambda c l$

Where, σ_λ is the cross section of the absorbing species at wavelength λ, c is the concentration of the absorber and l is the path length of the optical system. Therefore if two absorbers, x and y, are anticipated in the experimental absorbance spectrum:

(ii) $A_{exptl,\lambda} = A_{x,\lambda} + A_{y,\lambda}$

(iii) $A_{exptl,\lambda} = l(\sigma_{\lambda,x} c_x + \sigma_{\lambda,y} c_y)$

c_x and c_y, the concentrations of species x and y, are the only unknown terms in the latter expression, since $A_{exptl,\lambda}$, $\sigma_{\lambda,x}$ and $\sigma_{\lambda,y}$ are known for up to 298 wavelength resolved values. Therefore up to 298 equations could be constructed in this form. In practice, only two such equations need to be constructed for the simultaneous solution of c_x and c_y. Since these calculations are performed on every spectrum recorded by the CCD, a computational method is implemented.

A numerical routine called *Gaussian elimination with partial pivoting* (*GEPP*) is used to solve the simultaneous equations described above. It is an enlargement of the familiar method, where a common, but unknown term is eliminated between a pair of equations. An example of this is given below for a chemical scheme comprising three absorbing species (n = x, y or z), where the numerical coefficients are dummy values for $\sigma'_{\lambda,n}$:

(iv) $l(\sigma_{\lambda,x} c_x + \sigma_{\lambda,y} c_y + \sigma_{\lambda,z} c_z) = A_{exptl,\lambda}$

$\sigma'_{\lambda,x} c_x + \sigma'_{\lambda,y} c_y + \sigma'_{\lambda,z} c_z = A_{exptl,\lambda}$

$$
\begin{array}{lllllll}
3c_x & + & c_y & + & 2c_z & = & 14 \\
c_x & + & 2c_y & + & 3c_z & = & 11 \\
2c_x & + & 2c_y & + & c_z & = & 10
\end{array}
$$

Multiplying the first equation by –1 and the second by 3 and adding will eliminate c_x. Similarly, multiplying the first equation by –2 and the third by 3 then adding also eliminates c_x:

$$
\begin{array}{lllllll}
3c_x & + & c_y & + & 2c_z & = & 14 \\
 & & 5c_y & + & 7c_z & = & 19 \\
 & & 4c_y & - & c_z & = & 2
\end{array}
$$

In the same way, c_y can be eliminated by multiplying the new second and third rows by 4 and –5 respectively, then adding:

$$
\begin{array}{lllllll}
3c_x & + & c_y & + & 2c_z & = & 14 \\
 & & 5c_y & + & 7c_z & = & 19 \\
 & & & + & 33c_z & = & 66
\end{array}
$$

Back substitution evaluates c_x , c_y and c_z as 3, 1 and 2 respectively. The same problem can be solved in exactly the same way using matrix notation, labelling the matrices p, c and q from left to right:

$$
\begin{bmatrix} 3 & 1 & 2 \\ 1 & 2 & 3 \\ 2 & 2 & 1 \end{bmatrix} \begin{bmatrix} c_x \\ c_y \\ c_z \end{bmatrix} = \begin{bmatrix} 14 \\ 11 \\ 10 \end{bmatrix}
$$

The arithmetic operations performed only affect the coefficients and the constant terms, so the coefficient matrix, p is augmented with the constant matrix, q for clarity, where the broken line is usually omitted:

$$p\,|\,q = \left[\begin{array}{ccc|c} 3 & 1 & 2 & 14 \\ 1 & 2 & 3 & 11 \\ 2 & 2 & 1 & 10 \end{array}\right]$$

The same elementary operations are carried out on each row, converting the matrix to an upper triangular form:

$$\begin{bmatrix} 3 & 1 & 2 & 14 \\ 0 & 5 & 7 & 19 \\ 0 & 0 & 33 & 66 \end{bmatrix}$$

Back substitution can be systematically performed by multiplying the second row by 33, multiplying the third row by -7, then adding the results:

$$\begin{bmatrix} 3 & 1 & 2 & 14 \\ 0 & 165 & 0 & 165 \\ 0 & 0 & -33 & -66 \end{bmatrix}$$

Similar steps effectively performing back substitution result in a fully diagonalized matrix:

$$\begin{bmatrix} -495 & 0 & 0 & -1485 \\ 0 & 165 & 0 & 165 \\ 0 & 0 & -6 & -12 \end{bmatrix}$$

Dividing each row by the associated diagonal element gives rise to solutions for the concentrations of species x, y and z:

$$p\,|\,q = \left[\begin{array}{ccc|c} 1 & 0 & 0 & 3 \\ 0 & 1 & 0 & 1 \\ 0 & 0 & 1 & 2 \end{array}\right] \Rightarrow \begin{bmatrix} 1 & 0 & 0 \\ 0 & 1 & 0 \\ 0 & 0 & 1 \end{bmatrix} \begin{bmatrix} c_x \\ c_y \\ c_z \end{bmatrix} = \begin{bmatrix} 3 \\ 1 \\ 2 \end{bmatrix}$$

Gaussian Elimination performs satisfactorily in this example but circumstances can arise where the method crashes. During the elimination steps of the routine, if a zero is found on the diagonal axis of the augmented matrix, the computer will attempt to divide by zero. A useful strategy to guard against this eventuality is to rearrange the positions of the rows before each elimination step, ensuring the coefficient of largest magnitude is on the diagonal (and hence acts as the divisor). This process is called *pivoting* and has the added advantage of minimising accumulated rounding errors, again by using the largest coefficient value at each elimination step. Full pivoting requires the interchanging of both rows and columns, but this is unnecessary for our purposes, since the numerical system always consists of a small number of equations (one for each absorbing species in the cell). The method of interchanging rows only is described as *partial pivoting*.

Naturally, if *GEPP* were applied in this simple manner, a large amount of data arising from the 2-dimensional nature the CCD would be wasted. A summation process over the wavelength axis is applied to the data to prevent this data wastage, and hence reduce the uncertainty limits associated with the output data. The details of this method are beyond the scope of this thesis, but a brief example is given for completeness. The augmented matrix for the simple two-absorber (for species x and y) fit takes the following form where A_p refers to the experimental absorbance and σ_p is the absorbance cross section at a given CCD pixel:

$$\begin{bmatrix} \sum_{p=1}^{298} \sigma_{x,p}^{\,2} & \sum_{p=1}^{298} \sigma_{x,p}\sigma_{y,p} & \sum_{p=1}^{298} A_p\sigma_{x,p} \\ \sum_{p=1}^{298} \sigma_{x,p}\sigma_{y,p} & \sum_{p=1}^{298} \sigma_{y,p}^{\,2} & \sum_{p=1}^{298} A_p\sigma_{y,p} \end{bmatrix}$$

By applying the *GEPP* routine to the absorbance spectrum generated from each row of CCD data a plot of species concentration(s) versus time can be assembled.

Appendix 4: Temperature Profile of the Reaction Cell

The internal temperature profile along the length of the reaction cell was measured with a Pt-100 resistance thermometer which was calibrated against the literature temperatures associated with the triple point of water and the a carbon dioxide\acetone bath. The end-piece was removed from the effluent end of the reaction cell and the resistance thermometer was inserted into the cell on a wire disc residing in the gas flow (1000 SCCM, typifying that of a kinetic experiment). The disc supported the probe, preventing it from touching the internal walls of the reaction cell which were in direct contact with the recirculating coolant fluid. However, the semi-hollow nature of the disc prevented significant disruption of the gas flow around the probe. The temperature was recorded at a minimum of 10 cm intervals along the length of the cell once the probe had been allowed to reach thermal equilibrium with its surroundings. This process was undertaken at several temperatures programmed at the coolant bath. The results are shown in figure 1.

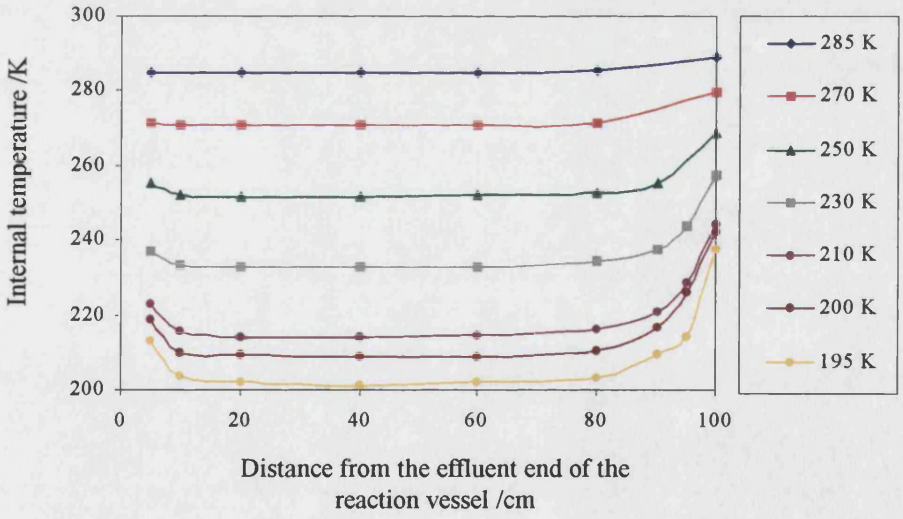

Figure A4.1: The internal temperature profile along the length of the cell. Respective temperatures at the coolant bath are indicated by the legend.

Despite the use of a pre-cooling unit a non-uniform temperature profile was observed along the length of the cell. The average temperature in the reaction cell was calculated by parameterising each profile with a high order polynomial then integrating this

function along the length of the cell. Figure A4.2 shows a plot of the actual (averaged) temperature against the programmed thermostatting bath temperature.

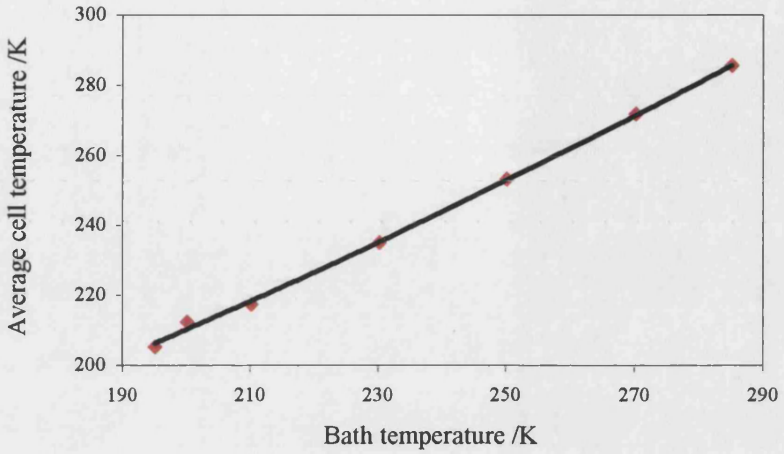

Figure A4.2: The mean temperature of the gas within the reaction cell versus the programmed temperature at the coolant bath.